School of Physics and Astronomy

Towards Optical Biosensors Based on Whispering-Gallery Modes in Microsphere Resonators

Muhammad H Islam

A THESIS SUBMITTED IN FULFILMENT OF THE REQUIREMENTS FOR THE DEGREE OF DOCTOR OF PHILOSOPHY

03-04-2019

STATEMENTS AND DECLARATIONS

STATEMENT 1

This thesis is submitted in partial fulfilment of the requirements for the degree of Doctor of Philosophy.

Signed 

Date 03/04/2019

STATEMENT 2

This work has not been submitted in substance for any other degree or award at this or any other university or place of learning, nor is it being submitted concurrently for any other degree or award (outside of any formal collaboration agreement between the University and a partner organisation)

Signed 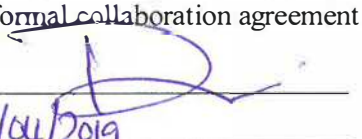

Date 03/04/2019

STATEMENT 3

I hereby give consent for my thesis, if accepted, to be available in the University's Open Access repository (or, where approved, to be available in the University's library and for inter-library loan), and for the title and summary to be made available to outside organisations, subject to the expiry of a University-approved bar on access if applicable.

Signed 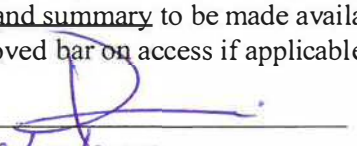

Date 03/04/2019

DECLARATION

This thesis is the result of my own independent work, except where otherwise stated, and the views expressed are my own. Other sources are acknowledged by explicit references. The thesis has not been edited by a third party beyond what is permitted by Cardiff University's Use of Third Party Editors by Research Degree Students Procedure.

Signed 

Date 03/04/2019

WORD COUNT 40 000

(Excluding summary, acknowledgements, declarations, contents pages, appendices, tables, diagrams and figures, references, bibliography, footnotes and endnotes)

Contents

Chapter 1

Introduction

1.1 Background and Motivation

Biosensors have been developed and used since many decades, for example in 1956 a sensor was developed for for oxygen detection [1]. Biosensors have nowadays become important devices in life science research, biomedical diagnostics, drug discovery, environmental monitoring, point-of-care monitoring of treatment and disease progression, food control, forensics, defence and security, among others. This development was driven by the ability of biosensors to enable detection of disease markers from biological samples, provide kinetic information pertaining to biomolecular interactions, monitor environmental pollutants and enable early detection of biowarfare agents [2, 3]. Owing to their widespread utility, the biosensor industry is currently worth billions of dollars with medical diagnostic companies accounting for the majority [4]. One widely commercialized optical biosensor system to date is the Biacore platform using surface plasmons of gold films [5].

The objective of this chapter is to provide a general introduction to biosensors, the necessity and challenges that exist in the field of biosensor research and different types and applications of biosensors.

1.1.1 Definition of biosensors

A sensor is a device that responds to its physical environment, for example to the surrounding gas or liquid, light, temperature, or pressure. The output of a sensor, encoding the response, is typically an optical or electrical signal. This output signal is then transmitted over a network for further processing and usage. The task of the sensor is therefore to convert a physical quantity into a signal suitable for further processing. The signal conversion inside the sensor takes place by an element called 'transducer', forming the integral part of a sensor device. The schematic of a sensor system is shown in Fig. 1.1.

A biosensor is a "biological sensor", an analytical device which provides quantitative information regarding biologically relevant quantities. A schematic of a biosensor system is shown in Fig. 1.2, and consists of the following components:

- An analyte, which is the substance of interest that is to be detected. For example, glucose is the "analyte" in a biosensor designed to detect glucose.
- A transducer, converting a biochemical signal to an electronic or optical sig-

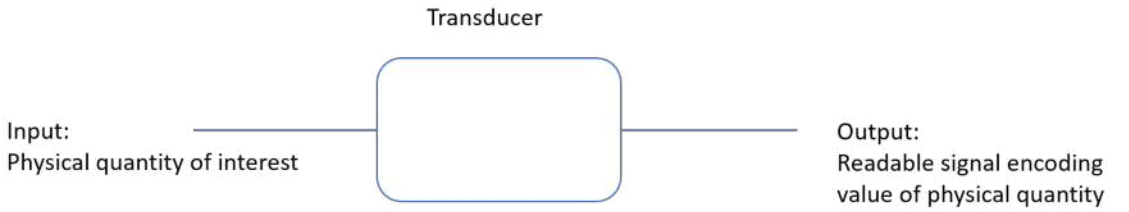

Figure 1.1: Schematic of a sensor system. The sensor system takes physical quantity as input and converts it into a suitable signal for processing at the output. The conversion takes place inside the transducer.

nal. A transducer in a biosensor is known as biotransducer and consists of two parts: a bioreceptor and a transducer. A molecule that specifically recognizes the analyte is known as a bioreceptor or biosensor recognition element. The biosensor recognition element is typically a binding protein such as an antibody which specifically binds with the analyte. However employing modern biotechnology techniques, biosensor recognition elements can be synthesized artificially. Typical biosensor recognition elements include antibodies, neuroreceptors, enzymes, nucleic acids (Deoxyribonucleic acid, DNA or Ribonucleic acid, RNA), molecular imprints and lectins [6]. The process of signal generation upon interaction of the biosensor recognition element with the analyte is termed biorecognition. The biosensor recognition element must be highly specific to the analyte and be stable under simple storage conditions. The choice of recognition elements depends on the required selectivity and specificity of the biosensor application.

The operation principle of a biosensor as shown in Fig. 1.2 can be explained as follows. In a biosensor system, analytes are introduced by an external unit. The bioreceptor of the sensor system binds or otherwise reacts with the analytes to create a physical or chemical response.

The bioreceptor is typically immobilised on a solid support, so that the sensor can be reused after cleaning. There are various methods to immobilize bioreceptors as explained in Sec. 5.3.

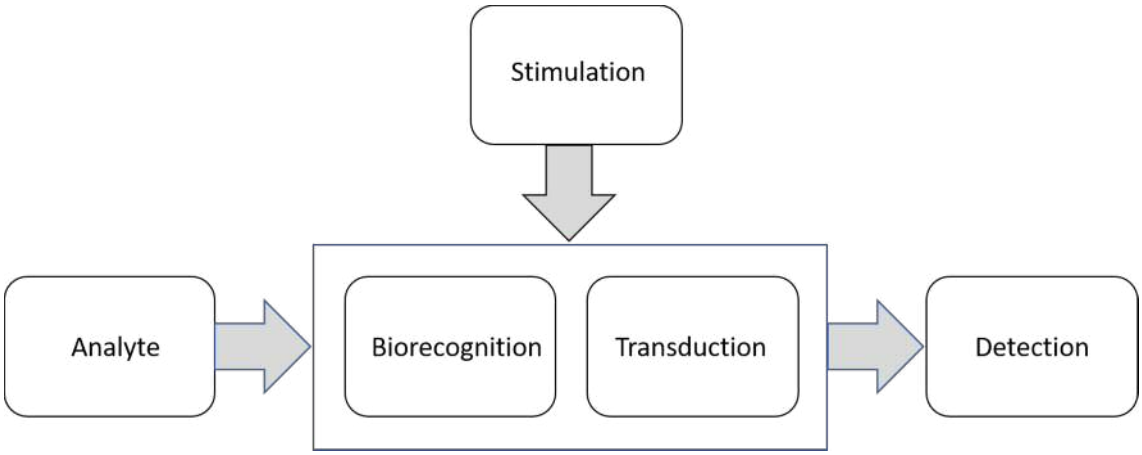

Figure 1.2: Operation principle of a Biosensor.

Stimulation into the biosensor system can be provided by optical, electrical, or other kinds of fields to extract a response as a result of biorecognition. External stimulation, is not always needed, for example, in the case of chemifluorescence, or electrical signals created by redox reactions. The transduction process transforms the bio recognition response into an optical or electrical signal. This signal is then detected by the detection unit. The detection unit is a signal processing system that converts the optical or electrical signal into a readable form [7].

1.1.2 Applications of biosensors

The field of biosensor technology has emerged as a topic of great interest in recent years in general health care monitoring, clinical analysis and diagnosis of disease, early detection and screening of disease, environmental bioagent detection to minimize the disaster of bioterrorism and spread of infectious diseases, food industry during the quality control processes, drug discovery and environmental pollution control. Biosensors provide many advantages in comparison to standard analytical detection methods such as minimal sample preparation and handling, faster analysis, simpler analysis methods, suitability for use by non-skilled personnel, and portability for field applications [8].

One of the most important applications where biosensors have been established is in blood glucose monitoring. Since the control of elevated levels of blood glucose in patients with diabetes decreases the complications, self-monitoring of blood glucose (SMBG) systems, and continuous glucose monitoring systems (CGMS) have become valuable tools for real-time information, enabling the patient to adjust medications, dietary regimes, and physical activity in order to achieve glycemic goals [9, 10, 11]. As the biosensors can give faster results, they are now widely used to determine and monitor glucose levels for diabetes management, in point of care testing (POCT) devices, SMBG, CGMS, and noninvasive glucose monitoring systems [12].

Although the development of glucose biosensor technology in POCT devices and glucose monitoring systems has been significantly improved during the last few decades, challenges remain, related to the achievement of accurate and reliable glucose monitoring [12]. For example, the American Diabetes Association (ADA) recommends the accuracy of a blood glucose POC assay to be within 5% of the measured value, which is not met by many POC devices. Biosensor technology is therefore presently less accurate than the methods used in central laboratories and needs to be improved [13].

Biosensor technology can also be used in screening of diseases such as cancer. Early diagnosis of cancer and other chronic diseases decreases the death rate and treatment expenses [14]. Biosensors can be designed as tools for early detection of cancer biomarkers. Biosensors for detection of cancer includes detection of biomarkers from tumors and body fluids by utilizing a suited recognition element. By measuring the levels of certain proteins emitted by the tumor cells, biosensors can detect whether a tumor is present, whether it is benign or cancerous and whether treatment has been effective in reducing or eliminating cancerous cells [15].

However, in order to be effective as POCT device in cancer detection, biosensors should be able to detect multiple analytes since most types of cancer involve multiple biomarkers. In addition to this, biosensors should provide an accuracy and reliability comparable to that of the laboratory techniques [16].

1.2 Biosensing Modalities

1.2.1 Types of biosensors

Biosensors demonstrated in the literature use a variety of transduction mechanisms. Based on the transducer operation principle, biosensors can be broadly categorised as shown in Fig. 1.3. Electrochemical biosensors dominate the current commer-

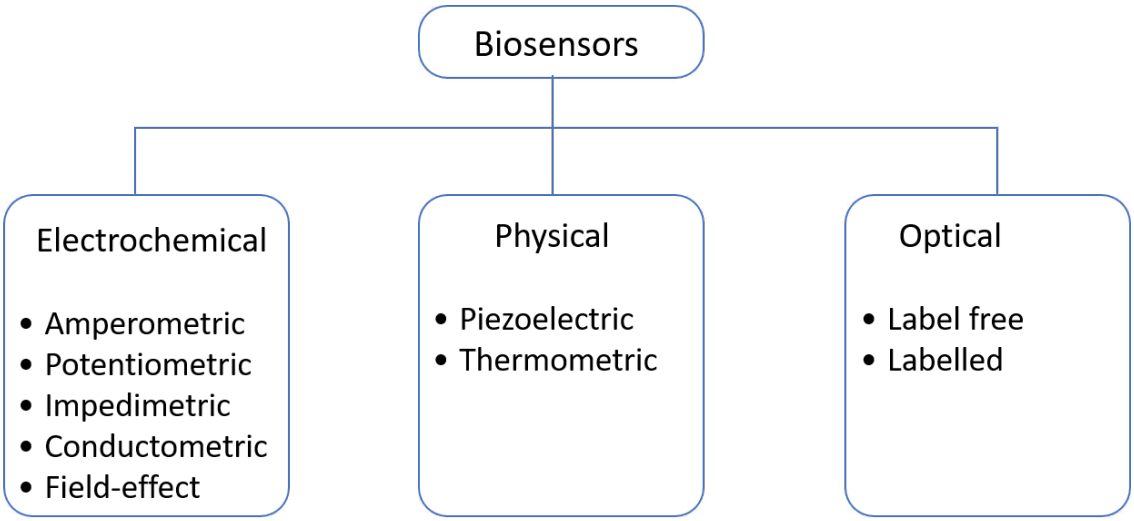

Figure 1.3: Types of biosensors according to the transducer operation principle.

cial market since the introduction of the first generation glucose oxidase (GOx) biosensor in 1962 [7]. Although biosensors employ a variety of recognition elements, electrochemical detection techniques use predominantly enzymes, known as redox enzymes, due to their specific binding capabilities. Electrochemical biosensors consist of a reference electrode, a counter or auxiliary electrode and a working electrode, also known as the sensing or redox electrode. The reference electrode is kept at a distance from the reaction site in order to maintain a known and stable potential. The working electrode serves as the transduction element in the biochemical reaction, while the counter electrode establishes a connection to the electrolytic solution so that a current can be applied to the working electrode. Since the electrodes should be both conductive and chemically stable platinum, gold and silicon compounds are commonly used. The reaction between the analyte and the enzyme in electrochemical biosensors would either generate a measurable current (amperometric), a measurable potential or charge accumulation (potentiometric) or measurably alter the conductive properties of a medium (conductometric) between electrodes, measurable impedance (impedimetric), and measurable current as a result of a potentiometric effect at the gate electrode of a transistor (field-effect) [17].

Physical biosensors use transduction mechanisms based on temperature or mechanical forces, and include thermometric and piezoelectric biosensors. Thermometric transduction exploit fact that biochemical reactions are associated with an enthalpy of reaction, which either produces or consumes heat. The change in temperature caused by the reactions between the analyte and the enzyme is measured [18]. Piezo-electric crystals such as quartz couple mechanical motion with an electric field. This can be used to electrically drive and read out a mechanical resonance of the crystal. The frequency of this resonance depends on the crystal geometry and

crystallographic orientation. This resonant frequency changes as molecules adsorb or desorb from the surface of the crystal, dominantly due to the change of mass, or mechanical impedance of a liquid in contact. A piezoelectric biosensor is thus based on the fact that changes in the mass, density, or viscosity of the analyte in contact with its active surface will change the resonant frequency of the sensor device. They are categorized according to the associated acoustic transducer into Bulk Acoustic Wave (BAW) and Surface Acoustic Wave (SAW) biosensors [19].

In an optical biosensor, the stimulation is provided in the form of an optical input, and the transducer produces an optical output. Recent advances in fiber optics and integrated optics, and the availability of microlasers have made optical biosensors an attractive alternative for many applications. The transduction process induces a change in the phase, amplitude, polarisation, or frequency of the input light in response to the physical or chemical change produced by the biorecognition process [20]. An early optical biosensor was reported in 1975 [21]. The increasing demand for a portable, real time detection and monitoring has attracted over the last decades research in the field of optical biosensors due to their speed, flexibility, low cost, and the advance of supporting optical technology [22].

1.2.2 Optical biosensors

Optical biosensors can be broadly classified into two general modes: label-free and label-based to detect the interaction between the analyte and biosensor recognition element. Biosensors which need a label in the form of fluorophores [23], quantum dots [24], magnetic particles [25] or radioactive molecules [26] to generate the optical signal by either colorimetric, fluorescent or luminescent method are known as label-based biosensors. Labels are either attached to the transducer or the analyte molecule. Upon analyte binding, the amount of the label is measured in the output signal. In label-free biosensors, the detected signal is generated directly from the intrinsic properties of the analyte molecules, such as mass, size, dielectric permittivity and impedance, when the analyte interacts with the biosensor recognition element.

Optical biosensors employ a number of transduction process as shown in Fig. 1.4. Phase change produced by a change in the real part of the refractive index (RI) provides a change of light polarisation, propagation, or spatial distribution. Amplitude change derived from absorption or reflection produces changes in the intensity of the sensing light. Frequency changes associated with biosensing utilize fluorescence or Raman scattering, where the optical signal generated is at a Stokes-shifted frequency. Biosensors can also utilize frequency shift by a nonlinear optical interaction mechanism such as second-harmonic generation [20].

1.2.2.1 Fluorescence and phosphorescence based sensors

The principle of the fluorescence process of a fluorophore molecule can be described as follows. Fluorescence occurs when a fluorophores molecule absorbs a photon at a given wavelength, and subsequently emits a photon, typically at a longer wavelength. The difference of excitation and emission wavelengths is called Stokes shift. In detail, the absorption of the excitation photon promotes the molecule from its electronic ground state to a higher energy state. This higher energy state is unstable, and the molecule eventually returns to its ground state on a time-scale of nano-seconds (ns) releasing the energy by emitting a photon. Internal relaxation between vibra-

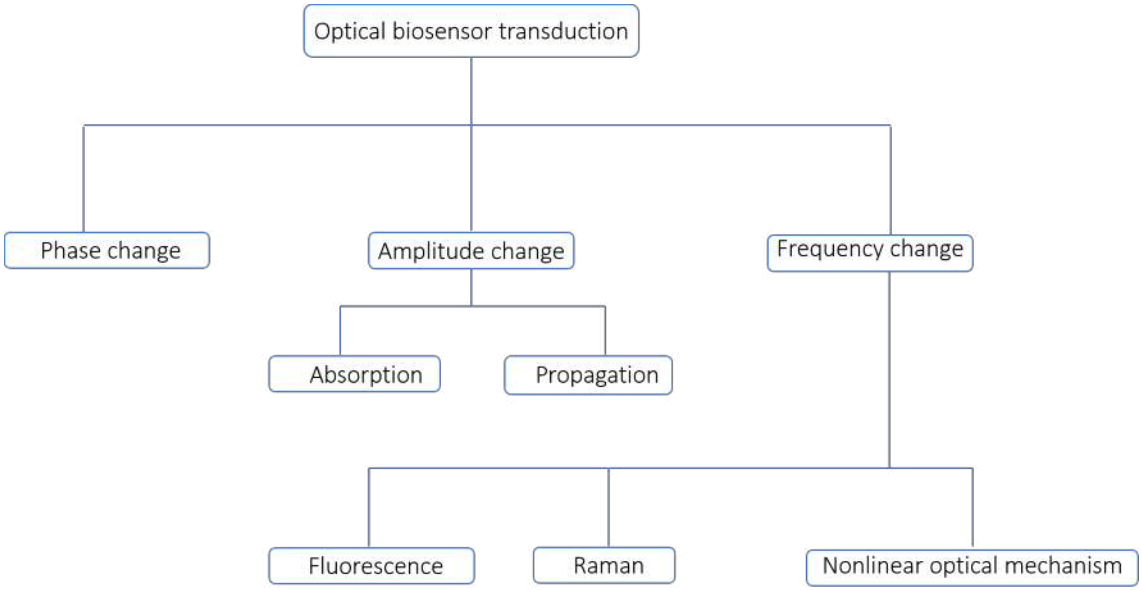

Figure 1.4: Transduction mechanisms of optical biosensors [20].

tional levels accurs typically on a timescale of picoseconds, via interaction with the environment This dynamics can be sketched in a Jablonski diagram as shown in Fig. 1.5. Advances in optical spectroscopy and microscopy in 1990's have made it possible to detect single molecules [27, 28]. Optical biosensors based on fluorescence [29] to detect single molecule are the most common form of optical biosensors [30], using the fact that fluorescent properties of most organic fluorophores are highly susceptible to environment changes [31], and simple protocols exist to attach them to biomolecules [32]. Fluorescent biosensors provide high sensitivity and another advantage is that they are in principle background free, i.e., they produce bright signal against a dark background [33]. The first chemically synthesized fluorescence probes for specific analytes became available in the 1980s [34]. Since then these type of biosensors have been used in the detection of nucleic acids [35], proteins [36], bacteria [37], viral agents [38] and in studying DNA hybridization [39].

The fluorescence sensing scheme can be direct or indirect. In the direct scheme, a change in the fluorescence property takes place as a result of the analyte binding with the biosensor recognition element. For example, the change in fluorescence intensity is measured when a fluorescent-labelled antibody (the biosensor recognition element) binds to the analyte. The fluorescence intensity is then correlated to the amount of analyte bound to the biosensor recognition element.

In the indirect sensing scheme a fluorescent ion is generally used. An ionic analyte will interact with the fluorescent ion to result in either displacement in case of ions of same charge or ion pair in case of oppositely charged ions with the fluorescent ion. Thus the fluorescent ion works as an optical transducer in response to biorecognition of a charged analyte [20]. The signal produced in this detection scheme is independent of the spectral properties of the analyte and suitable for analysis of charged analytes [40].

Fluorescence quenching, a process that decreases the fluorescence intensity, is one of the mechanisms used for biosensing. Such quenching is provided by Förster resonance energy transfer (FRET). If the emission spectrum of the so-called donor fluorophore overlaps with the absorption spectrum of the so-called acceptor fluo-

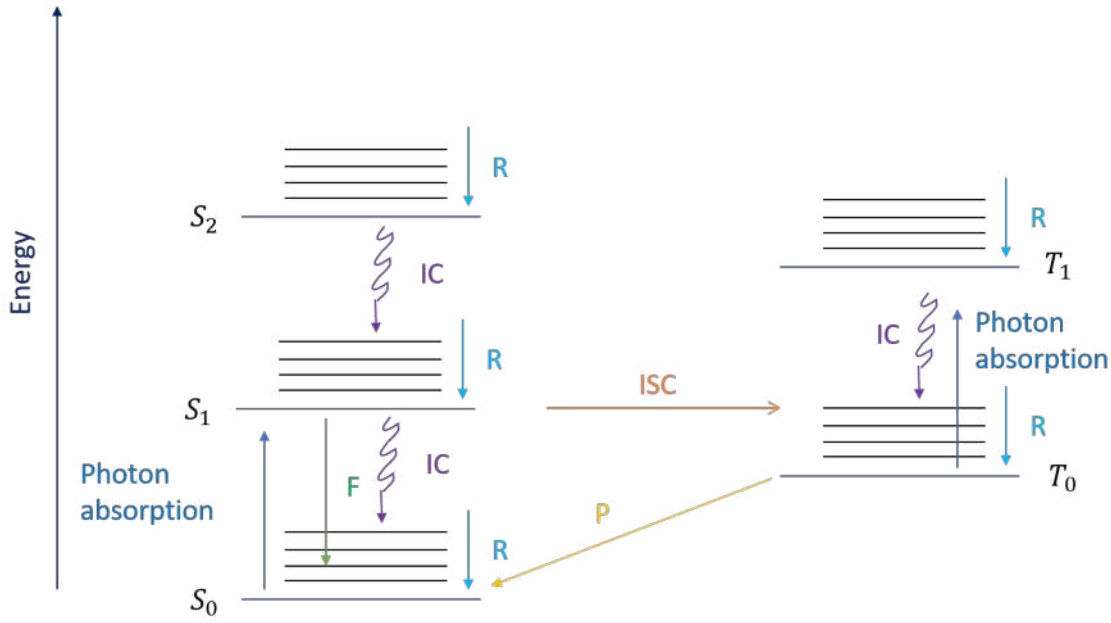

Figure 1.5: Jablonski diagram for a fluorescent molecule. S_0 is the singlet electronic ground state, S_1 is the singlet excited state, and T_0 is the lowest energy triplet state of the electrons. Both intersystem crossing (ISC) and internal conversion (IC) are non-radiative process. When a photon is absorbed the molecule moves from the ground state (S_0) to a higher energy state (S_1). After a rapid vibrational relaxation (R) the molecule returns to the ground state by emitting photons. This emission is known as fluorescence (F), and takes place over a ns timescale. The excited state S_1 can couple to T_1 through ISC, involving a spin flip. This is slow (µs) in organic molecules due to the weak spin-orbit interaction. After a rapid vibrational relaxation (R), the radiative process from T_0 to S_0, involving another spin-flip, is called phosphorescence (P) which takes place on a µs timescale. IC can take place from excited state S_1 to ground state S_0 via coupling to the environment, and is limiting the fluorescence quantum yield.

rophore, and the two fluorophores are in close proximity, typically closer than 10 nm, then the donor can transfer energy via the electrical near field (non-radiatively) to the acceptor fluorophore. The acceptor thereby acts as a fluorescence quencher. When a donor-acceptor pair is used to label two interacting molecules, i.e., analyte and biosensor recognition element, they can be used for biosensing. FRET can thus be used to measure the distance between donor and acceptor.

Recently advances allow both the donor and the acceptor molecules to be incorporated into single biological molecules such as proteins [41] and nucleic acids (e.g., molecular beacons) [42, 43]. When these sensing molecules are in their native conformation, the donor and the acceptor are in proximity and therefore low fluorescence signals from the donor are obtained. This results in quenching of the acceptor fluorescence. This can be changed by two mechanisms.

Firstly, upon interaction with the analyte, the donor can transfer the electron to become a positively charged unit. Therefore, photo excitation of the acceptor is now unable to induce electron transfer from the donor to the acceptor group. Consequently, there is no quenching of the acceptor fluorescence. Therefore, the optical transduction here is the appearance of the acceptor fluorescence in the presence of an analyte.

Secondly, a conformational change can occur upon analyte binding, which spatially separates donor and acceptor, causing an increase in the fluorescence from the donor [44]. This is used in molecular beacons.

The most commonly used fluorescent molecules in biosensors are organic dyes. They are safer and more convenient to use than radioactive tracers. Furthermore different fluorescent molecules can be used simultaneously, allowing for multiplex detection, provided that their emission or excitation spectra do not overlap. Thus biosensing with fluorophores is relatively simple, however some of the drawbacks of fluorescent labels are:

- They are potentially toxic.
- The fluorescence intensity depends on the local environment such as pH of the solution.
- They are susceptible to photo bleaching.
- Labelling with fluorescent tags requires trained personnel in a well equipped laboratory thus prevents its application where real-time detection or point of care service is required thereby increases the cost and time.
- The development of specific sensors for biochemically relevant analytes is challenging due to the fact that fluorescence probes might not have adequate water solubility, suitable affinity constants, and a spectral change upon ligand binding [33, 45].

The discovery of fluorescent proteins addresses the limitations of fluorescent labels in biosensors. The sources of these proteins are marine organisms such as the jellyfish Aequorea victoria that produce the green fluorescent protein (GFP) [46]. GFP is highly fluorescent, with a quantum efficiency of approximately 80% and is stable to heat (80-95 °C) and pH (5.5-12) [47].

However, stability of the immobilised protein depends heavily on the quality of the substrate itself. An ideal substrate should be able to retain protein functionality

with relatively high signal-to-noise ratios. It should also possess both high protein-binding capacity and long shelf life. The stability of the immobilisation can be improved by using a variety of immobilisation protocols in the preparation of the sensor, however the total immobilisation process is tedious. The other issue is that the intrinsic fluorescence of proteins is often low and requires excitation light in the ultra violet (UV) range of the spectrum [33]. Some of these limitations are overcome by using enzymes as labels.

Enzymes can be used in a biosensor to extract analyte from a sample matrix, followed by complexation with an antibody labeled with a secondary enzyme. The process can be described briefly as follows: The antigen is primarily immobilised on the surface of the substrate. The primary antibody binding to the immobilised antigen is then allowed to react with the enzyme-labelled secondary antibody. One of the widely commercialized enzyme based immunoassays is the enzyme linked immunosorbent assay (ELISA) [48].

Although labels can be used to enhance the signal, they have drawbacks. Presence of labels either on the analyte or the ligand molecules can structurally and functionally interfere with the assay, therefore can alter the binding properties and introduce systematic error to the biosensor analysis [49, 50]. If the labels are attached to secondary antibodies (indirect detection) instead of primary antibodies, they can potentially bind to off-target analytes which results in non specific detection. This is critical in microarrays where hundreds of analyte molecules are detected on a single sensing platform [51]. In addition to all these, in label-based assays, as the output signal is a measure of the amount of label and not the analyte itself, only indirect detection of the analyte is possible. Label-free biosensors have therefore become an alternative in recent times [52].

1.2.2.2 Label-free optical biosensors

The POCT biosensors have been used as a promising tool because of their lower cost and convenient use in medical diagnosis. In order to develop POCT biosensors the following properties are required: label-free, low cost, high sensitivity, and high selectivity. Out of many proposed methods, optical biosensors such as evanescent wave based, surface plasmon resonance (SPR) and optical cavity based biosensor are attractive because of their label free operation and high sensitivity. The optical biosensors can have high selectivity if the surface is functionalised such a way that the biosensor allows multiple analyte detection.

The first evanescent wave fiber optic biosensor was developed by Hirschfeld in 1984 and was further optimized by Sutherland et al. [53] and Andrade et al. [54]. Evanescent wave sensors rely on the principle of total internal reflection (TIR) for light propagation and guiding. TIR is observed at the planar interface between two dielectric media with different indices of refraction. TIR is described by Snell's law

$$n_1 \sin\theta_1 = n_2 \sin\theta_2 \,, \tag{1.1}$$

where n_1 and n_2 are the refractive indices of the medium in which light is incident and the surrounding medium, respectively; θ_1 is the incident light angle; and θ_2 is the angle of the transmitted light. Total internal reflection requires that $n_1 > n_2$ and occurs when the angle of incidence is greater than the critical angle, θ_c, given by

$$\theta_c = \arcsin(n_2/n_1)\,. \tag{1.2}$$

For $\theta_1 > \theta_c$, the transmitted light forms an evanescent wave, which decays exponentially with distance from the interface, with a decay length typically in the sub-wavelength regime, and of the order of 10-100 nm. Evanescent wave sensors can utilize a planar waveguide (WG) or a fiber geometry [44]. Evanescent wave biosensing can utilize a number of optical detection mechanism such as measurement of absorbance and fluorescence intensity. In order to measure the intensity fluorescence is generated from the analyte specifically binding with a biosensor recognition element which is immobilised on the surface of the WG or a fiber [20]. The penetration depth, d_p, the distance at which the intensity of the evanescent wave is $1/e$ of its value at the surface, is given [55] by

$$d_p = \lambda / \left(4\pi\sqrt{n_1^2 \sin^2\theta - n_2^2}\right) \tag{1.3}$$

An evanescent wave biosensor scheme using a planar WG for fluorescence sensing is shown in Fig. 1.6.

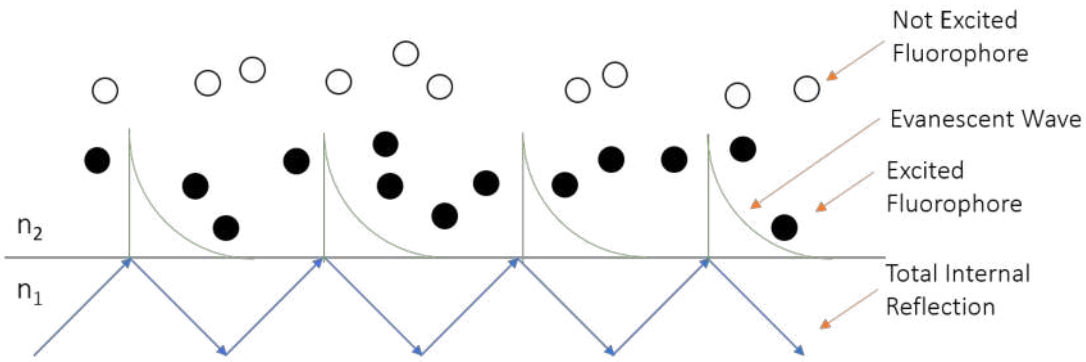

Figure 1.6: Fluorescence sensing scheme to excite the fluorophores with the evanescent field. n_1 and n_2 are the refractive indices of the medium in which light is incident and the surrounding medium, respectively. If the fluorophores are positioned in close proximity to the WG surface the evanescent field protruding from the WG will excite the fluorophores to induce fluorescence.

In 1983, Nylander and Liedberg exploited surface plasmon waves excited in the Kretschmann geometry [56] of attenuated total reflection (ATR) for biosensing [57]. Biosensors based on resonant excitation of surface plasmon waves are known as surface plasmon resonance (SPR) biosensors. The first commercial SPR biosensor was launched by Biacore International AB based on the Kretschmann geometry of the attenuated total reflection method and angular modulation. Since then SPR biosensors have been developed by several companies based on the same principle. These include the IBIS system developed by British Windsor Scientific Ltd. (U.K.), Johnson & Johnson Clinical Diagnostics (United Kingdom), SPR-670 and SPR-CELLIA systems by Nippon Laser and Electronics Laboratory (Japan) and Spreeta SPR sensor developed by Texas Instruments Inc.(USA).

The concept of SPR biosensors can be explained as follows. Let us consider a planar interface composed of two semi-infinite homogeneous, non magnetic, isotropic media as shown in Fig. 1.7. Since the materials involved are non-magnetic, only transverse magnetic (TM) modes can be supported by the metal-dielectric interface

[58]. If the dielectric constant of the metal ϵ_m is negative and its absolute value is smaller than the dielectric constant of the dielectric material ϵ_d then a surface plasma wave (SPW) can propagate along the interface, decaying exponentially to both sides away from the interface. SPW at a metal-dielectric interface can be excited by a light wave if the component of light's wave vector that is parallel to the interface matches that of the surface plasma wave. However, SPWs cannot be excited directly by light incident onto a smooth metal surface since the propagation constant of SPWs at a metal-dielectric interface is larger that of propagating light in the dielectric. For this reason, the SPW are typically excited from a second dielectric medium of higher RI. Prism couplers in the Kretschmann configuration are the most popular choice, shown in Fig. 1.8. In the Kretschmann configuration,

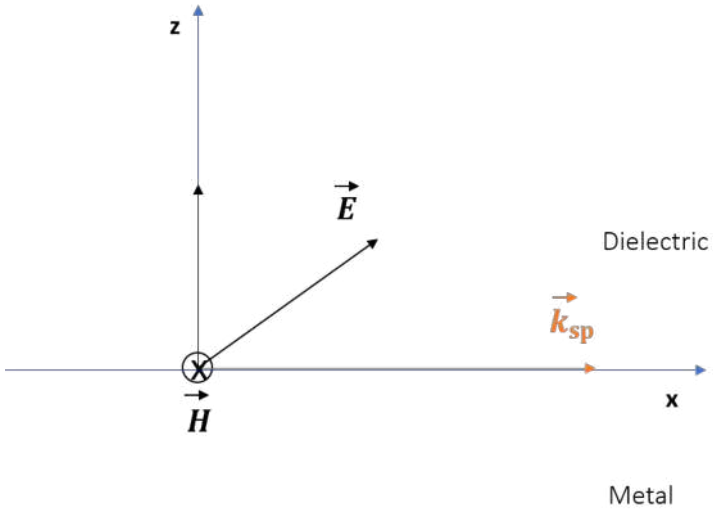

Figure 1.7: Metal-dielectric geometry. The metal occupies the region $z < 0$, while the dielectric medium occupies the region $z > 0$. TM wave at the metal-dielectric interface.

the metal layer is chosen sufficiently thin to that the SPW penetrates the metal film up to the interface to the prism of higher RI, where it can couple to propagating light. Fig. 1.8.

The propagation constant of the SPW excited is controlled by the angle of incidence. Neglecting the influence of the prism, the coupling condition may be expressed as [59]

$$\sqrt{\epsilon_p}\sin\theta = \sqrt{\frac{\epsilon_m \epsilon_d}{\epsilon_m + \epsilon_d}} \tag{1.4}$$

where θ denotes the angle of incidence, ϵ_p, ϵ_m and ϵ_d denote dielectric functions of the prism, the metal film and the dielectric medium and $\epsilon_p > \epsilon_d$. The SPW field penetrates into the dielectric, probing the dielectric medium. A small change in the RI of the dielectric produces a change in the propagation constant of the SPW [60]. Changing the refractive index close to the metal layer, the resonance angle θ shifts. Thus, the binding of an analyte at the surface manifests as a change in the resonance angle [59].

Label-free optical biosensors can also use optical resonators. The basic sensing principle of this type of biosensors is based on monitoring the frequency shifts of

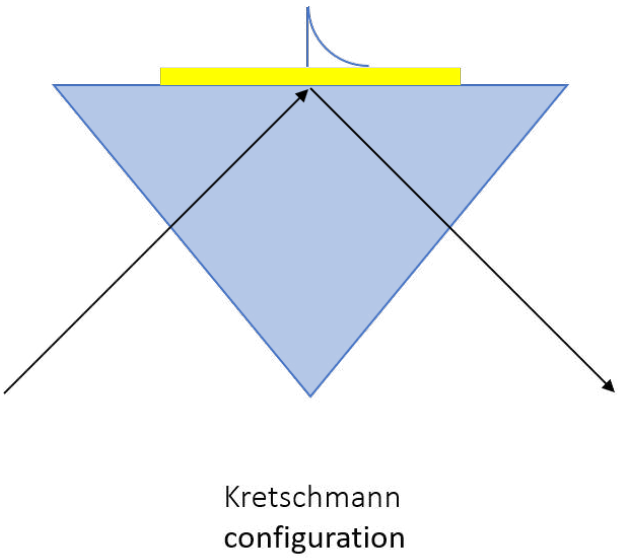

Figure 1.8: Excitation of surface plasma wave on smooth metal surface by attenuated total reflection. (a) Kretschmann configuration, (b) Otto configuration.

the optical resonators. There are a number of resonator devices including microrings, microdisks, microtoroids, capillary tubules and photonic crystal cavities have been reported as the transduction element in biosensor development. Among the different types of optical biosensors based on optical resonators, microsphere (MS) based biosensor is especially promising. Light can be confined at the surface inside the MS by total internal reflection (TIR) at specific wavelengths known as optical resonances. The optical resonance of a MS is also known as whispering gallery mode (WGM). The WGM modes of the MS are excited by the evanescent field from an optical fibre or WG by frustrated total internal reflection (FTIR). Sensitive biosensors based on WGM have been reported [61]. Since light takes many round trips around the MS the analyte is probed multiple times, which makes the biosensor highly sensitive. The quality factor (Q factor) of the resonance is given by the number of oscillations until decay, which is proportional to the number of round-trips. The Q factor of dielectric micro spheres has been reported as high as 4×10^6 for a diameter of 30 µm at 790 nm wavelength [62], corresponding to about 20000 round-trips. Therefore, with this high Q factor, micro spheres are potential candidates for highly sensitive biosensors.

The principle of optical sensors based on microsphere resonators is as follows: when light is confined inside a dielectric resonator and brought to interfere with itself, only specific optical frequencies can reside within the resonator without suffering large losses. If the geometry or material properties of the resonator changes, resonance parameters, for example, light intensity is also changed. The resonator thereby acts as an optical signal transducer [63]. The transduction mechanism for bio sensing is measurement of the shift of WGM's when evanescent field interacts with surrounding environment. Since the light in WGMs can orbit many thousand times before escaping the resonator, the detection sensitivity of this method as compared to planar surface based methods can be enhanced greatly [64]. It has been estimated that the smallest detectable molecular weight that can be detectable in a WGM based sensor is around 50 Da with a corresponding quality factor (Q) of a given resonance of ˜ 2×10^6 [65]. This is lower than the detection limit of SPR

based biosensors can detect, i.e., 180 Da [66]. Biosensors based on WGMs in microspheres resonators have therefore attracted a significant level of interest to detect single molecules and their interactions [30, 67, 68]. When different biorecognition molecules are immobilised on different microspheres, the array can be used to detect multipleanalytes.

1.3 Thesis Outline

This thesis is arranged in the following chapters.

Chapter 1 presented a brief overview of the development of optical label-free biosensors and motivation to develop novel label-free optical biosensors to meet the demand of single molecule detection.

In Chapter 2, relevant background theory will be discussed. In our proposed sensor device the evanescent wave from the WGs will be coupled to microspheres by frustrated total internal reflection (FTIR). Therefore, a brief theory on WGs and WGMs in microspheres will be given, including their quality factor (Q) and the shift of resonance frequency due to a change in RI. Differential interference contrast (DIC) microscopy will be presented as it has been an important characterization technique in this work. The principle of curing a material by ultra-violet (UV) light will be briefly discussed as the cladding layer of the WGs has been cured by UV light.

In Chapter 3, a portable biosensor device will be proposed to detect change of RI in the surrounding medium. Choice of material, fabrication process of the device, characterization of the WGs and curing process of the separation layer will be discussed. Optical method to measure thickness of the WGs will also be discussed.

In Chapter 4, the setup used for measurements in this work will be discussed. A software for triggering the camera and laser in the setup as well as for data acquisition from the measurements has been developed and is presented.

In Chapter 5 results of the experiments and future improvements will be presented, including refractive index sensing.

In Chapter 6 a summary of this work will be presented.

A range of appendices include additional detailed information referenced in the thesis.

Chapter 2

Background

In this thesis we have realised a novel biosensor device based on the whispering gallery modes (WGM) of polystyrene microspheres, attached on the surface of an array of WGs, providing multiplexing and evanescent coupling to the WGMs. In this chapter, we will introduce relevant underlying concepts. These include planar WGs in Sec. 2.1, optical resonators in Sec. 2.2, WGMs in Sec. 2.3, the background for the implemented detection scheme in Sec. 2.4, and quantitative DIC microscopy to determine height and RI of several structures and materials in Sec. 2.5.

2.1 Planar waveguides

Optical WGs are the basic elements for confinement and transmission of light over a distance, and can be used to connect photonic devices. They are fundamental to the operation of many optoelectronic devices, such as the WGs providing optical confinement in semiconductor lasers. Furthermore, they form important active or passive photonic devices by themselves, such as WG couplers and modulators [69]. In this section, the basic characteristics of a dielectric WG will be discussed.

2.1.1 Structure of planar waveguides

The basic structure of a planar dielectric optical WG consists of a longitudinally extended high-index optical medium, called the core, which is transversely surrounded by low-index media, called the cladding. Guided optical waves propagates in the WG along its longitudinal direction. These waves travel inside the core by repeated total internal reflection (TIR), and form distinct optical modes.

2.1.2 Modes in planar waveguides

An optical mode is a solution of Maxwell's wave equation without sources. Assuming non-magnetic materials, so that the permeability $\mu = 1$, the wave equation can be written as

$$\nabla^2 \mathbf{E}(\mathbf{r}) = \frac{n^2(\mathbf{r})}{c^2} \frac{\partial^2 \mathbf{E}(\mathbf{r})}{\partial t^2}, \tag{2.1}$$

where $\mathbf{E}$ is the electric field vector, $\mathbf{r}$ is the position vector, $n(\mathbf{r})$ is the index of refraction, and c is the speed of light. Assuming a harmonic time-dependence, the

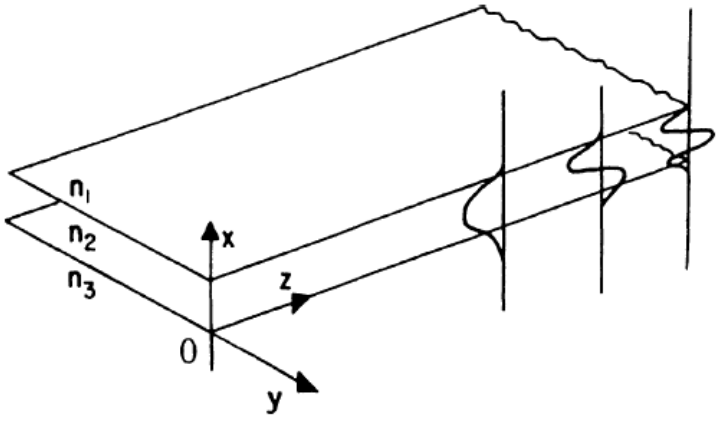

Figure 2.1: A diagram of a planar WG structure. Refractive indices are n_1, n_2 and n_3 for cladding, core, and substrate layers respectively. It is assumed that $n_1<n_3<n_2$. Three modes are shown with distributions of the electric field in the x-direction. Adapted from [70].

solution of Eq. (2.1) can be written as

$$\mathbf{E}(\mathbf{r},t) = \mathbf{E}(\mathbf{r}) \exp(i\omega t) \ , \tag{2.2}$$

where ω is the angular frequency. Substituting Eq. (2.2) into Eq. (2.1), we obtain

$$\left[\nabla^2 + k^2 n^2(\mathbf{r})\right] \mathbf{E}(\mathbf{r}) = 0 \, , \tag{2.3}$$

where $k = \omega/c$ is the wave number. For a uniform plane wave propagating in the z direction, which is a translationally invariant direction of the structure considered, and x and y being the cross-section of the structure, we find

$$\mathbf{E}(\mathbf{r}) = \mathbf{E}(x,y) \exp(-i\beta z) \ , \tag{2.4}$$

where β is the propagation constant. Eq. (2.3) then can be written as

$$\left[\frac{\partial^2}{\partial x^2} + \frac{\partial^2}{\partial y^2} + k^2 n^2(\mathbf{r}) - \beta^2\right] \mathbf{E}(x,y) = 0 \tag{2.5}$$

Let us now consider a simple three-layer planar WG structure as shown in Fig. 2.1. The layers are assumed to be infinite in y and z directions. For transverse electrical (TE) waves, we have $E_x = E_z = 0$, and Eq. (2.4) becomes

$$E_y(x,z,t) = \mathcal{E}_y(x) \exp(i\omega t - i\beta z) \tag{2.6}$$

Since the layers are assumed to be infinite in y and z directions, there is no explicit y and z dependence of $\mathbf{E}(\mathbf{r})$, and therefore Eq. (2.5) becomes

$$\left[\frac{\partial^2}{\partial x^2} + k^2 n^2(\mathbf{r}) - \beta^2\right] E_y(x) = 0 \tag{2.7}$$

The solutions of Eq. (2.7) are either sinusoidal or exponential functions of x in each of the regions, depending on whether $(k^2 n_i^2 - \beta^2)$, $i = 1,2,3$, is positive or negative. Assuming $n_1 < n_3 < n_2$, the mode shape changes as a function of β as shown in

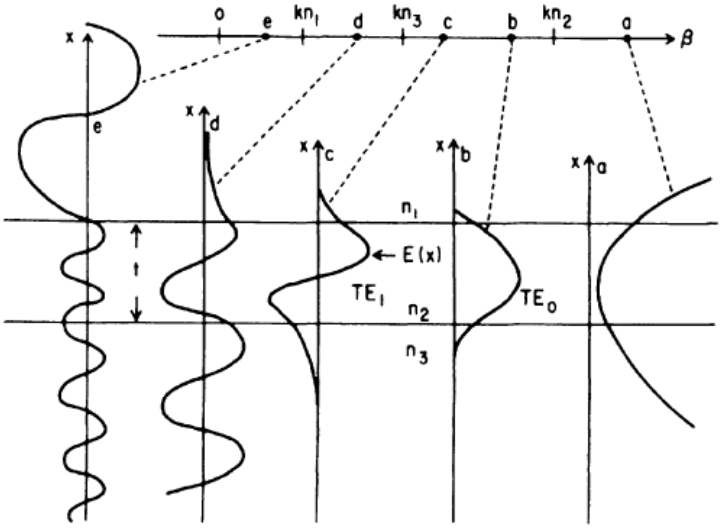

Figure 2.2: Possible modes in the planar WG sketched in Fig. 2.1. The distribution of the electric field in x direction is shown for different ranges of β. Adapted from [70].

Fig. 2.2. For $\beta > kn_2$, $E_y(x)$ is exponential in all the three layers and resulting mode is exponentially diverging, forming a so-called anti-bound mode, as shown in Fig. 2.2a. For $n_2 < \beta < kn_3$, bound modes in the core are forming, see (b) and (c), featuring exponentially decaying tails into cladding and substrate layers. For $kn_1 < \beta < kn_3$, the mode is radiating in the substrate, see (d), and is therefore unbound. For $\beta < kn_1$, the mode is radiating in substrate and superstrate, see (e), and is also unbound.

Using the boundary conditions of Maxwells equations, we find

$$\tan(hd) = \frac{p+q}{h\,(1-pq/h^2)}\,, \tag{2.8}$$

where $q = \sqrt{(\beta^2 - k^2\,n_1^2)}$, $h = \sqrt{(n_2^2\,k^2 - \beta^2\,)}$, $p = \sqrt{(\beta^2 - k^2\,n_3^2)}$, and d is the core thickness. This equation can be graphically solved by plotting the RHS and LHS of Eq. (2.8) for a given d, to determine the discrete propagation constants β. Since wavelength and the materials are often fixed parameters in a given application, the number of guided modes that can be supported depends on the thickness d of the core layer. The intersection points on the horizontal axis are the discrete values of β. This corresponds to the guided modes in the WG.

The possible regimes are summarised in Table 2.1 in terms of the propagation constant β and also the associated ranges of the transverse propagation constant k_3 in the substrate.

2.2 Optical resonators

In this section we discuss two basic types of optical resonators.

Table 2.1: Propagation constants and various mode types.

Case	β	p	q
Anti-guided	$kn_2 < \beta$	imaginary	imaginary
Guided	$kn_3 > \beta > kn_2$	imaginary	imaginary
Substrate radiation	$kn_1 < \beta < kn_3$	$0 \ldots k\sqrt{n_3^2 - n_1^2}$	imaginary
Radiation	$0 < \beta < k_{n_1}$	$k\sqrt{n_3^2 - n_1^2} \ldots kn_3$	$0 \ldots kn_1$

2.2.1 Fabry-Pérot resonator

When a set of two or more mirrors are arranged to cause light to propagate in a closed path is called an optical resonator or optical cavity. There are two basic types of optical resonators such as the standing wave resonator and the travelling wave resonator [71]. A Fabry-Pérot (FP) resonator is a standing wave optical resonator. A steady state radiation field in an optical resonator depends on the wavelength of the radiation and on the mirror spacing. Steady state means that both the amplitude and the phase reproduce themselves after one round trip [72]. Both the conditions are accomplished if the resonator length is an integral multiple of half the wavelength, and the mirrors have unity reflectivity. Only in this case standing waves inside the resonator can be obtained with nodal intensity points on the mirror surfaces.

A FP resonator consists of two highly reflecting mirrors with some small transmissivity, separated by a distance d as shown in Fig. 2.3. Light at a wavelength λ entering the resonator will be partially reflected by mirror 1. The transmitted intensity is then reflected back and forth between the two mirrors. The incoming light thus makes multiple round trips within the cavity. With each reflection a part of the intensity is coupled out of the FP resonator in both the forward and backward direction.

Let us consider a ray of light incident at an angle θ as illustrated in Fig. 2.3. The path difference p between laser beams 1 and 3 can be obtained from the geometry as

$$p = \overline{A_1A_2} + \overline{A_2B} \tag{2.9}$$

From the figure we find that

$$A_2B = \overline{A_1A_2}\cos(2\theta) \tag{2.10}$$

Using equation Eq. (2.10) in Eq. (2.9) we get, using the relation $\overline{A_1A_2} = d/\cos(\theta)$, and $\cos(2\theta) = 2\cos(\theta)^2 - 1$,

$$p = 2d\cos(\theta)\,, \tag{2.11}$$

where the factor of two is accounting for the two reflections between plates, and θ is the angle of incidence of the beam inside the cavity. The phase difference δ is then given by

$$\delta = 2\pi\frac{np}{\lambda} \tag{2.12}$$

where n is the RI of the medium in the cavity. The intensity transmittance T is given by

$$T = \frac{1}{1 + F\sin^2(\delta/2)}\,, \tag{2.13}$$

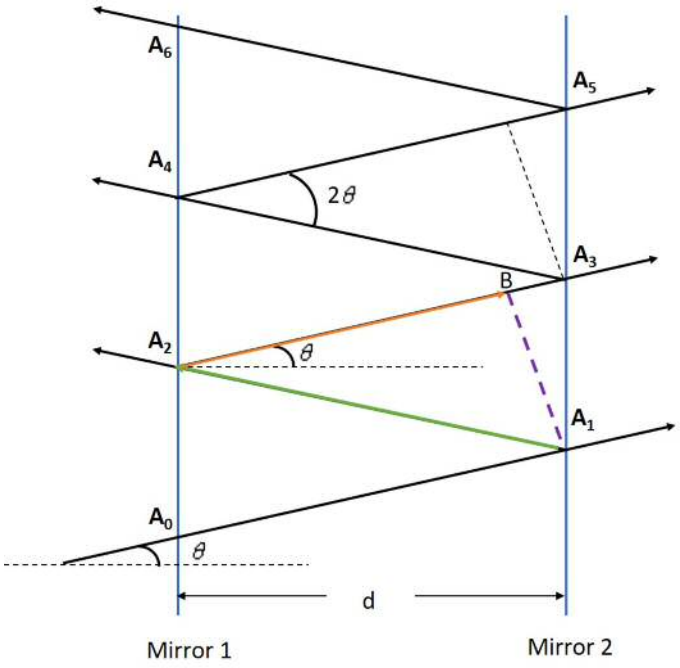

Figure 2.3: Sketch of a Fabry-Pérot resonator including reflected and transmitted light rays.

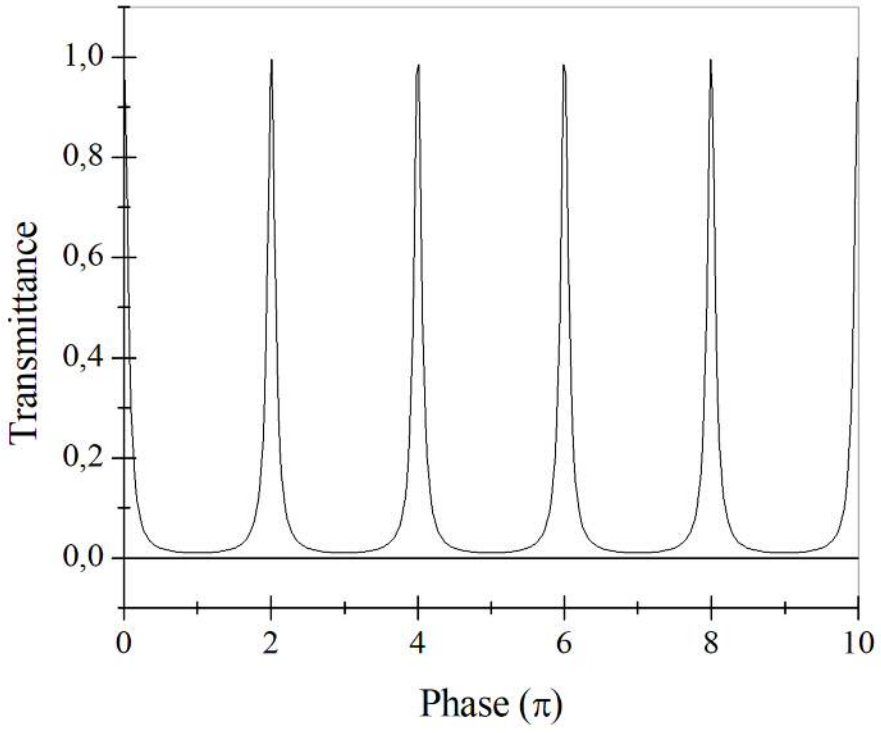

Figure 2.4: The transmittance of a Fabry-Pérot resonator of finesse $F = 100$ is as a function of the phase difference δ, according to Eq. (2.13).

where F is the coefficient of finesse, which depends on the amplitude reflection coefficient r of the mirrors, and is given by

$$F = \frac{4r^2}{(1-r^2)^2}\,. \tag{2.14}$$

Constructive interference occur when the phase difference δ between adjacent beams is an integer multiple of 2π. From Eq. (2.12) we see that the condition for constructive interference is met when the optical path difference np is an integer number of wavelengths. Since δ is proportional to p and thus to the mirror spacing d, the spectrum shown in Fig. 2.4 as function of δ is of the same shape as function of d. The condition for resonant wavelengths λ_q is given by

$$\lambda_q = \frac{2dn}{q}\,, \tag{2.15}$$

where q is a natural number, known as axial or longitudinal mode order, which represents the number of wavelengths for one round-trip inside the resonator cavity. A resonator thus exhibits a periodic sequence of resonance frequencies

$$\nu = \frac{c}{\lambda_q} = \frac{qc}{2dn} \tag{2.16}$$

which are separated by the free spectral range (FSR)

$$\nu_{\mathrm{FSR}} = \frac{c}{2dn} \tag{2.17}$$

According to Rayleigh criterion the separation of the peaks corresponding to two closely separated wavelengths must be at least the full width half maximum for the two peaks to be resolved. If we assume that the half maximum occurs when $T = 0.5$ then Eq. (2.13) can be rearranged as

$$\sin\frac{\delta}{2} = \frac{1}{\sqrt{F}} \tag{2.18}$$

For small phase change δ is small therefore, we can use the following approximation that $\delta \approx \sin(\delta)$, so that Eq. (2.18) yields $\delta \approx 2/\sqrt{F}$, and the FWHM (full width half maximum) in frequency is

$$\nu_{\mathrm{FWHM}} \approx \nu_{\mathrm{FSR}}\frac{4}{2\pi\sqrt{F}} = \nu_{\mathrm{FSR}}\frac{1-r^2}{\pi r} = \nu_{\mathrm{FSR}}/\mathcal{F} \tag{2.19}$$

where $\mathcal{F}$ is the finesse. The quality factor of the resonator is defined as the ratio of a nominal resonant frequency to the FWHM of the transmittance peaks

$$Q = \frac{\nu}{\nu_{\mathrm{FWHM}}} = \frac{\nu}{\nu_{\mathrm{FSR}}}\mathcal{F} \tag{2.20}$$

Using mirror with high reflectivity close to unity results both in high finesse $\mathcal{F}$ and quality factor Q.

2.2.2 Whispering gallery resonator

In 1910, John William Strutt, also known as Lord Rayleigh, published a study of sound waves along the inside wall of the dome of St Paul's Cathedral in London. St Paul's Cathedral is an ovally shaped structure of 32 m in diameter and situated 30 m above the floor. In his study he showed that a whisper against the wall at any point is audible to a listener with an ear held to the wall at any other point around the gallery. In his publication 'The Problem of the Whispering Gallery' [73], Lord Rayleigh attributed this phenomenon to the refocusing effect of the curved surface as the sound travels along the gallery wall. The resulting circulating modes are known as whispering gallery modes (WGMs). Lord Rayleigh also suggested that such propagating modes would exist for electromagnetic waves.

WGM exist in dielectric microspheres for electromagnetic waves at certain resonance frequencies [63], so that microspheres can act as high quality optical resonators. The confinement can be simplistically described in terms of geometrical optics by the optical rays which are totally internally reflected and focused by the surface itself. WGMs are sometimes also referred to as morphology dependent resonances (MDRs) [74], referring to their dependence on geometry and dielectric properties.

Fig. 2.5 shows the analogy between the acoustic modes and optic modes. Ad-

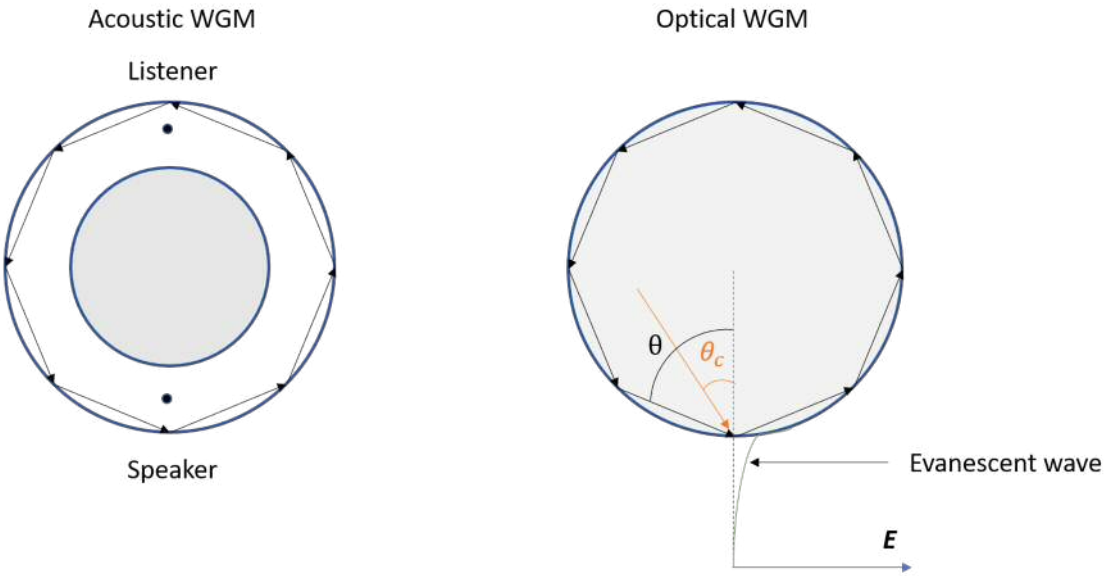

Figure 2.5: Analogy between the acoustic and optic WGM. (a) Acoustic WGM is reflected by large impedance mismatch between the wall and air. For an optical WGM that would corresponds to metal surface. The position of the speaker and the listener is marked with dots. (b) Optical WGM in a cavity relies on TIR at the cavity interface. The RI of the cavity is n_1 and that of the medium is n_2. TIR occurs when a propagated wave strikes a medium boundary at an angle θ, larger than critical angle, θ_c, with respect to the normal to the surface and $n_1 > n_2$.

vancement in micro fabrication technology has made it possible to fabricate micron-scale optical resonator structures by conventional integrated circuit deposition and etching techniques. Various geometries such as micro-pillars [75], micro-rings [76], micro-disks [77], micro-toroids [78, 79] and photonic-crystal cavities [80] have been

explored. However microspheres are the simplest three-dimensional WGM resonators which can be made of dielectric materials offering high-Q resonance modes [63]. Microspheres of ten to hundred micrometers in diameter are readily available and host WGMs with equatorial, radial, as well as polar field dependencies [81]. They can be coated with different functional coatings [82], which enables multiplex detection functionality to biosensors. Microsphere resonators [83, 84] based on WGMs, therefore, have attracted increasing attention for optical biosensing [62, 65, 85, 86, 87]. Since free-space optics does not allow efficient coupling with high-Q WGMs [88, 89], evanescent wave coupling, via frustrated total internal reflection, from dielectric prisms, slabs or WG structures [90, 91] are used.

2.3 Whispering gallery modes in spherical resonators

In 1908, Gustav Mie published a first outline of how to compute light scattering by small spherical particles, using Maxwell's electromagnetic theory. Electromagnetic scattering by a homogeneous, isotropic sphere is therefore commonly referred to as Mie scattering. Mie theory [92] gives an exact analytical solution to the problem of scattering of the electromagnetic wave by a homogeneous sphere of arbitrary size and dielectric constant. This theory can be applied to derive approximate asymptotic formulae to calculate position and width of the WGMs [74]. In the scattering of electromagnetic waves by a dielectric sphere, the WGMs lead to a series of sharp peaks as a function of the resonator size and wavelength [93, 94, 95]. In a WGM light is confined inside the sphere by total internal reflection (TIR) and returns in phase after each revolution [96]. The trapped light leaks through the evanescent region close to the sphere by tunneling [97].

In this section, we will describe briefly the theory of WGMs in microsphere dielectric resonators.

2.3.1 Resonant mode numbers

A resonant mode in a dielectric sphere is characterised by the three mode numbers, n, l, and m [98]. The mode index number $n = 1, 2, ...$, characterizes the radial dependence. The mode number l describes the total angular momentum. For increasing l, modes are confined closer to the surface of the sphere. The azimuthal mode number m can take values from $-l$ to l, and describes the z-projection of the angular momentum of the $2l + 1$ degenerate modes of given l. Modes are further characterised by their polarisation - transverse electric (TE) and transverse magnetic (TM) - having the electric or magnetic field orthogonal to the radial direction. The radial mode number n, along with the angular mode number l and the label TE or TM, uniquely identifies a resonance. at a given l, the fundamental WGM, $n = 1$, has the highest quality factor Q.

2.3.2 Field solutions

The optical modes of a dielectric sphere in terms of its size parameter will be derived here. Two distinct polarisations, i.e., TE and TM, can be supported in an isotropic

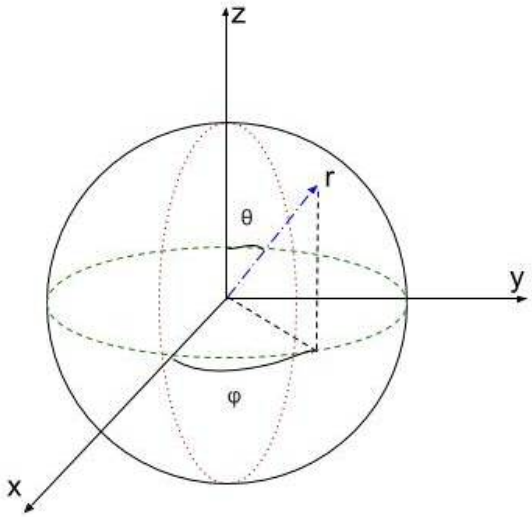

Figure 2.6: Spherical coordinate system.

resonator, which will be considered separately. The sphere is assumed to be non-magnetic, i.e., the relative magnetic permeability is μ=1. The radius of the particle is denoted by a and the RI $m(r)$ of the sphere depends only on the radial distance r from the centre. This section is based on the work by Johnson [99] and Teraoka et al.[100].

The electric field $\mathbf{E}$ of a EM wave satisfies the vector wave equation:

$$\nabla \times \nabla \times \mathbf{E} - k^2 \tilde{n}^2(r)\mathbf{E} = 0 \tag{2.21}$$

where, $\tilde{n}(r)$ is the complex RI as a function of the radial co-ordinate r. The solution to Eq. (2.21) is the electric field in spherical polar coordinates (see Fig. 2.6) specified by l and m and given as

$$\mathbf{M}_{l,m}(r,\theta,\phi) = \frac{\exp(im\phi)}{kr} S_n(r,k)\mathbf{X}_{l,m}(\theta) \tag{2.22}$$

for the transverse electric (TE) modes, and

$$\mathbf{N}_{l,m}(r,\theta,\phi) = \frac{\exp(im\phi)}{k^2\tilde{n}^2(r)}\left[\frac{1}{r}\frac{\partial T_n(r,k)}{\partial r}\mathbf{Y}_{l,m}(\theta) + \frac{1}{r^2}T_n(r)\mathbf{Z}_{l,m}(\theta)\right] \tag{2.23}$$

for the transverse magnetic (TM) modes. The scalar functions $S_n(r,k)$ and $T_n(r,k)$ used are the radial Debye potentials for TE and TM mode respectively and are given below. The angular functions $\mathbf{X}_{l,m}(\theta)$, $\mathbf{Y}_{l,m}(\theta)$ and $\mathbf{Z}_{l,m}(\theta)$ are given by

$$\mathbf{X}_{l,m}(\theta) = i\pi_{l,m}(\theta)\hat{e}_\theta - \tau_{l,m}(\theta)\hat{\mathbf{e}}_\phi\,, \tag{2.24}$$

$$\mathbf{Y}_{l,m}(\theta) = \tau_{l,m}(\theta)\hat{e}_\theta + i\pi_{l,m}(\theta)\hat{\mathbf{e}}_\phi\,, \tag{2.25}$$

$$\mathbf{Z}_{l,m}(\theta) = n(n+1)P_n^m(\cos\theta)\hat{\mathbf{e}}_r\,, \tag{2.26}$$

where $\hat{\mathbf{e}}_r$, $\hat{\mathbf{e}}_\phi$ and $\hat{\mathbf{e}}_\theta$ are the unit vectors of the spherical coordinates, P_n^m is the associated Legendre function, and $\pi_{l,m}(\theta)$ and $\tau_{l,m}(\theta)$ are defined as

$$\pi_{l,m}(\theta) = \frac{m}{\sin\theta}P_l^m(\cos\theta)\,, \quad \text{and} \quad \tau_{l,m}(\theta) = \frac{\partial}{\partial\theta}P_n^m(\cos\theta)\,. \tag{2.27}$$

The Debye potentials satisfy the following second-order differential equations

$$\frac{\mathrm{d}^2\mathrm{S_l(r)}}{\mathrm{dr}^2} + \left[k^2\tilde{n}^2(r) - \frac{l(l+1)}{r^2}\right] S_l(r) = 0 \tag{2.28}$$

$$\frac{\mathrm{d}^2}{\mathrm{dr}^2}T_l(r) - \frac{2}{\tilde{n}(r)}\frac{\mathrm{d}}{\mathrm{dr}}\tilde{n}(r)\frac{\mathrm{d}}{\mathrm{dr}}T_l(r) + \left[k^2\tilde{n}^2(r) - \frac{l(l+1)}{r^2}\right] T_l(r) = 0 \tag{2.29}$$

The solution of Eq. (2.28) is expressed by spherical Ricatti-Bessel functions

$$\psi_l(x) = x j_l(x) \quad \text{and} \quad \chi_l(x) = x n_l(x)\,, \tag{2.30}$$

where j_l and n_l are spherical Bessel function and spherical Neumann function of order l, respectively. In the external region, $r > a$, with RI $\tilde{n}_2$, the general solutions for TE and TM modes are linear combinations of the Riccati-Bessel functions given by

$$S_l(r) = B_l\left[\chi_l(\tilde{n}_2 kr) + \beta_l\psi_l(\tilde{n}_2 kr)\right]\,, \tag{2.31}$$

$$T_l(r) = A_l\left[\chi_l(\tilde{n}_2 kr) + \alpha_l\psi_l(\tilde{n}_2 kr)\right]\,, \tag{2.32}$$

where A_l, B_l, α_l, and β_l are constants. In the internal region $0 \le r \le a$, with RI $\tilde{n}_1$ they are given by

$$S_l(r) = T_l(r) = \psi_l(\tilde{n}_1 kr)\,. \tag{2.33}$$

Thus the solution of the TE mode can be written as

$$S_l(r) = \begin{cases} \psi_l(\tilde{n}_1 kr) & \text{for } r \le a \\ B_l(k)\,\phi_l(\tilde{n}_2 kr) & \text{for} r > a \end{cases}\,, \tag{2.34}$$

where $B_l(k)$ is independent of r, and

$$\phi_l(\tilde{n}_2 kr) = \chi_l(\tilde{n}_2 kr) + \beta_l(\tilde{n}_2 kr)\,\psi_l(\tilde{n}_2 kr)\,. \tag{2.35}$$

Continuity of the tangential component of the electric field and of the normal component of the electric displacement requires that

$$\psi_l(\tilde{n}_1 kr) = B_l(k)\,\phi_l(\tilde{n}_2 kr) \tag{2.36}$$

$$\tilde{n}_1\,\psi_l'(\tilde{n}_1 kr) = B_l(k)\,\tilde{n}_2\,\phi_l'(\tilde{n}_2 kr)\,, \tag{2.37}$$

where the prime denotes the derivative with respect to the argument.

One can use a quantum mechanical analogy to formulate the problem in such a way that understanding and intuition from quantum-mechanics can be used to understand the resulting solutions. In order to do this let us assume that $\hbar^2/2\mu = 1$, where $\hbar$ is the Plank's constant and μ is the reduced mass. The radial Schrödinger equation can then be written as [99]

$$\frac{\mathrm{d}^2\psi(\mathrm{r})}{\mathrm{dr}^2} + \left[V(r) + \frac{l(l+1)}{r^2}\right]\psi(r) = E\psi(r)\,, \tag{2.38}$$

where $V(r)$ is the potential energy and E is the state energy. Comparing with Eq. (2.24) the total potential of a sphere of constant RI $\tilde{n}$, in vacuum, is given by [99]

$$V_l(r) = \begin{cases} k^2(1-\tilde{n}^2) + l(l+1)/r^2 & \text{for } r \le a \\ l(l+1)/r^2 & \text{for } r > a \end{cases} \tag{2.39}$$

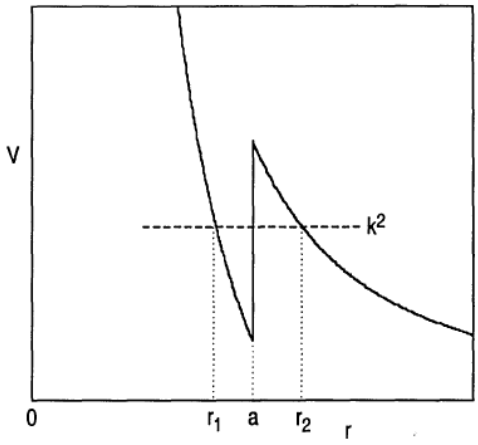

Figure 2.7: Effective potential associated with the EM modes of a sphere of radius a [99].

The term $k^2(1-\tilde{n}^2)$ is the height of the barrier at $r=a$, creating a potential well. The classically allowed region in this well is $r_1 < r < a$, having a real local wave number p_l given by $p_l^2(r) = E - V_l(r)$. The potential well is surrounded by the two classically forbidden regions $0 \leq r < r_1$ and $a < r < r_2$ in which $p_l^2(r) < 0$. The shape of the potential well changes with k^2. Particles can tunnel through the forbidden region into the allowed potential well. For certain values of energy k^2 particles will be trapped temporally inside the well and will oscillate back and forth few times before they tunnel back through the forbidden region to the outside world. These quasi-bounds states can form sharp resonances. For some value of k the energy k^2 will coincide with the bottom of the potential well. Modes that occur at the bottom of the well must tunnel through a larger barrier than the upper levels. Therefore the lowest level has the longest lifetime and hence narrowest width and highest Q factor. Fig. 2.7 shows the potential function $V_{40}(r)$ associated with a spherical dielectric particle of radius a, mode number $l = 40$, refractive index m=1.47 and wave number=33/a [99].

Returning to the original problem with, we see that in the classically forbidden region function $\psi_n(kr)$ exhibits an exponential growth while the function $\chi_n(kr)$ exhibits an exponential like decrease. The condition that determines the discrete energy levels of a quasi-bound shape resonance is the requirement that the wave function exhibit an exponential like decay in the barrier region so that, if the barrier extended to infinity ($r \to \infty$) the wave function would decay to zero and the quasi-bound state would become a true bound state. This means that only the exponential like decreasing function is allowed in the barrier region. Thus the condition for outgoing resonance requires that coefficients that multiply the increasing function $\psi_n(kr)$ must be zero therefore at resonance $\beta_l(k_0) = 0$. Thus at resonance of the TE mode we have

$$\tilde{n}_1 \frac{\psi_l'(\tilde{n}_1 ka)}{\psi_l(\tilde{n}_1 ka)} = \tilde{n}_2 \frac{\chi_l'(\tilde{n}_2 ka)}{\chi_l(\tilde{n}_2 ka)}\,, \tag{2.40}$$

which is the secular equation determining the TE resonance wavenumbers k for the given l, numbered by n.

Similarly, for the TM mode the solution can be written as

$$T_l(r) = \begin{cases} \psi_l(\tilde{n}_1 kr) & \text{for } r \leq a \\ A_l(k)\,\phi_l(\tilde{n}_2 kr) & \text{for } r > a \end{cases} \tag{2.41}$$

where $A_l(k)$ is independent of r, and

$$\phi_l(\tilde{n}_2 kr) = \chi_l(\tilde{n}_2 kr) + \alpha_l(\tilde{n}_2 kr)\,\psi_l(\tilde{n}_2 kr)\,. \tag{2.42}$$

Continuity of the tangential component of the electric field and of the normal component of the electric displacement requires that

$$\psi_l(\tilde{n}_1 ka) = A_l(k)\,\phi_l(\tilde{n}_2 ka) \tag{2.43}$$

$$\psi_l'(\tilde{n}_1 ka)/\tilde{n}_1 = A_l(k)\,\phi_l'(\tilde{n}_2 ka)/\tilde{n}_2\,. \tag{2.44}$$

For resonance we require that $\alpha_l(k_0) = 0$, so that we have

$$\frac{1}{\tilde{n}_1}\frac{\psi_l'(\tilde{n}_1 ka)}{\psi_l(\tilde{n}_1 ka)} = \frac{1}{\tilde{n}_2}\frac{\chi_l'(\tilde{n}_2 ka)}{\chi_l(\tilde{n}_2 ka)}\,, \tag{2.45}$$

which is the secular equation determining the TM resonance wavenumbers k for the given l. Compared to the TE modes Eq. (2.45), the RI factors are inverted. The resonances of a spherical resonator can thus be found by solving 2.40 and 2.45 for ka for TE and TM mode respectively. For given values of $\tilde{n}_1$ and $\tilde{n}_2$ there is an infinite series of solutions of increasing k, which are numbered by the radial quantum number n. These modes are called first order mode ($n = 1$), second order mode ($n = 2$) etc. with increasing magnitude of ka.

2.3.3 Approximations for numerical solution

An exact analytic solution of Eq. (2.40) and Eq. (2.45) is not available, and this solutions have to be found numerically in comples ka space. However, one can find analytical approximations for ka of WGMs of high Q factors. For example, the asymptotic expansions of Lam et al. [74] and Schiller [101] utilize an analytic approximation of the Bessel functions [102] to give approximate positions and linewidths of WGMs in spherical resonators. These approximate formulae are valid for spheres much larger that the wavelength $\tilde{n}_1 ka \gg 1$, and low mode order n. In this section position and width of the WGMs for microsphere resonator in any medium will be derived. This section is based on the work by Lam et al. [74] and Teraoka et al. [100].

The positions of the resonances can be derived from Eq. (2.40) and Eq. (2.45) by translating the spherical Bessel and Neumann functions j_i and n_l to their cylindrical counterparts and introducing the variable $\nu = l+1/2$. The position of the resonances in terms of size parameter $x = ka$ are given as

$$\begin{aligned}\tilde{n}_1\, x_{n,l} = \nu + 2^{-1/3}\,\alpha_i\,\nu^{1/3} - \frac{P}{(\tilde{n}^2-1)^{1/2}} + \left(\frac{3}{10}\,2^{-2/3}\right)\alpha_i^2\,\nu^{-1/3} \\ - \frac{2^{-1/3}\,P(\tilde{n}^2 - 2P^2/3)}{(\tilde{n}^2-1)^{3/2}}\alpha_i\,\nu^{-2/3} + O(\nu^{-1})\end{aligned} \tag{2.46}$$

where $\tilde{n} = \tilde{n}_1/\tilde{n}_2$, and

$$P = \begin{cases} \tilde{n}_1 & \text{for TE mode} \\ 1/\tilde{n}_1 & \text{for TM mode} \end{cases} \tag{2.47}$$

Parameter	Symbol	TE	TM	Unit
Resonance position	λ_0	783.42	783.42	nm
Resonance width	γ_0	6.9×10^{-6}	8.9×10^{-6}	nm

Table 2.2: Resonance position and width of a PS microsphere for $n = 1$ and $l = 180$ mode.

Assuming a real $\tilde{n}_1$ and $\tilde{n}_2$, i.e. neglecting absorption, the resonance width can be approximated as

$$\gamma_{n,l} = \frac{2}{Nx^2 n_l(x)^2} \tag{2.48}$$

where n_l is the spherical Neumann function and

$$N = \begin{cases} \tilde{n}^2 - 1 & \text{for TE mode} \\ (\tilde{n}^2 - 1)\left[\mu^2 + (\mu^2/\tilde{n}^2 - 1)\right] & \text{for TM mode} \end{cases}, \tag{2.49}$$

and $\mu = \nu/x$. et for the TE mode

$$\gamma_{n,l\,(\mathrm{TE})} = \frac{2\tilde{n}_2}{\tilde{n}_1^2 - \tilde{n}_2^2} \frac{1}{\left[\chi_l(\tilde{n}_2 ka)\right]^2}, \tag{2.50}$$

and for TM mode

$$\gamma_{n,l\,(\mathrm{TM})} = \frac{2\tilde{n}_2}{\tilde{n}_1^2 - \tilde{n}_2^2} \frac{1}{\left[\chi_l(\tilde{n}_2 ka)\right]^2} \frac{1}{\left[\mu^2 + (\mu^2/\tilde{n}^2 - 1)\right]} \tag{2.51}$$

A numerical solution of Eq. (2.40) gives WGM positions and width for $n = 1$, $l = 40$ and $m = 1.47$ in terms of size parameter as 31.058854 and 8.7×10^{-5} respectively [99].

For WGM order number $n = 1$ and mode number $l = 180$, resonance position and width of a (PS) microsphere of diameter 30 µm and RI 1.57 at wavelength of 784 nm in water of RI 1.33 have been calculated for both TE and TM polarisation using Eq. (2.46),Eq. (2.48). The position and width are given in unitless frequencies in Eq. (2.46) and Eq. (2.48). They are converted into wavelength of light according to Eq. (2.52) and Eq. (2.53). Calculated resonance position and width is listed in Table 2.2.

$$\lambda_0 = \frac{2\pi a}{1.33 x_{n,l}} \tag{2.52}$$

$$\gamma_0 = \frac{\gamma_{n,l}}{\frac{dx_{n,l}}{d\lambda_0}} \tag{2.53}$$

2.3.4 Quality factor of WGMs

2.3.4.1 Ideal dielectric spheres

Once the position and width are calculated we can determine the intrinsic Q factor of the modes. The Q factor is the relation between centre frequency and linewidth of

Parameter	Symbol	TE	TM	Unit
Intrinsic Q factor	Q	1.13×10^8	8.9×10^7	-
Lifetime	τ	47.2	36.53	ns

Table 2.3: Intrinsic Q factor and lifetime of a PS sphere with a radius of 15 µm in water, $n = 1$ and $l = 180$.

the mode and characterizes a sphere's ability to store electromagnetic energy. The theoretical Q factor is given [62]

$$Q = \frac{x_{n,l}}{\gamma_{n,l}}, \tag{2.54}$$

where γ is the is the linewidth which originates from the imaginary part of k. The width of the resonance is inversely proportional to the lifetime of the trapped energy [99]. The storage time, therefore, can be computed as [62]

$$\tau = \frac{Q}{Re(k)\, c}, \tag{2.55}$$

where, c is the speed of light and $Re(k)$ is the real part of the resonant wavenumber. For WGM order number $n = 1$ and mode number $l = 180$, the intrinsic Q factor and lifetime of a 30 µm diameter polystyrene (PS) sphere of RI $\tilde{n}_1 = 1.5788$ at wavelength of 784 nm in water of RI of $\tilde{n}_2 = 1.33$ have been calculated for both TE and TM polarisation using Eq. (2.54) and 2.55 and listed in Table 2.3.

Fig. 2.8 shows the relation between the intrinsic Q factor of a PS microsphere with a varying diameter in water at 784 nm. This shows that the radiative Q factor can be in the order of 10^8 at around 30 µm and increasing for larger microsphere thus intrinsic losses can not be dominating these Q factors.

The results shows that the Q factor of the WGM ($n = 1$ and $l = 180$) of a PS sphere of diameter 30 µm, and RI of 1.5788 can be as high as 1.75×10^8 at 784 nm wavelength for TE polarisation. However, experimental values of the Q factor have been measured around 10^6 [62]. Clearly, there is a discrepancy between the theoretical and experimental Q values. This discrepancy may be because of scattering losses due to material and intrinsic loss, and residual surface inhomogeneity.

2.3.4.2 Material loss

Q factor due to material loss can be small. The absorption by water at 784 nm reduces the Q factor to about 1.3×10^8. The intrinsic absorption in PS at 784 nm can be estimated by the typical losses of polymer fibres of less than 1000 dB/ km, corresponding to an absorption coefficient of $0.23\,\mathrm{m}^{-1}$. This would reduce the Q factor of the considered PS sphere to about 5×10^7 [62]. Intrinsic losses decrease exponentially with the radius of the sphere, thus if the sphere is sufficiently larger than the wavelength, intrinsic losses are negligible [103]. Therefore the observed Q factor is dominated by surface roughness rather than the intrinsic or material losses for the considered PS spheres.

2.3.4.3 Surface roughness

The most important extrinsic mechanism limiting the Q factor for optical WG modes is the scattering by surface inhomogeneities [103]. The surface of a sphere can be

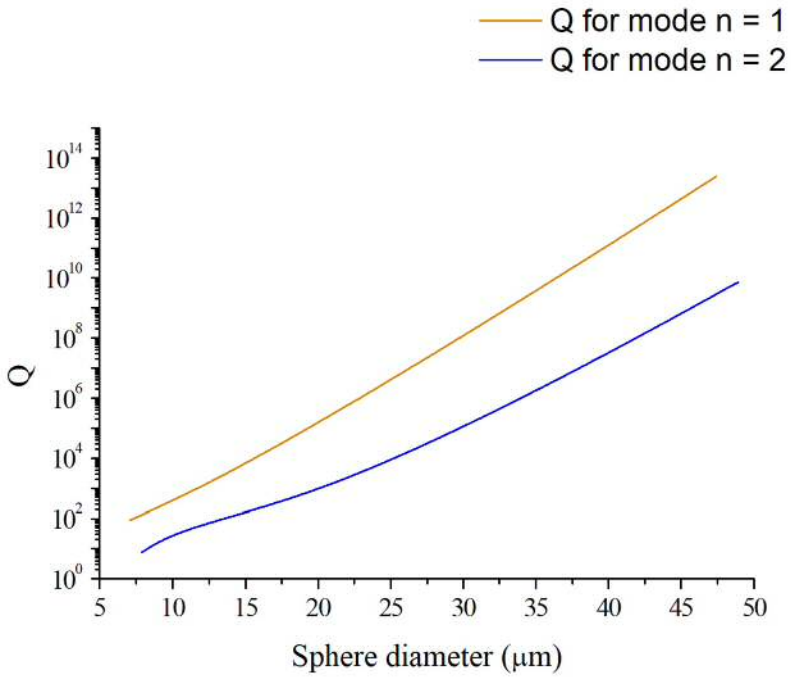

Figure 2.8: Intrinsic Q factor of WGMs of a polystyrene microsphere of RI 1.5788 in water of RI 1.33 at 784 nm wavelength, versus diameter, for TE polarisation and radial quantum numbers $n = 1$ and $n = 2$, as labeled. The intrinsic Q factor has been calculated by using the approximate formulas.

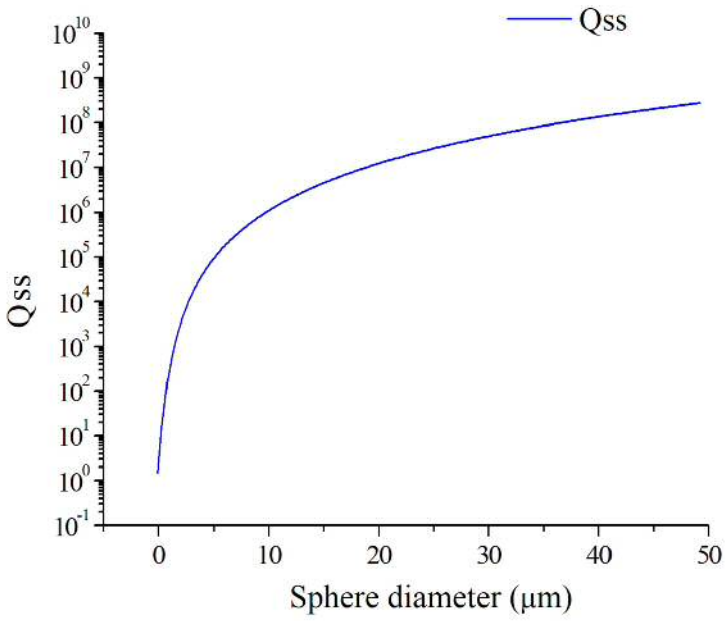

Figure 2.9: Q factor limit of a polystyrene microsphere due to surface roughness with varying microsphere diameter for mode $n = 1$. Surface roughness was assumed as 10 nm.

considered as having random roughness and thus can be characterised by the root mean square (RMS) surface roughness profile, i.e. σ_{rms}. If the RMS size of the inhomogeneities σ is less than the wavelength λ then the surface loss Q_{ss} can be estimated as [103]

$$Q_{\mathrm{ss}} \approx \frac{3\lambda^2 l^{10/3}}{16\pi^5 \sigma_{rms}^2 \tilde{n}_1^2 n^{5/2}} \tag{2.56}$$

where, $\tilde{n}_1$ is the RI of the microsphere, n is the mode order and σ_{rms} is the the RMS size of surface roughness. Fig. 2.9 shows the relationship between Q_{ss} and microsphere diameter for TE polarisation.

2.3.5 Shift of resonance frequency

WGM sensors are based on detection by the evanescent wave at the transducer surface [104]. Any changes in the evanescent field can be detected as a shift of the resonant frequency [65, 100]. The changes will include a change in the RI of the medium surrounding the spheres [100], change in RI inside the spheres [105], adsorption of molecules in a thin layer on sphere surface [85].

For a uniform change in RI in the medium $\Delta\tilde{n}_2$, the shift of resonance frequency Δk can be written for the fundamental WGM when $ka \gg 1$ and $l \cong \tilde{n}_1 ka$ as [100]

$$\left(\frac{\Delta k}{k}\right)_{\mathrm{TE}} = -\frac{\tilde{n}_2\,\Delta\tilde{n}_2}{(\tilde{n}_1^2 - \tilde{n}_2^2)^{3/2}}\,\frac{1}{ka}\,, \tag{2.57}$$

$$\left(\frac{\Delta k}{k}\right)_{\mathrm{TM}} = -\frac{\tilde{n}_2\,\Delta\tilde{n}_2}{(\tilde{n}_1^2 - \tilde{n}_2^2)^{3/2}}\left(2 - \frac{\tilde{n}_2^2}{\tilde{n}_1^2}\right)\frac{1}{ka}\,. \tag{2.58}$$

Fig. 2.10 shows the plot of Eq. (2.57) and Eq. (2.58) of a microsphere of RI 1.5788 in water of RI 1.33 at 784 nm for radial mode number $n = 1$.

2.4 Detection scheme

The sensor detection scheme considered in this thesis is sketched in Fig. 2.11. When light propagates through a WG by total internal reflection (TIR), evanescent waves are created in the surrounding medium, exponentially decaying with distance, as discussed in Sec. 2.1. WGMs of a microsphere can be excited by this evanescent wave, if the sphere is sufficiently close to the WG. the WGM couples back to the WG, resulting in a resonance in the transmission, which is typically a reduced transmission due to the coupling of the WGM to other channels, scattering the light away from the WG mode. Measuring the transmission of the WG, one can deduce the resonance wavelength, which changes with the RI of the medium.

2.4.1 Coupling external light to WGMs

The excitation and detection of the WGMs is an essential prerequisite in practical applications. In this section we will briefly discuss different coupling methods.

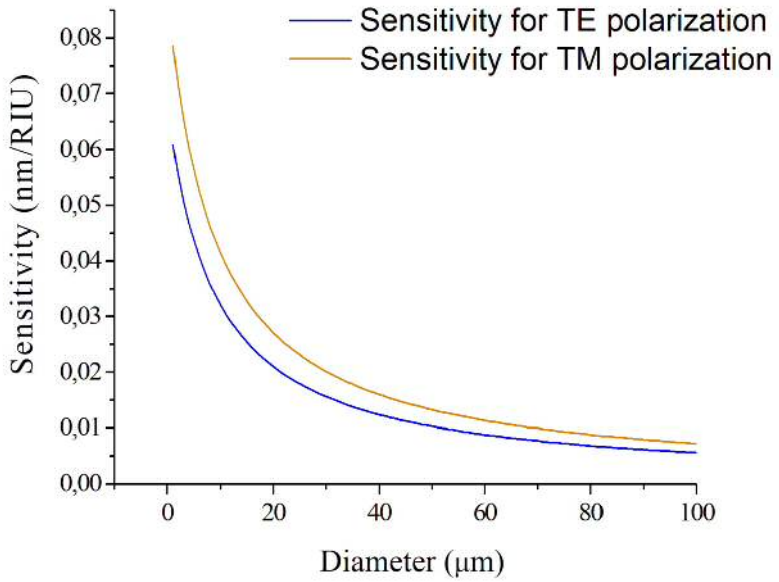

Figure 2.10: Sensitivity of a PS microsphere of RI 1.5788 in water of RI 1.33 at 784 nm with varying diameter for both TE and TM polarisation according to Eq. (2.57) and Eq. (2.58).

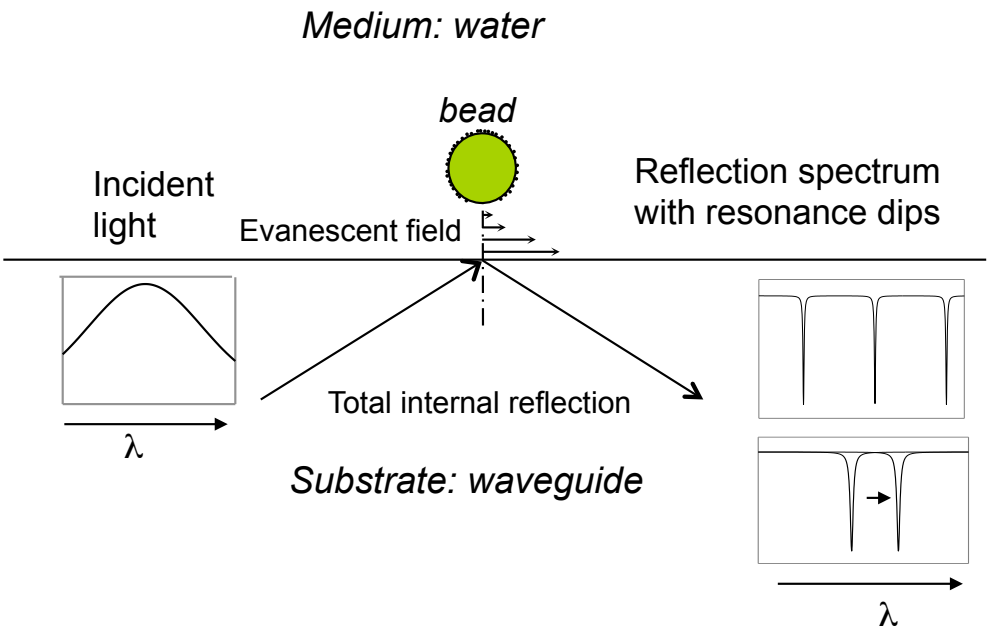

Figure 2.11: Sketch of the biosensor detection scheme. Light propagates along a WG by TIR which creates an exponentially decaying evanescent field at the interface of the WG core and cladding layer. A microsphere is attached at a short distance from the core layer of the WG. At resonance, the enhancement of the field in the microsphere increases the light extraction from the WG into other channels reducing the WG transmission. Any change such as change in RI in the vicinity of the microsphere will shift the resonances.

2.4.1.1 Free space coupling

This section is based on [88]. Free space coupling depends on radiative exchange of a WGM with external space. This radiative exchange is strongly dependent on the resonator radius and becomes extremely small when the radius exceeds several wavelengths, as we have seen in the large Q factors shown in Fig. 2.8. Therefore, free-space light does not efficiently couple to high Q WGMs.

Coupling efficiency η can be defined as

$$\eta = \frac{\pi}{\mathcal{F}} \frac{P_{\text{in}}}{P} \tag{2.59}$$

where,P_i is the power circulating inside the resonator, P is the external pump power and $\mathcal{F}$ is the finesse of the resonator. The resonator is under coupled if $\eta < 1$, critically coupled if $\eta = 1$ and over coupled if $2 > \eta > 1$. Critical coupling implies that the excitation is entirely transferred into other channels at resonance.

The coupling efficiency, η depends on both the ratio between the amount of radiative power of the pump beam penetrating into the mode scattering area, and the total optical pump power, and the ratio of the coupling related losses and losses into other channels.

Let us estimate the coupling efficiency of a pumping light beam interacting with an ideal sphere. The beam cross-section radius is comparable with the sphere radius a. The total cross-sectional area is thus $2\pi a^2$. Scattering cross sectional mode area is $a\lambda$. Therefore the fraction of the total power interacts with the sphere is

$$\frac{P_i}{P} = \frac{\lambda}{2\pi a}, \tag{2.60}$$

To estimate the ratio of the mode coupling quality factor Q_c and total quality factor Q, we assume that the radiative losses and optical pumping are of the same origin and are proportional to the interaction surface area. The radiative emission occurs from the entire sphere surface. The area is equal to $4\pi a^2$. The optical pumping is going through a surface belt with thickness λ. The area is equal to $2\pi a\lambda$. Therefore, the ratio of the coupling and total quality factors is proportional to the sphere radius

$$\frac{Q_c}{Q} = \frac{a}{\lambda}, \tag{2.61}$$

and the coupling efficiency is

$$\eta < \left(\frac{\lambda}{a}\right)^2. \tag{2.62}$$

The coupling efficiency of a free-space collimated beam is therefore small in experiments and applications where the resonators are much larger than the wavelength.

2.4.1.2 Near-field coupling

As discussed above, WGM of high Q optical microsphere resonators are not well coupled to free-space beams, demanding the employment of near-field coupler devices. At present, demonstrated coupler devices include prism coupler [90], WG [106] with frustrated total internal reflection, side polished fibre coupler [107] and fiber taper [108]. All these devices rely on the efficient exchange of energy between

the WGM in the resonator through the evanescent field of a guided wave or TIR spot in the coupler [89].

The concept of an evanescent field can be explained as follows. Let us consider a plane wave impinging on an interface between two media of refractive index of n_1 and n_2 ($n_1 > n_2$) as shown in Fig. 2.12. At the interface, refraction occurs at a small incidence angle. But when the angle of incidence exceeds critical angle, θ_c, the light beam is totally reflected from the interface. This process is called total internal reflection (TIR). Even under the condition of TIR, a portion of the incident wave penetrates through the interface and enters into the second medium due to the boundary conditions. This penetrating wave is called an evanescent field.

The critical angle θ_c is given by

$$\theta_c = \sin^{-1}(n_2/n_1) \tag{2.63}$$

An evanescent wave has a rapidly decaying electric field amplitude (vanishes at $z \to \infty$), with an imaginary propagation constant k. The decaying electric field amplitude $\mathbf{E_z}$ decays exponentially with distance z into the medium of lower refractive index n_2 as

$$\mathbf{E_z} = \mathbf{E_0} \exp(-\mathbf{z}/\mathbf{d_p}) \tag{2.64}$$

where E_0 is the electric field at the surface of the higher refractive index material and d_p is the penetration depth. The penetration depth is given as

$$d_p = \lambda / \left\{ 2\pi n_1 \left[\sin^2\theta - (n_2/n_1)^2 \right]^{1/2} \right\} \tag{2.65}$$

Efficient coupling with high-Q microspheres can be achieved in near field coupling

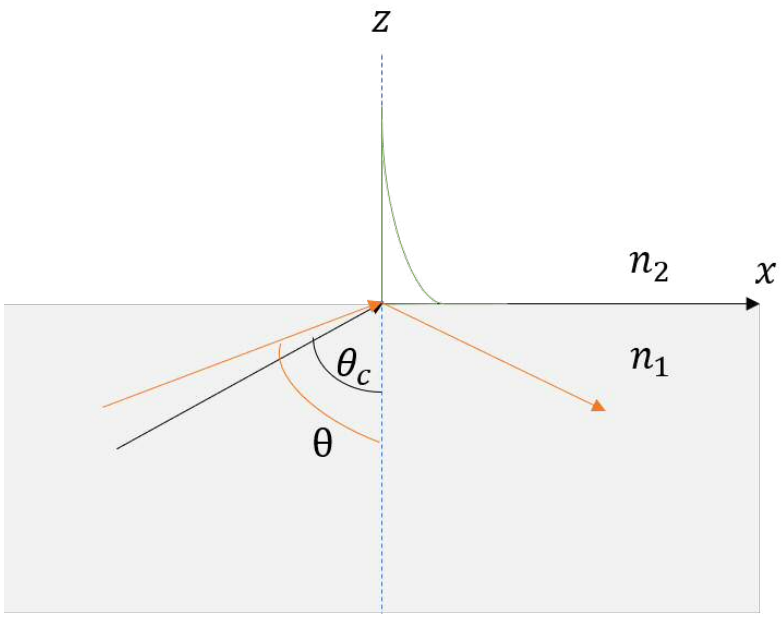

Figure 2.12: Sketch showing the creation of an evanescent wave by TIR. An evanescent wave is created when the plane wave is incident at an angle $\theta > \theta_c$ on an interface between two media of refractive index of n_1 and n_2 ($n_1 > n_2$).

method by fulfilling two conditions [89, 109],

1. spatial overlap of the WGM and the WG mode, which implies optimization of the distance between the microspheres and the WG.

2. phase matching between the modes in the overlapping region.

The displacement between the microsphere and the WG controls the coupling behaviour and hence the Q factor, so it is an important design parameter in this type coupled systems.

Prism coupling

Prism couplers with frustrated total internal reflection are among the simplest methods to couple light and WGMs. The simplest yet efficient prism technique is based on three main principles. First, the input beam is focused inside the high-index coupling prism under the angle that provides phase matching between the evanescent wave and the WGM. Second, the beam shape is tailored to maximize the modal overlap in the near field. And third, the gap between resonator and prism is optimised to achieve critical coupling. The best efficiency of prism coupling to WGMs reported up to date is 80% [89].

Wave-guide coupling

The prism coupling method is a suited method of coupling, but requires alignment of the excitation spot to the microsphere. A solution to these limitations is provided by positioning the isolated microspheres on optical WGs by chemical or topographical means. The planar configuration offers robust construction and photo lithographic techniques will permit multiple microspheres to be placed in well defined positions on a substrate. For a biosensor this gives an additional advantage of multiplex sensing. Coupling between microspheres and WGs is quantified as a function of displacement from the wave guide [110].

The coupling efficiency can be controlled by adjusting the distance between the microspheres and the WG, so that the photon escape from the microsphere into the WG is adjusted [62] and thus eventually limited by the intrinsic losses inside the microsphere rather than by photon escape into the WG [86]. Fig. 2.13 shows a measured relation between the Q factor and the distance from the microspheres to WGs reported in [110].

The sample used in the measurement consisted of a BK7 glass microsphere of diameter 125 µm and RI of 1.42 at a wavelength of 589.29 nm positioned on a 4 cm long planar glass WG. The RI of the core and substrate layer of the WG was 1.52 and 1.50 at 1550 nm respectively. Teflon (AF2400) of RI of 1.29 at 1550 nm of varying height between 0 to 850 nm was deposited on the WG. This Teflon layer functions the separation layer between the WG and the microspheres.

2.4.2 Detecting the resonance in transmitted intensity and phase

This section is based on [86]. We note that WGMs with transverse electric (TE) and transverse magnetic (TM) polarisation have different resonance frequencies. Let us denote by E_{TE} and E_{TM} two polarisation field components in the transmitted beam. We assume here that we are probing a resonantly a TE WGM, while in TM no resonance is present at the excitation frequencies. Two detection schemes can be used to measure resonances, which are 'intensity' and 'phase' detection. In the

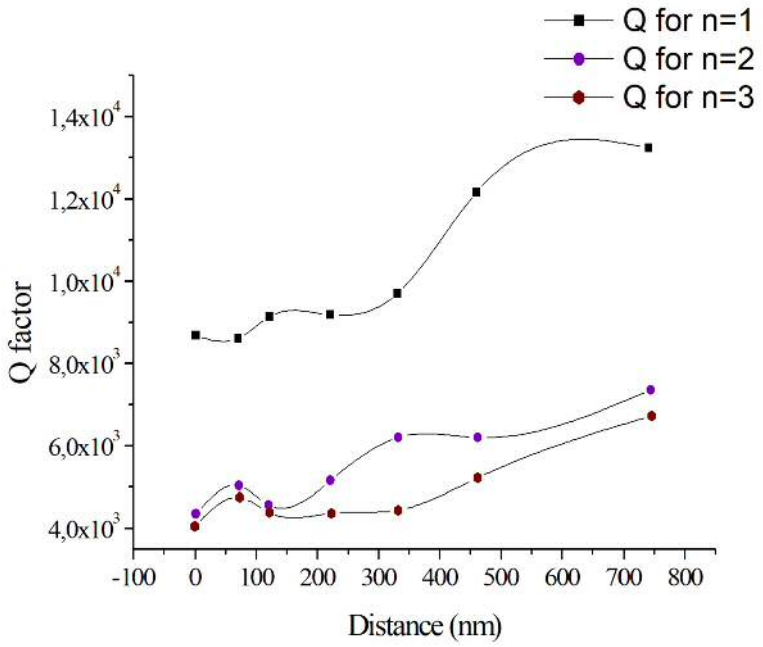

Figure 2.13: Relation between the Q factor of a microsphere and its distance to a coupling WG at 1465 nm for different modes. Reproduced from [110].

'intensity' detection scheme, the intensity difference of E_{TE} and E_{TM} is normalised to the intensity of E_{TM}. This can be written as

$$S_{\mathrm{I}} = \frac{\mid E_{\mathrm{TE}} \mid^2 - \mid E_{\mathrm{TM}} \mid^2}{\mid E_{\mathrm{TM}} \mid^2} \,. \tag{2.66}$$

The normalisation to the non-resonant TM field results in a unitless quantity and compensates for laser intensity noise. In the 'phase' detection, instead, we choose the detected polarisations at 45° to E_{TE} and E_{TM} and thus measure the interference between the two fields as

$$S_{\mathrm{P}} = \frac{\mid E_{\mathrm{TM}} - E_{\mathrm{TE}} \mid^2 - \mid E_{\mathrm{TM}} + E_{\mathrm{TE}} \mid^2}{\mid 2E_{\mathrm{TM}} \mid^2} \tag{2.67}$$

For a TE resonance of frequency ω_0 and polarisation decay rate γ, the amplitude of the field in the transmitted wave in TE polarisation can be written as

$$E_{\mathrm{TE}} = E_0(\omega) \left(1 + \frac{A\gamma}{i(\omega - \omega_0) - \gamma} \right) e^{i\psi} \,, \tag{2.68}$$

where $E_0(\omega)$ is the amplitude of the incident wave, A is a positive coefficient and ψ is a relative phase that can be adjusted by polarisation optics in the excitation. For the TM polarisation, where there is no resonance, we use

$$E_{\mathrm{TM}} = E_0(\omega) \,, \tag{2.69}$$

assuming that the excitation has equal amplitudes in both polarisations. The signal measured in the intensity detection is then given by

$$S_{\mathrm{I}} = \frac{A(A-2)\gamma^2}{\gamma^2 + (\omega - \omega_0)^2} \,, \tag{2.70}$$

which is a Lorentzian peak with the position and linewidth of the TE resonance. In the phase detection, the polarisation optics is adjusted to $\psi = \pi/2$, thus the signal measured in the phase detection is given by

$$S_{\mathrm{P}} = \frac{-2A\gamma(\omega - \omega_0)}{\gamma^2 + (\omega - \omega_0)^2}\,, \tag{2.71}$$

which is a differential Lorentzian, providing a signal linear with detuning close to resonance.

2.5 Differential Interference Contrast (DIC) microscopy

In this project we have developed a novel technique to evaluate the height of SU-8 photo resist WG structure by differential interference contrast (DIC) microscopy. We have also utilised the DIC technique to evaluate the RI of polystyrene microspheres. We therefore present here the principle of DIC microscopy. This section is based on [111, 112].

DIC microscopy is a technique in which a specimen is sampled by pairs of closely spaced rays produced by a beam-splitter. If the members of a ray pairs traverse a phase object in a region where there is a gradient in the RI or thickness or both, there will be an optical path difference between the two rays upon emergence from the object. This optical path difference is translated into a change in amplitude in the image. Fig. 2.14 shows a sketch of the amplitude profile and optical path length of a transparent specimen.

Amplitude in DIC microscopy correspond to the derivative of the optical path difference profile along the shear direction and not to the optical path directly. Thus, the first derivative of the optical path length versus distance across the specimen provides amplitude profile as seen by DIC microscopy; hence the name differential interference contrast microscopy.

Since optical path length is the product of the thickness and RI, we can determine thickness of the material from DIC image if we know the RI of the material.

A DIC microscope has four essential optical components. A polariser to produce plane-polarised light. A condenser DIC prism (a Wollaston prism) splits the beam in direction and polarisation. The resulting split distance after the condenser lens at the sample is called the shear distance. An objective DIC prism (a Normarski prism) recombines the two beams in the objective back focal plane. An analyser is directed 45° with respect to the shear and thus to the polarisation directions of the two beams so that the transmitted light is an equal superposition of the fields of both beams, providing the interference. The optical components of a DIC microscope are shown in Fig. 2.15.

2.5.1 DIC image formation

The progression of rays through the DIC microscope is shown in Fig. 2.16. In the absence of a specimen in Fig. 2.16 (a) coherent O and E rays of each ray pair subtend the same optical path length between the object and the image. The objective prism recombines the two waves and generates waves of linearly polarised light

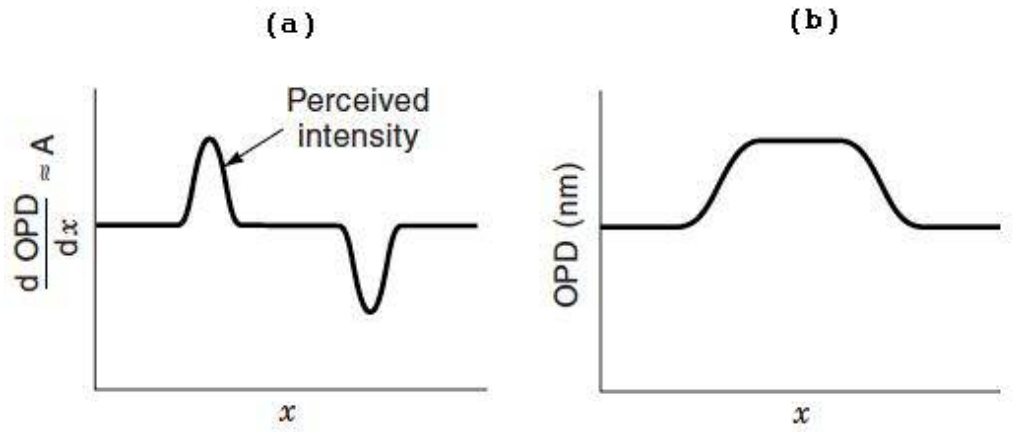

Figure 2.14: Gradients in optical path length produces differences in amplitude. Adapted from [111]. (a) Derivative of the optical path difference, giving amplitude profile as seen by DIC microscopy. (b) Optical path difference.

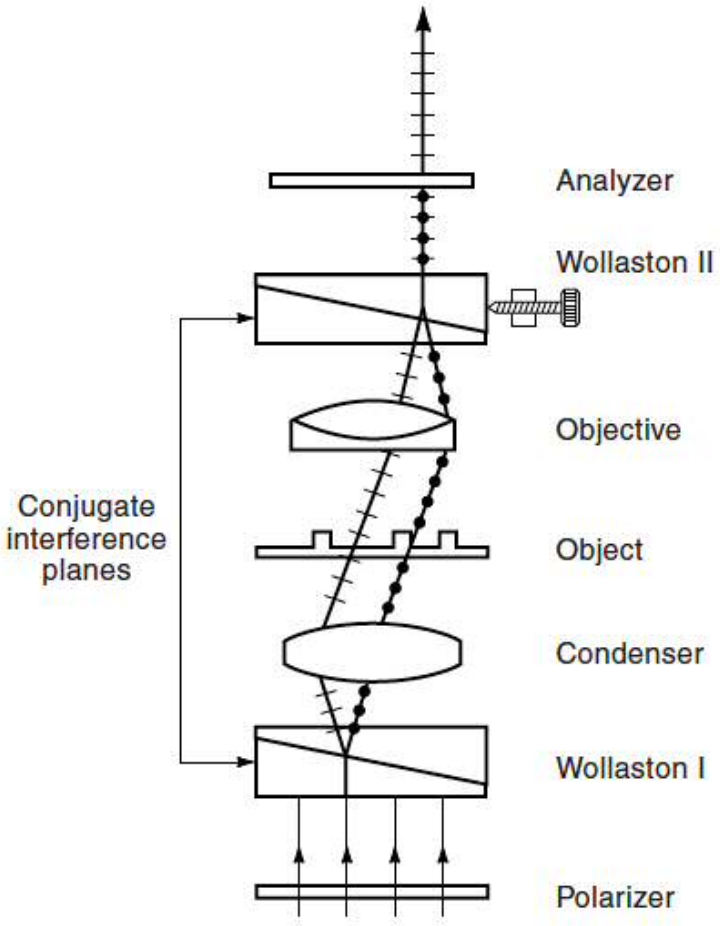

Figure 2.15: Optical components of a DIC microscope. The dots and dashes indicate the mutually perpendicular polarisations of the two components of the split ray [111].

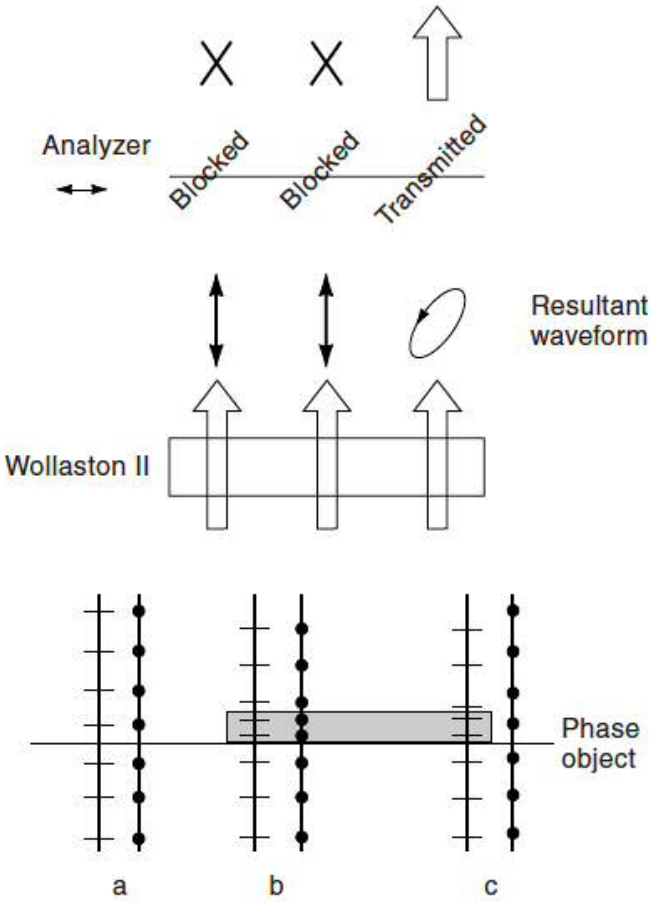

Figure 2.16: (a),(b) Recombined linearly polarised light is completely blocked by the analyser. (c) Recombined elliptically polarised light is partially transmitted by the analyser resulting in a linearly polarised component with a finite amplitude [111].

whose electric field vectors vibrate in the same plane as the transmission axis of the polariser. The resultant rays are therefore blocked by the analyser and the image background looks black, a condition called extinction. The direction of the splitting and recombination are parallel to each other and fixed at a 45° angle with respect to the transmission axis of the polariser and analyser. The same phenomenon is observed for a specimen of the same height as shown in Fig. 2.16 (b). When the O- and E-ray pair encounters a phase gradient in the specimen, two beams will have different optical paths and this acquire a mutual phase shift. Waves emerge from the prism as elliptically polarised light as shown in Fig. 2.16 (c). These rays are partially passed through the analyser to produce rays that are linearly polarised and plane parallel, they interfere in the image plane to generate a finite amplitude image of the object.

In order to produce shadow-cast, relief-like DIC images, a phase offset is introduced between the O and E rays. This is known as a "bias retardation". Introducing bias retardation makes objects much easier to see, because phase gradients in the specimen are now represented by bright and dark patterns on a gray background.

2.5.2 Extraction of differential phase from experimental data

The extraction of the differential phase from experimental data can be described briefly as follows: The intensity of light that is recorded on DIC images is given by [112],

$$I_{\text{out}}(\mathbf{r},\psi) = \frac{I_{\text{ex}}}{2}[1-\cos(\psi-\delta(\mathbf{r}))]\,, \tag{2.72}$$

with the excitation intensity I_{ex}, and the resulting DIC image intensity $I_{\text{out}}(\mathbf{r},\psi)$ as a function of the position in the sample plane $\mathbf{r}$, and the phase offset of the incident light ψ, and the differential phase $\delta(\mathbf{r})$ is the difference of optical phases ϕ for the two beams that pass the sample plane in two adjacent points separated by the shear vector $\mathbf{s}$:

$$\delta(\mathbf{r}) = \phi(\mathbf{r}+\mathbf{s}/2) - \phi(\mathbf{r}-\mathbf{s}/2) \tag{2.73}$$

To derive the differential phase $\delta(\mathbf{r})$ from $I_{\text{out}}(\mathbf{r},\psi)$, two measurements of the DIC images are taken at two opposite phase offsets $\pm\psi$, resulting in two DIC image intensity as I_+ and I_-, respectively, and are used to form a contrast image $\xi(\mathbf{r})$ given by

$$\xi(\mathbf{r}) = \frac{I_+(\mathbf{r}) - I_-(\mathbf{r})}{I_+(\mathbf{r}) + I_-(\mathbf{r})} \tag{2.74}$$

The contrast image formed this way cancels the effect of non-uniformity of the local illumination intensity I_{ex}, and we find using Eq. (2.72),

$$\xi(\mathbf{r}) = -\frac{\sin(\psi)\sin(\delta)}{1-\cos(\psi)\cos(\delta)}\,. \tag{2.75}$$

For a known experimental value of ψ, this equation can be solved with respect to the differential phase, δ. With the assumption that the differential phase is not exceeding the phase offset, $0 \le \left|\delta(\mathbf{r})\right| \le \left|\psi\right| \le \pi/2$, we find

$$\sin(\delta) = -\xi\frac{1-\cos\psi\sqrt{1-\xi^2}}{\sin\psi}\frac{1}{1+\xi^2\cot^2\psi}\,. \tag{2.76}$$

2.5.3 Calculation of absolute phase retardation from differential phase

To obtain the absolute phase retardation $\phi(\mathbf{r})$ from the differential phase $\delta(\mathbf{r})$, we need to perform a digital "integration" of the DIC contrast images. The integration can be done in Fourier domain and a Wiener filtering approach can be used to minimize the root mean square (RMS) deviation of the deconvolved image for a given signal to noise ratio κ. To integrate the $\delta(\mathbf{r})$ image, its Fourier transform ($\mathcal{F}$) is multiplied by a corresponding multiplier $G(\mathbf{k})$, and transformed back, so that

$$\phi(\mathbf{r}) = \mathcal{F}^{-1}[\mathcal{F}[\delta(\mathbf{r}))G(\mathbf{k}]] \tag{2.77}$$

where k is the wave vector. Considering the two probed points displaced by the shear $\mathbf{s}$, $\mathcal{F}[\delta(\mathbf{r})]$ is given by

$$\mathcal{F}[\delta(\mathbf{r})] = g\mathcal{F}[\phi(\mathbf{r})], \quad \text{with} \quad g = 2i\sin\left(\frac{\mathbf{s}\cdot\mathbf{k}}{2}\right) \tag{2.78}$$

where g is the Fourier representation of the DIC image formation. The Wiener deconvolution multiplier $G(\mathbf{k})$ corresponding to g for a given κ is

$$G(\mathbf{k}) = \left(g + \frac{1}{\kappa g*} \right)^{-1} . \tag{2.79}$$

The value of κ determines an effective cut-off frequency of a spatial high pass filter in the resulting phase, since g is proportional to k for small k, so that the regularization term $1/(\kappa g*)$ has equal magnitude as g in $G(\mathbf{k})$ for $|g|^2 = 1/\kappa$. With increasing κ used in the retrieval, the extension of noise-induced stripes, as well as the retrieved structures, is increasing. Resulting phase images using different κ are shown in Fig. 3.34 in Sec. 3.5.2.2.

2.5.4 Evaluation of thickness

For thin planar dielectric films of uniform refractive index with small thickness $t(x, y) \ll \lambda_0$, the local near field phase ϕ_n of the transmitted light is given by

$$\phi(\mathbf{r}) = k_0(n_d - n_m)t(\mathbf{r}) \tag{2.80}$$

where n_d and n_m are refractive indices of the dielectric film and the medium, respectively, and k_0 is the free space wave vector. The thickness of a uniform WG, Δt can be estimated by measuring the absolute phase difference $\Delta\phi$ between the top of the WGs with respect to that away from the WG, as

$$\Delta t = \frac{\Delta\phi}{k_0(n_d - n_m)} . \tag{2.81}$$

Examples are given in Sec. 3.5.2.2.

2.5.5 Evaluation of refractive index

Since DIC measures the optical thickness gradient, the DIC contrast vanishes if the RI of the specimen and the RI of the surrounding medium are equal. Thus the RI of the specimen can be evaluated by using a medium with adjustable RI, minimizing the DIC contrast. Specifically, using a mixture of two RI matching oils as medium, the RI can be continuously changed. By using different mixtures we can evaluate the RI for which no structure from the specimen is visible. We will use this in Sec. 3.5.2.3 to determine the Refractive index (RI) of SU-8.

The refractive index of a mixture of miscible liquids has been proposed by Biot-Arago and compiled by Wilfried Heller [113]. The empirical equation can be written as

$$n = \phi_1 n_1 + \phi_2 n_2 , \tag{2.82}$$

where, n is the RI of the mixture, n_1, n_2 are the RI's of liquid 1,2, respectively, and ϕ_1, ϕ_2 are the volume fractions of liquid 1,2 in the mixture. In the case of volume additivity, ϕ_1 and ϕ_2 can be written as

$$\phi_{1,2} = \frac{V_{1,2}}{V_1 + V_2} , \tag{2.83}$$

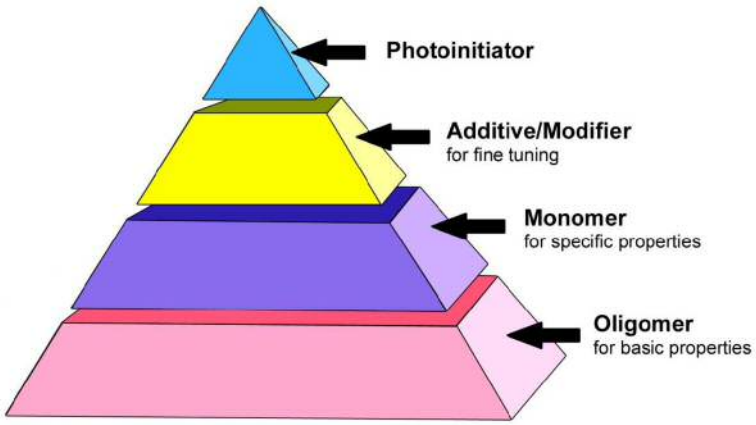

Figure 2.17: Components of a light-curable material (LCM).

where V_1 is the volume of liquid 1 and V_2 is the volume of liquid 2 before mixing. Eq. (2.82) then becomes

$$n = n_2 + (n_1 - n_2)\,\frac{V_1}{V_1 + V_2}\,, \tag{2.84}$$

which is used later in Sec. 3.5.2.3 and Sec. 3.5.3.1 to calculate the RI of miscible oils.

2.6 Light curable materials

We have used a low refractive index ultra violet (UV) light curable material (LCM), MY-133 [114], as the cladding of the WGs and the gluing layer on top of the cladding layer to attach the microspheres so that they can be excited by the evanescent wave from the WGs. In order to use this material as the cladding and gluing layer we needed to cure this material spin coated on the WGs. In this section we will describe briefly light curable materials. This section is based on [115].

A material which can be cured by ultra violet (UV) light can be called a light curable material (LCM). The curing process of an LCM is fast compared to moisture curable materials. The curing process uses free radical polymerization, which consists of three fundamental steps. These are initiation, which involves the formation of radicals followed by the radical's reaction with a monomer; propagation, which is the rapid and progressive addition of monomers to the growing polymer chain without a change of the active centre; and termination, which is the destruction of the growth active centre, usually by combination or coupling of the radicals of two growing polymer chains or by disproportionation.

The UV curing of a LCM is typically a free radical polymerization process. Illuminating the LCM with a light source of sufficient intensity, and a wavelength in the absorption range of the photo initiator in the LCM, the photo-initiator molecules within the LCM are activated by absorption of a photon. The activated photo-initiators typically split into reactive species called 'free radicals'. Free radicals then commence to form polymer chains from the monomers, oligomers, and other ingredients in the LCM, until the ingredients are depleted and the LCM has formed a solid polymer. Typical components of an LCM are shown in Fig. 2.17.

An important consideration for practical application is that the free radicals are reactive with molecular oxygen. Oxygen captures the free radicals to form stable peroxides, inhibiting the polymerization. The influx of oxygen into the coating layer during the irradiation therefore inhibits the polymerization reaction, at the surface to air. The thickness of the inhibited layer is a function of the reactivity of the formulation and of the rate of irradiation. A high dose rate of radiation helps to reduce the thickness of the non-polymerised layer. Longer irradiation time normally cannot substitute the need for an intense radiation. The most effective way to eliminate oxygen inhibition is to work in the absence of oxygen. That can be achieved by working in an inert atmosphere, such as nitrogen.

A UV curing unit has been designed and constructed within this work in order to cure MY-133. The design and construction will be discussed in Sec. 3.2.

2.7 Concluding remarks

In this chapter, we have discussed the underlying concepts relevant to the thesis. These includes planar WGs in Sec. 2.1, optical resonators in Sec. 2.2, WGMs in Sec. 2.3, the background for the implemented detection scheme in Sec. 2.4, and quantitative DIC microscopy to determine height and RI of several structures and materials in Sec. 2.5.

We have also discussed briefly the principle of light curable materials in Sec. 2.6 since we have cured both the cladding layer of the WG and the gluing layer (MY-133) to attach the microspheres by UV light.

Chapter 3

The sensor chip: Design, fabrication and characterisation

In this thesis a novel optical sensor device based on the excitation of the WGMs of the dielectric microsphere resonator in being developed and investigated. An effective way to excite and detect the WGMs is to use an external coupling device as discussed in Sec. 2.4.1.2. The coupling device can be an optical fibre or a WG [20]. Evanescent waves can be produced by guiding light though the optical fibre or the WG as discussed in Sec. 2.1. In order to fabricate an on-chip sensor device with multiplex sensing feature one can fabricate an array of WGs on a substrate. When the microspheres are placed at a small distance from the surface of the WGs, WGMs of the microspheres can be excited by frustrated total internal reflection (FTIR).

In this project, we have realised a small monolithic biosensor device by fabricating an array of optical WGs and attaching the microspheres at a distance from the core of the WGs in such a way that the sensor device can easily be fabricated and used for multiplexed sensing. A sketch of the structure is shown in Fig. 3.1. Microspheres are attached on top of the WGs using a gluing layer. Light coupled into the WG from one end of the chip, and guided through the WG by total internal reflection (TIR) creates an evanescent wave at the core-cladding interface. This evanescent wave couples to the WGMs of the microsphere, and transmission can be observed at the other end of the WG.

Design, fabrication and characterisation of the sensor device will be discussed in this chapter.

3.1 Design

In order to realise the monolithic biosensor device, we have to solve some design challenges. Firstly we need to design and manufacturable and suited array of WGs. The fabrication of WGs can be done in a clean room by photo lithography once the mask is designed and WG materials are selected. The fabrication process is described in Sec. 3.4. The design assumes a probe light wavelength of 784 nm, which is in a range of low absorption of the aqueous medium [86].

The substrate for the WGs can be microscope glass coverslips of RI of about 1.5, which are commercially available at low cost, having high surface quality and thickness between 0.1 and 0.3 mm. The WG dimension needs to be designed considering the WG material and working wavelength, to achieve single mode propagation.

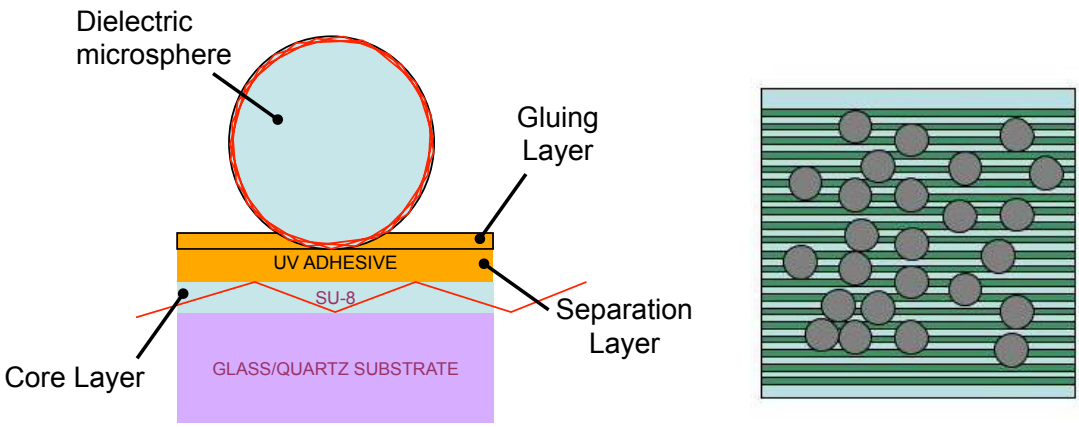

Figure 3.1: Sketch of the biosensor device structure. Left: Cross-section. The SU-8 layer acts as the core of the WG. A microsphere is attached at a fixed position on an adhesive layer which can be cured by ultra violet light, and has a refractive index matched to the surrounding medium (water). The same material is used as the separation layer, which is also the cladding layer of the WG. The distance between the WG and the microsphere is set by the thickness of the separation layer. Right: Top view. The stripes are the array of SU-8 WGs. Microspheres are randomly placed on the WGs.

The dimension such as width and height can be estimated as discussed in Sec. 2.1.2. Mask design for WG fabrication is discussed in Sec. 3.1.1.

SU-8 is a common high index polymer used in photolithography, which is optically transparent in the NIR and visible region [116], making it a suitable core material for the optical WGs, which can be spin coated on a glass surface. The height of the WGs core layer on the substrate can be controlled by the spin coating parameters. The height can be measured by an ellipsometer inside the clean room. We have developed an alternative technique to measure the WG height by optical method. The theoretical background of this technique is briefly described in Sec. 2.5.

The cladding layer of the WGs and the gluing layer holding the microspheres on top of the WGs need to be index matched to the medium in order to be invisible optically, thus not introducing scattering losses and retaining a high Q factor. Since the sensor device is designed to be submerged inside a microfluidic chamber in an aqueous medium, we need a cladding material with a RI close to that of water (1.33). This is lower than the RI of typical organic polymers in the 1.4 to 1.5 range, and requires a so-called low RI material, which can be created by fluorinating a polymer, i.e. replacing hydrogen with fluor. In previous works [86], cytop was used, which is heat-curable above 100 degrees C. However, applying such heat is typically incompatible with biofunctionalisation, and can also deform the PS microspheres. We therefore searched to replace cytop with a light-curable material (see Sec. 2.6), and selected MY-133. The properties of different considered candidate materials are discussed briefly in Sec. 3.1.2.2. The same material can be used as the gluing layer on top of the cladding layer of the WGs. We have designed a UV curing unit for MY-133, which is discussed in Sec. 3.2, and developed a curing process for MY-133 discussed in Sec. 3.4.2.4.

The distance between the microspheres and the WGs should be such that a critical coupling can be achieved to maintain high cavity Q factors as discussed

in Sec. 2.4.1.2. Critical coupling is achieved when the incident optical power from the WGs is entirely dissipated into the resonator and the transmission of the WGs at resonance reduces to close to zero [86]. The control of the distance between the WGs and the microspheres is therefore crucial. From the data shown in [86], we estimated the distance should be around 550 nm. We have characterised this distance in Sec. 3.5.3.2.

In this project we have used polystyrene microspheres whose RI is of about 1.5788 at 784 nm, which is similar to the RI of SU-8, and allows for a phase matching of the coupling. We have characterised the RI of the polystyrene microspheres by DIC microscopy as discussed in Sec. 3.5.3.1. Since the intrinsic losses decrease exponentially with the radius of the sphere as discussed in Sec. 2.3.4.2, a sufficiently large microsphere gives suited intrinsic losses. As shown in Fig. 2.9, the radiative Q factor of the fundamental WGM of a polystyrene microsphere (RI of 1.5788 at 784 nm) in water (RI of 1.33 at 784 nm) is of the order of 10^8 for a diameter around 30 µm. Increasing the diameter further is reducing the sensitivity, for both TE and TM polarisation, as shown in Fig. 2.10. Intuitively, with increasing diameter the mode is being less squeezed to the surface, reducing the evanescent field strength in the medium. We have therefore used polystyrene microspheres of about 30 µm diameter.

3.1.1 Waveguide structure

In order to fabricate WGs by optical lithography, a mask has been designed. Since the side walls of the WGs will have a certain roughness after fabrication (typically of a few hundred nanometres), too narrow WGs will have significant scattering losses. The WG width therefore has been chosen to limit such scattering losses limiting the minimum WG width to 2 µm. Requiring single mode operation in the lateral direction of the WGs, on the other hand, gives an upper limit on the width. This width can be controlled by the vertical confinement, and being close to the cutoff between guided modes and substrate modes (see Table 2.1) increases the maximum width for single mode operation. However, a design close to the cut-off sensitively depends on the SU-8 RI and thickness, making a reliable fabrication more complicated. The mask, therefore, consists of 2 µm, 3 µm, and 4 µm wide clear stripes. The pitch is 50 µm. A bright field chromium mask of size $4'' \times 4''$ has been ordered from Deltamask©. For negative resist, the clear stripes will produce the remaining WG material.

3.1.2 Waveguide materials

In this section we will discuss the selection of WG material for fabrication by optical lithography.

3.1.2.1 Optical waveguiding constraints

In order to guide light through the WGs by total internal reflection (TIR), the material of the core layer of the WG must have higher RI than both the substrate and the cladding layer. SU-8 has been chosen for it's RI of 1.566 [116] which is higher than both the Schott D263 glass substrate (1.5167) and low RI cladding layer (1.33) at a wavelength of 784 nm.

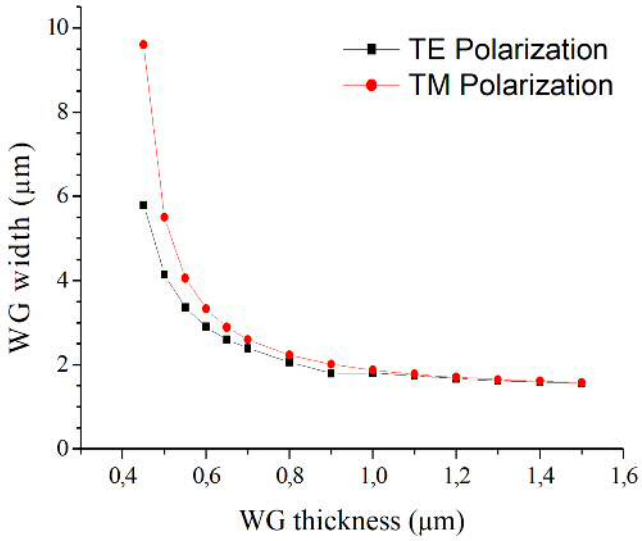

Figure 3.2: Relation between the thickness and maximum width of a SU-8 WG for single mode propagation. The calculation assumes that width ≫ thickness. The substrate is a glass coverslip and the cladding layer is MY-133. Properties of glass coverslip, SU-8 and MY-133 are discussed in Sec. 3.1.2.3. The graph shows that for an increasing thickness of the WG core layer the width of the WG should be decreased to maintain single mode propagation.

The critical dimensions for single mode propagation through a SU-8 WG on a glass coverslip and a cladding layer of MY-133 can be estimated by Eq. (2.8).

We first consider a planar waveguide of SU-8 thickness d, and find the cut-off thickness of the WG, below which no guided propagation is present, to be 340 nm for TE polarisation, and 380 nm for TM polarisation. Increasing the thickness, a second guided mode gets confined above 1.33 µm for TE polarisation and 1.37 µm for TM polarisation giving the maximum thickness for single mode operation of the planar WG.

Let us now consider the modes of the WG of a finite width in the lateral direction. Since the width of the waveguide is much larger than the thickness, we can estimate the confined modes with the one-dimensional model in Eq. (2.8), using the effective RI n_{eff} of the planar guided mode as RI of the core layer, using the WG width as thickness d, and the substrate RI, giving the highest propagation index without the SU-8 layer, as the cladding and substrate RI. Increasing the width, a second mode gets confined at a critical width, marking the limit of lateral single mode operation. Fig. 3.2 shows the relation between the SU-8 thickness and the critical width for single mode propagation.

3.1.2.2 Material compatibility

Coverslips made from Schott D263 glass of RI 1.5167 at 784 nm[117] or fused silica glass of RI of 1.453 at 784 nm [117] have been considered as the substrate of the WGs. These transparent coverslips give the option to image the WGs and microspheres from the substrate side. An alternative to these transparent glass substrate could be SiO_2 on silicon, which is used in silicon photonics. These substrates can be

cleaved easily due to the crystalline structure of silicon, to open the WGs facets, but would not be transparent at the operating wavelength, and thus inhibit imaging via the substrate. We have developed a standard operating procedure (SOP) providing an acceptable cleaving of glass coverslips, as detailed in Appendix B.4. Coverslips made of D263 Schott glass have been chosen as the substrate material because they are much cheaper than fused silica coverslips.

Cytop, supplied by Ashahi Glass Company, is a low RI material (1.346 at 784 nm [118]) and was used before to attach PS microspheres to a substrate [86]. It is a fluoropolymer of amorphous structure which can be dissolved in a fluorinated solvent. This makes it possible to spin coat for a thin film deposition. However, Cytop needs to be cured at high temperature (120 °C to 180 °C). Antibodies attached to the sphere surface will not tolerate temperatures above 60 °C. Therefore, an alternative to Cytop was needed, and a few materials have been considered as the cladding and gluing layer of the WGs. One of the materials has been Teflon manufactured by Chemours [119]. Teflon^{TM} is a fluoropolymer which is soluble in selected solvents such as FC-40 from 3M [120] and have the lowest index of refraction of any known polymer [121]. These properties of Teflon make it suitable for spin coating and thereby it can be the low RI cladding layer. RI of Teflon at 784 nm is 1.3038 according to Sellmeier parameters given in [121]. This is close to water, however, the curing temperature around 140° is even higher than Cytop [121], making it unsuitable for our application. In addition to this high temperature requirement for curing, a fume hood was required to process Teflon in the local clean room (CR), which was not available.

In order to meet the requirements of our application we choose MY-133, which can be spin coated to deposit on a substrate and cured either by ultra violet light or by heating at a high temperature [114]. Another low RI material, which became commercially available later than MY-133, is NOA 133 manufactured by Norland®. This material can be considered as the alternate to MY-133 as the refractive is 1.33 at 550nm and can be cured by ultraviolet light of (320 - 450) nm wavelength with a dose of 6 J/cm^2 [122].

3.1.2.3 Optical properties

To enable a high transmission of the WGs, the optical losses due to absorption, and scattering from the side walls have to be small. The core, cladding, and substrate materials should therefore have a high internal transmission. SU-8 is a chemically enhanced, negative tone photoresist, consisting mainly of Bisphenol A Novolak epoxy oligomer (EPON® SU-8 resin, Shell Chemical). The resin is made photosensitive by adding up to 10 wt% triarylsulfonium hexafluroantimonate salt (CYRACURE® UVI, Union Carbide), which acts as a photo-acid generator (PAG). When exposed to UV radiation of (350-400)nm wavelength, the salt decomposes to form hexafluoroantimonic acid and it's anionic part reacts with the solvent of the resist. This initiates a cationic polymerisation by ring-opening and subsequent cross-linking of the epoxy groups after application of heat during post exposure baking (PEB). The mixture is usually dissolved in an organic solvent such as Cyclopentanone in order to enable spin coating. The RI and transmittance curve of SU-8 is shown in Fig. 3.3. The absorbance curve is shown in Fig. 3.4.

The cladding layer material of the WG is a low refractive index UV light curable

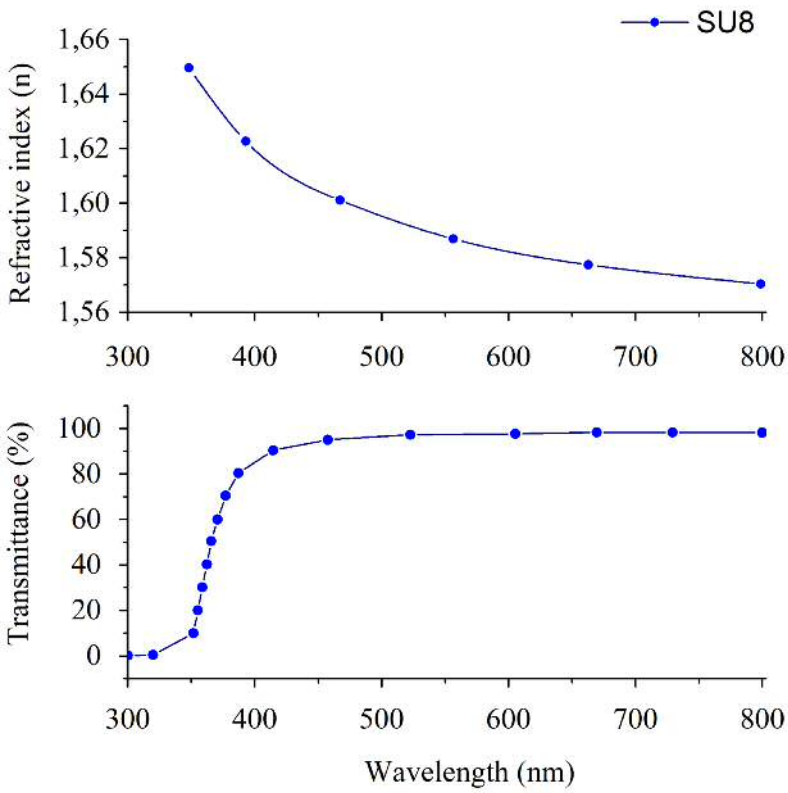

Figure 3.3: The graph shows refractive index relation in Fig. 3.3 (top) and transmittance relation in Fig. 3.3 (bottom) of SU-8 at different wavelength. The thickness of the SU-8 layer has been 50 µm in the experiment. Data has been obtained from the supplier [116].

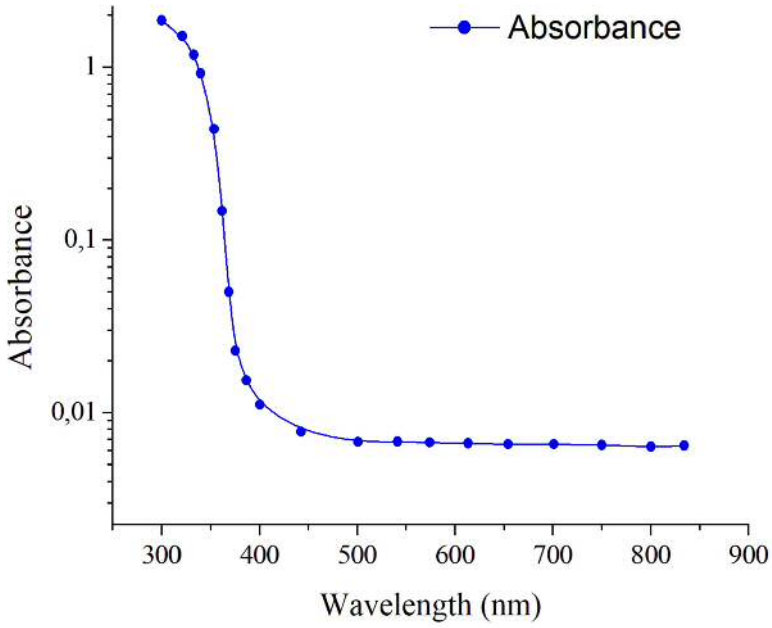

Figure 3.4: The graph shows the absorbance spectrum of uncured SU-8 photoresist with a thickness of 25 µm. Data has been obtained from [123].

material called MY-133, supplied by My polymers, has a refractive index of 1.33 at 589 nm [114]. MY-133 is fully soluble in a fluorinated solvent such as Novec HFE-7500 supplied by 3M [124], which allows spin coating. Since the material is UV curable, the high temperature baking step can be avoided in the curing process. Therefore, it is used as the cladding material. Refractive index for cured and non-cured MY-133 is shown in Fig. 3.5. The Material properties of MY-133 are listed in Table 3.1. The optical properties of glass coverslips are listed in Table 3.2.

Parameter	Symbol	Value	Unit
Refractive index (cured, at 770 nm)	n	1.332	
Refractive index (non-cured, at 770 nm)	n	1.328	
Viscosity	η	2000-3000	cps
Density	ρ	1.71	g/ml
Curing wavelength		300-400	nm

Table 3.1: Material properties of MY-133 [114].

Parameter	Symbol	Value	Unit
Refractive index (at 546.074nm)	n_e	1.5255	
Refractive index (at 589.3 nm)	n_d	1.5230	
Mean coeff. of thermal exp.	α	7.2×10^{-6}	K^{-1}
Density	ρ	2.51	g/cm^3
Glass temperature	T_g	736	°C

Table 3.2: Properties of Schott D263 glass of RI of 1.5167 at 784 nm coverslips [125].

3.2 Curing unit

In this section we will describe the UV curing unit that we have designed to cure the low refractive index material MY-133. Since the presence of oxygen during the curing process inhibits the polymerisation reaction, as discussed in Sec. 2.6, we have designed a curing device capable of producing high intensity UV light in an oxygen-free chamber, which is portable to be used in the clean room. The first version of the device consists of 9 (UV5TZ-390-15) UV LED supplied by BIVAR, Inc [126] with an inert chamber as shown in Fig. 3.6. The chamber has an inlet for N_2 gas. The chamber is not fully air tight, so that a continuous flow is applied. The top of the unit houses the electrical circuit, while the sample is placed below. The distance between the top and bottom plate is 32 mm. The electrical circuit consists of a 24 V switched mode power supply with three parallel resistors of 750 Ω each. This provides a current of 17.6 mA in each LED in the circuit. The maximum current rating for a UV5TZ-390-15 LED is 20 mA so with 750 Ω resistors in the circuit the LEDs will last long. The power that dissipates from each branch of the circuit is 0.23 W. The sketch of the electrical circuit is shown in Fig. 3.7.

The curing device has been characterised by using a 5.5mm×4.8mm Si PIN Photo diode (S6775), supplied by Hamamatsu Photonics [127] along with a multi-

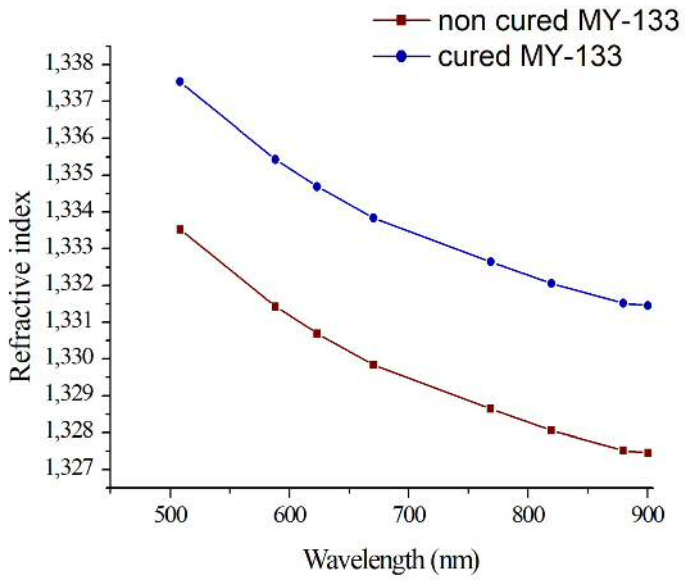

Figure 3.5: The graph shows the refractive index relation of cured and non-cured MY-133 at different wavelength. The data have been obtained from the supplier [114].

meter, supplied by Keithley Instruments Ltd [128]. Photo-current has been measured at six points on the bottom plate of the unit. Minimum photo current that has been measured as 0.31 mA which corresponds to a radiant flux of 1.7 mW and an intensity of 6.5 mW/cm^2. Considering the recommended curing dose required for MY-133 of 2.5 J/cm^2 [114], the required curing time is about 3.5 min. The technical specifications of the Hamamatsu S6775 Si PIN photo diode are listed in Appendix A.8. It was found that during the rather long curing time a high flux of N_2 was required to avoid the influence of remaining oxygen, which lead to a sticky resulting surface. In order to cure the MY-133 layer faster and reduce consumption of N_2, the curing unit has later been upgraded with new top part, containing a single LED of 365 nm peak wavelength, and a higher radiant flux of up to 800 mW supplied by LED ENGIN [129]. The LED circuit is fed by a switched mode plug-in power supply of 5 V, with a series resistor of 2 Ω, as shown in Fig. 3.8. The LED circuit is housed in a small box of dimensions $50 \times 50 \times 25$ mm^3. An extruded aluminium heat sink is mounted on top of the box for thermal management. All these components are supplied by RS Components Ltd [130]. Pictures of the device are shown in Fig. 3.9.

The new curing unit has been characterised by the same photo diode. The minimum photo current has been measured as 1.6 mA which corresponds to a radiant flux of 9.3 mW and therefore an intensity of 35 mW/cm^2. Thus, the required curing time is 72 s, about three times faster than the previous version. The spatial maps of the intensity of the two curing units are shown in Fig. 3.10. The measurements have been taken at the bottom surface, which is 32 mm away from the source.

3.3 Cutting tool

The biosensor samples have been fabricated on 0.13-0.17 mm thick Schott D263 glass substrate coverslips (thickness #1) of lateral dimensions 18×18 mm^2, supplied by

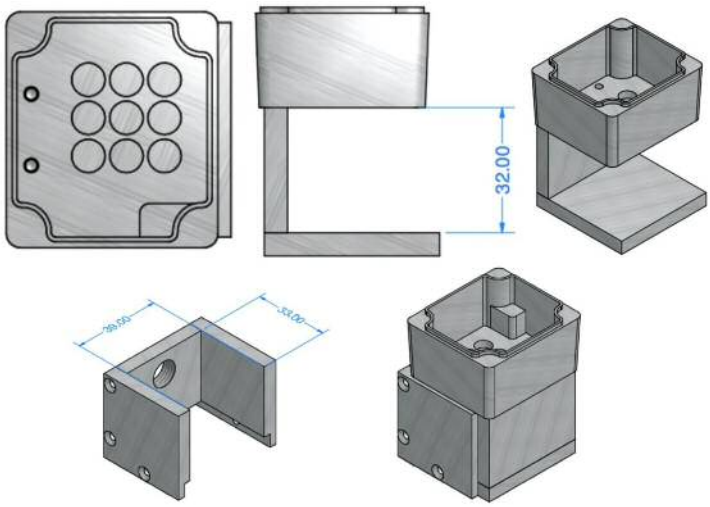

Figure 3.6: Drawings of the ultra violet light curing unit designed to harden the spin coated MY-133 layer. The unit consists of an inert chamber to prevent the presence of oxygen around the sample during the curing process.

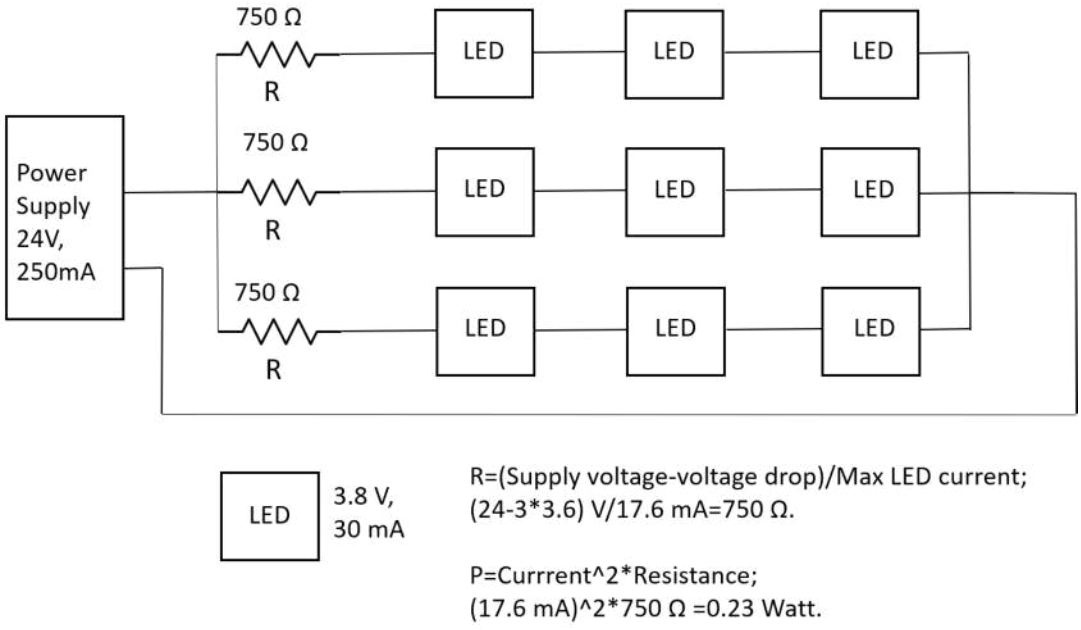

Figure 3.7: Electronic circuit for the UV curing unit. Resistances in the circuit limits the current flow through the LED. The circuit consists of 9 LED supplied by Bivar Inc. [126]. Technical specification of the LEDs is given in Appendix A.6.

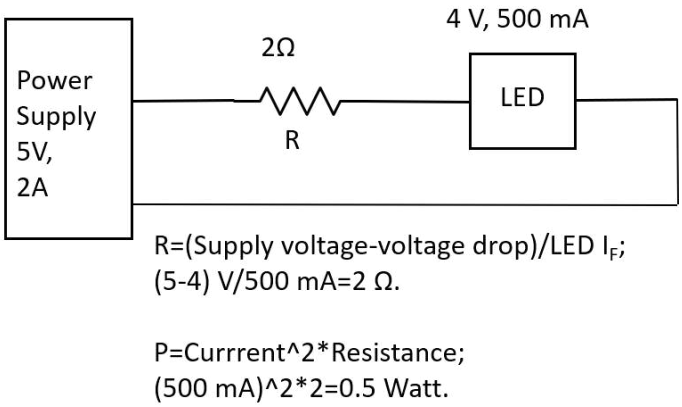

Figure 3.8: Electronic circuit of the upgraded UV curing unit. The circuit consists of an UV LED, supplied by LEDENGIN [129]. The technical specification of the LED is given in Appendix A.7.

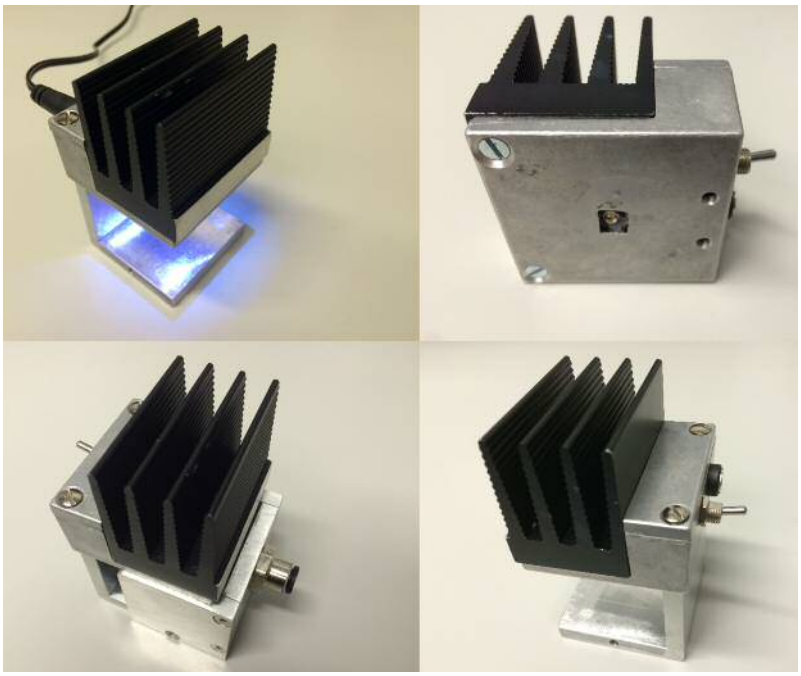

Figure 3.9: The upgraded UV curing unit. The curing unit has a single die LED of peak wavelength at 365 nm and high radiant flux up to 800 mW. A standard extruded heat sink is mounted on the top of the curing unit. This curing unit is 3 times faster than the previous one.

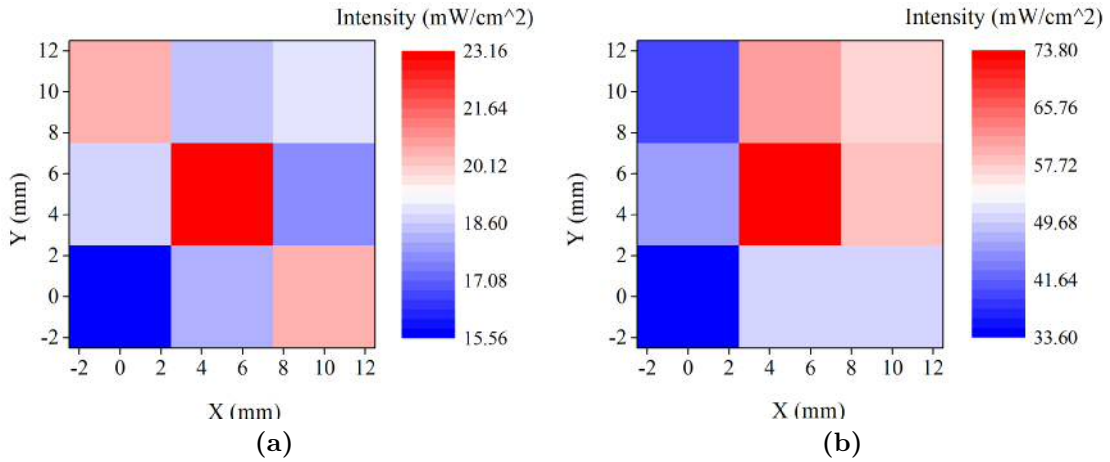

Figure 3.10: Intensity maps of the (a) original and (b) upgraded UV curing unit

Fisher Scientific, catalog number: S17521. Both SU-8 and MY-133 layers have been deposited on the coverslip substrate by spin coating. Spin coating leaves uneven SU-8 and MY-133 layers at the edge of the coverslips. These unwanted layers are removed from the coverslip edge before the following photo lithography step. To provide a clean facet terminating the WGs, for optical in and out coupling, the fabricated sensor chips need to be cleaved. The dimension of the cleaved sample is chosen to fit inside the fluid chamber and onto the sample holder block as discussed in Sec. 4.4.1.1.

A cutting tool has been designed for this purpose as shown in Fig. 3.11. It consists of a sample and diamond scribe holder and a movable guide. This guide allows the sample to be cut to any desired size. The tool allowed for simple (typical setup time is about 5 min, and time to cut per sample is also about 5 min) and accurate ($\pm$0.2 mm) cutting process. The corresponding protocol to cleave the sample we developed is given in Appendix B.4.

3.4 Fabrication

3.4.1 Controlling the separation layer thickness

Since the distance between the WG and the microsphere is crucial for achieving critical coupling, we need to determine the thickness of MY-133 on top of the SU-8 WGs. In order to determine this distance d_{cld}, a model has been developed, using the geometrical considerations sketched in in Fig. 3.12. Importantly, the measurements available are the surface topography before and after adding the separation layer, measured by a profilometer, as well as the thickness of the separation layer d_0 on a flat substrate under the applied spin coating protocol. We use mass conservation, that is, conservation of the cross-sectional area of the separation layer, over one period P of the WG array, to obtain

$$d_{\mathrm{chn}} P + A_{\mathrm{dif}} - A_{\mathrm{WG}} = d_0 P \,. \tag{3.1}$$

On the left hand side (LHS) is the total cross-sectional area of the structure with WGs, consisting of the channel thickness d_{chn} times P, plus the measured cross-sectional area A_{dif} of the separation layer topography, minus the measured cross-

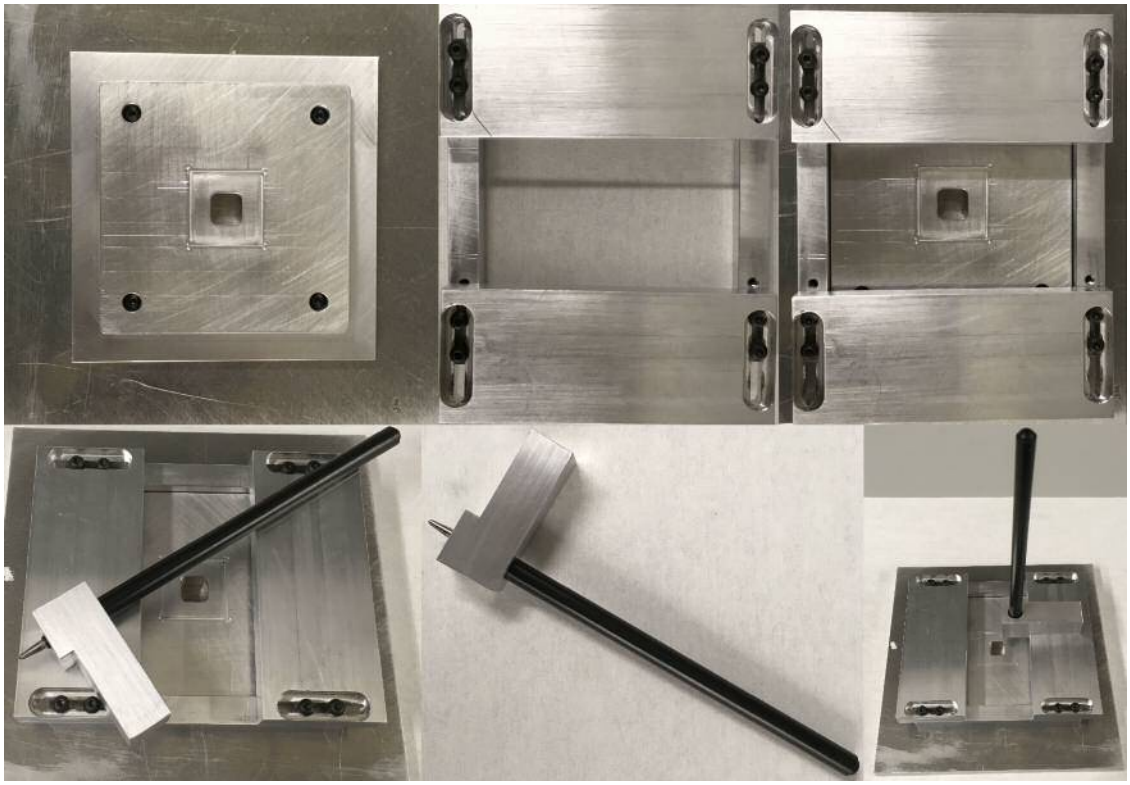

Figure 3.11: Images of parts of the cutting tool for cleaving the sample to fit inside the fluid chamber for optical coupling.

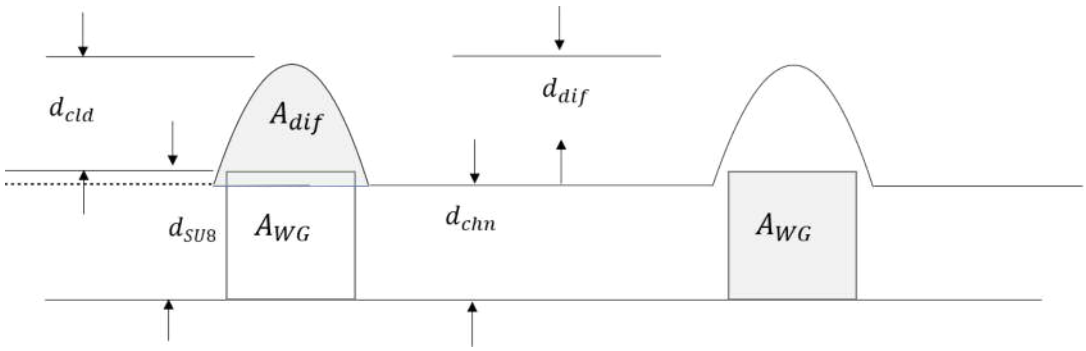

Figure 3.12: Geometrical model to estimate the separation layer height on the WGs

sectional area A_{WG} of the WG topography. The right-hand side (RHS) is the corresponding cross-sectional area of the layer on a flat substrate. Using Eq. (3.1), we determine d_{chn}. The cladding thickness d_{cld} can then be determined using the measured d_{dif} and d_{WG} as

$$d_{\mathrm{cld}} = d_{\mathrm{chn}} + d_{\mathrm{dif}} - d_{\mathrm{WG}} = d_0 + d_{\mathrm{dif}} - d_{\mathrm{WG}} - (A_{\mathrm{WG}} - A_{\mathrm{dif}})/P\,. \tag{3.2}$$

To achieve the required d_{cld}, multiple samples have to be fabricated with varying d_0, and for each of them d_{cld} has to be determined. To speed up the convergence of this process, a hypothesis concerning the dependence of A_{dif} on d_0 has been developed. For $d_0 = 0$, we have $A_{\mathrm{dif}} = A_{\mathrm{WG}}$ by construction. For $d_0 \gg d_{\mathrm{WG}}$, we expect a flattening of the surface. We therefore conjecture the dependence to be

$$A_{\mathrm{dif}} = \frac{A_{\mathrm{WG}}}{1 + \left(\frac{d_0}{d_{\mathrm{WG}}}\right)^{\alpha}}\,, \tag{3.3}$$

which has one adjustable parameter $\alpha > 0$, controlling the speed of the flattening. After fabricating a first sample, one can determine the value of α from Eq. (3.3). The value of d_0 to be used for the next sample can then determined using A_{dif} according to Eq. (3.3) in Eq. (3.2), and solving for d_0.

3.4.2 Waveguides

In this section we discuss the fabrication steps of SU-8 WGs on glass coverslips, covered by MY-133 as the cladding and separation layer. WGs have been fabricated by photo lithography in a class 1000 cleanroom. SU-8 has been deposited by spin coating on 18×18 mm glass substrates. The fabrication process steps used for the WG fabrication are sketched in Fig. 3.13.

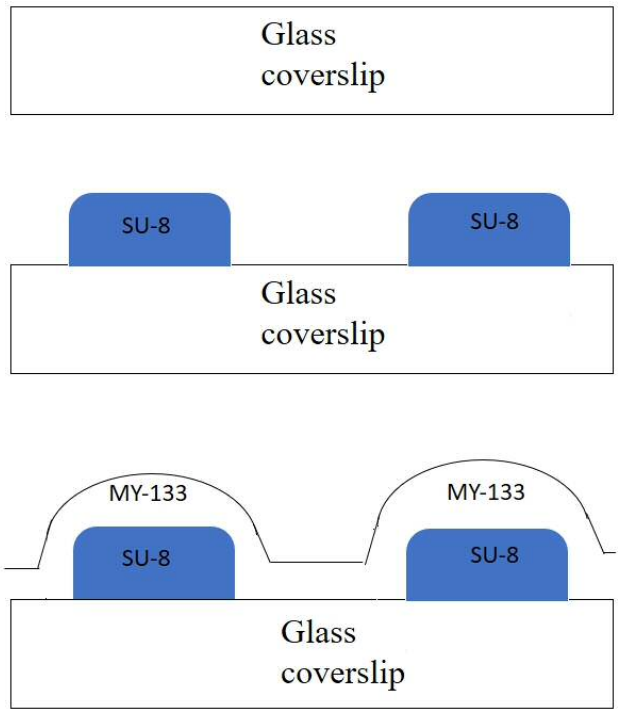

Figure 3.13: Process steps in WG fabrication.

3.4.2.1 Substrate preparation

Schott D263 glass coverslips have been used as the substrate for the fabrication of the WGs. Their properties are given in Table 3.2. Before the fabrication process starts these glass substrates need to cleaned. Piranha solution, which is a 3:1 mixture (v/v) of (98% H_2SO_4 and 30% H_2O_2), can be used to clean these glass substrates from organic residues and make them hydrophilic. We have cleaned few glass substrates in this way. Alternatively, Schott glass substrates can be cleaned by a series of different solvents, such as Acetone, Methanol, and Isopropanol. The solvents are first preheated at 80°C on a hotplate. Each glass substrate is submerged first in Acetone, then in Methanol, and then in Isopropanol, for 5 min each. We have cleaned few glass substrates by this method as well and found that the second methods cleaned the substrates equally good as the first method. We have therefore used the second cleaning method to clean our glass substrates because it saves a lot of clean room time.

Adhesion of hydrophobic SU-8 is rather poor on a hydrophilic substrate like glass and can be improved by using primers [131]. Primers can be costly and their use introduces an additional processing step in WG fabrication. In this project we have baked the substrates for 1 min at 180°C on a hotplate to remove the moisture from the surface and to improve adhesion between SU-8 and the glass surface [132], which proved to be sufficient.

3.4.2.2 Spin coating of SU-8

In order to start fabricating WGs we need to deposit SU-8 of a defined thickness on the glass coverslips. The required thickness of the SU-8 is determined by the WG properties as discussed in Sec. 3.1.2.1, and is in the order of 1 µm.

After fabricating planar WGs with different thicknesses, we found that a 900±50 nm thick SU-8 layer produced suited WGs inside the optical setup discussed in Chap. 4. The thicknesses have been measured by Dektak[3]. An alternate method for measuring the thickness of this step like samples such as WGs has been developed. The theoretical part of this method has been discussed in Sec. 2.5. The practical part of the technique will be discussed in Sec. 3.5. The target thickness for SU-8 has been set to 900±50 nm.

We have used SU-8 2000.5, supplied by MicroChem®, to deposit SU-8 on the glass coverslip by spin coating in a spinner supplied by SPS-Europe [133]. Spin coating is a procedure used in micro fabrication to deposit thin films of homogeneous thickness on a flat substrate. The measured SU8 thickness versus spin speed of SU-8 2000.5 is shown in Fig. 3.14, showing that the target thickness can be achieved at a low spin speed around 400 rpm. Using this speed the process has been found not reproducible in later fabrication attempts. Therefore, SU-8 2002, which is another variant of SU-8, supplied also by MicroChem®, has been investigated for SU-8 deposition. We have spin coated SU-8 2002 at two different speeds. The thickness versus spin speed curve in Fig. 3.15 shows that the deposited SU-8 is too thick compared to target thickness. In order to reduce the thickness, different accelerations were investigated, for 8000 rpm final speed, as shown in Fig. 3.16. The SU-8 thickness decreases with acceleration, but only reaches 1200 nm , larger than the target value. The results show that we require a SU-8 solution with properties in-between the two investigated ones. Therefore SU-8 2002 has been mixed with SU-8 2000.5 in a volumetric ratio of (1:1) and (2:1) according to Table 3.3, and the resulting thicknesses

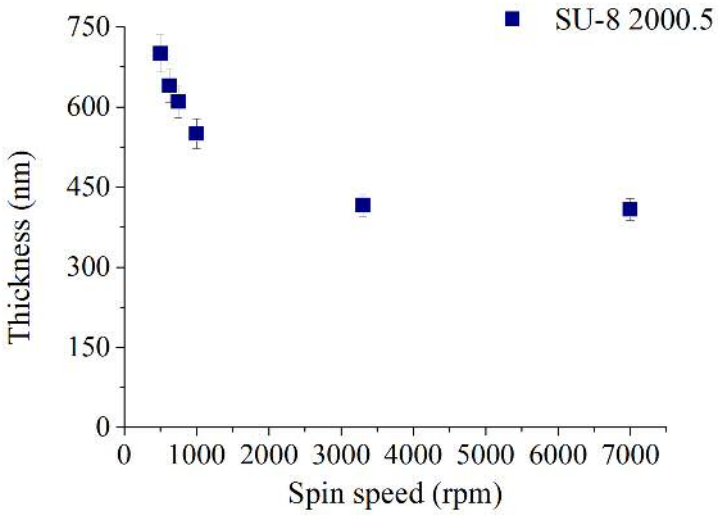

Figure 3.14: SU8 film thickness versus final spin speed using of SU-8 2000.5, spin coating for 45 s with an acceleration of 300 rpm/s. Each sample has been measured at 5 different points. Error bars indicate the variation from the average of the measurements.

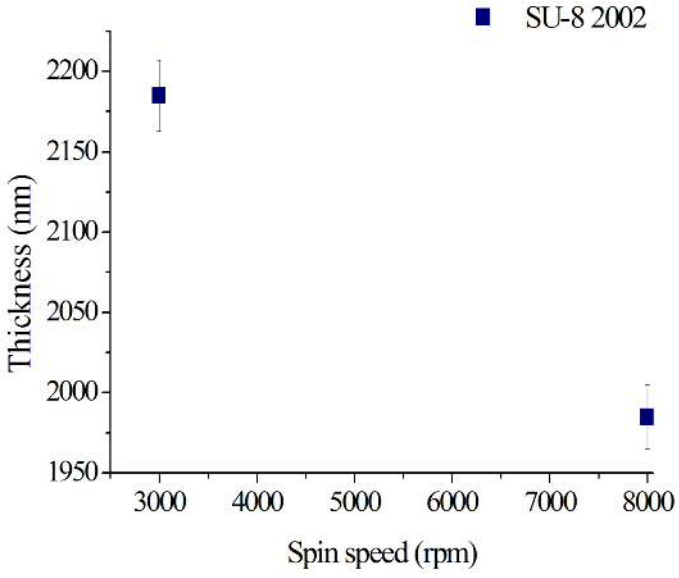

Figure 3.15: As Fig. 3.14, but for SU-8 2002.

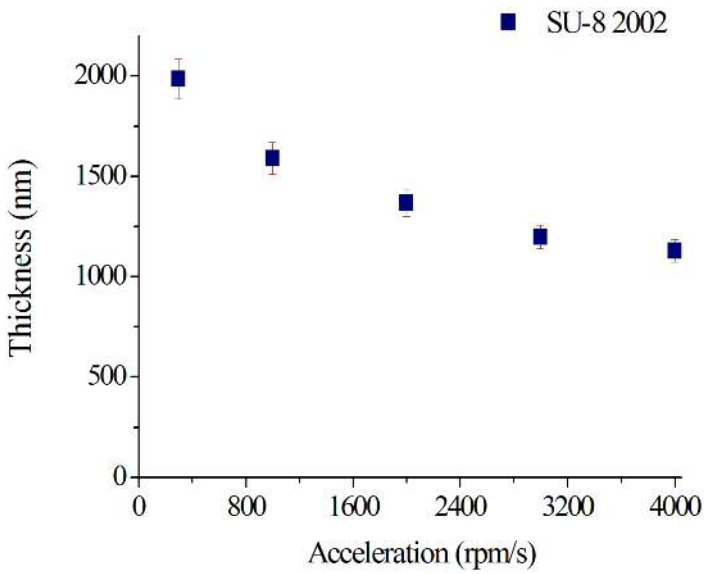

Figure 3.16: As Fig. 3.15, but versus acceleration for a final speed of 8000 rpm.

are given in Fig. 3.17, showing that a (1:1) ratio provides a thickness close to the target. To operate at somewhat higher speeds, a ratio of (2:1) was the choosen, and the spin speed relation for this ratio is shown in Fig. 3.18. Since the spin coating of

SU-8 2002	SU-8 2000.5	Total Amount	Ratio
5 mL	5 mL	10 mL	1:1
10 mL	5 mL	15 mL	2:1

Table 3.3: SU-8 2002 diluted by SU-8 2000.5.

SU-8 leaves edge microsphere this uneven SU-8 layer around the edge of the sample has been removed by EC solvent. EC solvent has been used as a developer later in the fabrication process. The technical specification of EC solvent is given is appendix A.1. We have spin coated 2 mL of SU-8 solution to deposit the target height.

3.4.2.3 Exposure, soft baking, development and hard baking of SU-8

After spin coating, the sample has been baked for 3 min on a hotplate at 95°C, to evaporate the remaining solvent. After this soft baking step, the sample has been exposed to ultraviolet (UV) light in a KarlSuss mask aligner with an intensity of 55 mW/cm^2. Exposing SU-8 in UV light initiates the cross-linking process as explained in Sec. 3.1.2.3.

We found that an optimisation of exposure time is important to obtain suited WG structures, as underexposure leads to soft, non-straight WGs, and overexposure leads to tails of the waveguides depending on the mask contact, creating roughness. Fig. 3.19 shows underexposed and optimally exposed SU-8 WGs and Fig. 3.20 shows overexposed sample after the full fabrication process. The optimal exposure time has been found as 1 s.

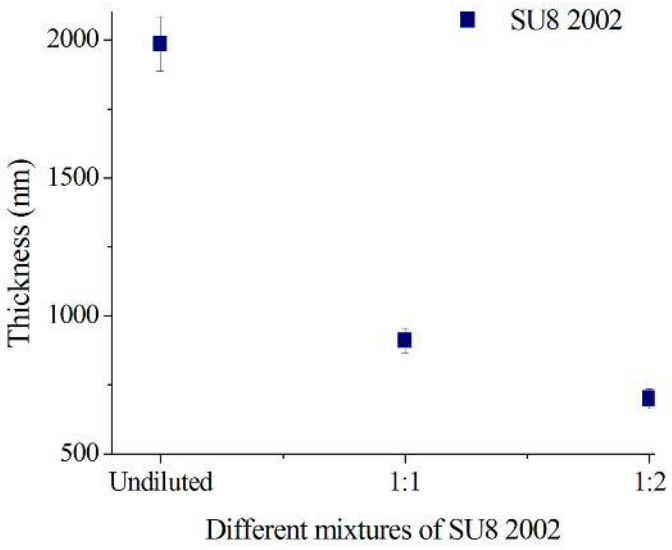

Figure 3.17: SU-8 thickness of mixtures of SU-8 2002 and SU-8 2000.5 in the volume ratios as labelled. Final speed 3000 rpm, other settings as in Fig. 3.14.

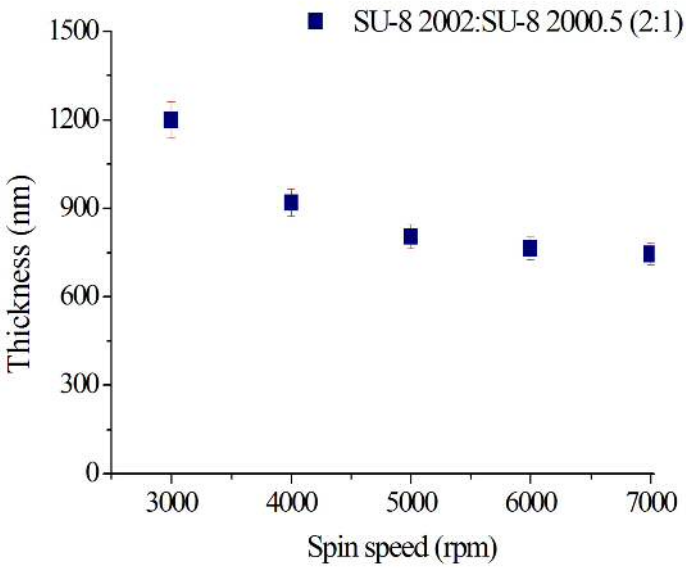

Figure 3.18: As Fig. 3.14, but for a mixture of SU-8 2002 with SU-8 2000.5 in a volumetric ratio of 2:1.

After the exposure step, the sample is heated on a hotplate for 3 min at 95 °C to complete the cross-linking process initiated by the UV exposure. The sample is then developed to remove the non cross-linked SU-8. A hard baking step follows the development process to remove any remaining solvent present in the sample. The optimised standard operating procedure (SOP) to fabricate the SU-8 WG on glass coverslips is given in Appendix B.1.

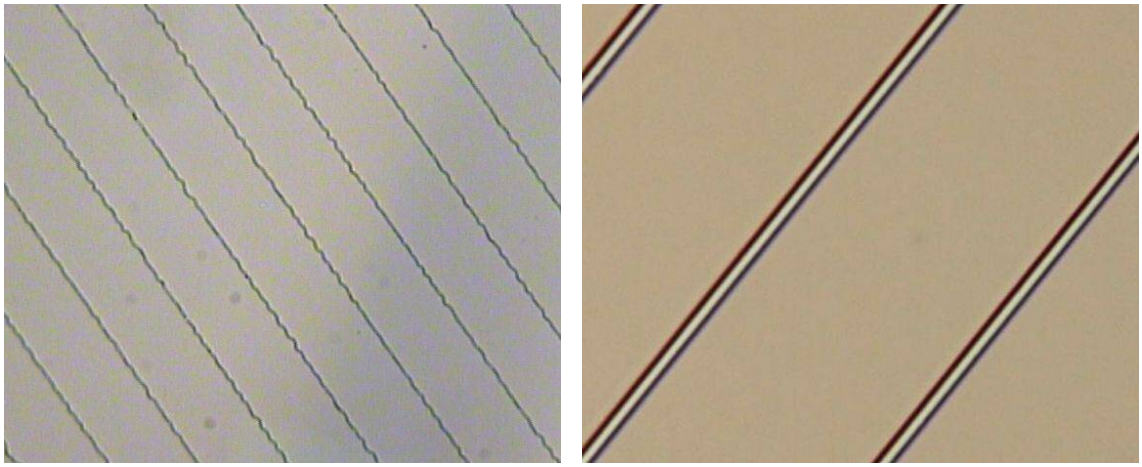

(a) (b)

Figure 3.19: Transmission optical images of SU-8 WGs on glass coverslip of width 3 µm. Samples have been exposed to UV light for different times. (a) Underexposed sample, exposed for 30 s (b) Sample with optimised exposure dose, exposed for 1 s. Images sizes are (a) 285 µm × 235 µm and (b) 115 µm × 95 µm.

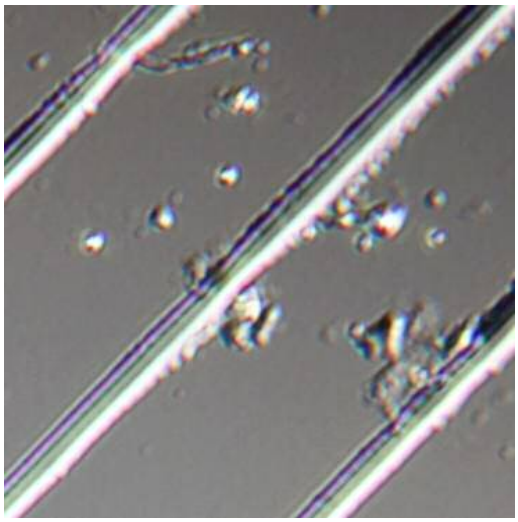

Figure 3.20: Over exposed sample. The sample has been exposed for 3 s. Image size is 100 µm × 101 µm.

3.4.2.4 Spin coating and curing of MY-133

The cladding layer of the SU-8 WG is MY-133 which is manufactured and supplied by MyPolymers [134]. MY-133 is a highly viscous, low RI UV light curable material

UV adhesive	HFE-7500	Total Amount	Ratio
2 ml	2 ml	4 ml	1:1
2 ml	4 ml	6 ml	1:2
2 ml	6 ml	8 ml	1:3

Table 3.4: MY-133 solution in HFE-7500 solvent.

(LCM), discussed in Sec. 2.6 and Sec. 3.1.2.2. It can be diluted by a fully fluorinated solvent for spin coating [114]. A list of different solvents that can be used to dilute MY-133 is given in Appendix A.4. We have chosen HFE-7500 from Novec [124] because it is fully soluble and it has a rather high boiling point of 128°C. The technical specifications of HFE-7500 are listed in Appendix A.5. There are a few alternatives to HFE-7500, for example HFE-7100 which is also a fully fluorinated solvent. However, its boiling point of the solvent is only 60°C, which makes it more volatile. Since we will be heating the spin coated MY-133 layer to 150°C, we can use HFE-7500. Since we do not bake the gluing layer at high temperature HFE-7100 might be a better option as it is cheaper and supply time is much shorter.

In order to spin coat MY-133, it has been diluted in HFE-7500 with different volume fractions according to Table 3.4, and then placed in an ultrasonic bath for 30 s to promote mixing. The solution then has been spin coated with different rotational speeds and accelerations for a total of 45 s, and cured to deposit a separation layer of 550±50 nm on top of the SU-8 WG. This required a planar layer of 700±50 nm thickness, according to the method discussed in Sec. 3.4.1. The measured thickness versus spin speed curve is shown in Fig. 3.21. The SOP for depositing MY-133 on a SU-8 WG sample is given in Appendix B.2.

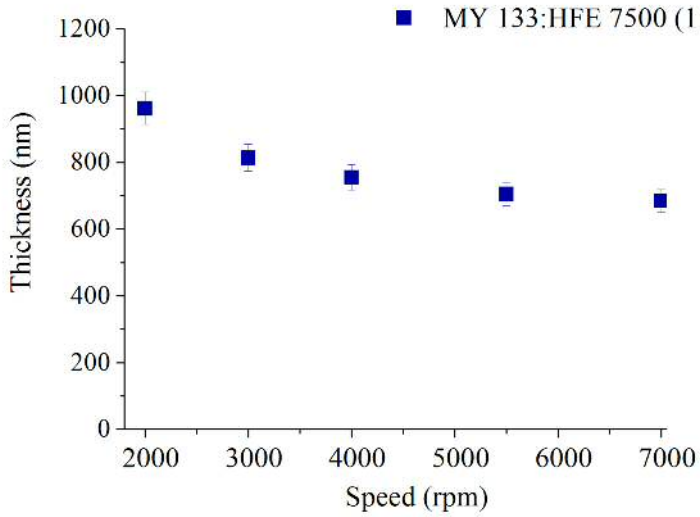

Figure 3.21: Thickness versus final spin-speed for MY-133 diluted with HFE-7500 (1:2) on a glass substrate at an acceleration of 7000 rpm/s, and a total spin coating time of 45 s. Each sample has been measured at 5 different points. Error bars indicate the standard deviation of the measurements.

MY-133 exhibits oxygen inhibition of the curing process. One way to address this issue is by removing oxygen around the UV curing area during the curing process.

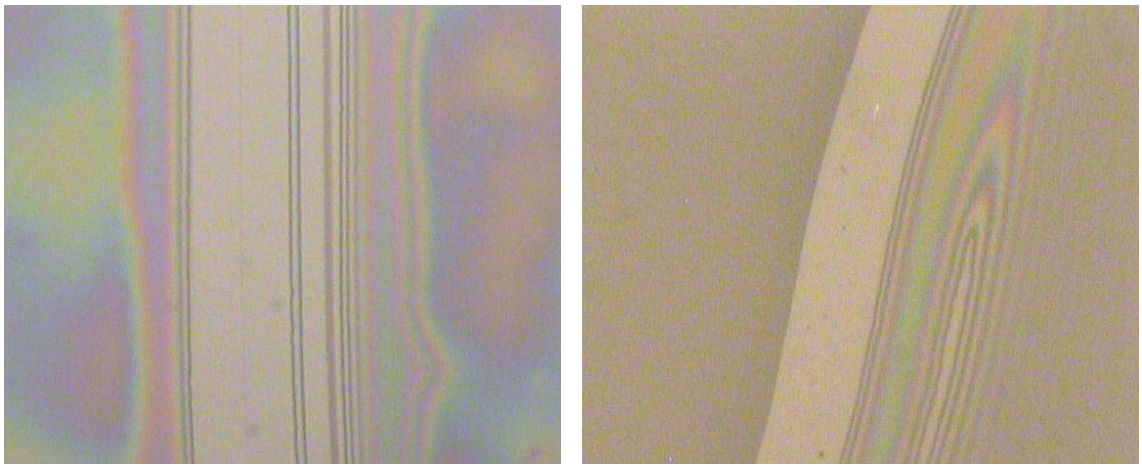

(a) **(b)**

Figure 3.22: Transmission images of MY-133 layer. MY-133 diluted by HFE-7500 in volumetric ratio of 1:2 and then spin coated on glass coverslip at a rotational speed of 7000 rpm, an acceleration of 300 rpm/s, and a total spin coating time of 45 s. We have borrowed an UV lamp to expose the samples. The maximum intensity of the lamp has been 0.3 mW/cm^2. Samples have been submerged under water and then exposed for 10 min (Fig. 3.22a) and for 1 h (Fig. 3.22b). The fringes around the scratches show thickness changes, indicating that the layer is still soft. Images sizes are (a) is 145 µm× 120 µm, and (b) 285 µm × 235 µm.

This can be done by submerging the spin coated MY 133 samples into water and then expose the samples to UV light. We have borrowed a UV lamp which has a maximum intensity of 0.3 mW/cm^2 from the department and exposed the samples for sufficient long time to produce the recommended dose. To evaluate if the MY-133 film was hardened we have scratched the film by a tweezer. The resulting transmission images of the scratch, shown in Fig. 3.22, exhibit fringes on both sides around the scratch, indicating gradual thickness changes, revealing that the film is still soft. Since the polymerisation process of an LCM (see Sec. 2.6) is a function of curing time and intensity of the light source, a higher light intensity seems required for this curing method. Therefore we have designed a curing device as discussed in Sec. 3.2. The curing unit provides not only the sufficient exposure dose required but also a continuous supply of N_2 during the curing process of the MY-133 layer. We have cured the deposited MY-133 layer with the curing unit under the N_2 flow. In order to find out if the MY-133 layer is fully cured, i.e. hardened, we have scratched the MY-133 layer. The scratched MY-133 layers different thickness are shown in Fig. 3.23. There are no fringes near the scratches, and the film has partially detached from the substrate while keeping its film structure. This clearly indicates that the MY-133 film is hard. After curing the spin coated MY-133 layer, the topography of the samples around a scratch has been measured by Dektak^3 to determine their thickness. An example of a layer of MY-133, cured and hard baked, along with the measured topography is shown in Fig. 3.24.

The effect of baking on a cured MY-133 layer has been investigated. For this, the thickness of the sample has been measured before and after baking for 10 min at 150 °C. A thickness reduction of about 25% was found, attributed to evaporation of HFE-7500 solvent present in the cured layer. Baking for another 10 min at 150°C

(a) **(b)**

Figure 3.23: Transmission images of scratches in cured MY-133 layers. The samples have been placed inside our designed curing unit and exposed for 10 min at an exposure intensity of 6.5 mW/cm^2 under a constant N_2 flow. The samples have been baked for 10 min on a hot plate then. (a) Two layers of MY-133. The first layer of MY-133 has been diluted by HFE-7500 in volumetric ratio of 1:2, with a rotational speed of 8000 rpm, an acceleration of 2000 rpm/s, and spin coated for a total of 45 s. The second layer of MY-133 diluted by HFE-7500 in volumetric ratio of 1:3 spin has been coated with exactly the same parameters as the first layer. Topography of the scratch in the MY-133 layer has been measured by Dektak^3. The step height at the film edge gives its thickness, which was found to be 675±25 nm. (b) MY-133 diluted by HFE-7500 in volumetric ratio of 1:2, with a spin speed of 4000 rpm, an acceleration of 1000 rpm/s, and spin coated for a total of 45 s. The sample has been place in the same exposure unit and exposed for 10 min at an exposure intensity of 6.5 mW/cm^2. The sample has also been baked for 10 min under a constant N_2 flow. Topography of the scratch in the MY-133 layer has been measured by Dektak^3. The step height at the film edge gives its thickness, which was found to be 825±50 nm. Image sizes are 285 µm × 235 µm.

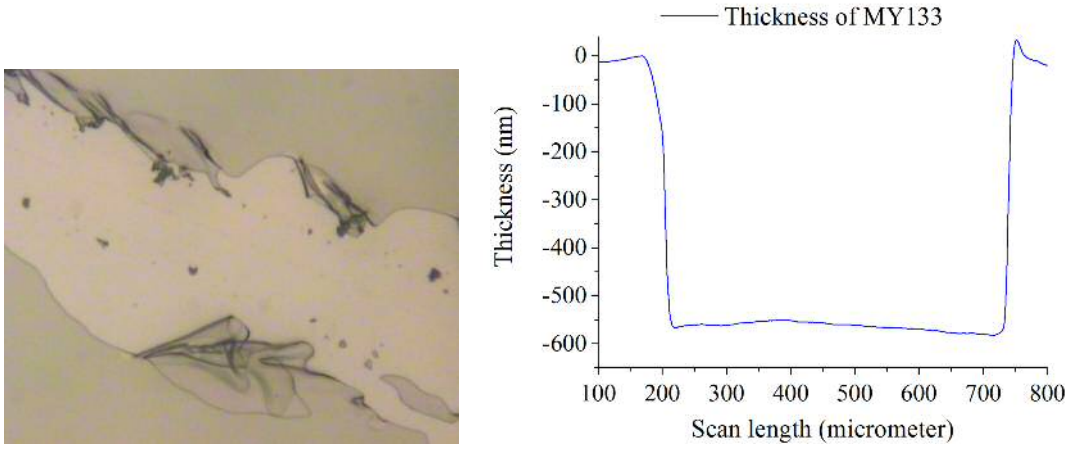

Figure 3.24: MY-133 diluted by HFE-7500 in volumetric ratio of 1:2 spin coated on a on glass coverslip for a total of 45 s with a rotational speed of 8000 rpm and and acceleration of 2000 rpm/s , exposed to UV light inside the curing unit at an intensity of 6.5 mW/cm^2 with a constant flow of N_2 for 10 min and baked for 10 min at 150 °C. (a) Transmission image of a scratch in the MY-133 layer after curing. Image size is 380 µm × 315 µm. (b) Topography of the scratch in the MY-133 layer shown in (a), measured by Dektak^3. The step height at the film edge gives its thickness, which was found to be 550±20 nm.

did not produce a significant change in thickness. Baking the sample after curing is, therefore, an important step to achieving a cured layer of RI close to 1.33. The result of this experiment is shown in Fig. 3.25.

The effect of baking on a non-cured MY-133 layer has also been investigated. For this, a layer of spin-coated MY-133 on a coverslip has been heated at 150°C for 10 min and then exposed to UV light with the usual total flux and N_2 inside the curing unit. This experiment has resulted in a soft film as shown in Fig. 3.26. This is attributed to a activation and depletion of the photo initiators during the baking, where the presence of oxygen was suppressing the polymerisation. The thickness of this layer cannot be measured by Dektak as it is too soft, causing the stylus to penetrate into the film and get contaminated.

For this project, the target height of the MY-133 on the SU-8 WG is $d_{\mathrm{cld}} = 550 \pm 50\,\mathrm{nm}$. The planar thickness of MY-133 needed to achieve this can be estimated as discussed in Sec. 3.4.1, which requires measuring the topography of the SU-8 WGs before and after depositing the MY-133 seperation layer, an example of which is shown in Fig. 3.27 for a nominal MY-133 thickness of d_0=550 nm. From the topography, we determine A_{WG}=4044 nm^2, A_{dif}=1777 nm^2, d_{dif}=117 nm and d_{WG}=367 nm and calculate using Eq. (3.2), d_{chn} = 595 nm, and dd_{cld}=334 nm. From these values, we find by using Eq. (3.3) the smoothing parameter α=0.64. For another sample fabricated with the same d_0, we measured values of $A_{\mathrm{dif}} = 1787\,\mathrm{nm}^2$, $A_{\mathrm{WG}} = 4043\,\mathrm{nm}^2$, $d_{\mathrm{dif}} = 106\,\mathrm{nm}$, and $d_{\mathrm{WG}} = 367\,\mathrm{nm}$ resulting in α=0.58.

Using Eq. (3.2) with Eq. (3.3), d_{cld} can be predicted as function of d_0, and therefore also d_0 as function of d_{cld}, which can then be used for next fabrication run. For example, for $d_{\mathrm{cld}} = 550\,\mathrm{nm}$, and $\alpha = 0.58$ we find a predicted value of $d_0 = 715\,\mathrm{nm}$ to be used to fabricate a sample with the required d_{cld}.

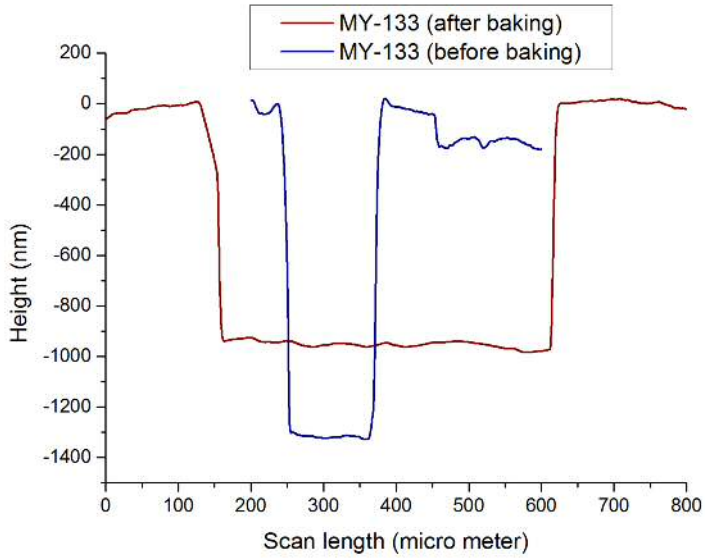

Figure 3.25: Effect of baking on a cured MY-133 layer. MY-133 has been diluted by HFE-7500 in volumetric ratio of 1:2 spin coated on a glass coverslip for a total of 45 s with a rotational speed of 7000 rpm and an acceleration of 2000 rpm/s, exposed to UV light inside the curing unit at an intensity of 35 mW/cm^2 with a constant flow of N_2 for 2 min. Topography of a scratch in the MY-133 layer shown in blue, measured by Dektak^3. The step height at the film edge gives its thickness, which has been found to be 1300±50 nm. The sample has been baking for 10 min at 150°C. The topography is shown in dark red. The step height has been found to be 980±20 nm.

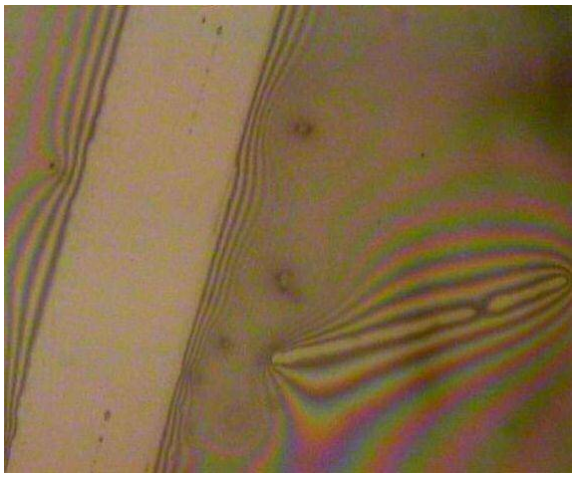

Figure 3.26: Transmission image of a scratch in a MY-133 layer which was baked at 150°C before UV curing. MY-133 has been diluted by HFE-7500 in volumetric ratio of 1:3 spin coated on a on glass coverslip for a total of 45 s with a rotational speed of 7000 rpm and and acceleration of 300 rpm/s, The fringes around the scratch show that the film is soft. Image size 380 µm × 315 µm.

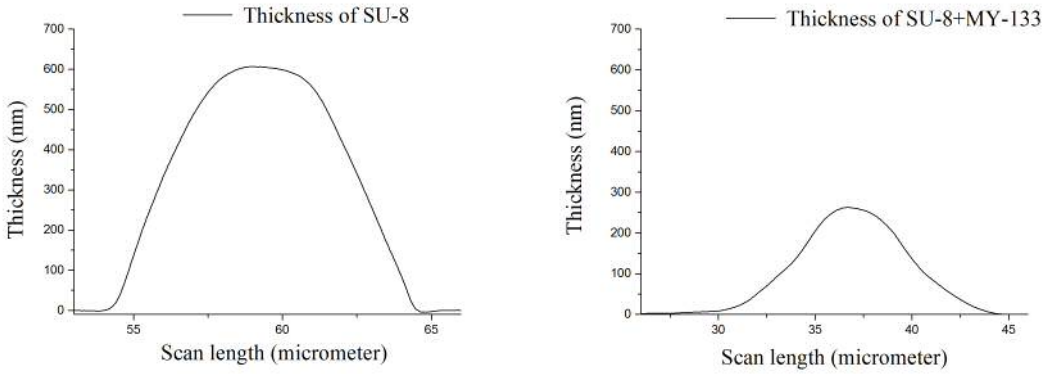

(a) **(b)**

Figure 3.27: Surface topography measured by DekTak[3]. (a) SU-8 WGs of width 3 µm, providing the area A_{WG}=4044 nm^2 and height d_{WG} = 340 nm. (b) MY-133 separation layer of d_0 = 550 nm on top of the WGs shown in (a), providing the area A_{dif}=1787 nm^2 and height d_{dif} = 262 nm.

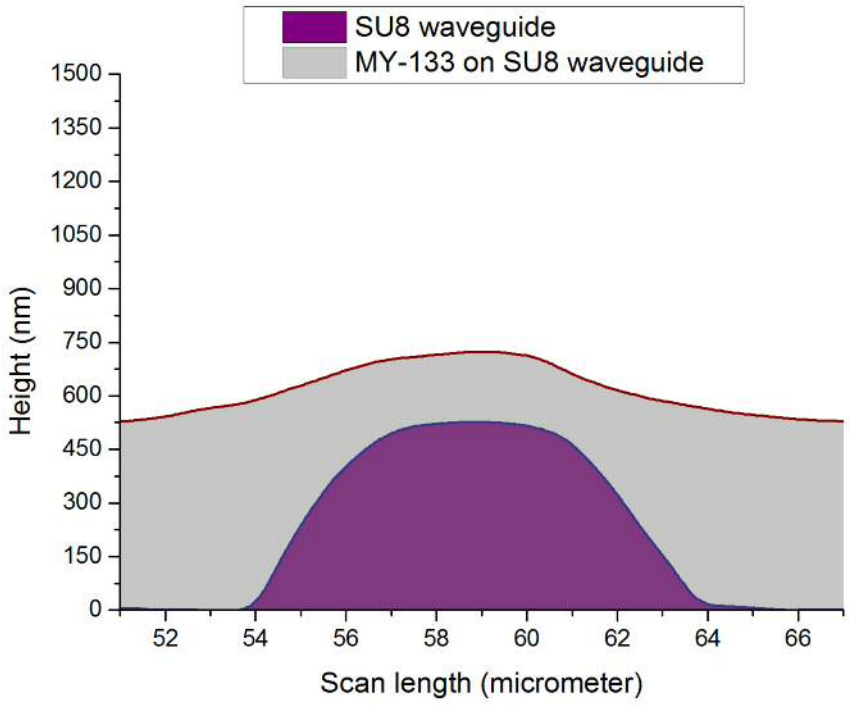

Figure 3.28: Cross-section of a MY-133 layer spin coated on SU-8 WGs. The height profiles are measured by Dektak[3], and the MY-133 profile is vertically shifted by the deduced d_{chn}, and laterally centred to the WG.

To give a clear picture of the cross-sectional structure of the WG with cladding layer, we show in Fig. 3.28 the measured topography of a sample before and after applying $d_0 = 360$ nm of MY-133 on SU-8 WGs. The corresponding values are $A_{\mathrm{dif}} = 1707\,\mathrm{nm}^2$, $A_{\mathrm{WG}} = 4040\,\mathrm{nm}^2$, $d_{\mathrm{dif}} = 127\,\mathrm{nm}$, and $d_{\mathrm{WG}} = 340\,\mathrm{nm}$. The MY-133 topography has been shifted vertically according to mass conservation, i.e. by d_{chn} determined by Eq. (3.1), and laterally to be centred on the WG. According to Eq. (3.2), the height of MY-133 on SU-8 is 195 nm.

3.4.3 Microsphere resonators

In this section we will discuss the microsphere material, the attachment of the microsphere resonators on the SU-8 WGs, and functionalisation of the microspheres.

3.4.3.1 Microsphere materials

The choice of microsphere material is important to obtain a high Q of the WGMs. A primary prerequisite is a low optical attenuation. A further requirement is the RI of the material, which must be significantly above the RI of the aqueous medium to provide a high Q at a small resonator size. We have chosen polystyrene (PS) as the resonator material. As discussed in Sec. 2.3.4.2 the material loss due to absorption of PS microsphere is rather small. In addition to this, the RI of PS is 1.5788 at 784 nm which is significantly greater than 1.33, the RI of water. Alternative to PS, microspheres made of glass, or Polymethylmethacrylate (PMMA) could be used. However, their RI is smaller, so that larger microspheres are required to achieve a high Q factor, as shown in Fig. 3.29, where a comparison between Q factor of PS, PMMA and glass microspheres for different sizes is given.

3.4.3.2 Fixing the microspheres on the WGs

After curing and post-backing the spin coated MY-133 cladding layer, an additional gluing layer of MY-133 has been spin coated to attach PS microspheres. It is assumed that the microspheres will be sinking into the gluing layer, touching the surface of the cladding layer. In order to limit the area covered by the gluing later, which is not accessible to the medium for sensing, a thin layer was used, in the order of 100 nm thickness. To fabricate such a thin layer, MY-133 has been diluted with HFE-7500 in a volumetric ratio of 1:3 and spin coated at a speed of 8000 rpm and acceleration of 2000 rpm/s for 45 s and baked at 150°C for 10 min. This results in a layer of thickness about 130±10 nm measured by Dektak[3].

In order to attach PS microspheres on the cladding layer covered with this gluing layer, a droplet of PS microsphere suspension in water can be drop cast on the attachment layer. Fig. 3.30 shows the droplet containing PS microspheres of 30 µm nominal diameter on the sample which is about to be cured. The microspheres as sinking to the attachment layer by gravity. Since the My-133 is a hydrophobic material, it attaches to the rather hydrophobic PS spheres, pulling them towards the cladding layer. The attachment layer along with the microspheres is then cured inside the curing unit with a constant flow of N_2. We have found that a curing time of 1 min is sufficient to cure the film with an intensity of $35\,\mathrm{mW/cm}^2$. The sample is then post-baked for 10 min at 40°C, compatible with retaining the function of sensitised PS microspheres, see Sec. 5.3. Microspheres attached on the sample are

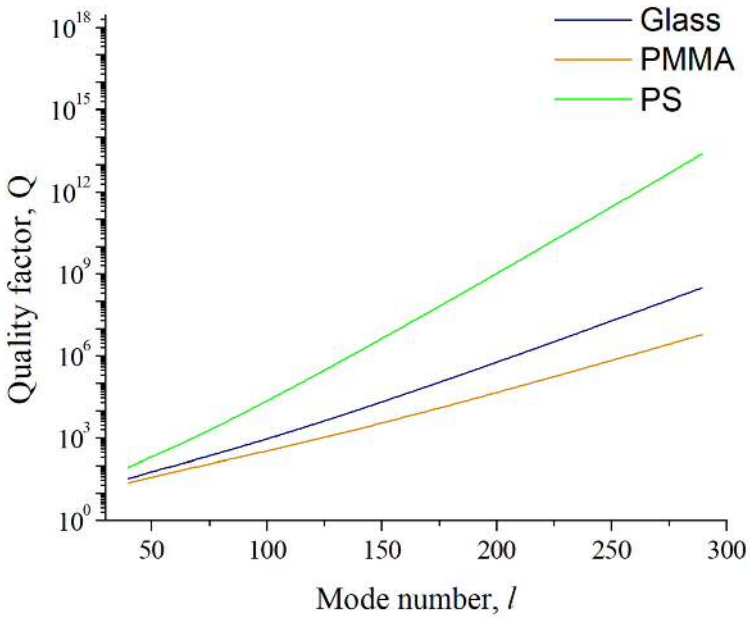

Figure 3.29: Q factor of the fundamental WGM for PS (1.5788), PMMA (1.487) and glass (1.5111) microspheres in water, versus WGM mode number l. The corresponding microsphere diameter is given approximately by $l\lambda/(\pi\tilde{n}_1)$, which is approximately 33 µm for $l = 200$, $\tilde{n}_1 = 1.5$, and $\lambda = 784$ nm.

shown in Fig. 3.31, for a low density in the suspension and a higher density leading to a nearly full surface coverage, in Fig. 3.32. In the latter image we find spheres with different contrast. These differences result from different depths in the gluing layer. Note that the glueing layer after spin-coating is still liquid, so that it can move laterally to reduce the contact area with water. It can therefore cover the beads up to different heights. One can also see the micro-lensing by the beads, magnifying and shifting the WG image. The geometry of the glueing layer with respect to the spheres is characterised in the next section.

3.5 Characterisation by qDIC

Device characterisation is an essential step in any design and fabrication process. Evaluation of WG characteristics serves as a feedback for modification and optimisation of the wave guide design fabrication. The major characteristics include layer thickness and the RI of the WG material after fabrication. In this section, thickness and RI of the fabricated WGs will be characterised by using quantitative DIC (qDIC). The theory behind qDIC is discussed in Sec. 2.5.

3.5.1 Technique

In this subsection we will discuss briefly the practicalities of the qDIC technique. Measurements are performed in an Olympus BX-50 microscope equipped with DIC contrast, using the following DIC specific components:

1. A universal condenser with polariser U-UCDB and a DIC module U-DIC20,

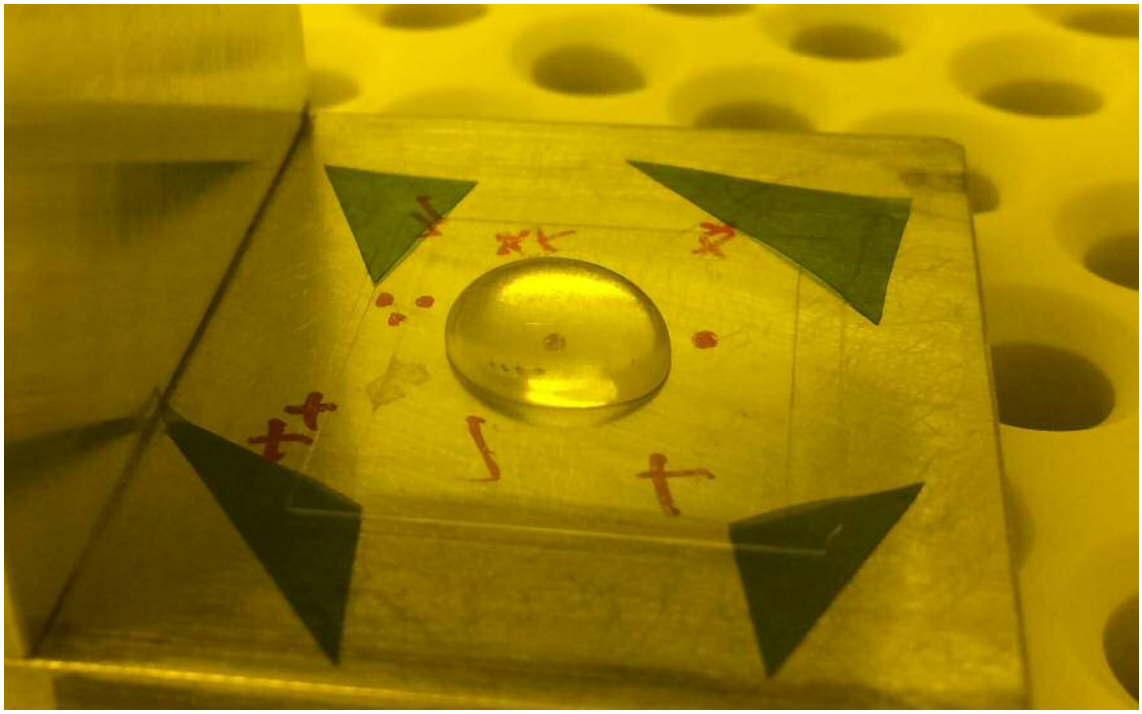

Figure 3.30: Droplet of water containing PS microspheres drop cast on the sample placed into the UV curing tool. Blue tape at the corners has been used to keep the glass cover sample fixed at the position so that it does not fly within the curing unit during the curing process.

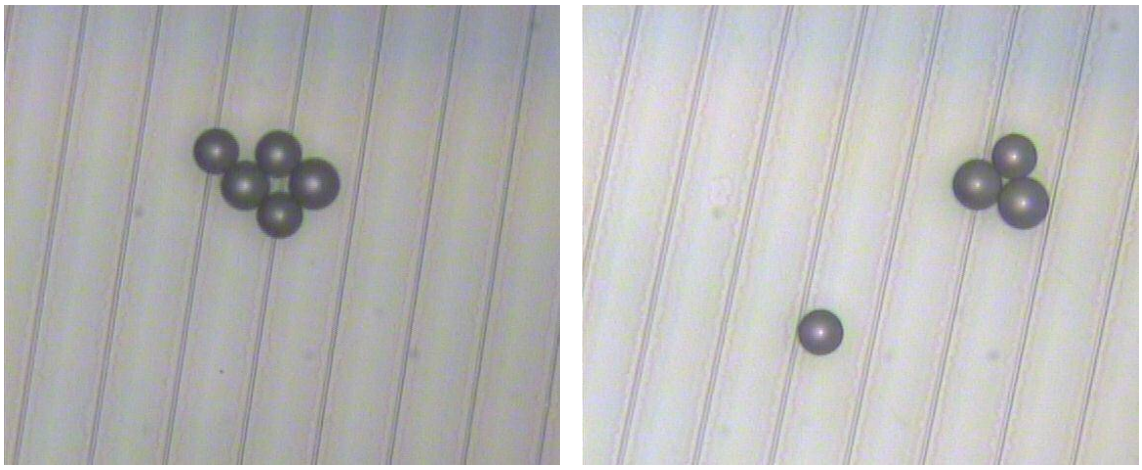

(a) **(b)**

Figure 3.31: Transmission image of 30 µm PS microspheres glued on SU-8 WGs. WGs are 3 µm wide and 600±10 nm thick. The nominal thickness of MY-133 layer, d_0 is 550 nm. Image size 380 µm × 315 µm.

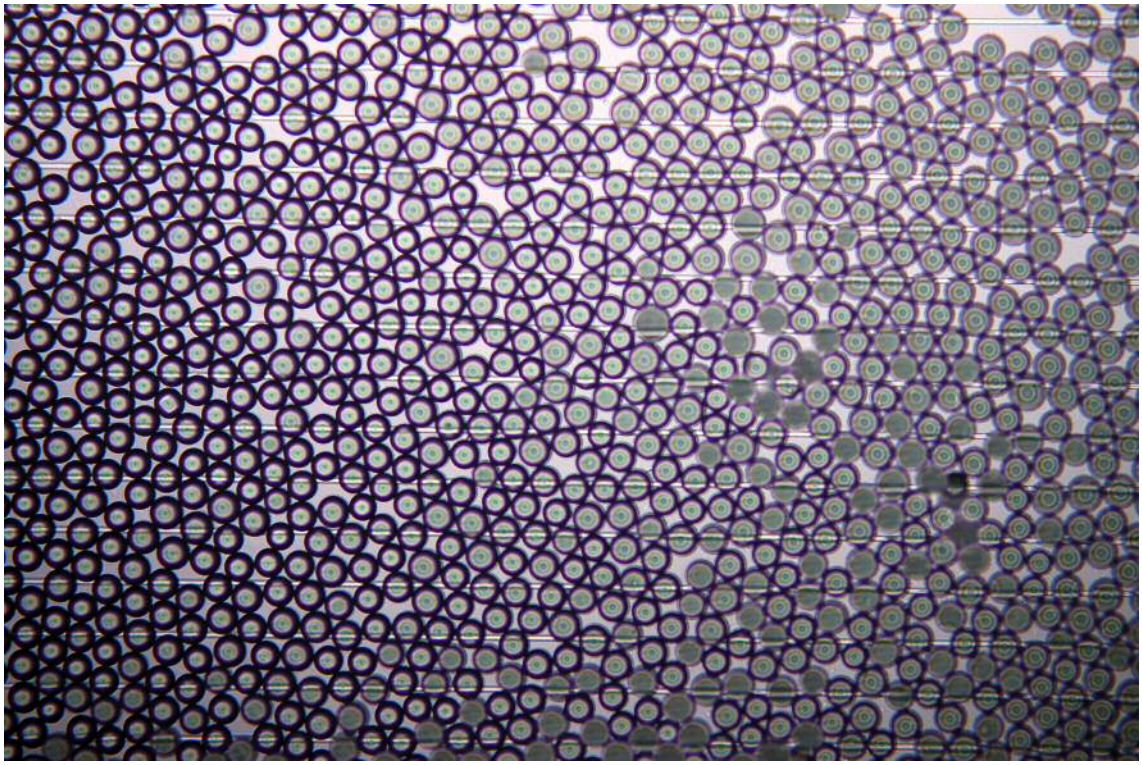

Figure 3.32: Transmission image of 30 µm PS microspheres glued on the SU-8 WGs, for a high density. The sample specification is the same as Fig. 3.31. Image size 1570 µm × 1045 µm.

2. A transmitted light DIC slider U-DICT (tilted Nomarski Prism) with a transmitted light analyser U-ANT.

The illumination used a tungsten filament lamp and the condenser numerical aperture (NA) stopped down to 0.5NA. A dry objective lens of 20× magnification and 0.5NA (Olympus UPLFL20XP) and the tube-lens imaged the sample onto the digital camera (Canon EOS500D) of resolution 4752 pixels × 3168 pixels The green channel (560-520 nm) of the images, stored in raw format (Canon cr2), providing a 14bit linear conversion, are been used for analysis. An application, developed in the group, and written in matlab, called "qDIC", has been used for quantitative DIC analysis as discussed in Sec. 2.5, extracting the absolute phase from DIC images. The application first subtracts a background image, and then produces the contrast image, see Eq. (2.74). Using a Wiener deconvolution procedure, the phase is determined using Eq. (2.80). An example of the DIC images with reversed phase offset taken by the DIC microscope for analysis are shown in Fig. 3.33. Parameters used in qDIC application for analysis are listed in Appendix A.2. The method of extracting absolute phase from DIC images is given in Appendix C.1.

One important adjustable parameter for Wiener deconvolution is the Signal-to-noise (S/N) ratio κ. The higher the value the more extended are artefacts, and the less systematic effects by the effective spatial high-pass filtering close to the edges of the WGs are present. Therefore, κ is chosen to provide a spatial extension of the high-pass filtering much larger than the WG width, so that the phase profile across the WG are reliable. Resulting phase images for different S/N are shown in Fig. 3.34.

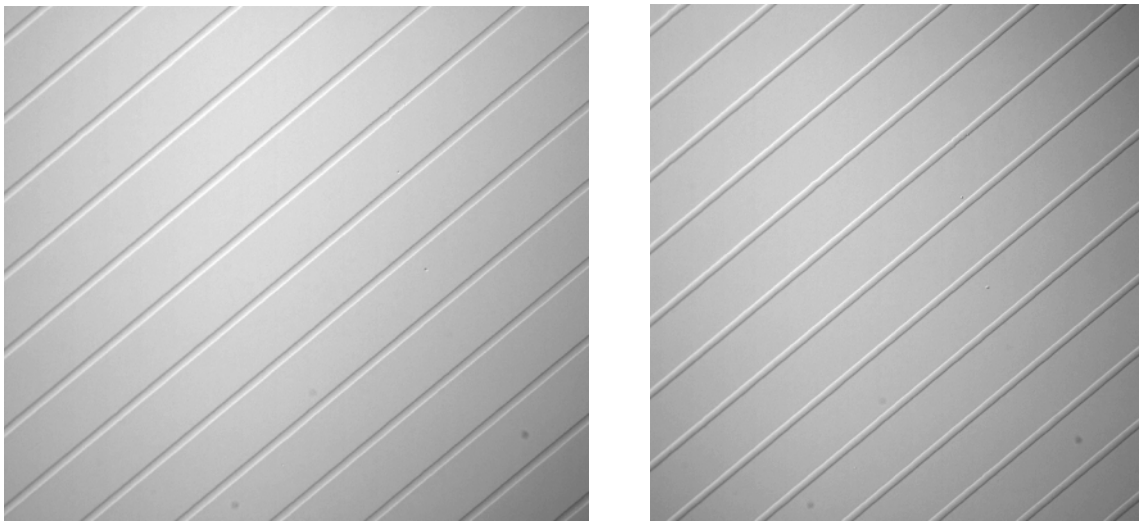

(a) **(b)**

Figure 3.33: DIC images of SU-8 WGs fabricated on glass coverslip for qDIC analysis. These images have been used for height profiling of the WGs as discussed in Sec. 3.5.2.2. (a) +90° phase offset, (b) -90° phase offset. Image sizes are (a) 295 µm × 260 µm, (b) 270 µm × 285 µm. The corresponding phase images are shown in Fig. 3.34.

3.5.2 Waveguides

3.5.2.1 Introduction

The thickness of the SU-8 WGs can be determined by measuring the step height of a patterned layer by scanning the surface profile of the sample by a stylus profilometer. However, if such a profilometer is not available or not suitable to take measurement then alternative techniques must be employed. qDIC can be the alternative technique which involves light to pass through the specimen. It also allows imaging, i.e. determination of the roughness of the WGs. A method for determining the thickness of the WGs by qDIC microscopy has been developed. This method will be described here. The result obtained will be compared with stylus profilometer measurement.

3.5.2.2 Height Profiling

The thickness or height of the WG core layer can be determined by qDIC, using the phase difference between the transmission through the core and the surrounding region. In order to determine the phase difference, phase profiles across the WG, ideally along the shear direction to reduce noise, are extracted from the qDIC phase images. The step-height $\Delta\phi$ introduced by the WG is then determined from the profile. Knowing the RI of the material, the thickness can be calculated from

$$\Delta\phi = \frac{2\pi}{\lambda}\left(n_{\mathrm{s}} - n_{\mathrm{m}}\right) t\,, \tag{3.4}$$

where t is the thickness, n_{s} is the RI of the structure, n_{m} is the RI of the surrounding medium, and λ is the light wavelength.

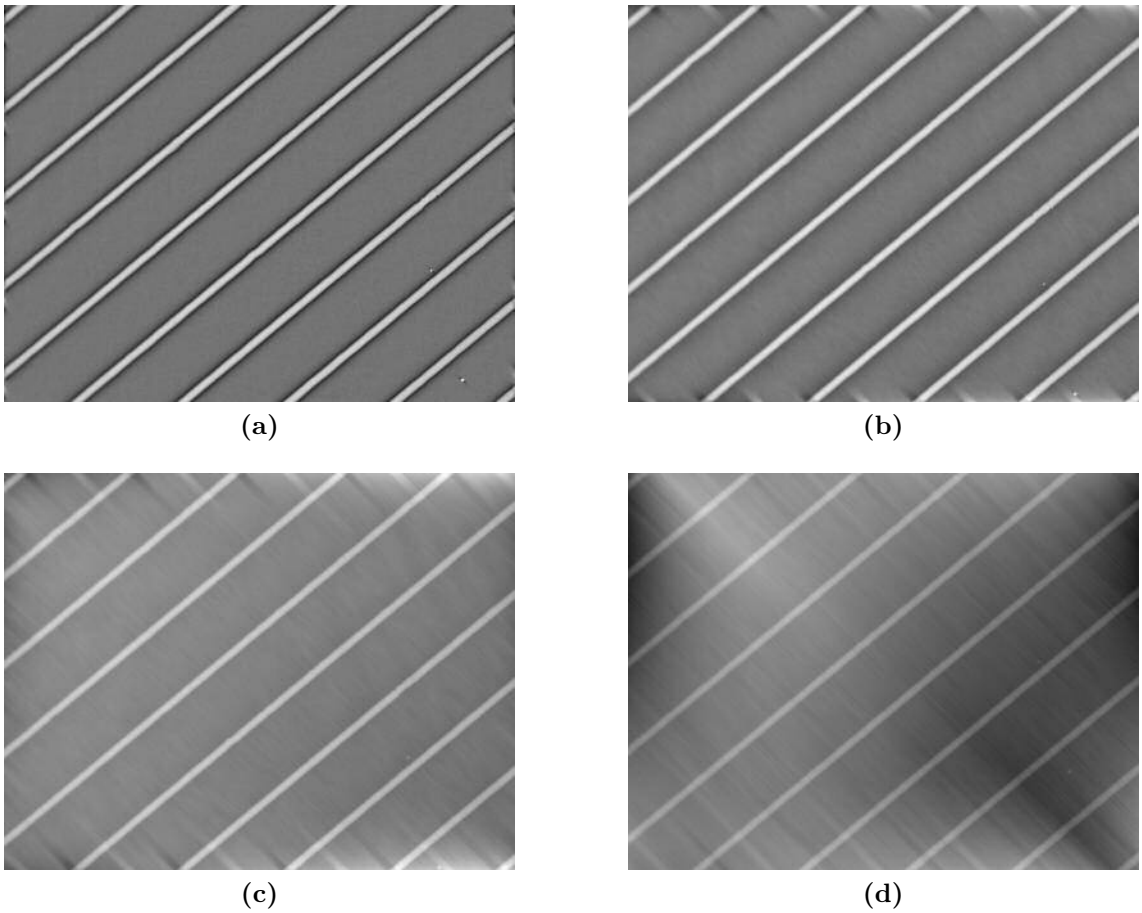

(a) **(b)**

(c) **(d)**

Figure 3.34: Phase image deduced from DIC image with different S/N ratio κ: (a) 10, (b) 100, (c) 1000, (d) 10000. Artefacts of different extension are visible for different κ as explained in Sec. 2.5. Image size is 375 µm × 290 µm. Grey scale ranges are (a) -0.04 to +0.04 radian, (b) -0.08 to +0.09 radian, (c) -0.14 to +0.15 radian, (d) -0.26 to +0.27 radian.

3.5.2.3 Refractive Index Profiling

DIC can be used to determine the RI of a material, as discussed in Sec. 2.5.5. RI of cross-linked SU-8 has been determined from the fabricated WGs by miscible liquids of RI (1.46,1.55,1.64)± 0.0002 at 589.3 nm wavelength and at 25°C supplied by Cargille labs [135]. The mixing procedure is described in [135]. The RI of the SU-8 WGs has been determined as follows. The phase shift between oil of different refractive indices and SU-8 WGs have been determined by qDIC, and is shown in Fig. 3.35. The data are consistent with the expected linear dependence of the phase shift with n_m, as exemplified by the linear fit given. The RI of this cross-linked and hard-backed SU-8, given by the condition of zero phase shift, is determined from the linear fit to be 1.604±0.002 at 550±10 nm.

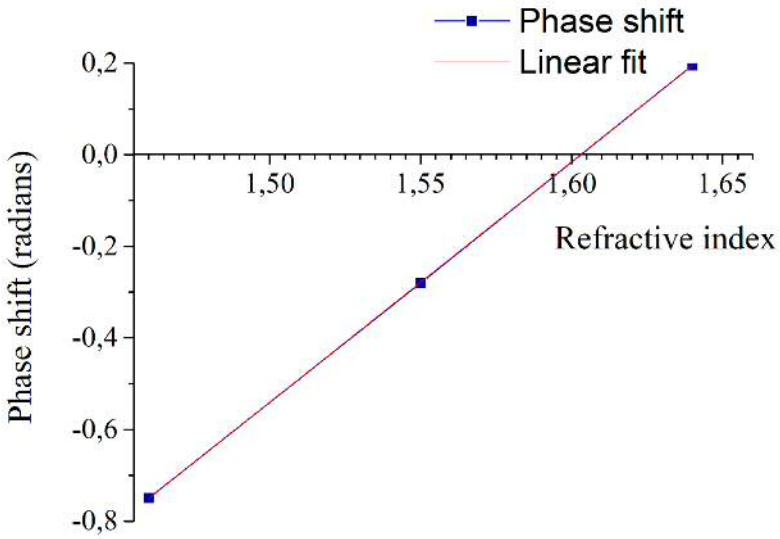

Figure 3.35: Phase shift by a SU-8 WG of thickness 550±50 nm measured by qDIC to determine the RI of cross linked SU-8. The sample consists of SU-8 WGs on glass cover slip. The sample has been covered by RI matching oil. The phase shift for different RI matching oils has been plotted. The RI at zero phase shift indicates the RI of SU-8 wave guides at 550±10 nm wavelength.

3.5.2.4 Comparison with stylus height profiling

Stylus profilometers are used extensively in the clean room to measure deposition thickness of films at edges, etch depths, or the roughness of surfaces. The results obtained from qDIC have therefore been compared with the measurements taken on a Dektak^3 instrument, manufactured by Veeco [136]. The technical specification of the Dektak^3 stylus profilometer is given in Appendix A.3.

A comparison of height profiles determined by qDIC and Dektak^3, of a 3 μm wide WG is shown in Fig. 3.36. The sample has been fabricated by diluting SU-8 2002 by SU-8 2000.5 in a volumetric ratio of 1:2, at a spin speed of 8000 rpm, acceleration of 1000 rpm/s for 45 s and exposed for 1 s.

Several other measurements obtained from Dektak^3 and qDIC are listed in Table 3.5. All these samples have been prepared for a spin time of 45 s, exposure time

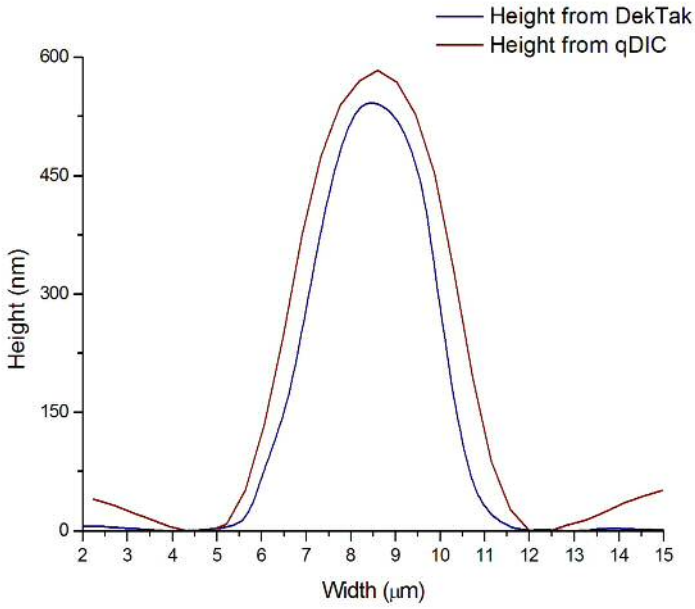

Figure 3.36: Comparison of height measured in DekTak and qDIC of a SU-8 WG sample of 3 µm width. The S/N ratio has been 1000 for DIC analysis. The SU8 RI has been assumed as 1.6 and the surrounding material has been air.

of 1 s and development time of 1 min. SU-8 2002 has been diluted by SU-8 2000.5 in Sample 3. Undiluted SU-8 2002 has been used in sample 4 and 5. A standard microscope immersion oil of RI 1.516 has been used as the medium and the RI of SU-8 has been assumed as 1.602 at 550 nm to determine the height using Eq. (3.4) for measurement in DIC technique. The results show that the measured thickness of the SU-8 stripes by qDIC is agreeing with the DekTak measurements within about 10% relative error.

Sample	Spin speed	Acceleration	Dilution	Measurement	Thickness	Unit
Sample 3	3000	300	1:2	DekTak	697±13	nm
Sample 3	3000	300	1:2	DIC	757±25	nm
Sample 4	8000	2000	-	DekTak	1347±34	nm
Sample 4	8000	2000	-	DIC	1404±29	nm
Sample 5	3000	300	-	DekTak	2191±29	nm
Sample 5	3000	300	-	DIC	2216±98	nm

Table 3.5: Thickness of SU-8 wave guides from DekTak and DIC method.

3.5.3 Microspheres

3.5.3.1 Refractive Index Profiling

We have shown in Sec. 3.5.2.3 that the RI of cross linked SU-8 can be determined by qDIC. The same principle can be used to determine the RI of microspheres. Here we have determined the RI of PS microsphere supplied by Thermo Scientific

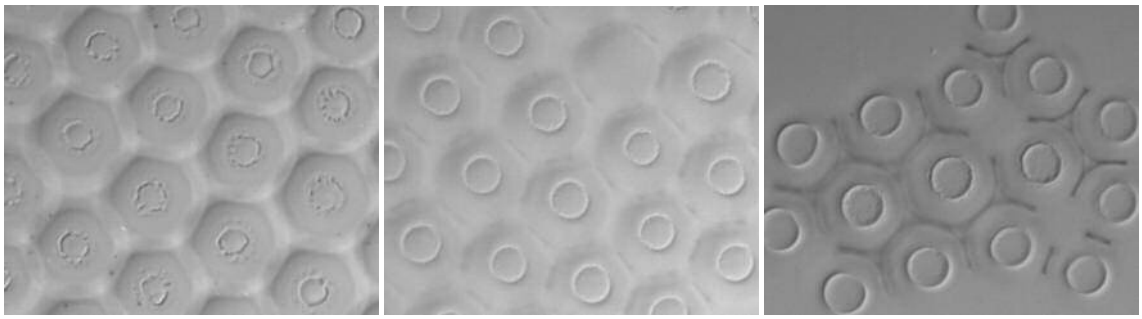

(a) (b) (c)

Figure 3.37: DIC images of the PS microspheres covered by matching oil with RIs of (a) 1.589, (b) 1.591, and (c) 1.592. Image size is 132 µm× 110 µm.

Corporation 2000 series Duke standards [137], catalogue number is 2030A, using a mixture of miscible liquids supplied by Cargille labs [135], as discussed in Sec. 2.5.5.

DIC images of PS microspheres submerged in oil of different RI are shown in Fig. 3.37. According to Eq. (2.84) mixing an oil of RI $n_1 = 1.64$ with another one of RI $n_2 = 1.55$, using $V_1 = 200$ µL, and $V_2 = 220$ µL, the RI of the mixture is $n = 1.592$. Fig. 3.37c shows the DIC image of PS microspheres using this mixture, revealing that the microspheres are almost invisible, as compared to the other RI used. We can thus conclude that the RI of the microspheres is 1.592 ± 0.001 at a wavelength of 550 nm. This is close to their nominal RI of 1.59 at a wavelength of 589 nm [137].

qDIC can also be used to determine the diameter of PS microspheres and their footprint in the glue layer. qDIC phase images of microspheres glued by the MY-133 gluing layer are shown in Fig. 3.37. The ring-shaped structure, marked by yellow circle, in Fig. 3.37 (a) is the diameter of the PS microspheres. The diameter of the microspheres is determined to be 30±1 µm, which agrees with the size specified by the supplier.

Fig. 3.37 (b) shows the deformed MY-133 surface round the microspheres marked by the yellow circle.

3.5.3.2 Footprint of microspheres in gluing layer

It is important to know the distance between the microsphere and the SU-8 layer. The distance can be determined by analysing of microsphere footprint on MY- 133 layer using the qDIC.

qDIC has been employed to determine the depth of the footprint of the PS microspheres on the MY-133 layer. In order to do this a layer of MY-133 has been spin coated straight on the glass substrate at a spin speed of 7000 rpm and acceleration of 4000 rpm/s for 45 s and then cured with the PS microspheres on the surface. The thickness of the deposited layer after curing and baked for 10 minat 150°Chas been measured by DekTak as 200±20 nm. Matching oil of RI 1.592 has been applied to cover the microspheres and then DIC images are taken for qDIC analysis. The resulting phase image of the sample is shown in Fig. 3.38. Edges of the microspheres are almost non-visible in Fig. 3.38 which means that the RI of the matching oil matches the RI of the PS microspheres. Smaller circle in Fig. 3.38 (b) corresponds to the footprint of the attachment region. A sketch of the cross-section

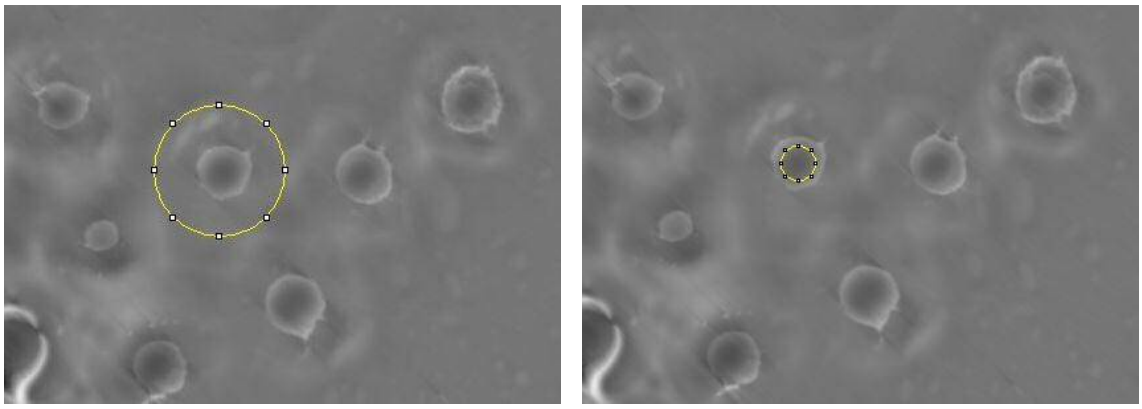

(a) **(b)**

Figure 3.38: Phase image obtained by qDIC using $\kappa = 1000$, of microspheres immersed in matching oil of RI 1.592. Images have been used to determine the diameter of the microsphere and its footprint on MY-133 layer discussed in Sec. 3.5.3.2. The yellow circle in (a) shows the diameter of a PS microsphere attached on MY-133 layer , and in (b) shows the attachment region. Images size 98 µm × 70 µm.

of a PS microsphere when attached on MY-133 layer is shown in Fig. 3.39. Surface profile of the footprint is shown in Fig. 3.40. The diameter of the footprint (below zero) has been estimated as 6.85 ± 0.1 µm. Taking the nominal microsphere radius as 15 µm, the submerged height in the MY-133 layer is expected to be 395 ± 5 nm. In qDIC analysis, the surrounding medium has been water of RI 1.33, shows a significantly lower height, which is not understood.

We therefore, suspected that the microspheres are deformed by the solvent present in MY-133 layer during the attachment. In order to verify this we tested the solubility of the PS microspheres in HFE-7500 solvent. The PS microspheres have been submerged in HFE-7500 solvent for 24 h. Microspheres were put back in water and the diameter of the microspheres was measured from the phase image taken by the DIC microscope. The measured diameter of the PS microspheres was similar to nominal diameter as supplied. Therefore, we can conclude that the solvent has not deformed the microspheres.

3.6 Concluding Remarks

In this chapter we have discussed the design and fabrication of a novel biosensor device, and qDIC, an optical technique to estimate height and RI of dielectric materials.

The biosensor device consists of an array of single mode optical WGs and microspheres, presented in Sec. 3.1. We have discussed the design constraints for single mode light propagation through the WGs and the choice of substrate, core and cladding material.

We have reported the design, build, and characterisation of a portable polymer curing unit to harden the MY-133 layer in Sec. 3.2.

MY-133 has been used as material for the cladding layer of the WGs and the gluing layer to hold the microspheres at a fixed position on top of the WG array, enabling microspheres to remain fixed at a certain distance from the core of the

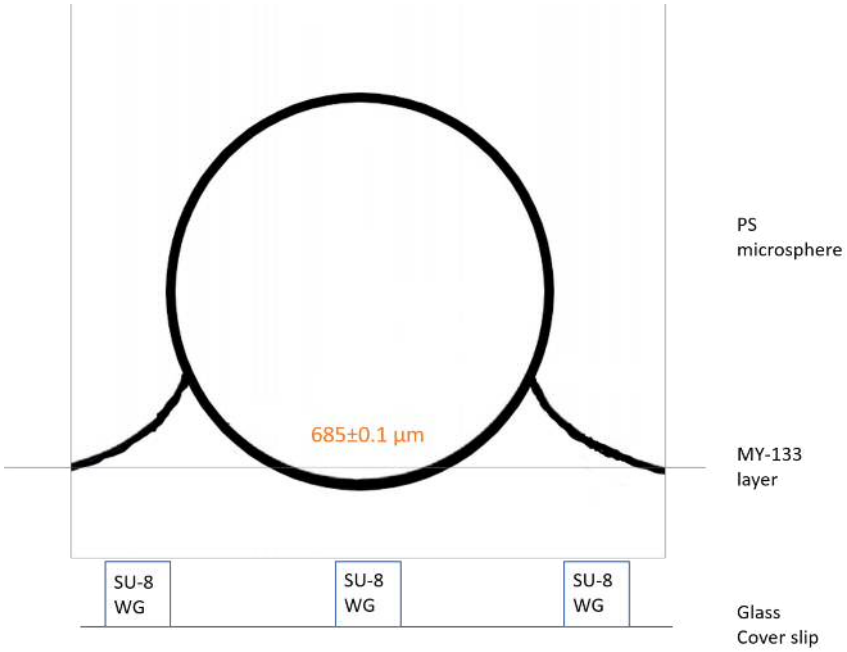

Figure 3.39: A sketch of the cross-section of a PS microsphere when attached on MY-133 layer. The distance between the microsphere and the SU-8 layer is important to maintain the high Q value of the microsphere. The distance can be estimated by DIC microscopy.

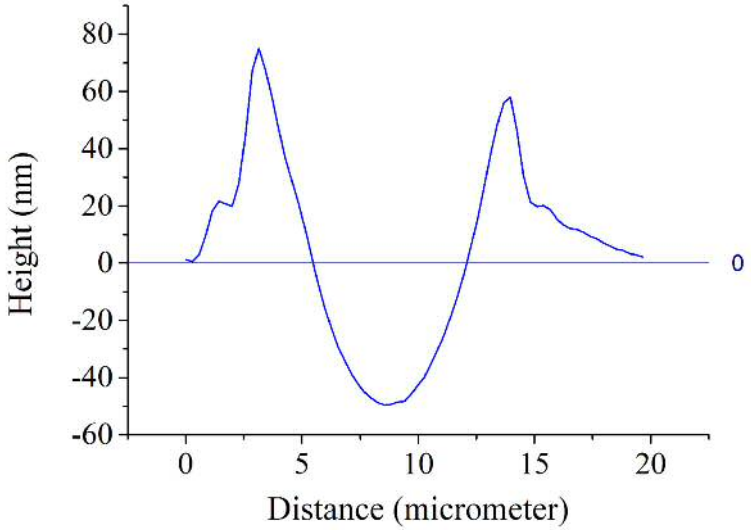

Figure 3.40: Surface profile of the footprint of a 30 µm diameter PS microsphere on a 200 ± 20 nm thick MY-133 gluing layer. The phase image of the sample is shown in Fig. 3.38 (b).

WG. The transducer in our biosensor device is the microsphere resonator. Notably, My-133 has a RI similar to the aqueous medium containing the analytes, therefore rendering it invisible for the optical properties, specifically retaining the high Q factor of the WGMs.

We have designed a cutting tool to cleave the sample to fit the biosensor device inside the fluidic chamber without breaking the WGs, presented in Sec. 3.3. The fluidic chamber in the measurement system will be discussed in Chap. 4.

The fabrication process of the sensor chip has been described in Sec. 3.4. The optimisation steps to improve the of SU-8 WG fabrication have also been discussed. This can serve as a guideline for future fabrication of a similar device. The WG array in our biosensor device is fabricated on a glass substrate. The core layer of the WGs is SU-8. The cladding layer is MY-133. We have cured the spin coated MY-133 layer by using the portable curing unit. The results obtained in different fabrication steps are presented for future reference. We have also discussed the choice of material for the microspheres in this section. The resonators in our biosensor device are polystyrene (PS) microspheres. They are glued onto the cladding of the WGs by a thin layer of MY-133. We have developed and optimised standard operating procedures (SOP) for SU-8 WG fabrication, curing of MY-133, and gluing the microspheres on MY-133. These SOPs are documented in Appendix B.1 and Appendix B.2. We have also briefly described the planned functionalisation process of microspheres. The fabrication section Sec. 3.4 will be useful as a guideline for reproduction of SU-8 WGs and curing of the polymer layer.

We have developed an optical technique qDIC by employing differential interference contrast microscopy (DIC) microscopy to characterise the height and RI of cross linked SU-8 which serves as the core layer of the WGs. The experimental process to determine the RI and height of SU-8 layer is described in Sec. 3.4. We have also characterised the diameter and RI of PS microspheres by the DIC technique. The process has also been described in Sec. 3.4.

DIC microscopy is a powerful technique to determine the RI of a material which has gone through several micro fabrication process. The qDIC technique is especially useful for the biosensor structure that we have proposed in this project. We have determined the height of the SU-8 WGs by using qDIC. We have verified the result by comparing with standard DekTak measurement. The comparison shows that the height that DIC technique measures can be comparable with that of a standard height measurement technique. We have also determined the RI of cross linked SU-8 and PS microspheres and verified with that of the manufacturer's data. Thus the DIC technique can be very useful in determining the step like height and the RI of a material. Since the distance between the SU-8 layer and the PS microsphere is an important parameter therefore it is essential to determine that distance. This distance can be determined from the footprint of the PS microsphere on MY-133 layer by DIC technique without destroying the sample. Therefore DIC is a better technique for our proposed biosensor structure. Theoretical background of qDIC and the experimental procedure have been discussed in Sec. 2.5 and Sec. 3.5, respectively.

Chapter 4

Optical biosensing setup

4.1 Introduction

In order to interrogate the sensor chip discussed in Chap. 3, we have developed an optical and fluidic setup which consists of both hardware and software. The hardware encompasses light sources, passive optical elements, a fluid chamber, and light detectors. The light sources are a distributed feedback (DFB) laser emitting a tune able wavelength of small linewidth for WGM probing, and light emitting diodes (LED) for general illumination, while light detectors consist of a charge coupled device (CCD) type line scan camera for multiplex scan recording, and an area scan CMOS camera and a consumer video camera for alignment and imaging of the chip.

In conjunction with the hardware, we have also developed a software to acquire experimental data from the line scan camera while scanning the DFB laser. The software allows to control the laser and camera parameters, as well as the scan parameters, and provides a real-time analysis fitting the recorded scans by multiple peaks. The acquired experimental data from the software can then be saved in digital format.

The optical setup and the working principle of the developed software will be discussed briefly in this chapter.

4.2 Design

4.2.1 Optical setup

An optical setup for sensing measurement had been designed in a previous work by Dr J. Lutti and Prof W. Langbein. The optical setup is mounted on a vibration isolated optical table, and consists of different optical elements and mounts as well as a flow chamber.

A functional schematics of the setup is sketched in Fig. 4.1. The narrow-linewidth emission from a distributed feedback (DFB) laser is collimated, and the relative amplitude of the linear polarisation components is controlled by rotation of a half-wave plate. The light is then focused onto the input facet of the WGs on the sensor chip. This can be done via a cylindrical lens, which focuses to a line along the facet, to enable coupling to many WGs along the chip. A mask in front of the WGs is used to suppress the light not coupling to the WGs. Alternatively, a spherical lens can be used instead of to the cylindrical lens, to achieve more efficient coupling

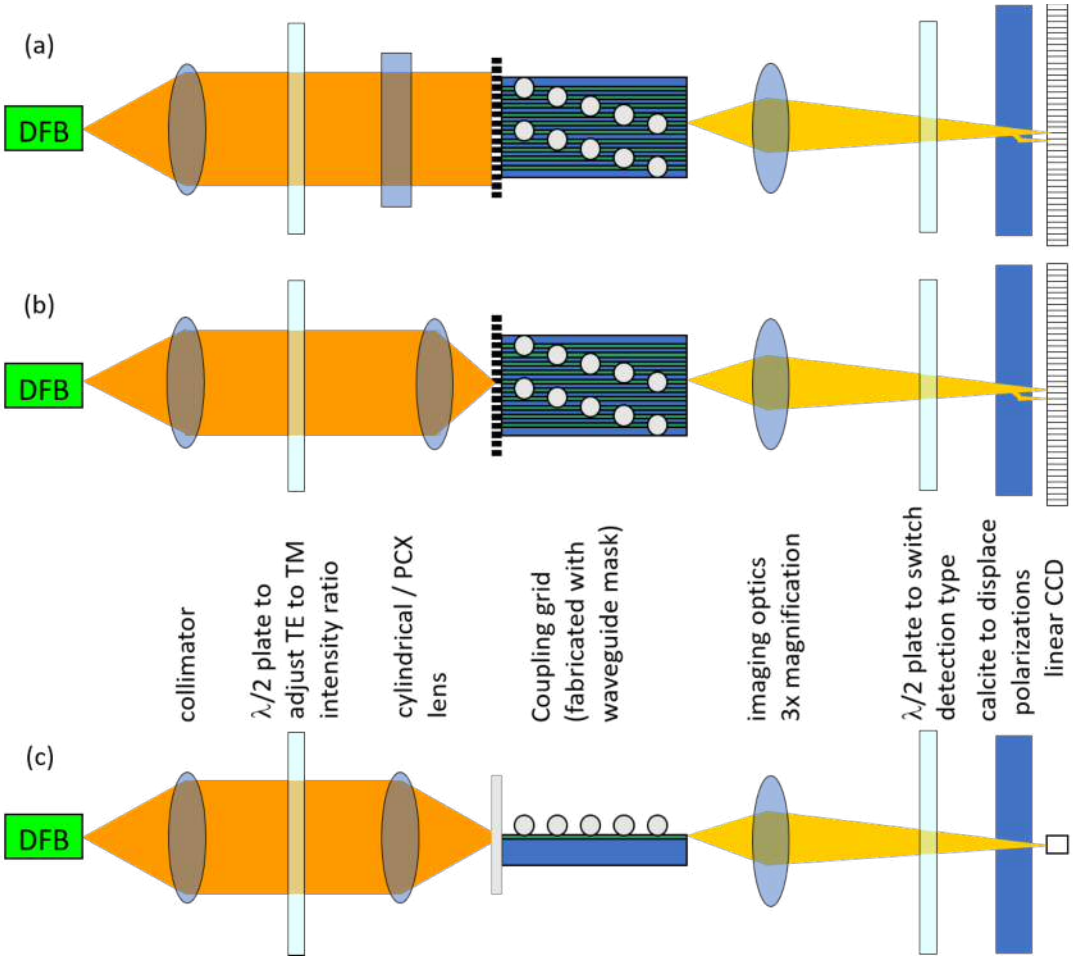

Figure 4.1: Functional schematic of the optical setup. (a) top view of the optical setup with the cylindrical lens to couple multiple WGs, (b) top view of the optical setup with the spherical lens, (c) side view of the optical setup. The elements are lebelled and described in the text.

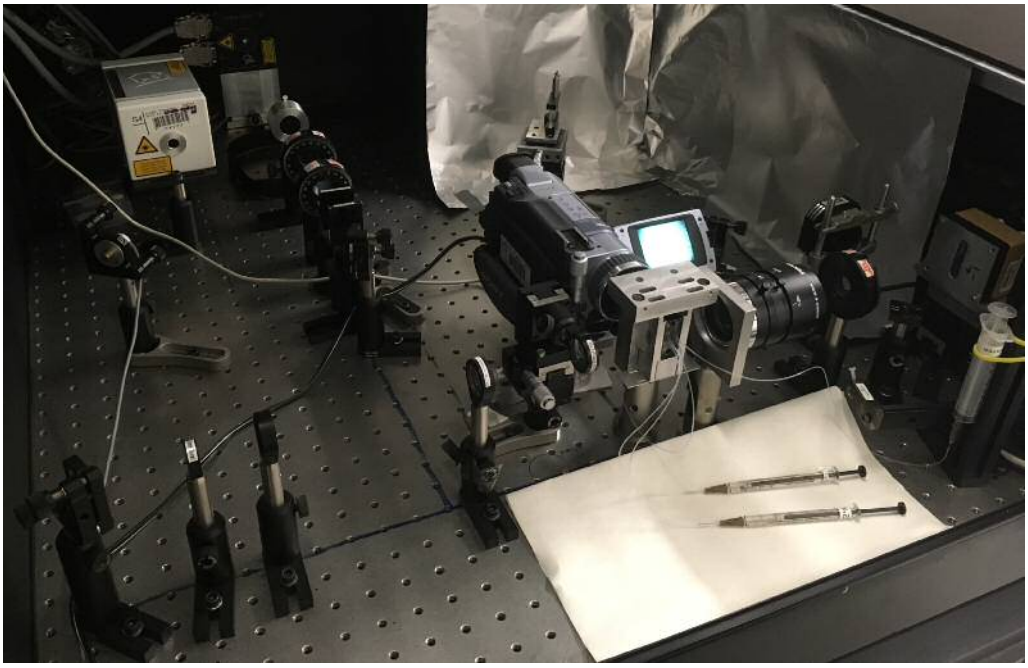

Figure 4.2: Picture of the optical setup used for the experiment.

to a single WG and suppress background. After transmission through the WGs, including coupling to the attached microspheres, the light emerging from the other side of the sensor chip is imaged by a lens onto a linescan camera, enabling to detect the emission from many WGs simultaneously. To provide separate detection of the TE and TM modes of each WG, a polarisation displacer spatially separates the two polarisations along the line-scan array, by a distance of about half the period of the WG array image on the camera. A half-wave and quarter wave plate are used to select the detection type as discussed in Sec. 2.4.

The drive current of the DFB laser is scanned, providing an approximately linear wavelength tuning with current, and for each current the linescan camera is read, with a line-rate up to 28 KHz. The spatial profile is then analysed to determine the WG mode intensity polarised along and across the displacer direction, which corresponds either to TE and TM intensity, for intensity detection (see Eq. (2.66)) or phase detection (see Eq. (2.67)), controlled by the waveplate rotation.

A picture of the setup mounted on the optical table is shown in Fig. 4.2, and the corresponding schematic is given in Fig. 4.3. The DFB laser, emitting a beam collimated by an aspherical lens, is transmitted through a crystal polariser set along its dominant linear polarisation to provide a linearly polarised beam of high polarisation purity ($> 10^5$). Subsequent transmission through a half and quarter wave plate of adjustable rotation allow to create an arbitrary polarisation state, enabling to control relative amplitude and phase coupled into the TE and TM mode of the WG. Two mirrors on kinematic mounts allow to adjust position and direction of the beam, to align the beam through the subsequent setup. The beam is focused using a 40 mm focal length plano-convex (PCX) lens onto a pinhole of 20 µm diameter, and afterwards recollimated by a 150 mm focal length PCX lens, providing a defined input direction, a mode filtering, and a larger beam diameter. The beam is then focused onto the sensor chip facet by an achromatic doublet lens of 60 mm focal length, to provide a focus size of about 8 µm. The lens is mounted on a 3-axis micrometric translation stage to adjust position of the focus in axial and lateral

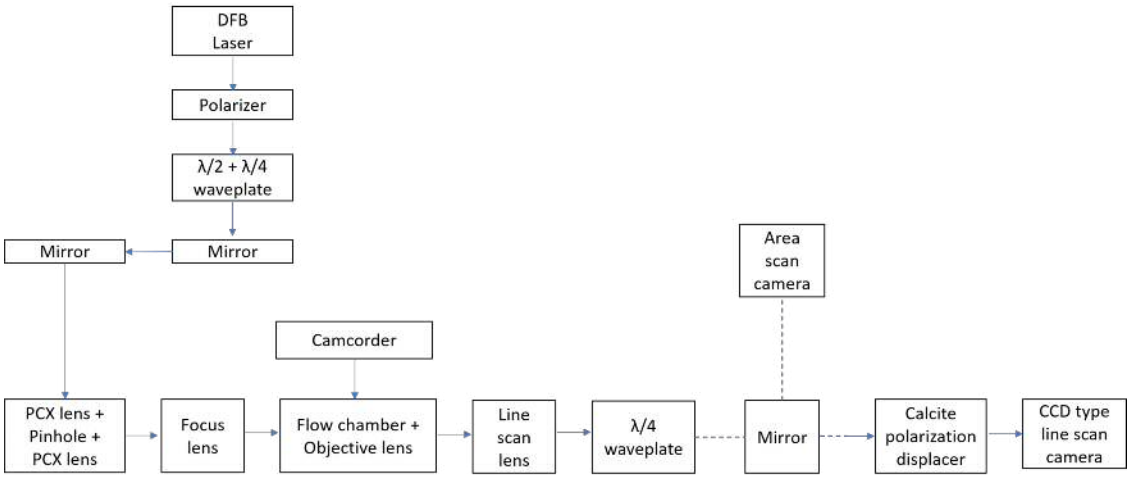

Figure 4.3: Schematic of the optical setup mounted on the optical table shown in Fig. 4.2.

directions, onto a WG at the input facet. An imaging of the sensor chip plane is enabled by an objective lens and a camcorder. The light emerging from the output side of the chip is then imaged by a linescan lens with a 1:3 magnification onto the linescan camera. The polarisation detection scheme can be controlled by a quarter-wave plate. A removable mirror optionally deflects the image of the output facet onto a CMOS camera for alignment of the input coupling.

4.3 Fluidic setup

A flow chamber in the measurement setup holds the sensor chip and enables liquid flow over the sensor surface so that when a liquid of different RI is injected into the chamber, the change of RI can be detected by the sensor chip. The flow chamber has also an objective lens to image the sensor chip plane containing WGs and microspheres on a video camera. The schematic diagram of the flow chamber encapsulating the sensor chip is shown in Fig. 4.4. The sensor chip holder uses a glass support block (see Fig. 4.5a) of 14 mm × 14 mm × 5 mm size, made of BK-7 glass, manufactured by UQG [138]. The sensor chip is mounted onto the block with immersion oil between the glass and the chip to avoid TIR.

The fluid chamber is made of a block of acrylic of dimension 15 mm × 32 mm. Components of the block are shown in Fig. 4.5 and 4.6. The external diameter of the O-ring is 11 mm. The chamber seal used inside the fluid chamber is shown in Fig. 4.5b.

A camera objective lens (see Fig. 4.6b), supplied by Edmund optics [139], has been mounted on the back side of the flow chamber to image the chip plane including the WGs and the microspheres attached on the sample as shown in Fig. 4.7a. It is a C-mount lens of 25 mm infinity focal length, with adjustable focus and aperture. A C-mount lens was chosen for its long nominal flange focal distance of 17.526 mm so that the distance between the mount and the chip sample can be large. With thickness of glass window support (4 mm, see Fig. 4.6a), the glass substrate (5 mm), and assuming the RI of glass window is 1.51, the distance of the mount from flange to sample needs to be $(17.526-4-5/1.51)\text{mm} = 10.21\,\text{mm}$ so that the microspheres are in the focal plane. The assembled flow chamber is shown in Fig. 4.7.

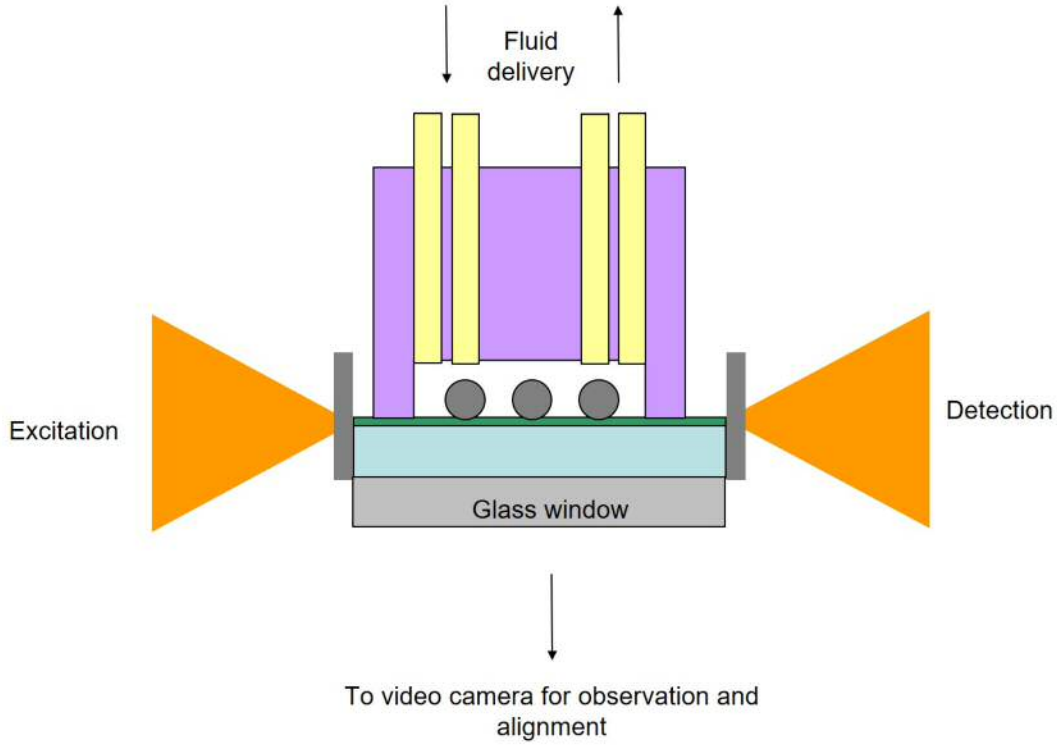

Figure 4.4: Schematic drawing of the flow chamber embedding the sensor chip. Components are labelled.

(a) Glass window supporting the sensor chip

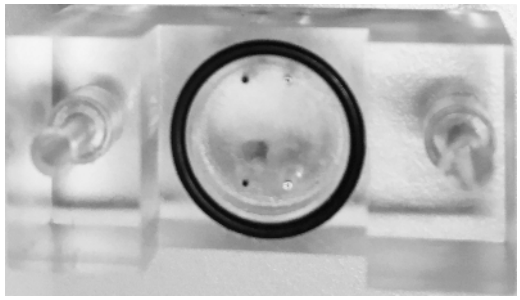

(b) Fluid chamber

Figure 4.5: Components of the flow-chamber block. (a) Glass block. (b) Fluid chamber made of acrylic. It has an O-ring to seal the chamber to the sensor chip, and 4 fluid inlets/outlets.

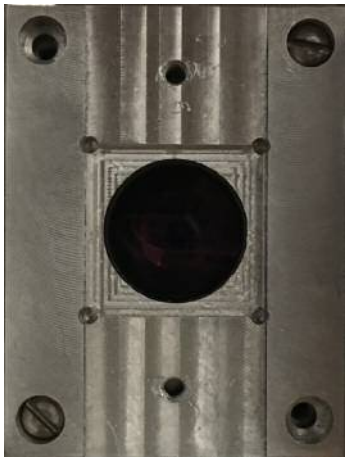

(a) Sample holder.

(b) Objective lens.

Figure 4.6: (a) Sample holder to mount the chip inside the flow chamber. The rectangular recess is to place the glass window. The circular hole is for the objective lens to image so that the microspheres and the WGs in a camcorder. (b) The C-mount objective lens of nominal focal length of 25 mm with adjustable focus and aperture, used to image the sensor chip plane.

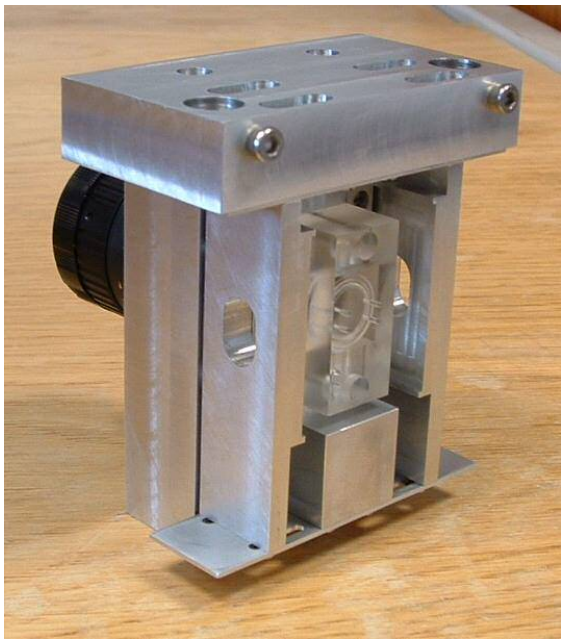

(a) Fluid chamber with two glass windows and objective lens in the flow chamber.

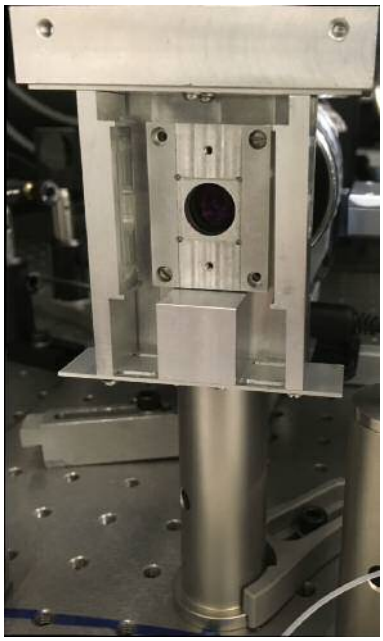

(b) Flow chamber on a pedestal pillar mount

Figure 4.7: Components of the flow-chamber block, continued.

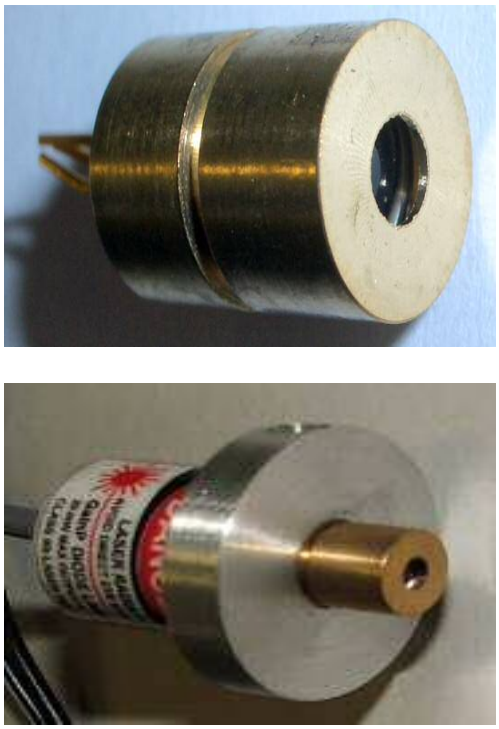

(a) Laser diodes (top), Laser diode assembly head (bottom)

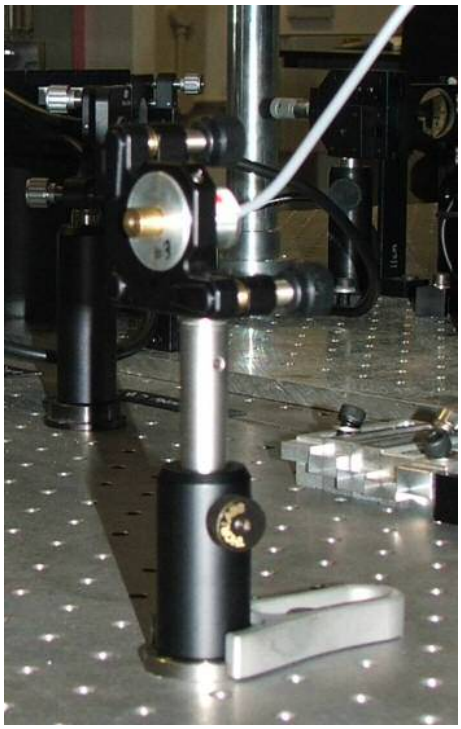

(b) The laser diode mounted in the setup

Figure 4.8: Laser diode used in the setup to reduce the usage of the DFB laser during the alignment process.

4.3.1 Light sources

4.3.1.1 DFB Laser

A DFB laser system provides the source of excitation for the WGs on the sensor chip and allows to sweep the wavelength. The output power is up to 100 mW. The laser system is temperature stabilised with a Peltier system and can be wavelength (photon energy) tuned via temperature (110 µeV/K) and current (4 µeV/mA). The system is distributed by Laser 2000 [140]. The diode of the laser system is supplied by AMS technology [141]. The full technical specification is given in Appendix C.2.

4.3.1.2 Alignment laser diode

In order to reduce the DFB laser usage, we have used a standard diode laser as a light source during the alignment process. The center wavelength of the diode is around 650 nm. The diode is shown in Fig. 4.8a. The diode runs by a fixed 2.5 V, voltage supply with series resistance of 47 Ω. The diode is mounted in a 1," diameter holder and connected to a small power supply. The diode assembly head is also shown in Fig. 4.8a. The laser is held in a kinematic mount to enable tip/tilt alignment. The specification of the laser diode is given in Appendix A.9. The optical diode laser mount is shown in Fig. 4.8b.

4.3.2 Light detectors

The measurement setup uses three different light detectors, a linescan camera, a camcorder and a areascan camera.

The linescan camera images the transmission from the WGs during the experiment. It has a Gigabit Ethernet (GigE) interface to avoid a frame grabber and allows for larger distances to the PC. This CCD type linescan camera is manufactured by e2V [142], and its technical specification is shown in Appendix C.5.

The linescan camera is a monochrome camera with 2048 pixels of 14 µm square size. The default transmitted pixel data format is "Mono 12 bit packed", and provides a 12 bit intensity resolution. A sketch of the format is shown in Fig. 4.9. For the camera to be triggered by an external source, supplied via the DAQ board used, the exposure mode of the camera is set to "Timed", for which the triggering scheme is shown in Fig. 4.10. This exposure mode allows to set the Integration time, i.e., exposure time of the camera T_i. The read-out time of the camera depends on the pixel number and pixel rate. For 2048 pixels and a rate of 62.5 MHz, the readout time is about 33 µs [143].

Pixel 2 (11..4) | Pixel 2 (3..0) Pixel 1 (3..0) | Pixel 1 (11..4)

Figure 4.9: In Mono12Packed pixel format, pixels are converted to 12 bits. Two consecutive pixels are aligned on three bytes [143].

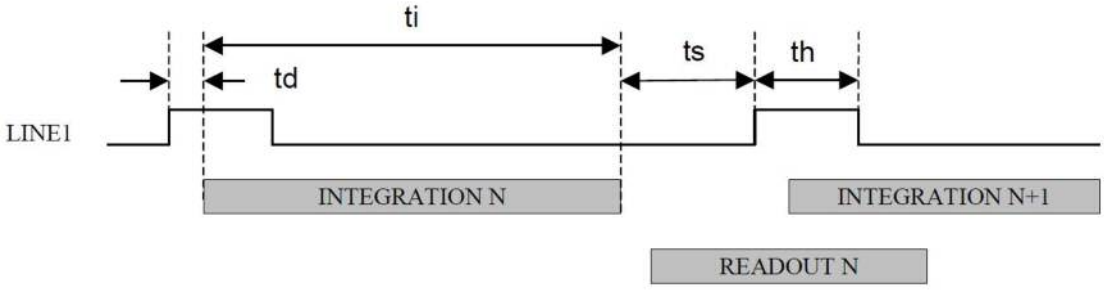

Figure 4.10: Camera triggering scheme for exposure mode "Timed" [143].

If "Line1" is selected as the trigger source, the integration time t_i starts at the rising edge of the trigger signal after a short delay, t_d, of about 2.4 µs. |The minimum hold up time (pulse high duration) t_{th} for "Line1" is 2 µs. After the integration period the collected photoelectrons are shifted into the readout register, and readout commences. The next integration can be triggered after time t_s which is 0 µs. [143]

A Sony DCR-TRV340E Camcorder of (752×568 pixels of about 4 µm size with a zoom lens of focal length 2.4 mm to 60 mm) is imaging the sensor chip plane via the objective lens shown in Fig. 4.6b of 25 mm focal length. At full zoom a pixel corresponds to 1.8 µon the sample. The LCD screen is helpful during the coupling process as well as during the experiment. The camcorder saves video the video on tape in Digital 8 format, has a night shot mode (allowing to record near infrared light such as the DFB laser, and can also take digital photos from single frames.

A 1.3 Mega pixel CMOS areascan camera with a universal serial bus (USB) 2.0 interface has been used in the setup for edge view of the sensor chip output facet for

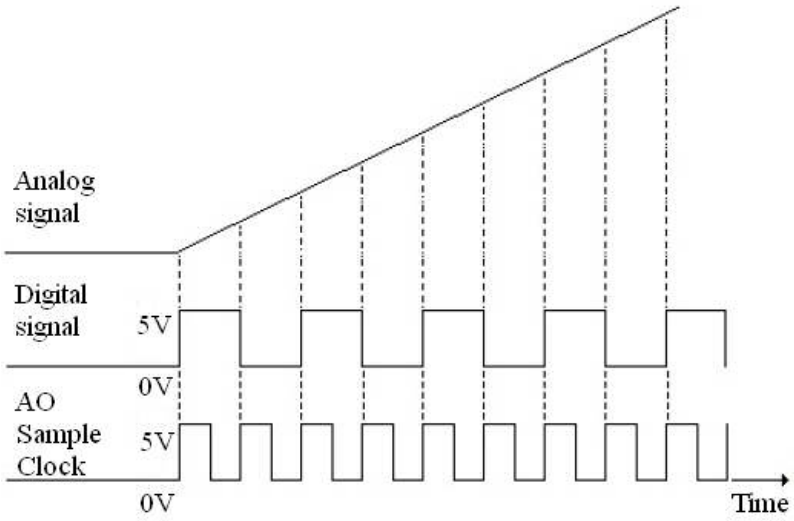

Figure 4.11: Timing diagram of the triggers.

optical alignment. This was supplied by EHD imaging GmbH [144]. A removable mirror on a magnetic kinematic mount is used to direct the transmitted light to this camera. It has an 8 bit output, black and white, 1280×1024 pixels of 6.7 µm size, corresponding to about 2.2 µm on the output facet considering the 1:3 magnification of the linescan objective.

4.3.3 Control and readout

4.3.3.1 Principle of operation

Both the linescan camera and the laser have to be controlled during the experiments to allow for a synchronisation of the wavelength scan and data acquisition by the camera. The current of the DFB laser is controlled by an analogue modulation input signal. This signal is created by a DAQ card. The laser wavelength changes approximately linear with the applied current, the wavelength scan can be defined by an initial and a final current and a ramp time t_{ramp} according to the laser specification as listed in Appendix C.2. The electronics of the setup is discussed in Sec. 4.3.3.2.

The camera trigger is a digital signal created at the same time by the DAQ, at a defined line rate. Thus the number of readouts n_{ramp} is the ramp period times the line rate r_{line}, $n_{\mathrm{ramp}} = t_{\mathrm{ramp}} r_{\mathrm{line}}$. The sampling clock of analog and digital output is set twice the line rate of the camera to create trigger pulses for the camera via a digital output waveform. A sketch of the timing diagram of the analog and digital triggers is shown in Fig. 4.11. With each rising edge of the camera trigger, the camera starts an exposure, with an adjustable exposure time, chosen to be below the inverse line rate, and subsequently reads out values from all of the 2048 pixels and send this data to a computer through an Gigabit Ethernet connection. This data is saved into a buffer, with a width given by the number of pixels and the height given by n_{ramp}. This data contains the recorded spectrum for each pixel, given by the pixel intensity as function of the trigger number. Each point in the spectrum corresponds to a specific wavelength. The maximum and minimum wavelength can be calculated as

$$\lambda_{1,2} = \beta(I_{1,2} - I_0) + \lambda_0 \tag{4.1}$$

where β: is the directive coefficient of the laser tuning, I_0 is the offset current in the laser controller, λ_0 is the laser wavelength at I_0, $I_{1,2}$: are the initial and final current of the ramp. The wavelength step, $\Delta\lambda$, between two readouts, can then be written as

$$\Delta\lambda = \beta\left(\frac{I_2 - I_1}{n_{\text{ramp}}}\right) \tag{4.2}$$

The wavelength corresponding to readout number $i = 0, 1...n_{\text{ramp}} - 1$ can thus be written as

$$\lambda(i) = \lambda_1 + i\Delta\lambda \tag{4.3}$$

In order to acquire the spectrum, the raw data from the camera for one period is stored in an array by the camera interface software (National instruments Vision Acquisition 8.6.1) in Mono 12 Bit Packed format. The Mono 12 Bit Packed data format is shown in Fig. 4.9. The data is then extracted into 16-bit format and shown as 2D grayscale image, and spectrally integrated in a line graph versus pixel. From this data a pixel region corresponding to a WG transmission peak, called a channel, can be selected. The developed software and it's functionalities are discussed in more detail in Sec. 4.3.3.3.

To compensate for the intensity change versus current, a normalised spectrum according to Eq. (2.66) or Eq. (2.67) is determined from a pair of pixel regions, corresponding to the two displaced images of different polarisation for one WG, see Fig. 4.1. By using the waveplates in the setup, as discussed in Sec. 4.4.1.4, either intensity or phase detection can be selected. The normalised spectrum of a channel pair is calculated by dividing the spectrum of the first channel in the pair by the spectrum of the second. In intensity detection, this references TE and TM transmission intensities relative to each other, making them independent of the increase of the laser power with current.

Regions in the normalised spectrum can then be selected and fitted with a Lorentzian peak each, using the 'NonLinearFitWithMaxIters' function in Advanced Analysis Library from LabWindows/CVI 2009®. The function uses the Levenberg-Marquardt algorithm to determine the set of coefficients that best fit the set of input data points (x, y) by a function

$$f(x; p, w, a, o) = o + \frac{a}{1 + 4((x - p)/w)^2}\,. \tag{4.4}$$

The model function uses a set of 4 coefficients: the center position p, full width at half maximum w, amplitude a, and offset o. The software can automatically fit a time series of spectra,to result in a sensing time trace of the parameters. Typical spectral rates are 1-10 Hz.

4.3.3.2 Electronics

The electrical signals to trigger the linescan camera and to create the current ramp are created by the data acquisition (DAQ) board PCI-6259 from National Instruments. The physical connections to the board use a 68-Pin Shielded Desktop Connector Block supplied by National Instruments. The technical specification of the DAQ board is listed in Appendix C.6. The schematic of the connection between the DAQ, camera and the laser is shown in Fig. 4.12.

Camera trigger is a digital signal which is routed from one of the digital outputs of the DAQ board using a digital output (DO) waveform. The ramp signal is routed

to the laser controller from one of the analog outputs of the DAQ board through a low pass filter and voltage divider, limiting the voltage range and the slew rate of the signal to protect the driver. The external modulation input has a response of 60 mA/V, so that the ±10V output range is converted to ±60 mA current modulation. The schematic of the RC filter is shown in Fig. 4.13. The sampling clock, "AO Sample clock" on the DAQ board is used as the source to generate the camera and the laser trigger. The frequency of the sampling clock is twice the line rate of the camera to create trigger pulses for the camera.

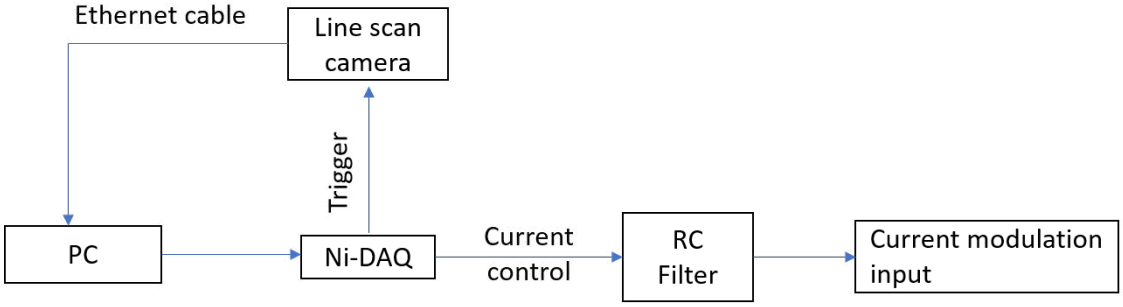

Figure 4.12: Schematic of the connection between DAQ, linescan camera and laser.

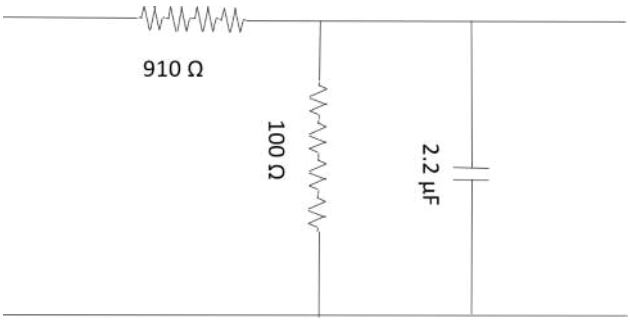

Figure 4.13: RC low pass filter and a 1:10 divider that is connected between the DAQ analogue output and the current modulation input of the laser controller. The RC time constant of the filter is 0.22 ms.

4.3.3.3 Software

A software was initially developed in a work by a summer intern Philippe Rouger and Prof Wolfgang Langbein in 2009. It acquires data, converts it to transmission spectra and then fits the selected data. The software has been developed in Labwindows/CVI 2009. The software works with a set of hardware consisting of a data acquisition (DAQ) board (PCI-6259) from National Instruments [145], a GigE Vision, CCD type Linescan camera from e2V [143] and a DFB laser system [146]. Data communication between the software and GigE Vision interface camera uses the Vision Acquisition Software, version 8.6.1 from National Instruments [145]. We have upgraded the software further in this project. In Sec. 4.3.3.4 we will describe the functionalities that have been added into the software briefly.

4.3.3.4 Functionalities of the software

The software has been upgraded to acquire real-time data from the experiments. In it's basic form the software could select channels from a simulated waveform to calculate normalised spectrum. Peaks could be selected from the normalised spectrum for fitting. The following functionalities were added during the upgrade:

1. The software can now generate a digital signal to create camera trigger and analogue signal to control laser current in a range in order to scan the wavelength of the laser during data acquisition from two separate 'Camera Settings' (see Fig. B.2) and 'Trigger Settings' (Fig. B.3) panels which are independent of each other. Properties of the camera trigger signal can be changed on the fly from the 'Camera Settings' panel. The resolution of the spectrum to be acquired and acquisition line rate can be changed from the 'Trigger Settings' panel.

2. An alignment mode option has been introduced in the 'Image Acquisition' panel (see Fig. B.5) for optical alignment process. In this mode data acquisition continues to run until stopped by the user.

3. It is now possible to define multiple channels from channel selection window and see individual channel spectra and normalised spectra in a 'Channel/Normalized spectrum' window in the 'Image Acquisition' panel as shown in Fig. B.5. In this upgraded version of the software, it is now possible to select multiple ranges in the normalised spectrum for fitting,

4. In the 'Multiple Acquisition' panel, as shown in Fig. B.6, it is now possible to set a number of spectra for multiple acquisitions. It has also an alignment mode which runs indefinitely unless it is stopped. Fitting can be observed for the selected channel in this panel. The fitted data is saved at the end of acquisition automatically at the pre-defined location on the disk.

5. It is possible to save experimental data, i.e., buffer, spectrum and peaks manually. Fig. 4.40 shows the plot of the content of the camera buffer and Fig. 4.41 shows split of the WG peak which have been saved by the software. The software saves all current device parameter settings, i.e., laser current, line rate etc., in disk automatically before exiting and reloads them at start.

(a) Cleaved sample mounted on the flow chamber block.

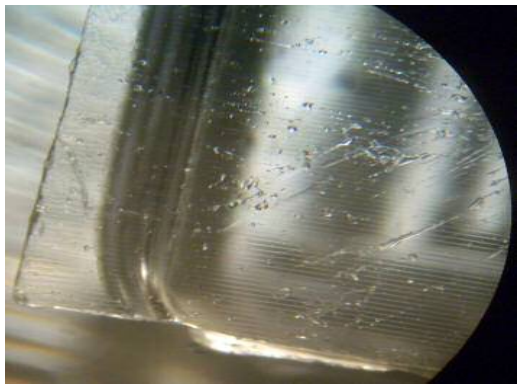

(b) Edge of sample in (a).

Figure 4.14: Mounting of the sensor chip.

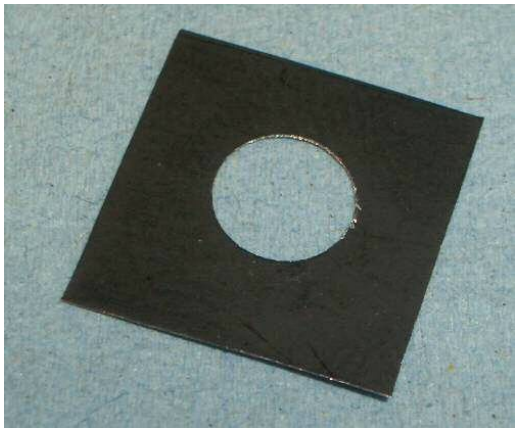

(a) Foil cut out to reduce light between the glass window and the sensor chip

(b) Sensor sample positioned on the flow chamber block with the foil cut

Figure 4.15: Mounting of the sensor chip including a black foil to suppress background.

4.4 Characterisation

4.4.1 Alignment

4.4.1.1 Mounting of the sensor chip

The fabricated sensor chip is mounted inside the flow chamber and kept submerged in water to observe the high Q modes of the polystyrene microspheres. The construction of the fluid chamber has been discussed in Sec. 4.3. The fluid chamber has been constructed such that during the experiment different liquids can be injected through the inlets to detect the shift of resonance position due to change in RI inside the fluid chamber. In order to mount the sensor chip inside the flow chamber, the sensor chip has been cleaved by the cutting tool that we have designed, see Sec. 3.3. The protocol for cleaving the sensor chip using the cutting tool is given in Appendix B.4. The chip has been cleaved such that it extrudes about 0.5 mm over the two horizontal sides of the glass block, as shown in Fig. 4.14. The immersion oil between the cover slip and the glass block should have removed a reflection of

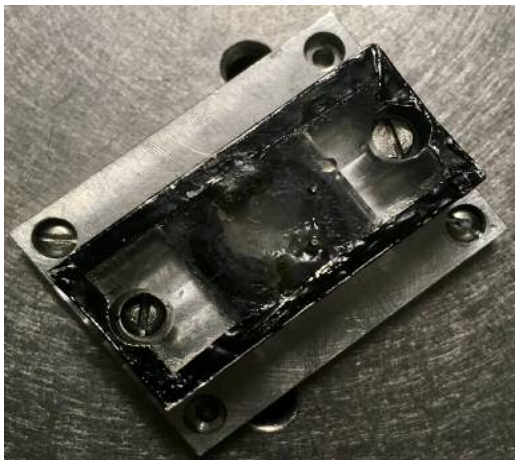

(a) Flow chamber block covered by black aluminium foil, top view

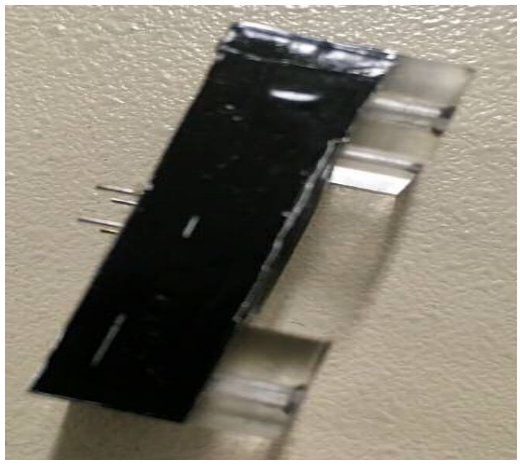

(b) Chamber seal of acrylic block covered by a by black aluminium foil, side view

Figure 4.16: Mounting of the sensor chip, continued.

(a) The fluid chamber covered by the black aluminum foil is placed on the sensor chip to create a water tight chamber

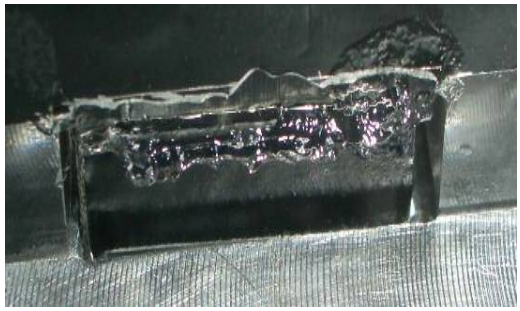

(b) Index matching gel is added at the facets of the chip to present a homogeneous optical environment at the WG ends. Anti-reflex-coated windows are positioned against the facet to provide an optically flat surface for imaging.

Figure 4.17: Mounting of the sensor chip, continued.

light at this interface, thus avoiding light guiding by the coverslip. However, strong background light was still present. We therefore added an anodised aluminium foil, supplied by Thorlabs, to create a light shield between coverslip and glass block, while still using immersion oil. The glass block side walls are also covered by black aluminium foil to absorb the scattered and unguided light, as shown in Fig. 4.15. The chamber, a transparent acrylic block, is also covered by the same black aluminium foil as shown in Fig. 4.16. The chamber seal, shown in Fig. 4.5b, has an O-ring of diameter of 11 mm. When this O-ring is squeezed onto the chip sample it creates a water tight seal. During assembly, the sample is first placed on the glass window as shown in Fig. 4.15b. The chamber is then placed on top of the sample chip as shown in Fig. 4.17a, and screwed on to form a tight seal. In order to index match the region at the sensor chip facet to the attached glass window we have first used immersion oil of RI 1.516 at 23°C and wavelength of 550 nm, supplied by Olympus [147]. However, we have found that RI matching gel of RI, (n_d) 1.51 at 25°C manufactured by Nye [148] is more stable, since it has some shape stability and sticks between the gaps, while oil flows down over time. Fig. 4.17b shows one of

the sensor chip facets covered with the index matching gel to present a homogeneous optical environment at the WG ends when the chip facets are positioned against the anti-reflex-coated glass windows (see Fig. 4.7a) to provide an optically flat surface for imaging. The corresponding improvement of the optical coupling process is shown in Fig. 4.18. The right most image in Fig. 4.18 shows a homogeneous structure when RI matching gel has been used. This means that there is no air remains between the sample and the glass window on both facets of the chip. The leftmost and the middle image are structures using RI matching oil. The black regions indicate air in the gap, deflecting the transmitted light beyond the collection angle of the imaging objective. We have therefore used RI matching gel in the following.

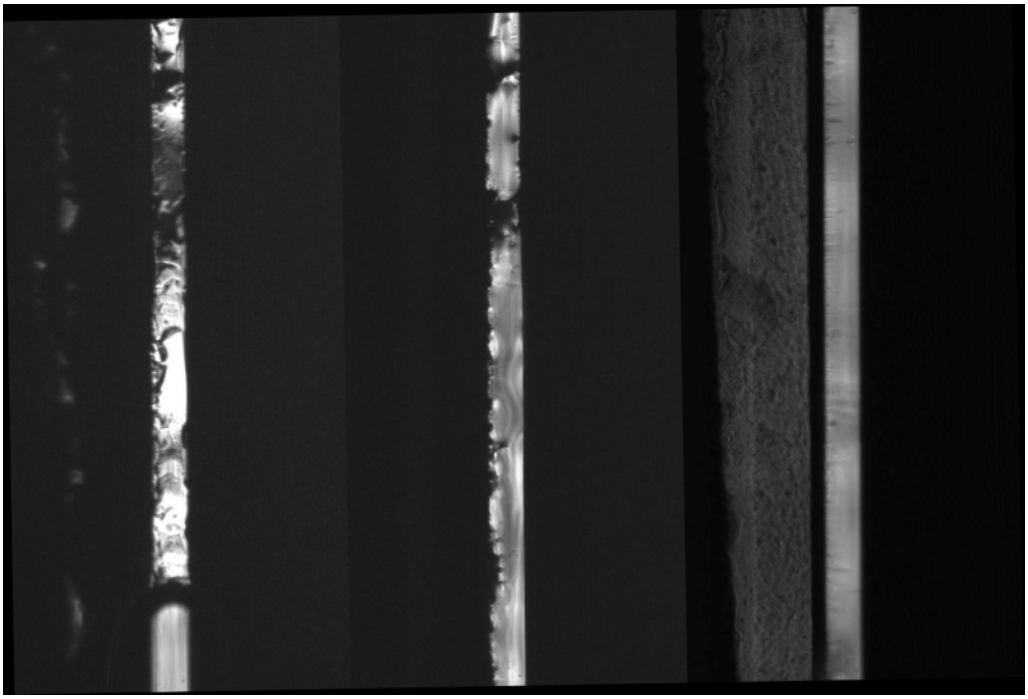

Figure 4.18: Index matching at chip facets. The right image shows a homogeneous structure when focused on the facet of the chip, when using matching gel. The left and middle images show some black regions, when using matching oil.

4.4.1.2 Coupling of laser

In order to produce the evanescent wave at the SU-8 core and MY-133 cladding interface, light must propagate through the WGs on the sensor chip. The source of excitation for our experiments is DFB laser as discussed in Sec. 4.3.1.1. Thus the laser has to be coupled with the WGs on the sensor chip mounted inside the flow chamber as discussed in Sec. 4.4.1.1.

The optical setup is described in Sec. 4.2.1. We have used two neutral density filters to attenuate light from the laser as required, as shown in is shown in Fig. 4.25. These filters are anti-reflection (AR) coated (MgF_2 optimised at 600 nm) of diameter of 1 ” and optical density of 0.5 and 1.0. They are supplied by Axicon [149]. The optical setup contains a combination of a pinhole of 20µm diameter, supplied by Thorlabs [150] and two planoconvex (PCX) lenses of 40 mm and 150 mm focal length, supplied by Casix [151], to produce collimated beam. The combination also

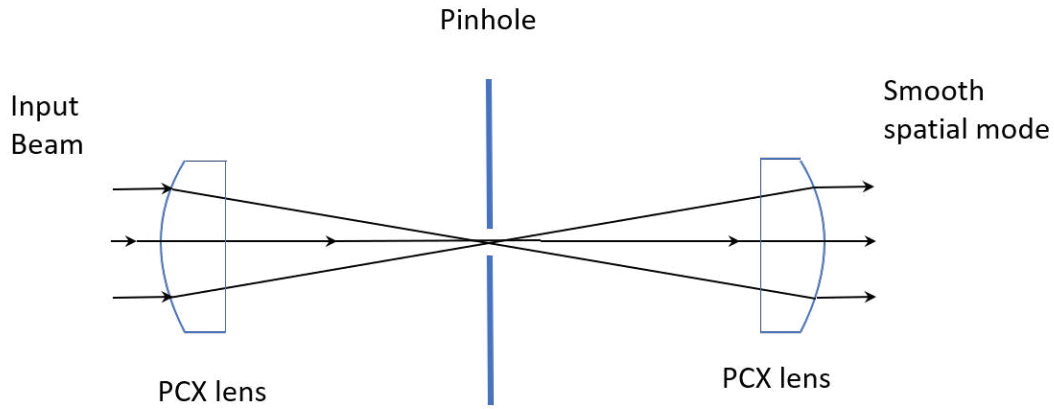

Figure 4.19: A spatial filter system with two PCX lens and a pinhole. Spatially varying intensity of a laser light is removed by this combination. This also serves as alignment pinhole, defining the input direction into the setup.

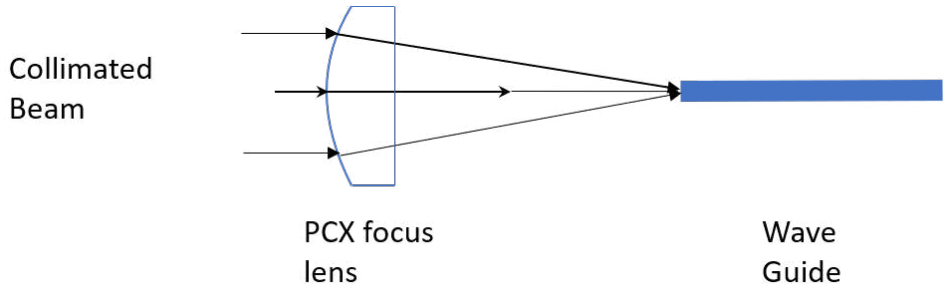

Figure 4.20: Coupling of laser light with a WG by using a PCX focusing lens.

works as a spatial filter system. The principle of operation of a spatial filter system can be explained as follows. When an input beam with spatially varying intensity is focused by planoconvex lens the input beam is transformed into a central spot with side fringes. By positioning a pinhole on a central spot, the mode shape is defined. A schematic of the spatial filter system is shown in Fig. 4.19.

Schematic of the focus lens to couple light with the WG is shown in Fig. 4.20. An achromatic doublet lens of 60mm focal length, supplied by Thorlabs [150] is used as coupling lens by focusing the collimated beam onto the end facet of a single WG. In the original optical setup a cylindrical lens was used to focus the collimated light on the WG array. However, guided light was not seen on the CCD camera due to the presence of strong background light. Therefore, the cylindrical lens was replaced by this spherical lens, focusing the light in both directions on a single WG. The coupling lens is mounted on a 3 axis stage to control the position of the lens by a micrometer screw, see (Fig. 4.21). Components used in this mount are manufactured and supplied by Thorlabs [150] and other companies.

A WG on the sensor chip needs to be coupled with the laser. To help the alignment a CMOS camera has been used to image the output facet. A camcorder, discussed in Sec. 4.3.2, has been used to image the . The setup is shown in Fig. 4.22.

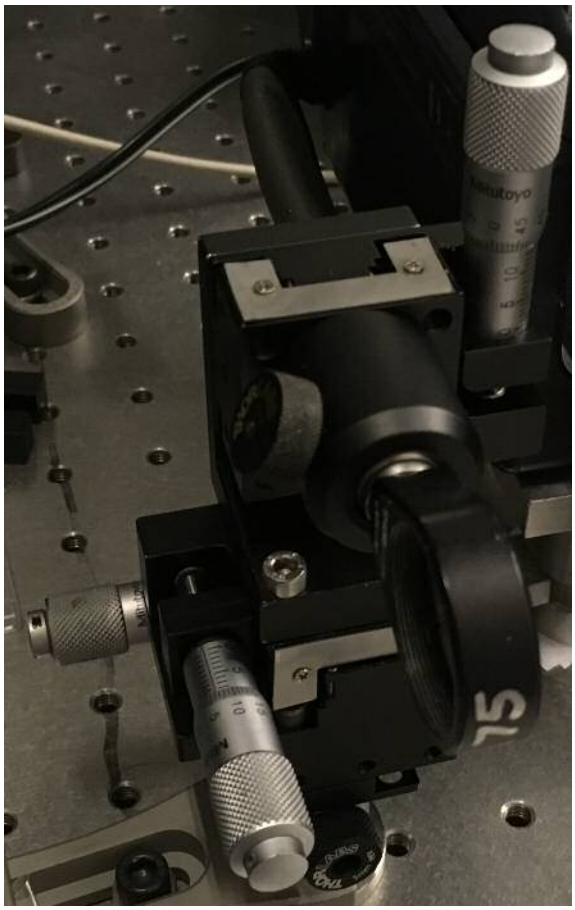

Figure 4.21: Coupling lens mount with an achromatic doublet lens of 60 mm The coupling lens has been used to couple light into one end of a single WG.

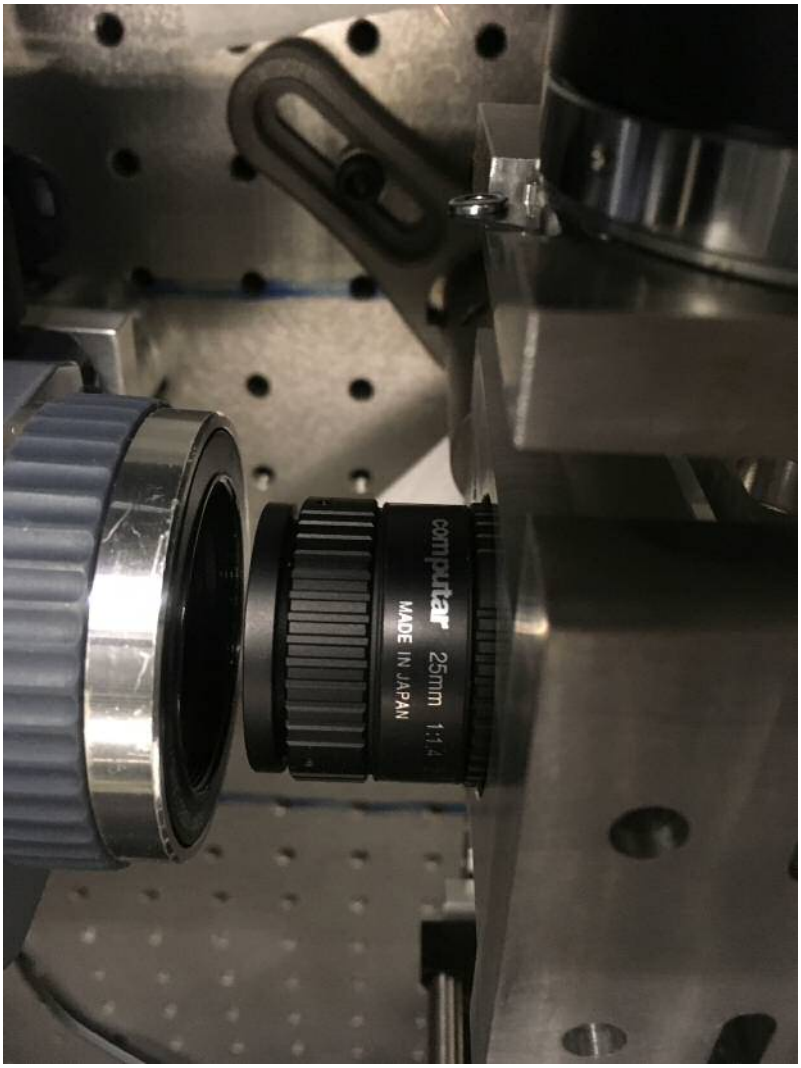

Figure 4.22: A Sony DCR-TRV340E Camcorder is mounted after the objective lens attached to the flow chamber, to image the sonser chip planes including the scattering by the WGs and microspheres.

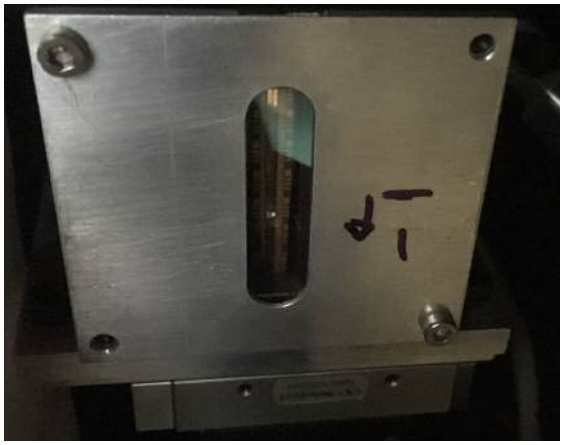

(a) Calcite polarisation displacer mounted on of the linescan camera, lowering the vertical polarisation by about 60 µm.

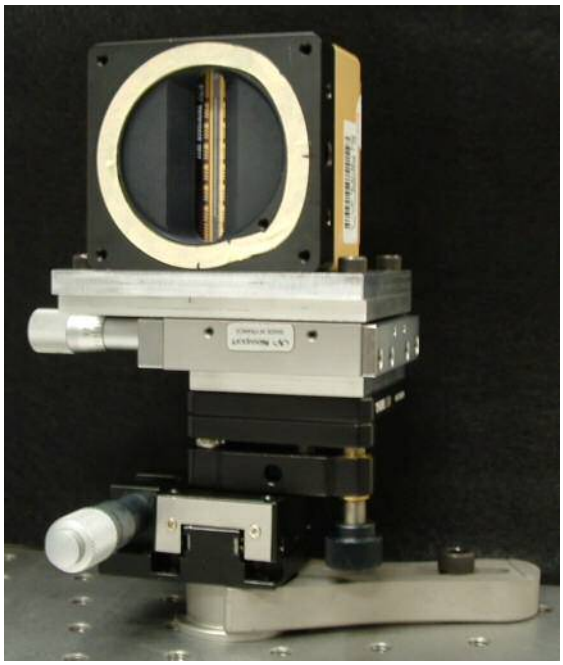

(b) Linescan camera mount .

Figure 4.23: Calcite polarisation displacer mounted in front of the linescan camera.

4.4.1.3 Alignment of the linescan camera

The linescan camera, discussed in Sec. 4.3.2, is used to detect the transmission of the WGs. In front of the camera, a polarisation displacer is mounted which shifts the image of vertical polarisation by about 60 µm vertically along the line array of the camera. This corresponds to about 4 pixels (14 µmpixel size), and about half the pitch of the WG array image of 150 µm considering a 1:3 magnification. It is made of Calcite and was manufactured by Altechna [152]. The calcite polarisation displacer is shown in Fig. 4.23a while the dimension and polarisation direction of a calcite displacer is shown in Fig. 4.24. The technical specification of the polarisation displacer is shown in Appendix C.2.

The linescan camera is mounted on a kinematic mirror mount with tip and tilt control, manufactured and supplied by Thorlabs [150]. In addition to this, two linear translation stages with micrometer adjusters allow for lateral and axial position adjustment, as shown in Fig. 4.23b. All provided degrees of freedom are required to align the line array onto the image of the WG array of the sensor chip facet.

4.4.1.4 Waveplates at source and detection

Two different detection schemes can be used to measure resonances in E_{TE} while exploiting E_{TM} as a reference as discussed in Sec. 2.4.2. In both cases, the excitation is adjusted so that the signal is zero out of resonance, i.e., a balanced detection is possible. This can be achieved by adjusting the excitation polarisation by the combination of $\lambda/4$ and $\lambda/2$ plates in the excitation side of the measurement setup, shown in Fig. 4.25. Setting the $\lambda/4$ plate to 45°, and rotating the $\lambda/2$ plate allows to control the phase offset between horizontal and vertical polarisation, in the same way as in a de-Sénarmont compensator used in DIC.

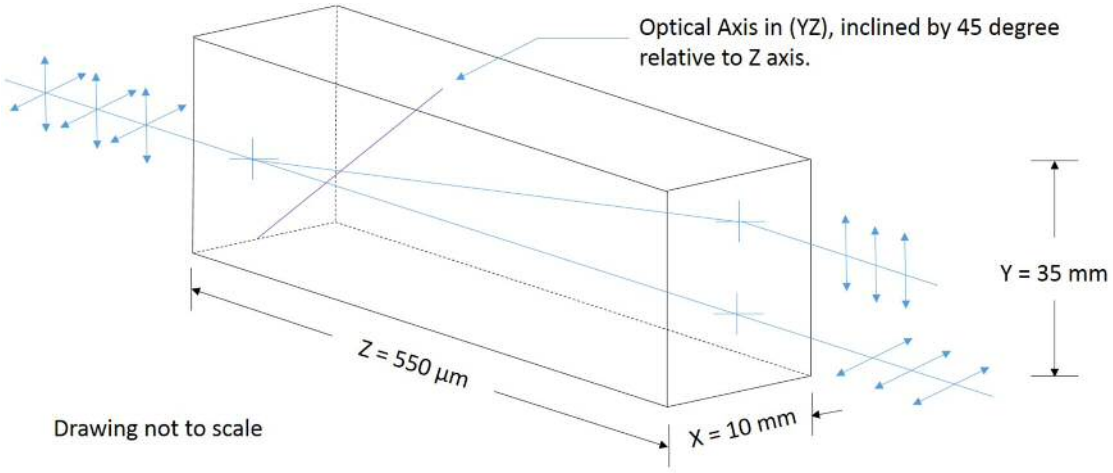

Figure 4.24: Geometry of the calcite polarisation displacer (not to scale). The polarisation displacer is mounted in front of the linescan scan camera as shown in Fig. 4.23a.

Figure 4.25: Combination of $\lambda/2$ and $\lambda/4$ waveplates to adjust the TE and TM intensity ratio and relative phase as discussed in Sec. 2.4.2. Additional elements are a polarizer on the left, neutral density filters and a mirror to the right.

The phase detection scheme requires that the detected polarisations are equal mixtures of E_{TE} and E_{TM} and thus measure the interference between the two fields. This can be achieved by rotating the axis of the $\lambda/4$ plate at the detection end (see Fig. 4.26) to 45°, and adjusting the phase offset between TE and TM fields using the $\lambda/2$ plate the excitation polarisation.

Due to different coupling and transmission efficiencies of the WGs for the two polarisations, the above idealised behaviour is not exactly realised. However, the wave plates in the excitation can produce an arbitrary ratio of TE and TM polarisation amplitude as well as of phase offset, and therefore, after setting the wave plate rotations nominally, it can be adjusted using the detected signal to provide the required properties.

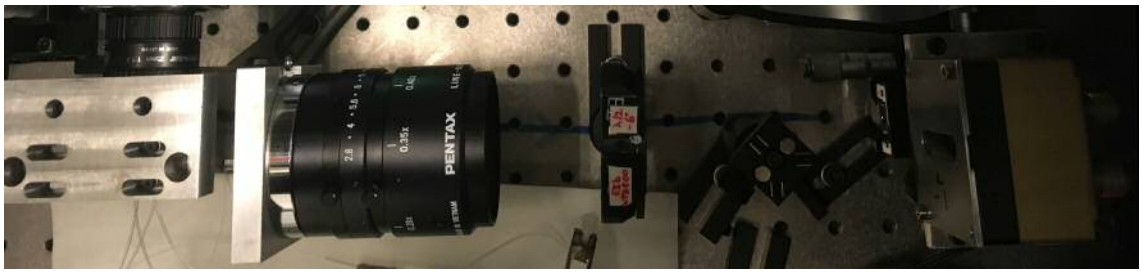

Figure 4.26: $\lambda/4$ waveplate on the detection side of the measurement system to choose between the intensity and phase detection scheme as discussed in Sec. 2.4.2.

4.4.2 Liquid handling

The flow chamber consists of a total of 4 inlets and outlets as shown in Fig. 4.27. Syringes filled with glycerol of different concentration have been used to change liquid inside the liquid chamber. This requires a manual handling during the liquid injection phase into the fluid chamber. Manual handling provides limited control of the liquid flow rate in an experiment when syringes with different concentration have been used. This can be overcome by a motorised control of the syringes. Therefore, a simple motorised system was built to inject medium into the fluid chamber in a controlled fashion. The system uses using a geared dc motor, supplied by RS components, driving a micrometer screw to push the plunger of the syringe, and other mechanical items, either supplied by Thorlabs or build in-house. The motor speed can be adjusted by a dc power supply. The syringe system is shown in Fig. 4.28 The motor speed is 9 rpm at the nominal 12 V supply voltage, corresponding to 75 µm/s plunger motion, and about 0.2 µl/s fluid delivery.

4.4.3 Results

4.4.3.1 Coupling to waveguides

To enable the readout of the WGMs, the laser has to be coupled through the WGs on the sensor chip mounted inside the flow chamber, and the WGs have to be able to guide the light at the wavelength of the laser. The flow chamber, as discussed in Sec. 4.3, should be filled with water to allow for a high Q factor of the WGMs. In order to establish experimentally the required WG core thickness for which the laser light can be guided through the WGs, we have fabricated a planar WG with

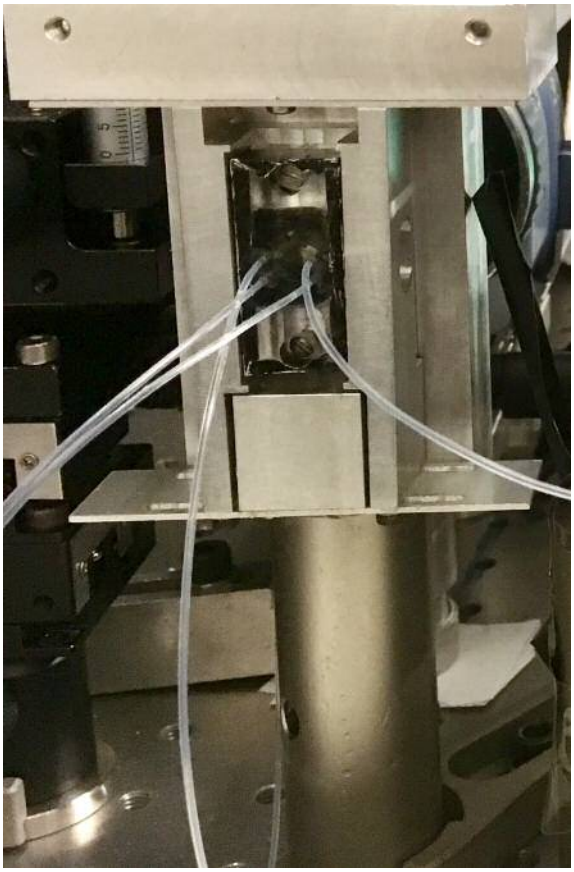

Figure 4.27: Flow chamber mounted on a pedestal pillar with the inlets and outlets.

(a) DC geared motor.

(b) Constructed motorised syringe system.

Figure 4.28: Motorised syringe system. The DC motor speed can be controlled by a DC power supply.

SU-8 as the core layer of different (550, 700 and 900 nm) thicknesses and MY-133 as the cladding layer (750 nm) on a glass cover slip. By using the diode laser and the cylindrical lens one can couple laser light to the WG. Fig. 4.29 shows the image taken from the opposite facet of the WG with the light coupled in from the other side via the cylindrical lens. Schematic in Fig. 4.30 shows the optical components used to capture the output of the planar WG coupled by the cylindrical lens (see Fig. 4.29).

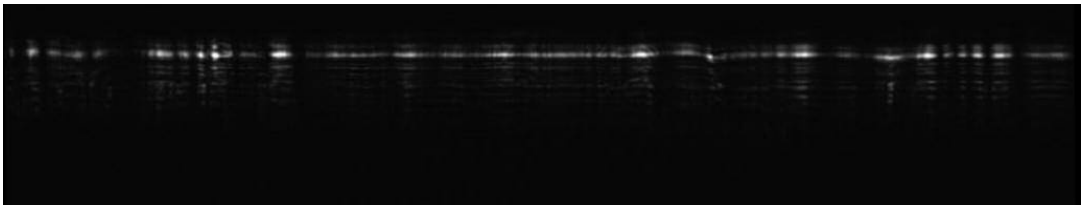

Figure 4.29: Transmitted guided wave from a planar SU8 layer on a glass substrate. The DFB laser has been used. Thickness of SU-8 layer is 900 nm and is covered by MY-133. No PS microspheres are present on the MY-133 layer. The image is acquired by the area camera.

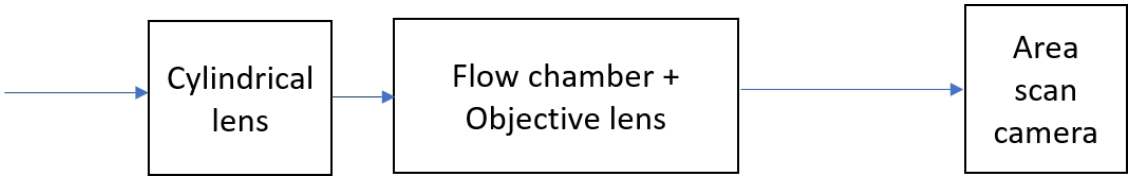

Figure 4.30: Schematic to explain Fig. 4.31. Laser light is coupled to one facet of WG through different optical components and then the output is taken from other facet of the WG and imaged on the area scan camera. Complete schematic of the optical setup is shown in Fig. 4.2.

Since a guided transmission has been possible for 900 nm thick SU-8 layer, this core thickness will be used as the required SU-8 thickness during the fabrication of the WG. By using the diode laser and the PCX lens one can couple a single WG. The transmission from the WG can be imaged by the 2D CMOS camera mounted at the detection end of the WG. Upon coupling and transmission through a WG, the image of the output facet features a bright spot on the top edge of the chip, indicating the end position of the WG, as shown in Fig. 4.31. Schematic in Fig. 4.32 shows the optical components used to capture the output of a single WG coupled with the DFB laser by the PCX focus lens (see Fig. 4.31).

The transmission through the WGs can also be observed on the camcorder during the coupling process to optimize the coupling and identify transmission loss through WGs due to defects in the WGs. In order to image the sensor chip surface, the camcorder focus is set to infinity, and the objective lens is focused to achieve a sharp image of the WGs. The resulting image, see Fig. 4.33, taken for optimised coupling to a single WG, which the scattering during propagation through WGs. Some background illumination was supplied via a flash lamp through the fluid chamber, allowing to make out the WG array and the microsphere arrays partially covering the WGs. The intensity drop-off towards the image edges is a vignetting of the imaging. The symmetric intensity profile indicates that the propagation losses

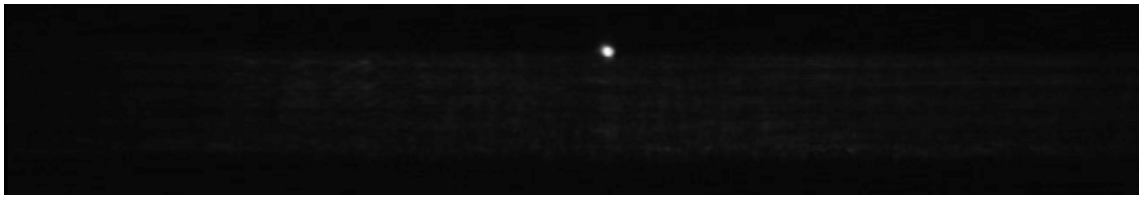

(a) WG output with negligible background.

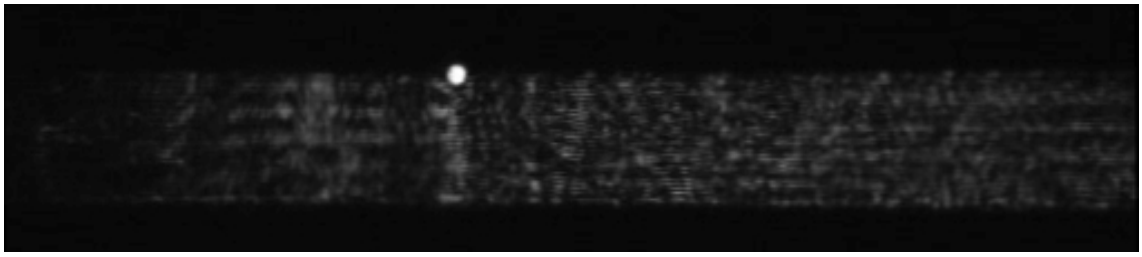

(b) Strong WG output with some background.

Figure 4.31: Image of the output facet of the sensor chip, while coupling the DFB laser light into a WG on the input facet. The bright spot is the transmitted guided wave. The area of background light below the spot is the glass substrate. The SU-8 WG has a core thickness of about 900 nm and is covered by a 200±20 nm thick MY-133 layer. Dimension of (a) is 1625 µm × 275 µm and that of (b) is 1275 µm × 275 µm.

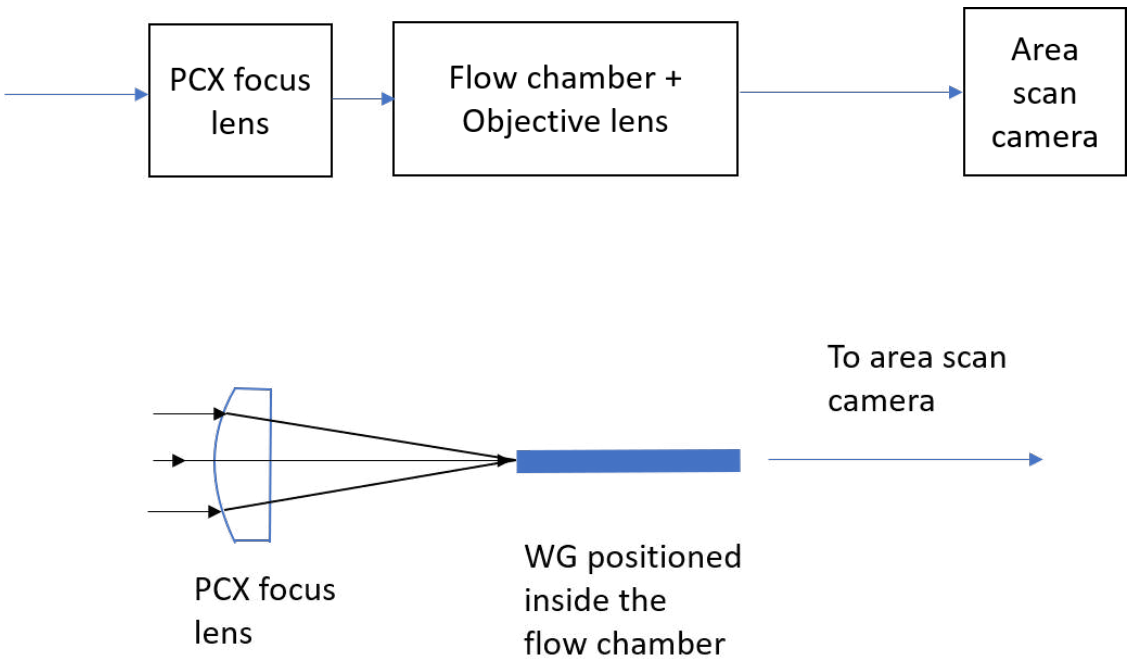

Figure 4.32: Schematic to explain Fig. 4.31. Laser light is coupled to one facet of WG through different optical components and then the output is taken from other facet of the WG and imaged on the area scan camera. Complete schematic of the optical setup is shown in Fig. 4.2.

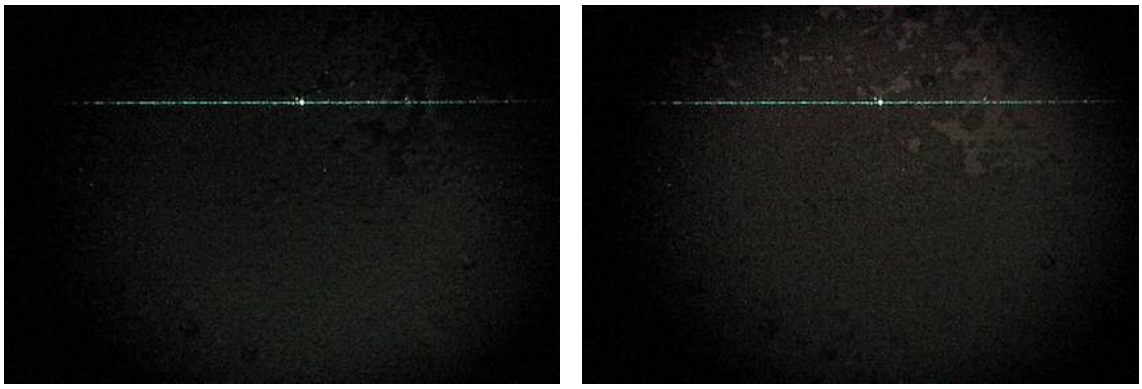

(a) Without background illumination. **(b)** With background illumination.

Figure 4.33: Image of the sensor chip plane containing the WG array and microsphere arrays, while the DFB laser is coupled on the input facet of the chip (to the right) into a WG, propagating along the WG from right to left. The light scattered by WG roughness is clearly visible, indicating the selected WG coupled to the laser. The bright spot close to the centre, along the coupled WG, is a microsphere which is coupled to the propagating light in the WG. The images are taken by the camcorder (see Fig. 4.2 and Fig. 4.22) and image an area of 11 mm × 8 mm.

through the WG are small over the imaged distance of about 10 mm. When the WG propagation is disrupted, the light is scattering in the microsphere array, as exemplified in Fig. 4.35, where the laser was coupled to a different WG of the same chip. Schematic in Fig. 4.34 shows the optical components used to capture the image shown in Fig. 4.33 from the camcorder when the DFB laser is coupled with a single WG by the PCX focus lens.

4.4.3.2 Coupling to microspheres

In the previous section we have seen how to identify a microsphere coupled to a WG. The question arises if this coupling is to specific high-Q WGMs, or a non-resonant scattering. To investigate this, we have scanned the laser current and wavelength as described in Sec. 4.3.3, while taking movies on the camcorder, providing 25 frames per second.

Fig. 4.36a shows an example of a microsphere that is coupled with the laser light, submerged in water inside the fluid chamber. This microsphere has been analysed.

We have used CCDPlot for data analysis. CCDPlot is a software tool, developed by Prof Wolfgang Langbein and his team, for data analysis processing. To begin the analysis we need to import the files in BMP format from the camcorder, as described in Appendix C.3. We have also calibrated the spatial coordinates by selecting the correct scaling taken from the WG separation.

Selecting an small area around the microsphere position, we show in Fig. 4.37 the evolution of the scattering while scanning the laser current can be visualised, as shown in Fig. 4.37. While the laser power is increasing with current along the frames shown, there is also a change of the scattering shape, indicating the influence of resonant scattering by a specific WGM mode.

This data is analysed in more detail in Fig. 4.38, where the time-dependent intensity of specific positions are given. Clearly, the time-dependence is showing

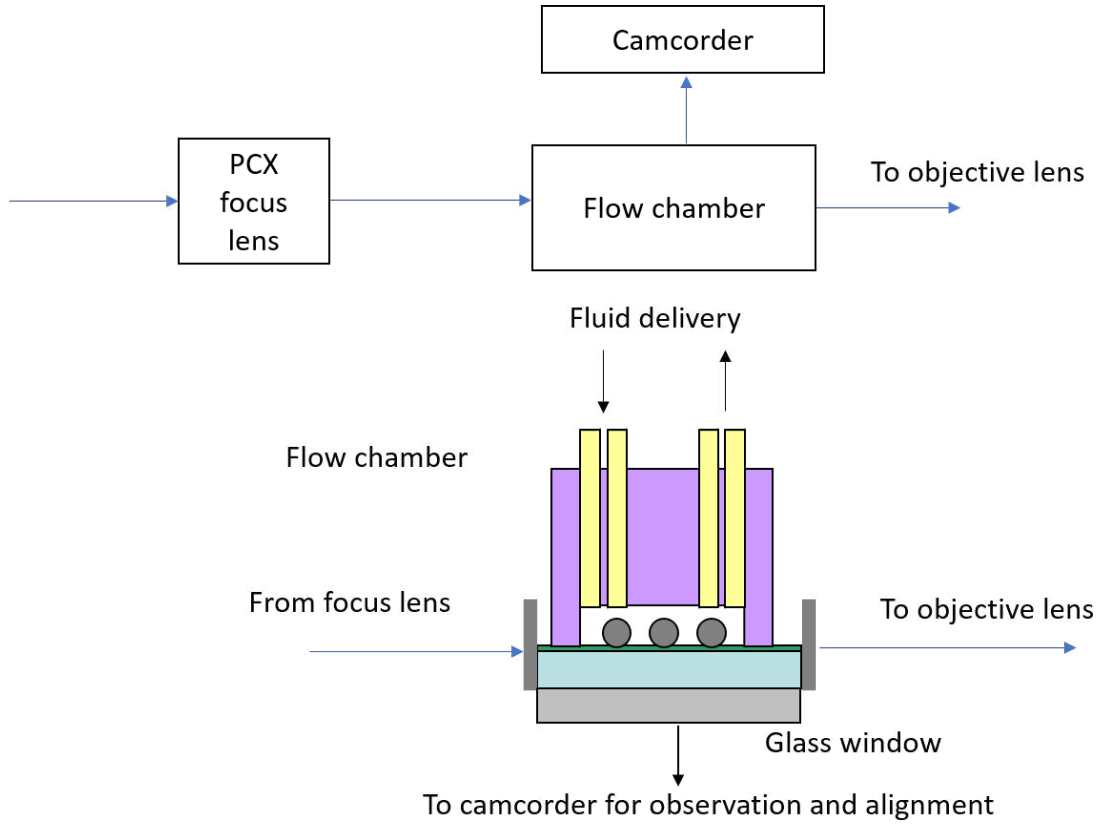

Figure 4.34: Schematic to explain Fig. 4.33. Laser light is coupled to one facet of WG through different optical components. The bright line is the coupled WG and the bright spot is the coupled WG. The image is taken from the camcorder. Complete schematic of the optical setup is shown in Fig. 4.2.

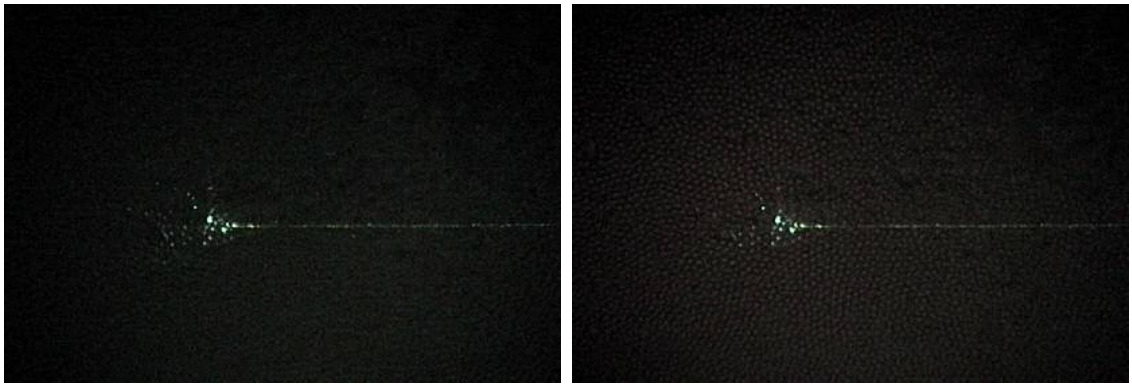

(a) No background illumination. **(b)** With background illumination. .

Figure 4.35: As Fig. 4.33, but coupling to a different WG which is disrupted along the propagation, leading to scattering into the microsphere array. Imaged size 2 mm $\times$ 1.5 mm.

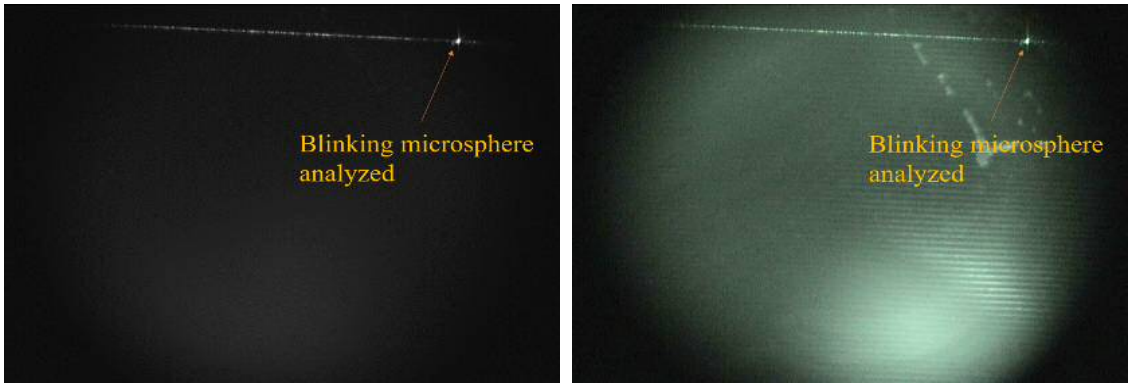

(a) No background illumination. **(b)** With Background illumination.

Figure 4.36: As Fig. 4.31, but for a different sensor chip. The arrow points to the microsphere that is coupled to the laser light. The microsphere is attached on top of a WG in a sample. This microsphere has been analysed. Imaged size is 3.95 mm $\times$ 2.96 mm.

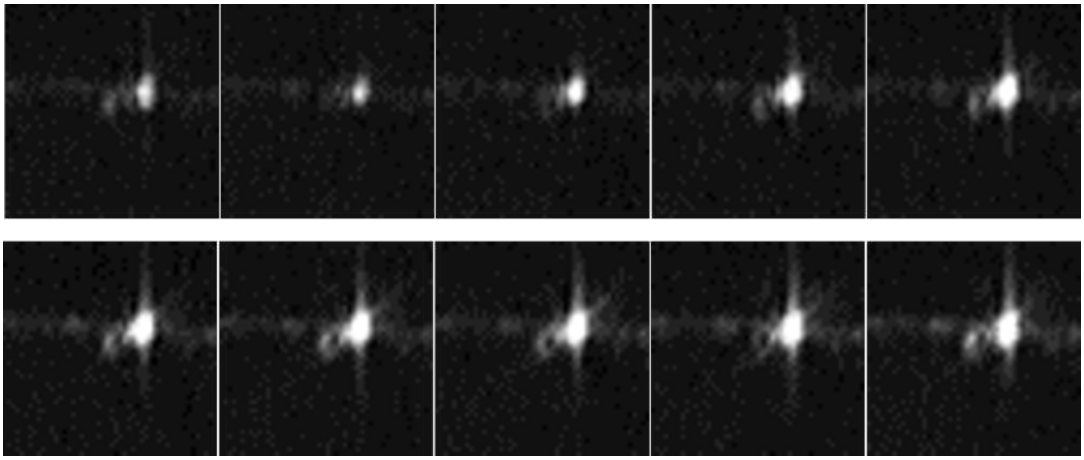

Figure 4.37: Scattering of a region around the selected microsphere, as function of time, from top right to left, continued in the next row. Taken at 25 Hz frame rate, corresponding to a period of 40 ms. The laser current is scanned at the same time. The change of the scattering shape, with laser current and thus wavelength, is visible, showing a spherical shap of the microsphere.

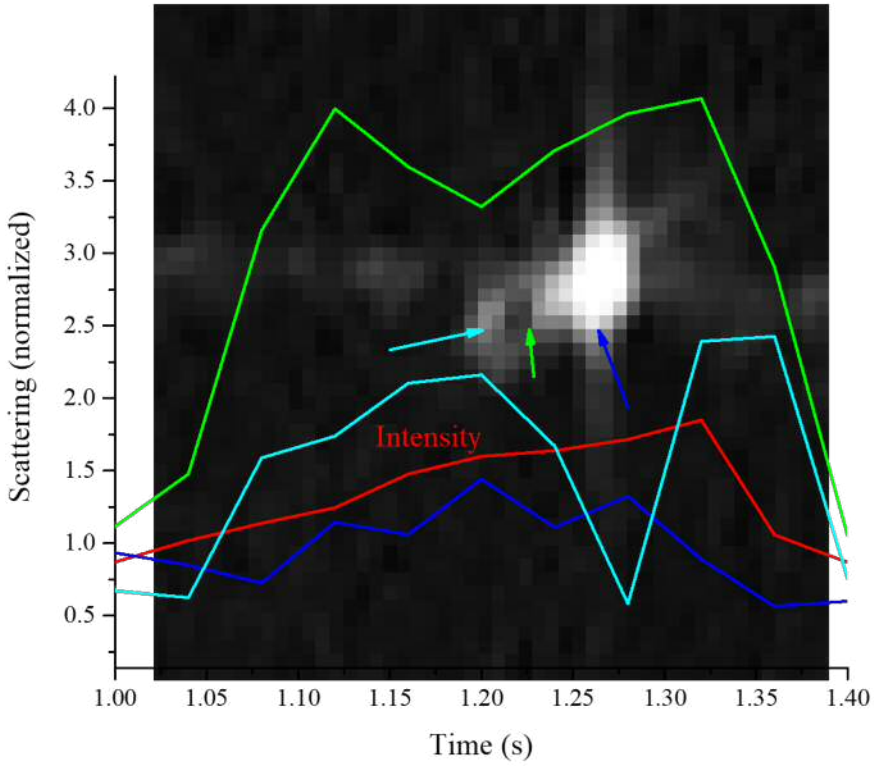

Figure 4.38: Scattering intensity vs. time taken from different positions, as indicated by the arrows. The cyan curve shows a clear resonance, while the red curve shows the change of the linear change of the laser intensity.

variations across the positions, and is not just given by the laser power, represented by the red curve, which is giving the average scattered power integrated over a different region of the image not containing microsphere. Specifically, we can see a strong destructive interference in the cyan curve, which is taken at the far end of the circular feature visible, given by a microsphere coupled to the WG.

This data shows that it is possible to couple microspheres to the WGs in the sensor chip, and that they can support sharp WGM modes, considering that the scan range of the laser in wavelength is around 0.06 nm it total of the frames shown.

4.4.3.3 Scan recording and analysis

The transmission from a WG is captured by the linescan camera, as discussed in Sec. 4.3.3. Exciting a single WG as shown in Fig. 4.31a, the output facet is imaged onto the linescan camera, and aligned to detect the WG output with maximum intensity, i.e. focusing the WG output onto the pixel line. The resulting spatial intensity along the WG array is shown in Fig. 4.40. A sharp peak from the WG output is visible, having a width of 2-3 pixels, as expected from the imaging quality of the linescan lens. Notably, we see a single peak, as the waveplates have been adjusted to exciton only the TM mode, which is helpful for alignment. Changing these waveplates, a second peak can be observed, corresponding to the TE mode, and the relative intensity of both peaks can be adjusted, as shown in Fig. 4.41. The peak splitting of 4 to 5 channels consistent with the design described in Sec. 4.4.1.2. To produce a balanced WG transmission has been tested. For a balanced detection, we adjust the peak areas to be similar. Schematic in Fig. 4.39 shows the optical components used to capture the transmission (see Fig. 4.40 and Fig. 4.41) from the linescan camera when a single WG is coupled with the DFB laser by the focus lens from the camcorder when the DFB laser is coupled with a single WG by the PCX focus lens.

4.4.4 Concluding remarks

In this chapter we have also discussed the optical and fluidic setup developed for biosensor experiments. The setup includes a distributed feedback (DFB) laser, fluidic chamber and camera to detect the WGMs of the MS among other optical components. The biosensor device was positioned inside the fluid chamber by resizing it using a cutting tool. We can align the laser light from the DFB laser to a single WG from the array of WG on the sensor device and observe the output light from the WG in a 2D camera. We can also determine the quality of the WGs by observing the light intensity at the end of the WG in that camera.

We have briefly described the working principle of the software and it's functionalities, developed to acquire experimental data from the line scan camera while scanning the DFB laser.

At the end, we have discussed the characterisation of the sensor chip while it is mounted inside the flow chamber.

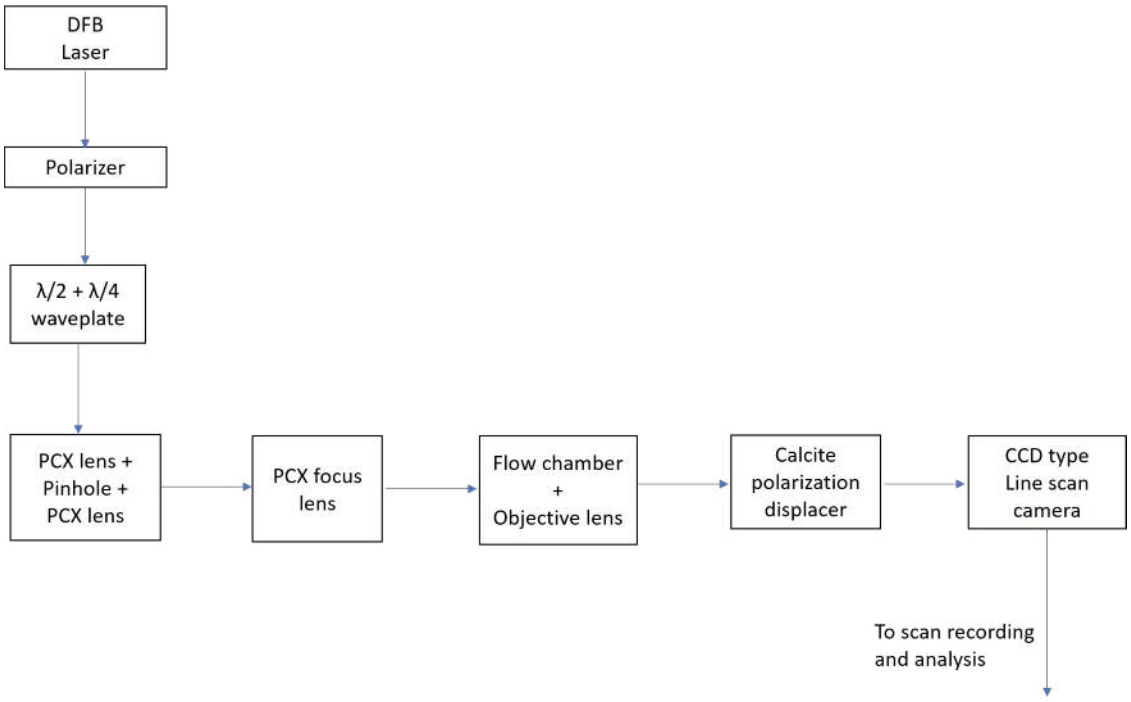

Figure 4.39: Schematic to show the optical components to capture scan recording for analysis. Complete schematic of the optical setup is shown in Fig. 4.2.

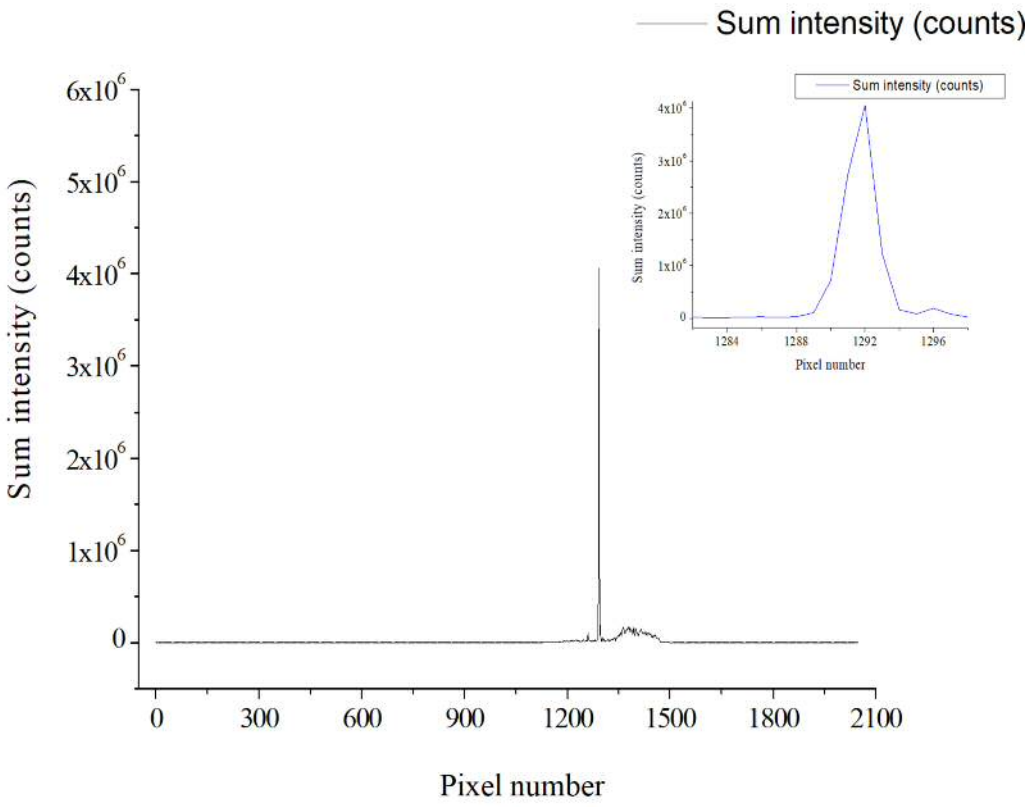

Figure 4.40: Transmission from a WG captured by the linescan camera. Average intensity of the pixels from all readouts (Top), Zoomed at the peak (inset). The peak is the image of the WG to which the laser is coupled.

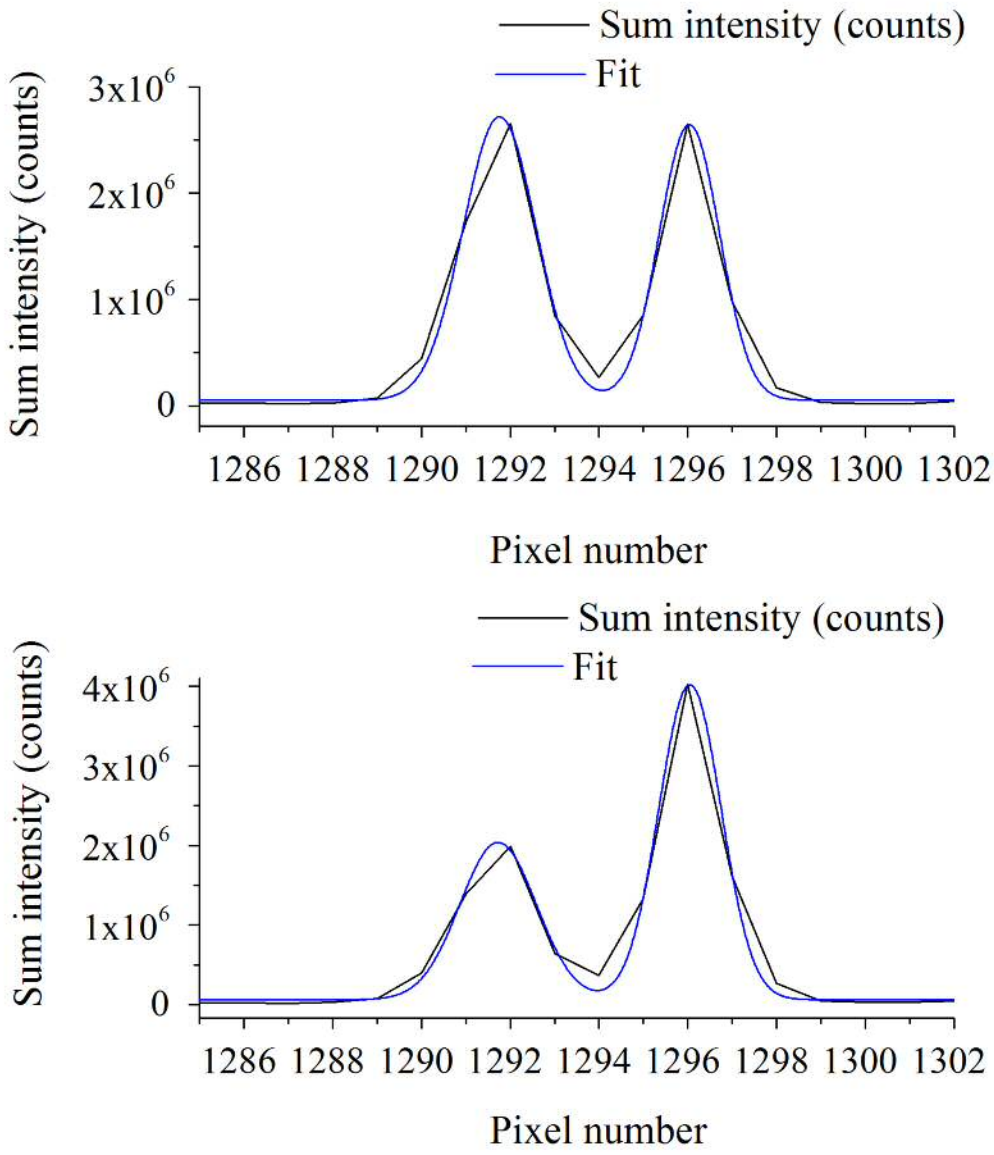

Figure 4.41: TE and TM peak from a WG. The intensity ration can be adjusted by varying the excitation polarisation.

Chapter 5

Towards Biosensing

5.1 Refractive index sensing results

5.1.1 Refractive index of glycerol water mixtures

In order to investigate the capability of the sensor device to detect changes of refractive index, glycerol has been mixed in water as it is infinitely soluble in water [153]. The solution has been prepared as shown in Table 5.1. The refractive index of Glycerol has been determined as follows. The refractive index of Glycerol with respect to wavelength at 25°C has been obtained first from reference [154]. The obtained data is then plotted and fitted by Cauchy's dispersion equation. Cauchy's dispersion equation is an empirical relationship between the refractive index and wavelength of light for a transparent material and can be written as

$$n = A + \frac{B}{\lambda^2} + \frac{C}{\lambda^4} \tag{5.1}$$

where, n is the refractive index at wavelength λ in µm, and A, B and C are the coefficients that can be determined for a material by fitting the equation to measured refractive indices at known wavelengths.

A fit of the Glycerol refractive index at 25°C by Cauchy's dispersion equation is shown in Fig. 5.1, and results in the coefficients $A = 1.45797$, $B = 0.00598$ and $C = -0.00036$. The refractive index of Glycerol solution can then be calculated by Eq. (5.1). The refractive index of Glycerol calculated at 784 nm and at 25°C as 1.4667.

However, data for the refractive index of Glycerol mixed in water is given in reference [155] for a wavelength of 589.3 nm and at a temperature of 20°C. From reference [154] we get the refractive indices of Glycerol at 830 nm as 1.467 for 20 °C, and 1.4659 for 25°C. From these values we can calculate the refractive index of Glycerol for the wavelength of 784 nm and 20°C by assuming that the difference between the refractive index at 20°C and 25°C is the same at 830 nm and 784 nm.

Glycerol	Water	Total Amount	Weight percent (wt%)
0.5 mL	5 mL	5.5 mL	9.09
0.5 mL	10mL	10.5 mL	4.76

Table 5.1: Glycerol solution in water.

Thus the refractive index of Glycerol is, according to Eq. (5.2),1.4678 at 784 nm and 20°C.

$$n_{g,784\text{nm},20°\text{C}} = n_{g,784\text{nm},25°\text{C}} - (n_{g,830\text{nm},25°\text{C}} - n_{g,830\text{nm},20°\text{C}}) \tag{5.2}$$

Cauchy's dispersion constants for water at 20°C are given in reference [154] as $A = 1.32043$, $B = 0.05430$ and $C = -0.00036$. These constants are valid for a wavelength range of (486.1 - 943.0)nm. The refractive index of water at 784 nm and 20°C can be calculated using the Eq. (5.1) as 1.328311. The refractive index of glycerol-water mixtures at 784 nm and 20°C can then be calculated using the known index of mixtures at 598 nm, corrected for the difference to 794 nm of the constituents as follows

$$\begin{aligned} n_{m,784\text{nm},20°\text{C}}(c) =& n_{m,589.3\text{nm},20°\text{C}}(c) + (n_{w,784\text{nm},20°\text{C}} - n_{w,589.3\text{nm},20°\text{C}})(1-c) \\ &+ (n_{g,784\text{nm},20°\text{C}} - n_{g,589.3\text{nm},20°\text{C}})c\,, \end{aligned} \tag{5.3}$$

where c is the weight/weight concentration, $n_{m,784\text{nm},20°\text{C}}(c)$ is the refractive index of glycerol / water mixtures at 784 nm, and $n_{g,589.3\text{nm},20°\text{C}}(c)$ is the refractive index of glycerol/water mixtures from reference [155]. $n_{g,784\text{nm},20°\text{C}}$ is the refractive index of Glycerol at 784 nm and 20°C calculated from Eq. (5.2). $n_{g,589.3\text{nm},20°\text{C}}$ and $n_{w,589.3\text{nm},20°\text{C}}$ are the refractive index of Glycerol and water at 589.3 nm and 20°C, respectively, from [155]. $n_{w,784\text{nm},20°\text{C}}$ is the refractive index of water at 784 nm and 20°C, calculated using Eq. (5.1).

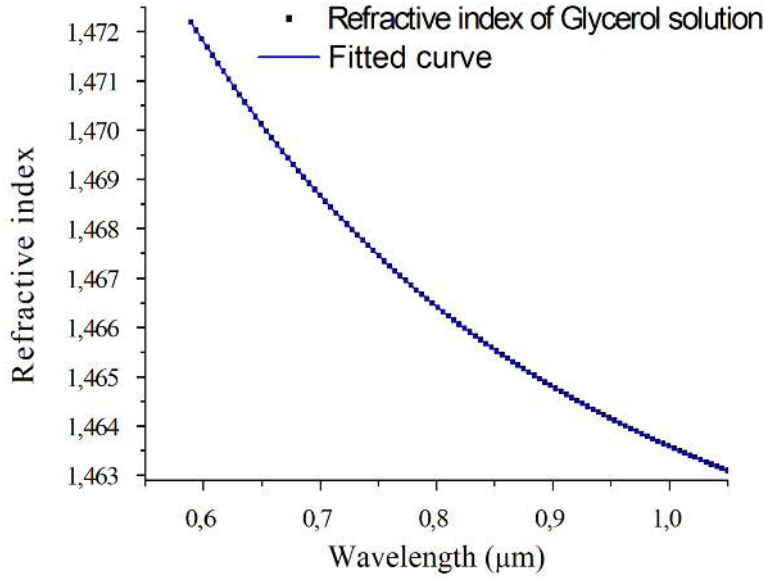

Figure 5.1: Refractive index of Glycerol at 25°C versus light wavelength. Squares show data from reference [117]. The data are fitted by Cauchy's formula Eq. (5.1) to obtain the parameters A, B, C.

5.1.2 Experiment

The fabricated sensor chip has been mounted inside the flow chamber as described in Sec. 4.4.1.1. After mounting (see Fig. 4.4), the laser has been aligned through the optical measurement setup (see Fig. 4.1) as discussed in Sec. 4.4.1.2.

Weight percent (wt%)	RI of Glycerol solution	Difference
0	1.3283	0.0
0.5	1.3288	0.0005
4	1.3328	0.0045
5	1.3340	0.0057
9	1.3387	0.0104
10	1.3399	0.0116

Table 5.2: Refractive index of Glycerol/water mixtures at 20°C and 784 nm for different weight percent (wt%) concentrations, used in the experiments. The difference in RI to pure water is also given, calculated from the RI of water at 20°C and 784 nm of 1.328311.

Glycerol/water mixtures are injected into the flow chamber by using two Hamilton® Gastight® syringes (1700 series, dispensing volume 500 µL), supplied by Sigma-Aldrich®. Each injection transfered 100 µL, which is equal to the volume of the fluid chamber, at a flow rate of about 10 µL/s.

The laser scanning parameters have been controlled by the software. The scanning parameters that we have used during the experiments are shown in Fig. B.3. For these parameters, and the directive coefficient of $\beta = 0.0020245\,\mathrm{nm/mA}$, the laser has been scanned by about 0.08 nm, nominally between 787.1012250 nm and 787.1822050 nm. The laser offset wavelength λ_0 has been more coarsely tuned by changing the temperature of the laser to probe a larger region of wavelengths for resonances, covering a few nm. A peak has been selected and then fitted to one Lorentzian and parameters saved for analysis as described in Sec. 4.3.3. The center wavelength p was used for the subsequent sensograms.

The same WG was used for all the experimental data shown here. Glycerol/water mixtures of different concentrations were sequentially added into the flow chamber. The resulting sensogram changing the mixture from 0% to 5% concentration is shown in Fig. 5.2, and from 5% to 9% in Fig. 5.3 and Fig. 5.4. Sensograms are fitted to find the step height at around injection and eventually to calculate sensitivity. Fit function is given by

$$f(x; a_0, a_1, p, w, s) = a_0 + a_1(x - p) + \frac{s}{2}\mathrm{erf}\left(\frac{x - p}{w}\right) \tag{5.4}$$

where s is the step height, p is the step x position, w is the step width and a_0, a_1 are offset and slope. The error function, erf(x), has the limiting values erf(∞) = 1 and erf($-\infty$) = -1. The sensitivity of the sensor is defined as [156]

$$S = \Delta\lambda/\Delta n \tag{5.5}$$

where, $\Delta\lambda$ is the shift of the sensor resonance in nm and Δn is the change in refractive index solution flowing into the sensor chamber. Sensitivity of the sensor for a change in refractive index (Fig. 5.2) was 0.52 nm/RIU according to equation 5.5 and the refractive index values given in Table 5.2. In other experiments two different concentrations of Glycerol solution were added into the sensor chamber. Resonance positions are shown in Fig. 5.3 and Fig. 5.4. Sensitivities were measured as 0.43 nm/RIU (5% change) and 0.22 nm/RIU (9% change) (see Fig. 5.3) and 0.31

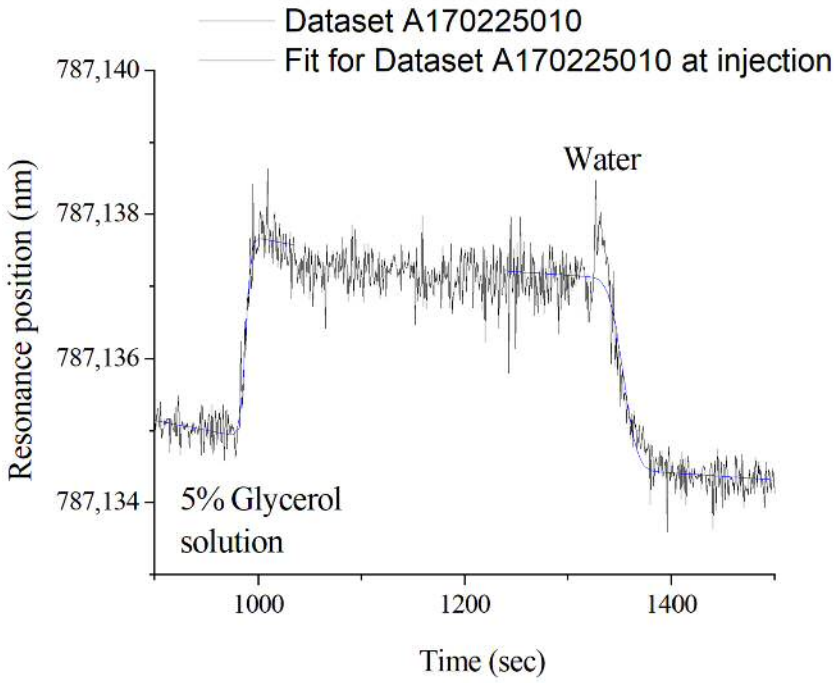

Figure 5.2: Sensogram showing the resonance position over time, when changing the fluid chamber content from 0% to 5% glycerol/water mixtures at a time around $t = 1000\,\mathrm{s}$, and back to 0% around $t = 1350\,\mathrm{s}$. Each spectrum has 2000 points with a ramp time of 400 ms and a line rate of 5000 Hz, providing about 2 spectra, and thus sensogram points, per second. The fits of the steps according to Eq. (5.4) are shown as blue lines, over the time range selected for the fit.

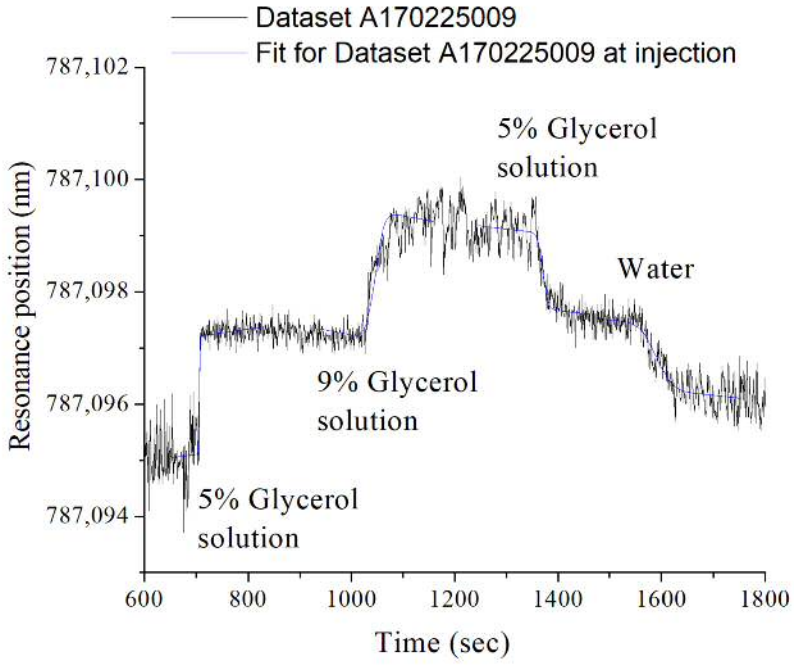

Figure 5.3: As Fig. 5.2, but changing the fluid chamber content from 0% to 5% around a time $t = 280\,\mathrm{s}$, then to 9% around $t = 405\,\mathrm{s}$, then to 5% around $t = 540\,\mathrm{s}$, and to 0% around $t = 625\,\mathrm{s}$.

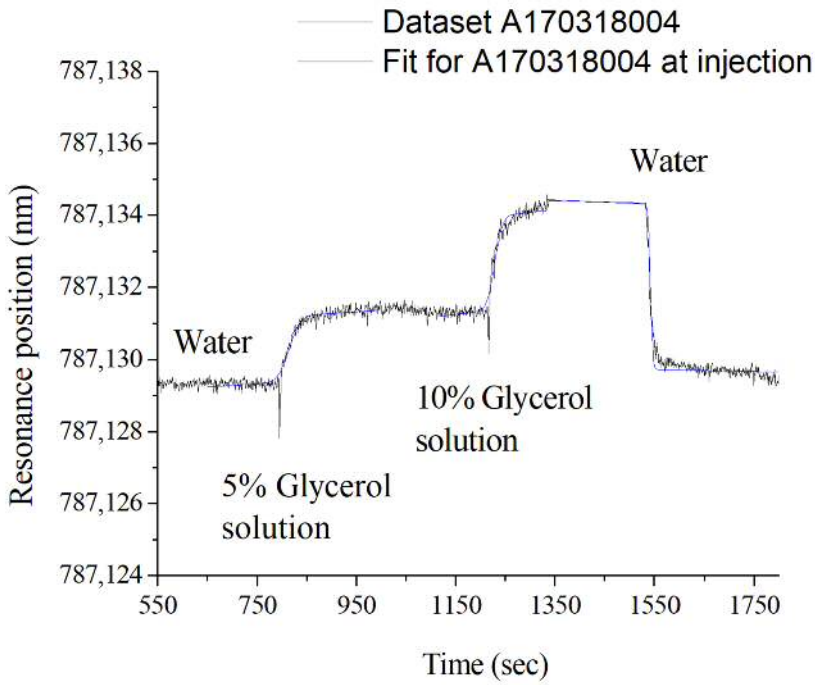

Figure 5.4: As Fig. 5.2, but changing the fluid chamber content from 0% to 5% around $t = 785\,\mathrm{s}$, then to 10% around $t = 1210\,\mathrm{s}$, and then back to 0% around $t = 1535\,\mathrm{s}$.

nm/RIU (5% change) and 0.22 nm/RIU (10% change) (see Fig. 5.4).

The Q factor of the WGM mode that was measured for these experiments was around 1×10^5, which is lower compare to reported Q factor around 1×10^6 for WGMs of comparable PS microsphere in [86]. A fitted resonance curve is shown in Fig. 5.5. The reduced value of the Q factor can be due to the distance between the microspheres and the WGs, or surface roughness and deformation of the microspheres as discussed in Sec. 2.3.4.3 and Sec. 2.4.1.2.

5.2 Future Improvement

There are improvements that can be done on both setup and sample. In this section these improvements will be proposed and discussed briefly.

5.2.1 Input coupling

The initial setup used a cylindrical lens to focus the excitation into a line, enabling to excite multiple WGs, providing the option of multiplex detection from multiple WGs. The cylindrical lens should be focusing the collimated beam from the spatial filter system as discussed in Sec. 4.4.1.2 onto the end facet of an array of WGs. The cylindrical lens is a 80 mm focal length, B-coated BK7 plano-convex Lens supplied by Thorlabs [150]. The cylindrical lens mount, shown in Fig. 5.7 (where the lens is focussing into a vertical line) is a kinematic mirror mount which can be adjusted by hand with a micrometer screw to move the lens and thus the focus sideways while two-adjusters are used for tip and tilt control. The adjusters allow to align the focal

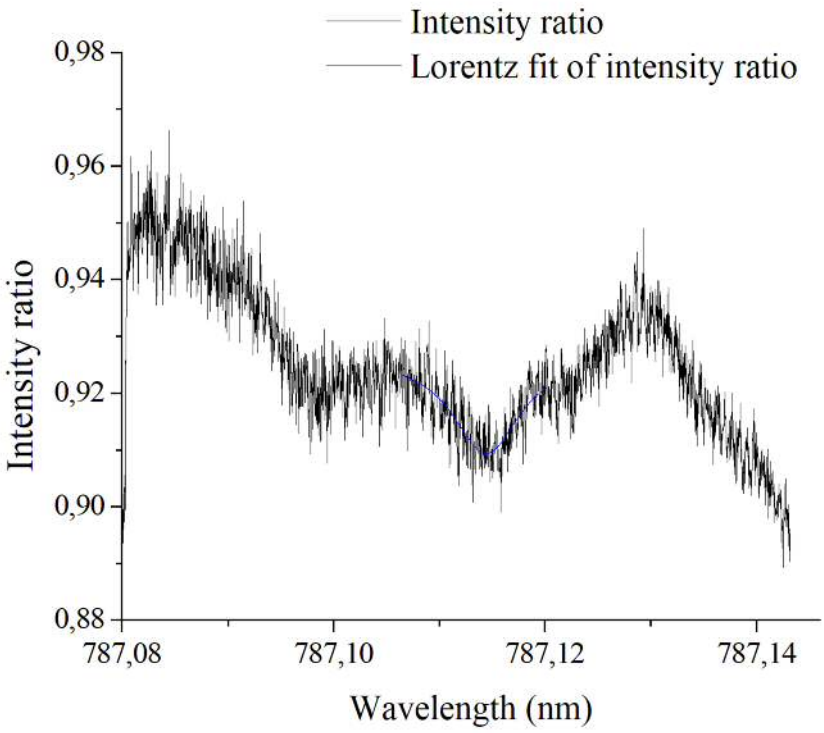

Figure 5.5: Fitted resonance curve.

line onto the WG facet. Components are manufactured and supplied by Thorlabs [150]. The micrometer stage is from microcontrole [157].

However, using this excitation, strong background light was present as shown in 5.8, hindering the selection of light from the WG. This is due to the low coupling efficiency into the WG relative to the total excitation light. In the original design a grating of stripe apertures were planned, having openings only at the WGs, to block the light not overlapping with the WG ends. This apertures would be fabricated on the glass window already present to provide a flat inteface, made of metal such as chromium or gold. The width of the stripes should be the gap between two WG, i.e., 46 µm. The fabrication of such a slit aperture array has been attempted using bi-layer lift-off resist process, but was unsuccessful and would need optimisation. The problem was that gold layer did not lift off homogeneously as shown in Fig. 5.6.

Another way to suppress the background light and at the same time increasing the coupling efficiency to the WGs is by mounting an array of micro lenses to focus light on individual WGs. The pitch of the microlens array has to match the pitch of the WGs, i.e., 50 µm). This would also lead to a more efficient use of the excitation light.

Another coupling approach considered was the use of grating couplers in the waveguides, changing the excitation to a direction normal to the chip. Its realisation was not attempted due to lack of time.

5.2.2 Thickness of MY-133 layer

In this project we kept both the cladding layer of the WG and the attachment layer fixed around 700±50 nm and 200±20 nm respectively. However, Q factor of the

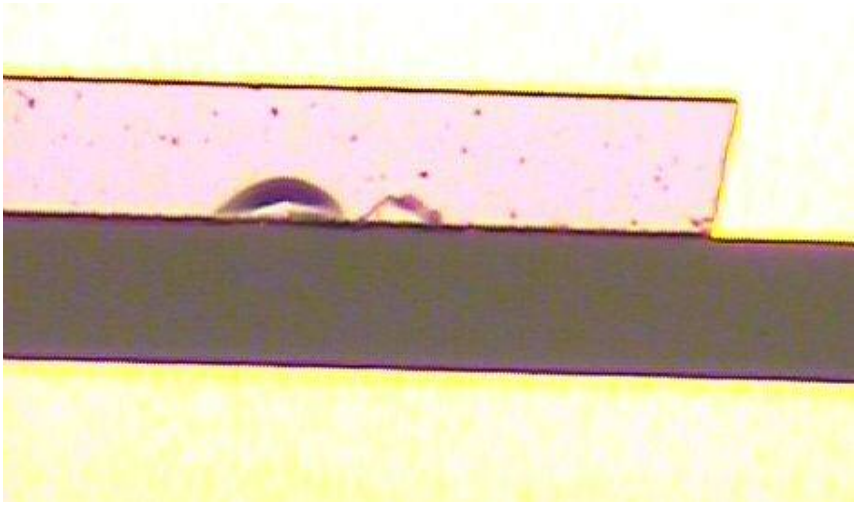

Figure 5.6: Reflection optical image. Bi-layer lift-off resist process in an attempt to fabricate a slit aperture array to reduce background light. Gold did not lift-off homogeneously. Dimension of the transmission image is 290 μm×170 μm.

Figure 5.7: Cylindrical lens mount for multiple WG excitation.

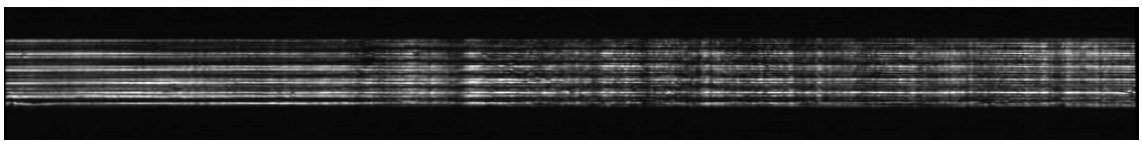

Figure 5.8: Image of the output facet of the chip with the light coupled in using the cylindrical lens. Transmitted light from the WGs is not visible amongst the background light through the substrate.

whispering gallery modes changes with distance between the microsphere and the source, as discussed in Sec. 2.4.1.2, and therefore the MY-133 height on SU-8 should be optimised for critical coupling. This has not been studied in detail due to lack of time.

5.2.3 Surface roughness and deformation of the microspheres

As the Q of the WGMs is dependent on surface roughness as light scatters more from rough microsphere surface and ellipticity produced by the functionalisation process of the microspheres as discussed in Sec. 2.3.4.3 we should characterise the microspheres to find suitable ones to use in the sample.

5.3 Microsphere functionalisation strategies

The biosensor recognition elements are usually immobilised on a solid support inside the biosensor. In case of an optical fibre, waveguide (WG) or microsphere based biosensors they act as a solid support for the biosensor recognition element. For proper sensing the analytes, the solid support must be functionalised properly. In this section we will discuss briefly possible the surface modification of polystyrene microspheres for both non-specific and specific sensing.

Protein immobilisation can be done either directly on plain PS microspheres, or by applying surface chemistries on the microspheres. Plain PS microspheres are hydrophobic and therefore the mechanism for adsorption is based primarily on attractions between the hydrophobic portions of the adsorbed protein and the polymeric surface of the microspheres [158]. This is the simplest procedure as no surface modification is required. This adsorption method has been used in many applications such as ELISA, antibody arrays and immuno-sensors [159].

Covalent coupling involves surface chemistry. A variety of surface modifications are applied to microspheres to produce a reactive surface i.e., Carboxyl or Amino-modified microspheres. By using a cross linking reagent such as Glutaraldehyde ($C_5H_8O_2$) [160], Protein A (for non-specific sensing of any antibody) or secondary antibody such as Rabbit anti-Mouse (for specific sensing of primary antibody hosted in mouse) can be immobilised on a amino modified microsphere surface [161]. The chemical structure of glutaraldehyde is shown below:

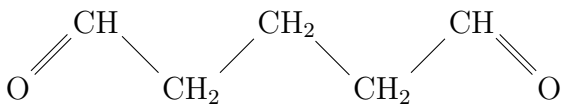

Glutaraldehyde

In a covalent coupling method the polymer surface must be functionalised by a chemical group in such a way that it becomes reactive towards the functional groups present in proteins. The simplest technique for immobilisation involves the use of chemical groups that react with primary amines ($-NH_2$) in proteins. Therefore, the first step in covalent protein immobilisation is to activate the functional groups such as carboxyl ($-COOH$), amine ($-NH_2$), hydroxyl ($-OH$) or N-hydroxysuccinimide esters ($C_4H_5NO_3$) on the surface of PS microspheres. The second step is to covalently couple these surface modified microspheres to amino groups present in the protein

with or without a cross linking reagent. APTES ($C_9H_{23}NO_3Si$) can be used to produce a surface terminated with amino groups. Amine coupling of the protein for immobilisation is used in the majority of reports [82]. EDC ($C_8H_{17}N_3HCl$) can also be used to activate carboxyl groups for direct conjugation to primary amines in the protein.

Glutaraldehyde is usually used as a cross-linker for amine activated PS spheres for immobilisation by the reductive amination method [162]. Glutaraldehyde is a bi-functional linker molecule with two identical functional groups which target primary amines in proteins. Glutaraldehyde is more stable than carbodiimide used as cross-linker for carboxyl activated spheres. Coupling with glutaraldehyde results in the proteins being bound approximately 2 nm away from the surface of the microspheres compared to approximately 0.5 nm in the case of carboxylate microspheres coupled using carbodiimide [163]. Thus glutaraldehyde acts as a spacer to extend the distance between the immobilised proteins and the microsphere surface. This offers some advantages over direct attachment of proteins on the surface. The direct attachment of a protein to a surface without a spacer can cause a steric constraint of the proteins reactivity or interaction capability compared to the protein in solution. Moreover, multiple direct contacts with the surface can induce denaturation or partial denaturation and thus a change in the protein binding properties. By introducing a spacer between the protein and the reactive group on the surface, these effects can be reduced. Surface functionalisation with a spacer can allow for attachment of potentially any desired reactive group. Larger spacers also allow more antibodies to bind on the surface, thus increasing the sensitivity of the sensor [164].

For specific detection we have bought functionalised (Rabbit anti-Goat IgG - secondary antibody) PS microspheres from Micromod ®. Anti-Goat secondary antibodies has specificity for goat immunoglobulins therefore we have bought conjugated (Alexa Fluor® 488) antibody (Goat IgG) to attach them on the functionalised PS microspheres. One has to be careful about the primary and secondary antibodies as the secondary antibody has to be raised in host species other than the host of the primary antibodies. For example, if anti-rabbit secondary antibody is raised in rabbit then primary antibody must be raised in a host species other than the rabbit.

Chapter 6

Summary

Whispering gallery mode (WGM) sensors have attracted a significant level of interest recently due to their high level of sensitivity in the field of life sciences as biosensors. However, integrated WGM sensor devices are still in their infancy. In this work, we introduced a sensor device structure which is a step closer to commercial exploitation and mass production of monolithic WGM sensor capable of multiplex detection.

The project started with the aim to design and then fabricate a sensor device which can utilize the advantages of high Q factor of the WGM to detect biomolecules. The sensing device would be able to detect small concentrations of biomolecules and would support multiplex detection.

In this project we have designed and fabricated the sensor device successfully. The design and fabrication of the sensor device consisted of fabricating an array of planar single mode SU-8 WGs on glass substrate, developing a method to spin coat and cure MY-133, which is a low RI material, matching the RI of water, and then immobilising the microspheres on top of the WGs.

The first task in designing and fabricating the array of WGs was to select the materials and estimate the dimension of the WGs which would serve the purpose of the project. Therefore, we needed to find the appropriate materials, i.e., for the substrate, the core, and the cladding layer of the WG and the microspheres. The array of planar WGs were fabricated on a glass cover slip serving as cost-effective substrate, and allowing to observe and analyse the light coupling into the WGs and microspheres from the substrate side when the sample would be submerged inside the fluid chamber filled with water in our measurement setup. Since the sensor device will be submerged into the water filled fluid chamber, we researched materials of RI close to that of water at the operating wavelength of the DFB laser (784 nm) to be used as the cladding material of the planar WGs.

We have researched materials which have a RI close to water at 784 nm. However many of these materials could only be cured by heating at high temperature. Such a temperature curing procedure was used previously in our group to cure the cladding layer on top the of SU-8 WGs and then an attachment layer to glue the microspheres. This temperature curing procedure involved temperatures above 100°C, which is not suitable for microspheres functionalised with biomolecules such as antibodies. A few alternative materials were investigated to address this issue. After going through extensive safety protocols for processing in the clean room MY-133, a low RI material was chosen for processing.

Apart from the safety issue, we choose MY-133 of RI 1.33 at 784 nm because it could be spin coated and then cured by UV light. The UV curing method provides

many advantages over high temperature curing, for example, the UV curing method is fast, and a low temperature method. Curing by UV light allows to work with biomolecules (antibodies) already functionalised on the microspheres. The principle of light curable materials was discussed in Sec. 2.6. We have developed a standard operating protocol to deposit MY-133 on SU-8 WGs given in Appendix B.2.

We choose SU-8 as the core material because it is highly transparent for the laser wavelength, and it has a high RI of about 1.6, which is higher than both the glass substrate and the cladding layer, allowing for light to propagate by total internal reflection.

After choosing the appropriate WG materials we estimated the WG dimension, discussed in Chap. 3. The thickness of the SU-8 layer for single mode propagation was estimated between 450 to 1000 nm for a 3 μm wide WG. We estimated that the thickness of the MY-133 on top of the WGs should be 550±50 nm for optimal coupling between the WGs and the microspheres.

The next challenging part in this project that we faced after choosing the material and estimating the dimension of the WG was to choose the correct type of SU-8 to deposit the estimated target thickness of about 900 nm that can be reproducible. We tried first with SU-8 2000.5 as this type of SU-8 is usually used to deposit a typical layer of thickness less than 1 μm. However it was hard to reproduce the target thickness. We therefore used SU-8 2002, which is usually used to deposit thicker layer of SU-8. We experimented with SU-8 2002 and found out that it needed to be diluted. We diluted SU-8 2002 with SU-8 2000.5 and found that a ratio of SU-8 to 2000.5 (2:1) is suitable for a reproducible SU-8 WGs of 900 nm thickness.

The second task in fabricating the planar WGs was to spin coat the diluted MY-133 and then cure the MY-133 layer. MY-133 can be purchased in the form of a gel and needs to be diluted by a fluorinated solvent in which MY-133 is completely soluble. We chose HFE-7500 for its high boiling point (128°C) compared to alternatives. The diluted MY-133 was spin coated to deposit an approximately 750 nm thick layer. We first tried to cure the deposited MY-133 layer by keeping the sample submerged under water while exposing to UV light. However, this process produced a tacky surface, so we had to develop a curing unit allowing to keep the sample under inert gas during exposure. The second generation of this curing unit can cure a MY-133 layer within one minute in inert gas such as nitrogen.

Once the WGs were fabricated we characterised them. Usually DekTak can be used to measure the thickness of the WGs but in this project we have developed an alternative method to measure the height of the WGs optically by using DIC microscopy. It is a non-destructive method of characterising transparent material. We have verified the DIC technique using DekTak measurements on the same samples. We have also used DIC to determine the RI of the cured SU-8 layer.

The third task in this project was to glue the PS microspheres on the WGs. For this we have spin-coated a layer of about 150 nm thickness of MY-133. Microspheres were then drop casted in water onto this layer, and they adhere to the layer, making cointact with the cladding layer underneath. We characterised the PS microspheres by first estimating the RI of the PS microspheres using the DIC technique. Then we wanted to determine the footprint of the microspheres in the MY-133 gluing layer. In this project we have used PS microspheres of 30 μm diameter, which gives the submerged height of the microspheres in the MY-133 layer about 400 nm. However, the DIC microscopy technique resulted in a significantly lower height - a point which is open for future investigation.

The next task was to cleave the sample so that it can be fitted within the fluid chamber. We have faced a set of issues, for example, when we were cleaving the samples to define facets of the WGs, the SU-8 layer was peeling off from the facet. In order to address this issue we have designed a cutting tool. The use of the cutting tool improved the peeling issue. Fig. B.1 shows sample where the SU-8 layer were peeled off when using a scriber to cleave the sample for opening the facet, and the improved result obtained using the cutting tool.

We have developed an optical setup for biosensor experiments. The setup includes a distributed feedback (DFB) laser, a fluidic chamber, and a linescan camera to detect the WGMs of the MS among other optical components. The biosensor device was positioned inside the fluid chamber by resizing it using the cutting tool, retaining the majority of WGs intact to allow light travelling from WG input to output. We can align the laser light from the DFB laser to a single WG from the array of WG on the sensor device and observe the output light from the WG in a 2D camera. We can also determine the quality of the WGs by observing the light intensity at the end of the WG in that camera.

We have further developed the experimental data acquisition software to generate and control trigger signals for the laser and camera in optical measurement setup. The software was also used for optical alignment and to save experimental data for future analysis. We have shown that the laser light couples to the WGs and analysed the blinking microspheres excited by the laser light. We have also analysed the scan recordings from the linescan camera. Finally, we presented the sensitivity result from our experiments in Chap. 5.

This work is an important first step towards an integrated biosensor based on WGMs of microsphere resonators. We have successfully fabricated an on chip sensor device and coupled the device with the laser light. We have also successfully excited the microspheres. However, the Q-factor that we obtained from our experiments is not as high as we expected. We have made suggestions to improve the Q factor discussed in Chap. 5. In order to be able to couple an array of WGs to excite many microspheres for multiple detection one should use the originally planned cylindrical lens in the setup as shown in Fig. 4.1, combined with a micro-lens array. Such an array could be fabricated by 3D laser writing with a Nanoscribe tool now available in the department.

We have fabricated a sensor device with non-functionalised microspheres. Thus this device can only be used for non specific sensing. Time did not allow us to fabricate a sensor device with functionalised microspheres but for specific sensing one needs functionalised microspheres glued on the sensor device. We have bought functionalised PS microspheres and discussed briefly about specific sensing in Chap. 5 as well. Importantly, the design and fabrication of the device was undertaken accommodating the use of batch-functionalised microspheres, so that once sensing with high-Q modes is achieved, introducing functionalised beads should not pose additional technical issues. Thus the next step would be to fabricate a sensor device with functionalised microspheres.

Appendices

Appendix A

A.1 SU-8 developer: EC Solvent

Properties	Value
Component	Ethyl lactate
CAS no.	97-64-3
pH	≈7
Water solubility	Completely soluble
Boiling point	153°C
Flash point	48°C

Table A.1: Specifications of the EC solvent for SU-8 development [165].

A.2 Parameter for qDIC application

Entity	Value
Image size	3168 × 4752
Polarizer angle and the shear vector direction	45°
Shear vector magnitude	650 nm
Pixel size for 20x objective	233 nm
Mean wavelength	550 nm
Signal to noise ratio	1000
Takes	1

Table A.2: Software parameters used in the qDIC program for quantitative DIC analysis.

A.3 Technical specification of Dektak^3

Parameter	Value	Unit
Radius of diamond stylus	12.5	µm
Stage diameter	12.7	cm
Scan Length Range	50 µm to 50mm	-
Scan Speed Ranges	Low, Medium, High	-
Scan Time Range	3-50	s
Vertical measurement range	20 to 65000	nm
Software Leveling	Two-point programmable or cursor leveling	-
Stage Leveling	Manual	-
Maximum Sample Weight	0.5	kg
Warm-up time	15	min
Sample Illumination	Variable intensity white light; IR and UV blocked	-

Table A.3: Technical specifications of the Dektak^3 stylus profilometer [136].

A.4 Solvents for MY-133

Solvent	Relative Volatility (BA=1)	Boiling point (°C)	Solubility
HFE-7100	>6	60	Full
HFE-7500	>6	128	Full
Acetone	6	56	>15
Butyl acetate (BA)	1	124	>25
Methyl amyl ketone	0.34	150	>25-30
PMA(propyleneglycol methyl ether acetate)	0.34	145	>25
Cyclohexanone	0.30	155	>20
Diisobutyl ketone DIBK	0.17	163-176	25-30
Isophorone	0.02	215	>40

Table A.4: Solubility of MY-133 in different solvents [114].

A.5 Technical specification of HFE-7500

Properties	Value	Unit
Boiling point	129	°C
Molecular weight	414	-
Water solubility	< 0.004	ppm
Dielectric constant	5.8	-
Viscosity	0.8	mm^2/s (at 25°C)
Density	1.63	g/mL (at 20°C)
Flash point	No Flash Point	-

Table A.5: Technical specification of HFE-7500 [124].

A.6 Technical specification of Bivar LED UV5TZ-390-15

Properties	Value	Unit
Forward current (max)	20	mA
Forward voltage (max)	3.6	V
Peak wavelength	390	nm
Emitting power (min)	10	mW
Viewing angle	15	°

Table A.6: Technical specification of UV5TZ-390-15 LED [126].

A.7 Technical specification of UV LED LZ1-00UV00

Properties	Value	Unit
DC Forward Current	700	mA
Radiant Flux	640-800	mW
Forward Voltage	3.5	V
Peak Wavelength	365	nm
Viewing Angle	70	°

Table A.7: Technical specification of UV LED LZ1-00UV00 [129]. Typical values.

A.8 Technical specification of Hamamatsu S6775 Si PIN photodiode

Properties	Value	Unit
Effective active area	26.4	mm^2
Spectral wavelength range	320-1100	nm
Photo sensitivity at 390 nm	0.184	A/W
Photo sensitivity at 365 nm	0.172	A/W

Table A.8: Technical specifications of Hamamatsu Si PIN photodiodes [127].

A.9 Technical specification of diode laser

Properties	Value	Unit
Optical output power	5	mW CW
Visible light output	635	nm
Maximum operating current	25	mA
Maximum operating temperature	50	°

Table A.9: Technical specification of the diode laser used [150].

Appendix B

B.1 Standard operating procedure of SU-8 WG fabrication

Process	Description	Recipe
Cleaning	Removes residues	Acetone → Isopropanol → Methanol
Pre-heating	Improves adhesion	at 180°C for 5 min on a hotplate
Spin Coating	Target 900±20 nm	4000 rpm, 3000 rpm/s for 45 s
Soft Bake	Evaporates solvent	at 95°C for 3 min
Expose	Karl Suss mask aligner	1 s, intensity 55 mW/cm^2
Post Bake	Cross-links the exposed SU-8	on a hotplate at 95°C for 3 min
Develop	Dissolves unexposed SU-8	in Microposit for 1 min
Rinse	Cleans the samples	in Isopropanol for 1 min
Hard Bake	Removes any remaining solvent	on a hotplate at 180°C for 5 min

Table B.1: SOP of SU-8 2002 diluted with SU-8 2000.5 (2:1).

B.2 Standard operating procedure of MY-133 polymer coating and curing

Process	Description	Recipe
Solution (cladding)	2 mL resin and 4 mL solvent	MY133:HFE-7500::1:2
Solution (attachment)	2 mL resin and 6 mL solvent	MY133:HFE-7500::1:3
Clean the coverslip	In order to improve adhesion	Acetone, Methanol and Isopropanol
Spin coating (cladding)	Target 700±50 nm	7000 rpm, 3000 rpm/s 45 s
Spin coating (attachment)	Target 200±20 nm	8000 rpm, 2000 rpm/s ,45 s
UV Curing (cladding)	Exposure unit	5 min in N_2 chamber
UV Curing (attachment)	Exposure unit	5 min in N_2 chamber
Baking (cladding)	On a hotplate to remove solvent	10 min at 150°C
Baking (attachment)	On a hotplate to remove solvent	10 min at 40°C

Table B.2: SOP to fabricate MY-133 layers.

B.3 Components of the optical measurement setup

Optical components used in the measurement setup and their purpose is listed here in brief.

Component	Purpose
DFB Laser System	Provides the source of excitation for the WGs and allows to sweep the laser wavelength. The output power is up to 100 mW at 25°C. The laser system is temperature (110 µeV/K) and current (4 µeV/mA) tunable. The system is distributed by Laser 2000 [140]. The diode of the system is supplied by AMS technology [141]. Full technical specification is shown in Appendix C.2.
Neutral density filter	Attenuates light from the laser. Two anti reflection (AR) coated (MgF_2 optimized at 600nm) filters diameter of 1 " and optical density (od) of 0.5 and 1.0 have been used in the setup. These filters are supplied by Axicon [149].
Wave plates	Combination of a half and a quarter wave plate after the DFB laser to adjust amplitude and phase of TE and TM mode excitation. A quarter wave plate in front of the line scan camera to select the detection type i.e., amplitude or interference [86]. Waveplates in setup are shown in Fig. 4.25 and 4.26. These wave plates are supplied by Casix [166].
Planoconvex lenses	Two planoconvex (PCX) lenses of 40 mm and 150 mm focal length supplied by Casix [151], and a pinhole of 20 µm aperture diameter, supplied by by Thorlabs [150] are used to produce collimated beam. A third PCX lens of 60 mm focal length, achromatic doublet PCX Lens, supplied by Thorlabs [150] focuses the collimated beam onto the end facet of a single wave guide. A cylindrical lens was used initially to focus the collimated light on the WG array. However, guided light was impossible to image on the CCD camera due to the presence of strong background light. Therefore, the cylindrical lens was replaced by this spherical lens.
Flow chamber	Holds the sample in the optical path. Its inlets allow to inject the fluid to interact with the sample. Flow chamber is briefly discussed in Sec. 4.3.

Table B.3: Optical components used in the sensing setup.

Component	Purpose
Pentax lens	F-mounted line scan lens of focal length 50 mm images the wave guide array onto the line-scan camera with an magnification of 1:3. This lens was supplied by Best Scientific [167].
Polarization displacer	Displaces one polarization by 60 µm along the axis of the camera. This is about 4 pixels (14 µm/pixel) and about half the pitch of the WGs with 1:3 magnification. It is made of Calcite. This polarization displacer is supplied by Altechna [152]. Technical specification and polarization direction is shown in Appendix C.4.
Linescan camera	Detects multiple wave guides in parallel while scanning the laser. It has a Gigabit Ethernet interface to avoid a frame grabber and allows for larger distances to the PC. This CCD type linescan camera is supplied by Alrad Imaging [142]. Technical specification is shown in Appendix C.5.
CMOS Camera	An additional camera in the setup to image WG transmission for optical alignment. This was supplied by EHD imaging GmbH [144].A mirror is used to direct the transmitted light on this camera as it is not mounted on direct light path. It is a digital, black and white, 1280×1024 pixel camera with a USB 2.0 interface.

Table B.4: Optical components in sensing setup, continued.

Component	Purpose
PCX lens mount	3 axis stage where position of the lens is controlled by micrometer screw. Components are manufactured and supplied by Thorlabs [150].
Flow chamber mount	The flow chamber is mounted on a Pedestal Pillar Post of height 75 mm manufactured by Thorlabs [150].
Linescan camera mount	Kinematic mirror mount is adjusted for tip and tilt control with an angular range of ± 4° , manufactured and supplied by Thorlabs [150]. In addition to this it has also a linear translation.

Table B.5: Different optical mounts in the setup.

B.4 Protocol for cleaving the samples

The protocol is described below:

1. Use ruler and vernier calipers to mark points on sample mount for guide alignment using fine liner pen. Use the edge of the recess and the edge of mount for reference.
2. Assemble the tool. Loosen the screws holding the guides in place.
3. Insert the scribe into the scriber holder and tighten the holding screw until it is just held in place.
4. Place the holder on a guide and hold firmly in place, whilst adjusting the scribe position such that the tip just touches the metal of the sample mount outside of the recess.
5. Use the alignment points and scribe to place the guide(s) in position and screw into place. Clean the scribe tip and recess using ethanol.
6. Remove the guide part for access and place the sample upside down in the recess, taking extreme care not to damage or drop the sample. Replace the guide part.
7. Hold the scribe mount firmly (flush against the guide) and score sample in one swift motion. Rotate guide part and repeat to score all four edges.
8. Remove the guide part and run a drop of purified water or ethanol along the score lines using a syringe. This aids in cleaving the sample cleanly.
9. Carefully remove the sample.

Images of samples cleaved by the cutting tool is shown in Fig. B.1.

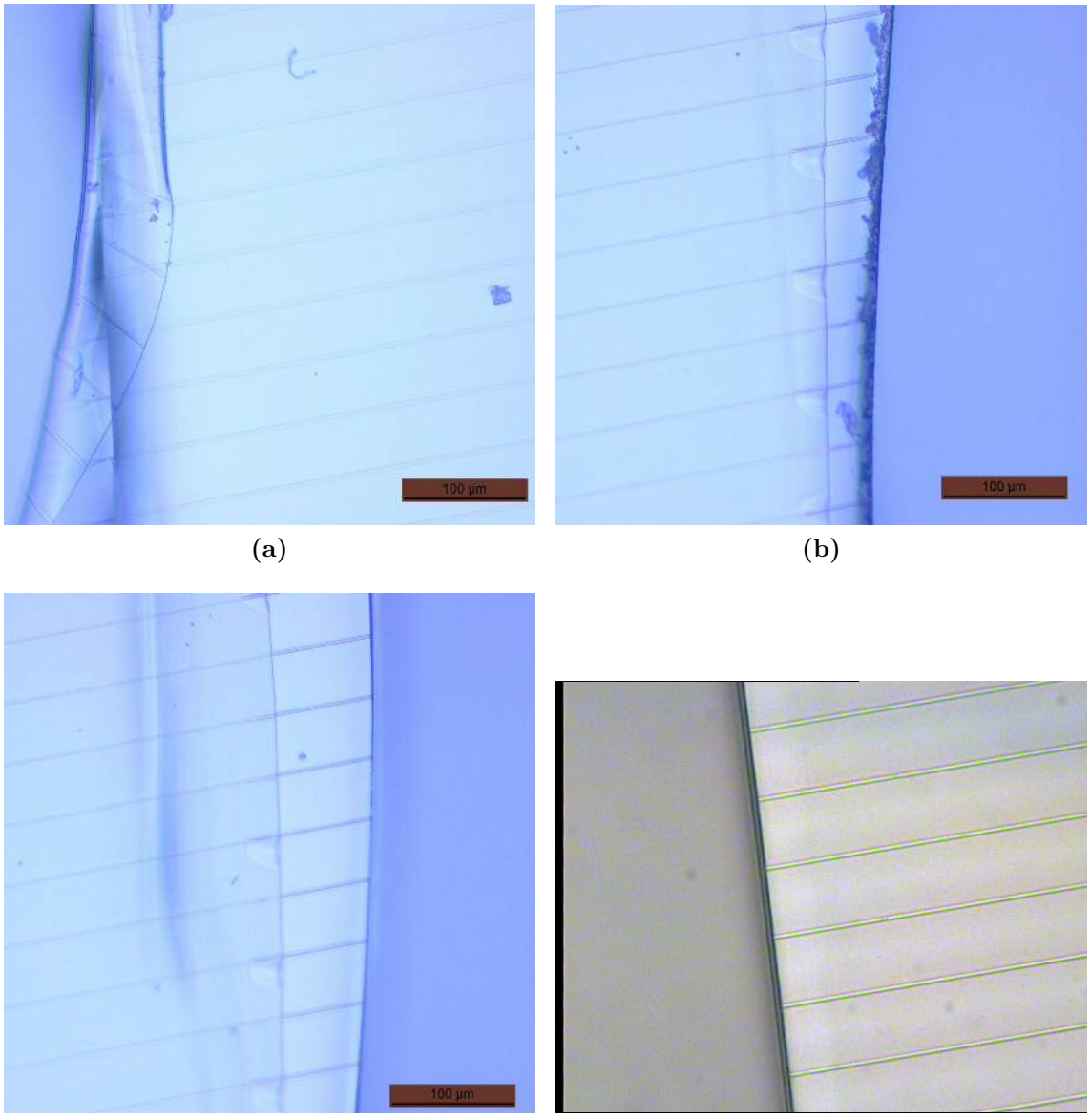

(a) **(b)**

(c) **(d)**

Figure B.1: Transmission images of chips after cleaving. Images (a)-(c) shows issues in cleaving, (a) MY-133 remains in the sample, (b) Rough WG facet where WGs are terminated before reaching the edge, (c) MY-133 layer has peeled off, (d) A good cleaving region. Dimension of image (d) is 390 µm × 315 µm.

B.5 Software panel

We have improved the existing biosensing software further to acquire experimental data from the CCD type line scan camera while scanning the DFB laser in an experiment. The software panels are shown here.

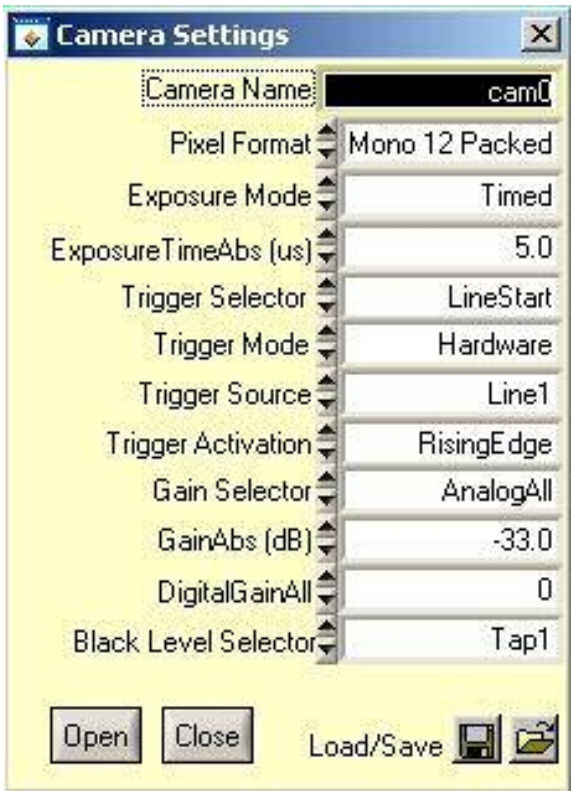

Figure B.2: Camera settings panel in the software.

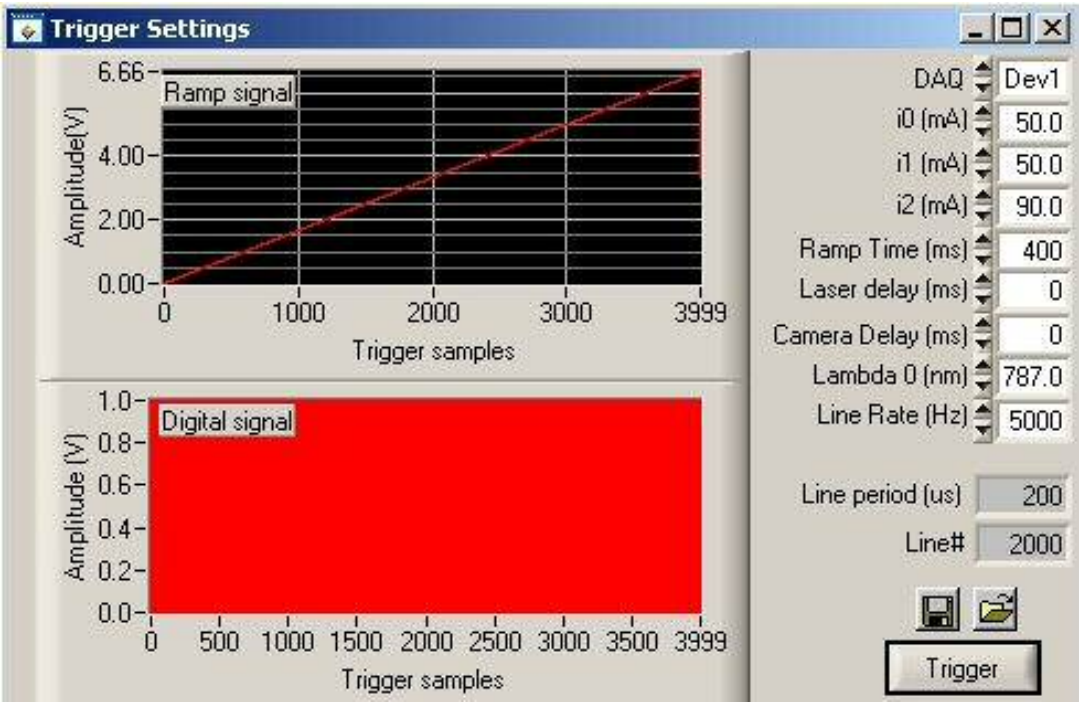

Figure B.3: Trigger settings panel in the software. Typical values used in the experiments are shown in the panel.

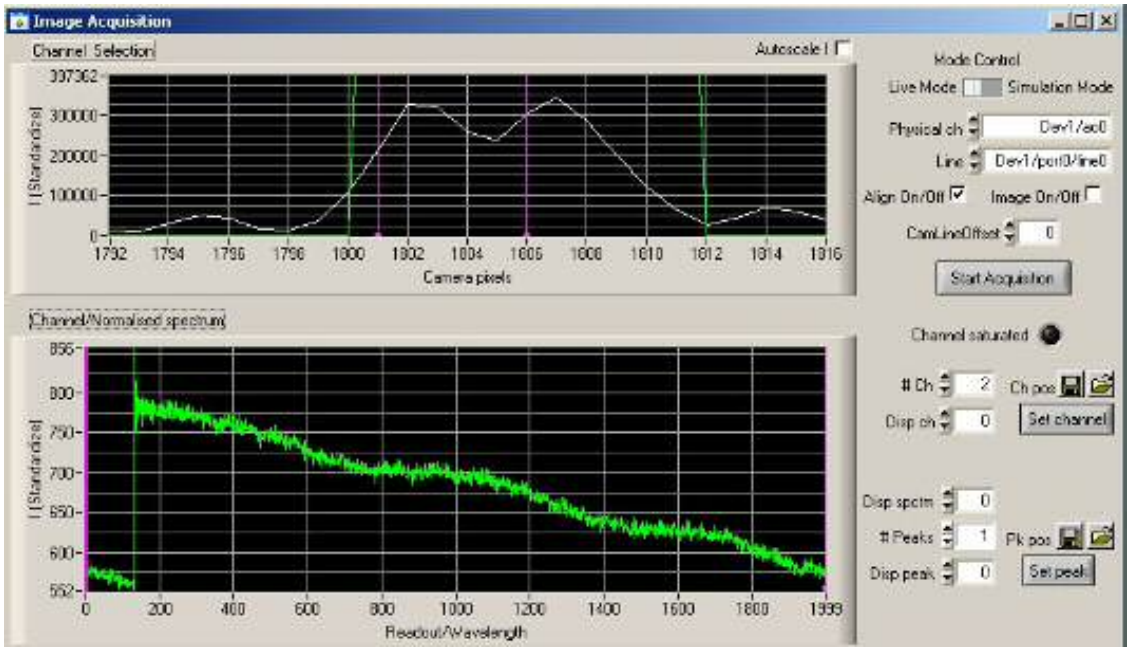

Figure B.4: Image acquisition panel to define channels, plot spectrum and define peaks for fitting. The channel is defined in the top (purple color). Spectrum of the selected channel is shown at the bottom.

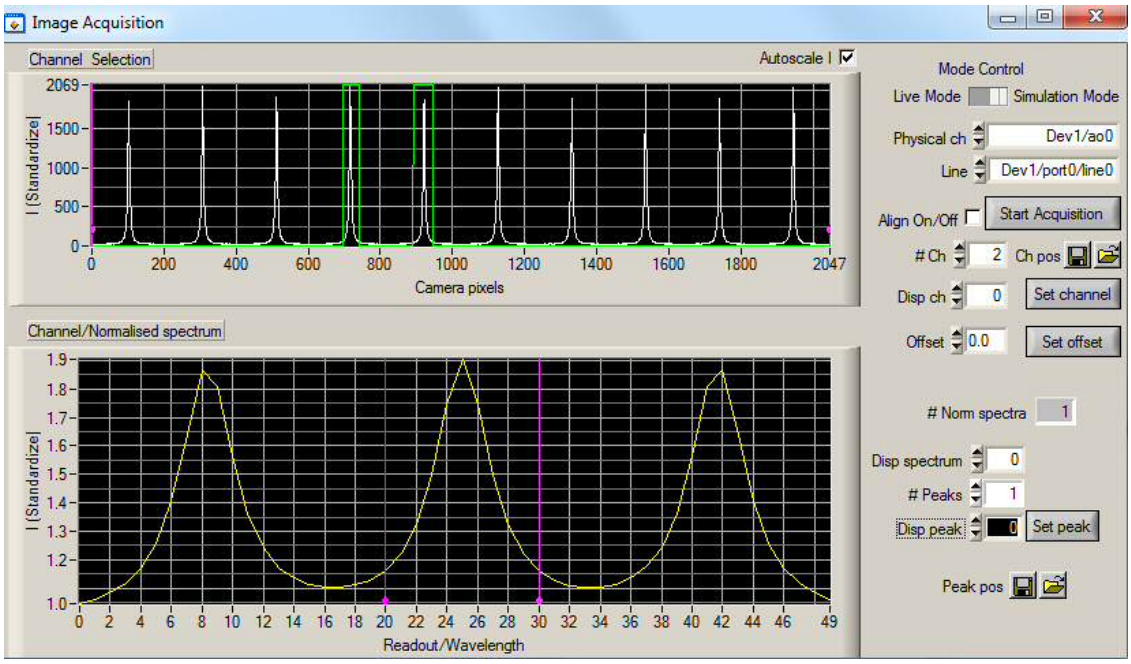

Figure B.5: Image acquisition panel to define channels, plot spectrum and define peaks for fitting. A simulated buffer is shown in the upper part of Fig. B.5 in which two channels are marked in green. Normalized channel spectrum is shown in lower part of Fig. B.5 with the selected peak marked in purple.

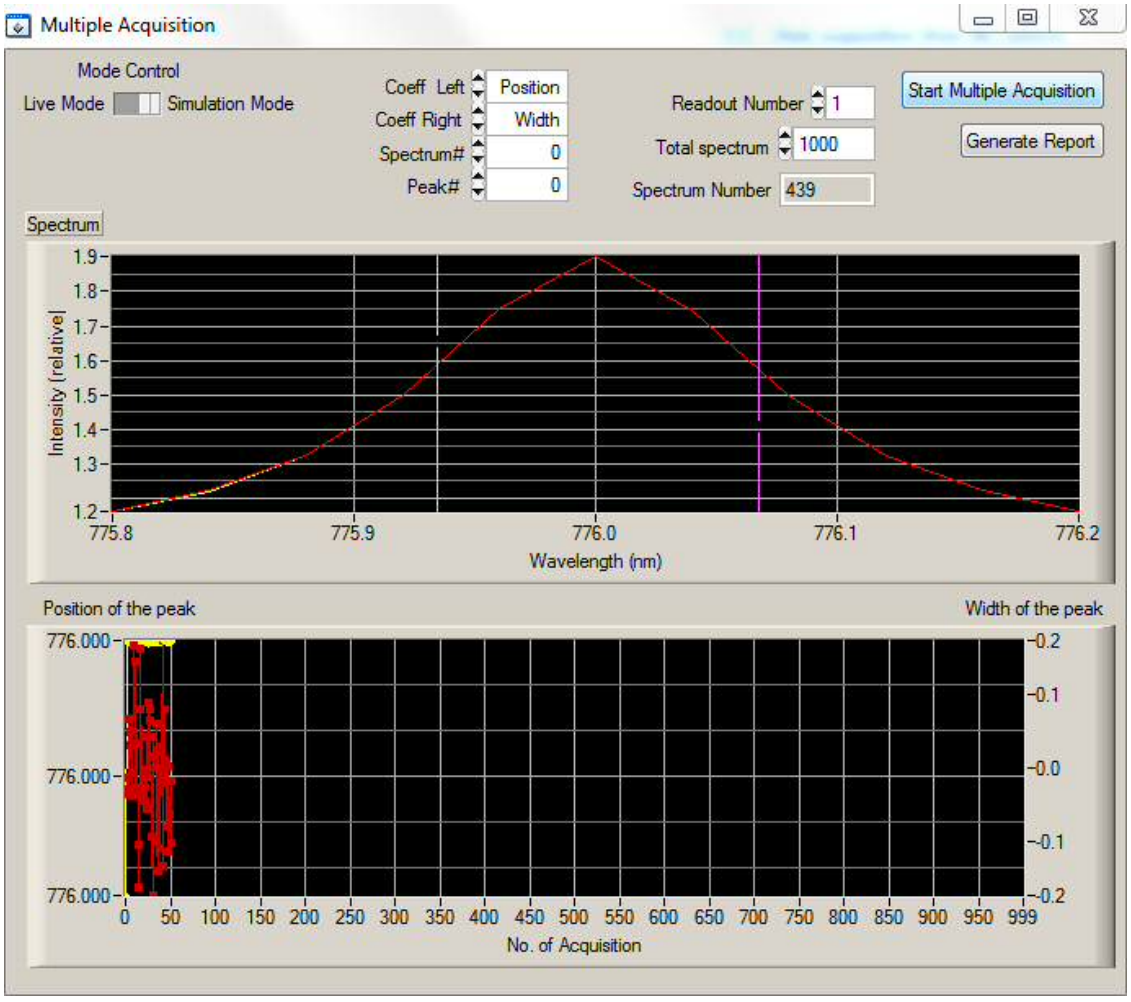

Figure B.6: Multiple acquisition panel in simulation mode. The selected and fitted data (top graph) and the position and width of the peak (bottom) are plotted.

Appendix C

C.1 Method of extracting absolute phase from DIC images

The method of extracting absolute phase from DIC images to determine the thickness of the SU-8 WGs, low RI polymer layer and a combination of SU-8 waveguides with low RI polymer layer on top is described below:

1. Switch on the PC and the camera. The EOS utility software should automatically start. If not, start it from the start menu.
2. Click the third heading in the list 'Camera settings/remote shooting'.
3. The dial next to the on/off switch on the camera should be set to 'Tv'; this setting allows selection of capture parameters like exposure time etc through the software.
4. On the panel that opens up, click 'Preference' to select a destination folder on the D drive. Use an extarnal drive to transfer the images.
5. On the same panel, click 'Remote live view shooting'. Set the sensitivity and select automatic white balancing.
6. LBD filter is needed to produce daylight balanced light. ND6 and ND25 filters are typically needed to avoid overexposure.
7. The eyepiece slider rod should be all the way out so that all the light enters the camera.
8. To acquire images without quantitative information, set the image format as 'Large normal' quality. The output file is in jpg format, with a non-linear intensity transfer function.
9. For quantitative analysis,i.e., for DIC measurement, set the image format as RAW. This saves images in the proprietary Canon format (extension CR2).
10. Use the linear transfer function by ticking the 'Linear' box in the Tool Palette panel (View-> Tool Palette).Use the full intensity range range (about -9..+3.8 stops).
11. To analyze the images, convert the CR2 file in Tiff16bit or Tiff8bit using the software Digital Photo Professional (File->Convert and Save).

12. Slid in the DIC prism, polarizer and analyzer in the beam path for DIC measurement.

13. Select 20x objective.

14. Adjust the polarizer such that the white dot is more or less point towards you.

15. Rotate the condenser turret to bring the appropriate DIC prism into place to have a DIC image, i.e. DP20 for 20x objective.

16. Minimize the background intensity using both the polarizer and the DIC slider insert. This is the zero phase image. Take the image. The arrow on the knob helps to point the reference.

17. Once the zero phase is determined take two more RAW images by rotating the analyzer knob by 237°clockwise and anticlockwise as 90°from the reference. 90°phase shift corresponds to a rotation of 237°.

18. Use the linear transfer function in the Tool Palette panel and convert the RAW images to 16 bit .tiff files.

19. Convert the 16 bit (.tiff) files to grayscale in IrfanView (Ctrl+G),

20. Count background in ImageJ (Ctrl+M) of the zero phase image.

21. Create a general folder and two sub-folders 'p' and 'm' inside the general folder. 'p' subfolder should have the image taken when the analyzer knob was rotated clockwise by 237°. 'm' subfolder should have the image taken when the analyzer knob was rotated anticlockwise by 237°. Rename the files as IMG000000000.tif in both these folders.

22. Write the path address where general folder is located. This folder should contain all the images with 'p' and 'm' sub-folders. Write 'p' for Plus folder and 'm' for Minus folder.

23. Prefix should be IMG and No. of digits should be 9, suffix should be left empty. Click on 'Check' to see if files are correctly named.

24. Click on 'Integral' button. Image of the plus polarization will appear.

25. Select a rectangular area of interest with a mouse.

26. Integrated data will be stored in the 'Out' folder.

27. Running the sequence again will overwrite all the files in 'Out' folder.

28. Open ImageJ to import 'phi.dat' file (File->Import->Text Image) produced by the software inside the out sub folder in the general folder.

29. Plot line profile (Analyze->Plot profile or Ctrl+K).

30. Profile height is the phase shift in radians, thickness of the sample is $Phaseshift/[k_0 * (n_s - n_m)]$, where k_0 is the free space wave vector, n_s is the refractive index of the sample and n_m is the refractive index of the medium where the sample is in.

C.2 Technical specification of Laser Diode in Sacher Laser System

Parameter	Value	Unit
Manufacturer	Eagleyard	-
Operational temperature (max)	40	°C
Forward current (max)	160	mA
Centre wavelength (at 25°C)	784 ± 1	nm
Spectral width (at 25°C, FWHM, typ)	2	MHz
Temperature coefficient of wavelength (at 25°C, typ)	0.06	nm/K
Output power (at 25°C, typ)	100	mW
Threshold current (at 25°C)	45 ± 15	mA
Operational current (at 25°C, max)	140	mA
Divergence (parallel, typ)	8	°
Divergence (perpendicular, typ)	21	°

Table C.1: Technical specification of Laser Diode in Sacher Laser System [168]. The laser system is temperature (110 μeV/K) and current (4 μeV/mA) tunable.

C.3 Procedure to analyze data by CCDPlot

CCDPlot is a tool for 2D data analysis and 2D data processing, created and developed by Prof Wolfgang Langbein and his team.

CCDPlot can import bitmap (BMP) image files to analyze experimental data. The procedure to create and import BMP files into CCDPlot is follows: we have to first convert the Audio Video Interleave (AVI) files from the camcorder to BMP files by running VLC media player in administrator mode. VLC media player is a media player. The Recording ratio for VLC media player has to be set 1 as the frame rate of the camcorder is 25 frame per second. This process creates 32 bit BMP files. Then one has to convert these 32 bit BMP files to 24 bit BMP files. This can be done in a batch conversation by using a graphic viewer application, IrfanView. Once the file conversion is completed the BMP files need to be imported into the CCDPlot to begin the analysis.

C.4 Technical specification of polarization displacer

Parameter	Value	Unit
Material	Calcite	-
Crystal cut with Optical axis	45± 0.5	°
Transparency Range	350-2300	nm
Density	2.3	g/cm^3
Refractive index (at 784nm, n_o)	1.6492	-
Refractive index (at 784nm, n_e)	1.4823	-
Thickness	550± 50	µm
Expected displacement (at 784nm)	60	µm

Table C.2: Technical specification of calcite polarization displacer [169].

C.5 Technical specification of Linescan camera

Parameter	Value	Unit
Manufacturer	e2V	-
Model name	AViiVA UM2-2014	-
Camera Type	CCD	-
Interface	Gigabit Ethernet	-
Number of pixels	2048	-
Pixel size	14	µm
Line rate (max)	29	kHz

Table C.3: Technical specification of the linescan camera used [143].

C.6 Technical specification of NI DAQ card

Parameter	Value	Unit
Manufacturer	National instruments	-
Product Family	Multifunction DAQ	-
Form Factor	PCI	-
I/O Connector	68	pin
Logic levels	TTL	-
Max Source Frequency	80	MHz
Analogue Input/Output resolution	16	bit
Analogue single-ended channels	32	-
Analogue differential channels	16	-
Analogue maximum voltage range	-10 to +10	V
Analogue ouput channels	4	-
Digital bidirectional channels	48	-
Digital maximum clock rate	10	MHz
Digital maximum voltage range	0 to +5	V
Triggering	Analog and Digital	-
Counters	2	-

Table C.4: Technical specification of NI PCI-6259 card used [145].

List of Figures

List of Tables

Bibliography

[1] William R. Heineman and William B. Jensen. Leland c. clark jr. (1918–2005). *Biosensors and Bioelectronics*, 21(8):1403–1404, feb 2006.

[2] N. Bhalla, P. Jolly, N. Formisano, and P. Estrela. Introduction to biosensors. *Essays In Biochemistry*, 60(1):1–8, jun 2016.

[3] Matthew A. Cooper, editor. *Label-Free Biosensors*. Cambridge University Press, 2009.

[4] Jeffrey D Newman and Anthony PF Turner. Home blood glucose biosensors: a commercial perspective. *Biosensors and Bioelectronics*, 20(12):2435–2453, 2005.

[5] Rebecca L. Rich and David G. Myszka. BIACORE j: a new platform for routine biomolecular interaction analysis. *Journal of Molecular Recognition*, 14(4):223–228, 2001.

[6] James Chambers, Bernard Arulanandam, Leann L Matta, Alex Weis, and James Valdes. Biosensor recognition elements. 10:1–12, 01 2008.

[7] Leland C. Clark and Champ Lyons. ELECTRODE SYSTEMS FOR CONTINUOUS MONITORING IN CARDIOVASCULAR SURGERY. *Annals of the New York Academy of Sciences*, 102(1):29–45, dec 2006.

[8] Georgia-Paraskevi Nikoleli, Stephanos Karapetis, Spyridoula Bratakou, Dimitrios P. Nikolelis, Nikolaos Tzamtzis, Vasilios N. Psychoyios, and Nikolas Psaroudakis. Biosensors for security and bioterrorism: Definitions, history, types of agents, new trends and applications. In *Biosensors for Security and Bioterrorism Applications*, pages 1–13. Springer International Publishing, 2016.

[9] The Diabetes Control and Complications Trial Research Group. The effect of intensive treatment of diabetes on the development and progression of long-term complications in insulin-dependent diabetes mellitus. *New England Journal of Medicine*, 329(14):977–986, sep 1993.

[10] Nalinee Poolsup, Naeti Suksomboon, and Somying Rattanasookchit. Meta-analysis of the benefits of self-monitoring of blood glucose on glycemic control in type 2 diabetes patients: An update. *Diabetes Technology & Therapeutics*, 11(12):775–784, dec 2009.

[11] G. H. Murata, J. H. Shah, R. M. Hoffman, C. S. Wendel, K. D. Adam, P. A. Solvas, S. U. Bokhari, and W. C. Duckworth. Intensified blood glucose monitoring improves glycemic control in stable, insulin-treated veterans with type 2

diabetes: The diabetes outcomes in veterans study (DOVES). *Diabetes Care*, 26(6):1759–1763, jun 2003.

[12] Eun-Hyung Yoo and Soo-Youn Lee. Glucose biosensors: An overview of use in clinical practice. *Sensors*, 10(12):4558–4576, may 2010.

[13] Bogdan Solnica, Jerzy W. Naskalski, and Jacek Sieradzki. Analytical performance of glucometers used for routine glucose self-monitoring of diabetic patients. *Clinica Chimica Acta*, 331(1):29 – 35, 2003.

[14] R A Smith, A C von Eschenbach, R Wender, B Levin, T Byers, D Rothenberger, D Brooks, W Creasman, C Cohen, C Runowicz, D Saslow, V Cokkinides, H Eyre, and ACS Endometrial Cancer Advisory Committee ACS Prostate Cancer Advisory Committee, ACS Colorectal Cancer Advisory Committee. American cancer society guidelines for the early detection of cancer: update of early detection guidelines for prostate, colorectal, and endometrial cancers. also: update 2001–testing for early lung cancer detection. *CA: a cancer journal for clinicians*, 51:38–75; quiz 77–80, 2001.

[15] Shaker Mousa. Biosensors: the new wave in cancer diagnosis. *Nanotechnology, Science and Applications*, page 1, dec 2010.

[16] Joseph Wang. Electrochemical biosensors: Towards point-of-care cancer diagnostics. *Biosensors and Bioelectronics*, 21(10):1887–1892, apr 2006.

[17] Dorothee Grieshaber, Robert MacKenzie, Janos Vörös, and Erik Reimhult. Electrochemical biosensors - sensor principles and architectures. *Sensors*, 8(3):1400–1458, mar 2008.

[18] David Gaddes, William Brian Reeves, and Srinivas Tadigadapa. Calorimetric biosensing system for quantification of urinary creatinine. *ACS Sensors*, 2(6):796–802, may 2017.

[19] N. Gözde Durmuş, Richard L. Lin, Mariel Kozberg, Deniz Dermici, Ali Khademhosseini, and Utkan Demirci. Acoustic-based biosensors. In *Encyclopedia of Microfluidics and Nanofluidics*, pages 1–15. Springer US, 2014.

[20] P.N. Prasad. *Introduction to Biophotonics*. Wiley, 2004.

[21] D. W. Lubbers and N. Opitz. Quantitative fluorescence photometry with biological fluids and gases. In *Advances in Experimental Medicine and Biology*, pages 65–68. Springer US, 1976.

[22] Matthew R. Foreman, Jon D. Swaim, and Frank Vollmer. Whispering gallery mode sensors. *Adv. Opt. Photon.*, 7(2):168–240, Jun 2015.

[23] Michael L. Metzker, Jing Lu, and Richard A. Gibbs. Electrophoretically uniform fluorescent dyes for automated dna sequencing. *Science*, 271(5254):1420–1422, 1996.

[24] Igor L. Medintz, Aaron R. Clapp, Hedi Mattoussi, Ellen R. Goldman, Brent Fisher, and J. Matthew Mauro. Self-assembled nanoscale biosensors based on quantum dot FRET donors. *Nature Materials*, 2(9):630–638, aug 2003.

[25] Daniel L Graham, Hugo A Ferreira, and Paulo P Freitas. Magnetoresistive-based biosensors and biochips. *TRENDS in Biotechnology*, 22(9):455–462, 2004.

[26] Kevin Catt and Geoffrey W Tregear. Solid-phase radioimmunoassay in antibody-coated tubes. *Science*, 158(3808):1570–1572, 1967.

[27] Shuming Nie and Richard N. Zare. OPTICAL DETECTION OF SINGLE MOLECULES. *Annual Review of Biophysics and Biomolecular Structure*, 26(1):567–596, jun 1997.

[28] S Nie, D. Chiu, and R. Zare. Probing individual molecules with confocal fluorescence microscopy. *Science*, 266(5187):1018–1021, nov 1994.

[29] Chris Rowe Taitt, George P. Anderson, and Frances S. Ligler. Evanescent wave fluorescence biosensors: Advances of the last decade. *Biosensors and Bioelectronics*, 76:103–112, feb 2016.

[30] Andrea M Armani, Rajan P Kulkarni, Scott E Fraser, Richard C Flagan, and Kerry J Vahala. Label-free, single-molecule detection with optical microcavities. *Science (New York, N.Y.)*, 317(5839):783–7, 2007.

[31] Tatiana Duque, Antonio Carlos Chaves Ribeiro, Henrique Santiago de Camargo, Paulo Alves da Costa Filho, Hannah Paula Mesquita Cavalcante, and Diogo Lopes. New insights on optical biosensors: Techniques, construction and application. In *State of the Art in Biosensors - General Aspects*. InTech, mar 2013.

[32] A WAGGONER. Fluorescent labels for proteomics and genomics. *Current Opinion in Chemical Biology*, 10(1):62–66, feb 2006.

[33] Maria Strianese, Maria Staiano, Giuseppe Ruggiero, Tullio Labella, Claudio Pellecchia, and Sabato D'Auria. Fluorescence-based biosensors. In *Methods in Molecular Biology*, pages 193–216. Humana Press, 2012.

[34] Maria Staiano, Paolo Bazzicalupo, Mose' Rossi, and Sabato D'Auria. Glucose biosensors as models for the development of advanced protein-based biosensors. *Molecular BioSystems*, 1(5-6):354, 2005.

[35] I. A. Nazarenko, S. K. Bhatnagar, and R. J. Hohman. A closed tube format for amplification and detection of DNA based on energy transfer. *Nucleic Acids Research*, 25(12):2516–2521, jun 1997.

[36] Gavin MacBeath and Stuart L Schreiber. Printing proteins as microarrays for high-throughput function determination. *Science*, 289(5485):1760–1763, 2000.

[37] Michael Hogardt, Karlheinz Trebesius, Anna M Geiger, Mathias Hornef, Josef Rosenecker, and Jürgen Heesemann. Specific and rapid detection by fluorescent in situ hybridization of bacteria in clinical samples obtained from cystic fibrosis patients. *Journal of clinical microbiology*, 38(2):818–825, 2000.

[38] Ying-Feng Chang, Sheng-Fan Wang, Jason C. Huang, Li-Chen Su, Ling Yao, Ying-Chang Li, Suh-Chin Wu, Yi-Ming A. Chen, Jo-Ping Hsieh, and Chien Chou. Detection of swine-origin influenza a (h1n1) viruses using a localized surface plasmon coupled fluorescence fiber-optic biosensor. *Biosensors and Bioelectronics*, 26(3):1068–1073, nov 2010.

[39] Richard A Cardullo, Sudhir Agrawal, Carlos Flores, Paul C Zamecnik, and David E Wolf. Detection of nucleic acid hybridization by nonradiative fluorescence resonance energy transfer. *Proceedings of the National Academy of Sciences*, 85(23):8790–8794, 1988.

[40] Werner G. Kuhr and Edward S. Yeung. Indirect fluorescence detection of native amino acids in capillary zone electrophoresis. *Analytical Chemistry*, 60(17):1832–1834, sep 1988.

[41] Homme W Hellinga and Jonathan S Marvin. Protein engineering and the development of generic biosensors. *Trends in Biotechnology*, 16(4):183–189, apr 1998.

[42] Sanjay Tyagi and Fred Russell Kramer. Molecular beacons: Probes that fluoresce upon hybridization. *Nature Biotechnology*, 14(3):303–308, mar 1996.

[43] Sanjay Tyagi, Salvatore A.E. Marras, and Fred Russell Kramer. Wavelength-shifting molecular beacons. *Nature Biotechnology*, 18(11):1191–1196, nov 2000.

[44] Frances S. Ligler and Chris Rowe Taitt. *Optical Biosensors: Present & Future*. Elsevier Science, 2002.

[45] A.S. Verkman, M.C. Sellers, A.C. Chao, T. Leung, and R. Ketcham. Synthesis and characterization of improved chloride-sensitive fluorescent indicators for biological applications. *Analytical Biochemistry*, 178(2):355 – 361, 1989.

[46] M Chalfie, Y Tu, G Euskirchen, W. Ward, and D. Prasher. Green fluorescent protein as a marker for gene expression. *Science*, 263(5148):802–805, feb 1994.

[47] Israel Biran, Xin Yu, and David R. Walt. OPTRODE-BASED FIBER OPTIC BIOSENSORS (BIO-OPTRODE). In *Optical Biosensors*, pages 3–82. Elsevier, 2008.

[48] Eva Engvall and Peter Perlmann. Enzyme-linked immunosorbent assay, elisa iii. quantitation of specific antibodies by enzyme-labeled anti-immunoglobulin in antigen-coated tubes. *The Journal of Immunology*, 109(1):129–135, 1972.

[49] Rebecca L. Rich and David G. Myszka. Survey of the year 2004 commercial optical biosensor literature. *Journal of Molecular Recognition*, 18(6):431–478, 2005.

[50] P. Damborsky, J. vitel, and J. Katrlik. Optical biosensors. *Essays In Biochemistry*, 60(1):91–100, jun 2016.

[51] Philipp Angenendt. Progress in protein and antibody microarray technology. *Drug discovery today*, 10(7):503–511, 2005.

[52] Martin Baaske and Frank Vollmer. Optical resonator biosensors: Molecular diagnostic and nanoparticle detection on an integrated platform. *ChemPhysChem*, 13(2):427–436, 2012.

[53] R M Sutherland, C Dähne, J F Place, and A S Ringrose. Optical detection of antibody-antigen reactions at a glass-liquid interface. *Clinical Chemistry*, 30(9):1533–1538, 1984.

[54] J.N. Lin, J.D. Andrade, and I.-N. Chang. The influence of adsorption of native and modified antibodies on their activity. *Journal of Immunological Methods*, 125(1-2):67–77, dec 1989.

[55] N .J. Harrick. *Internal Reflection Spectroscopy*. John Wiley & Sons Inc, 1967.

[56] E. Kretschmann and H. Raether. Notizen: Radiative decay of non radiative surface plasmons excited by light. *Zeitschrift fÃ¼r Naturforschung A*, 23(12), jan 1968.

[57] Bo Liedberg, Claes Nylander, and Ingemar Lunström. Surface plasmon resonance for gas detection and biosensing. *Sensors and actuators*, 4:299–304, 1983.

[58] A. D. Boardman. *Electromagnetic Surface Modes*. John Wiley & Sons Ltd, 1982.

[59] J Homola, Sinclair S Yee, and Günter Gauglitz. Surface plasmon resonance sensors: review. *Sensors and Actuators B: Chemical*, 54(1):3–15, 1999.

[60] Allan W. Snyder and John D. Love. *Optical Waveguide Theory*. Springer US, 1984.

[61] Frank Vollmer and Stephen Arnold. Whispering-gallery-mode biosensing: label-free detection down to single molecules. *Nature methods*, 5(7):591–596, 2008.

[62] Julie Lutti, Wolfgang Langbein, and Paola Borri. High Q optical resonances of polystyrene microspheres in water controlled by optical tweezers. *Applied Physics Letters*, 91(14):3–5, 2007.

[63] R. D. Richtmyer. Dielectric resonators. *Journal of Applied Physics*, 10(6):391–398, 1939.

[64] Alexandre Francois, Sivashankar Krishnamoorthy, and Michael Himmelhaus. Advances in label-free optical biosensing: direct comparison of whispering gallery mode sensors with surface plasmon resonance. *Proceedings of SPIE*, 6862(Afp 9):686211–686211–7, 2008.

[65] F. Vollmer, D. Braun, A. Libchaber, M. Khoshsima, I. Teraoka, and S. Arnold. Protein detection by optical shift of a resonant microcavity. *Applied Physics Letters*, 80(21):4057–4059, 2002.

[66] Robert Karlsson and Ralph Stahlberg. Surface plasmon resonance detection and multispot sensing for direct monitoring of interactions involving low-molecular-weight analytes and for determination of low affinities. *Analytical biochemistry*, 228(2):274–280, 1995.

[67] F Vollmer, S Arnold, and D Keng. Single virus detection from the reactive shift of a whispering-gallery mode. *Proceedings of the National Academy of Sciences of the United States of America*, 105(52):20701–20704, 2008.

[68] A. K. Naik, M. S. Hanay, W. K. Hiebert, X. L. Feng, and M. L. Roukes. Towards single-molecule nanomechanical mass spectrometry. *Nature Nanotechnology*, 4:445–450, July 2009.

[69] Jia ming Liu. *Photonic Devices*. Cambridge University Press, 2005.

[70] R.G. Hunsperger. *Integrated Optics: Theory and Technology*. Advanced texts in physics. Springer, 2009.

[71] F. Hadjaj, A. Belghachi, A. Halmaoui, M. Belhadj, and H. Mazouz. Study of a Fabry Perot resonator. *International Journal of Physical and Mathematical Sciences*, 7, 2013.

[72] Norman Hodgson and Horst Weber. *Optical Resonators*. Springer London, 1997.

[73] Lord Rayleigh O.M. F.R.S. Cxii. the problem of the whispering gallery. *Philosophical Magazine Series 6*, 20(120):1001–1004, 1910.

[74] C. C. Lam, P. T. Leung, and K. Young. Explicit asymptotic formulas for the positions, widths, and strengths of resonances in mie scattering. *J. Opt. Soc. Am. B*, 9(9):1585–1592, Sept 1992.

[75] JM Gérard, B Sermage, B Gayral, B Legrand, E Costard, and V Thierry-Mieg. Enhanced spontaneous emission by quantum boxes in a monolithic optical microcavity. *Physical review letters*, 81(5):1110, 1998.

[76] B.E. Little, S.T. Chu, H.A. Haus, J. Foresi, and J.-P. Laine. Microring resonator channel dropping filters. *Journal of Lightwave Technology*, 15(6):998–1005, jun 1997.

[77] S. L. McCall, A. F. J. Levi, R. E. Slusher, S. J. Pearton, and R. A. Logan. Whispering-gallery mode microdisk lasers. *Applied Physics Letters*, 60(3):289–291, jan 1992.

[78] D. K. Armani, T. J. Kippenberg, S. M. Spillane, and K. J. Vahala. Ultra-high-q toroid microcavity on a chip. *Nature*, 421(6926):925–928, feb 2003.

[79] Deniz Armani, Bumki Min, Andrea Martin, and Kerry J. Vahala. Electrical thermo-optic tuning of ultrahigh-q microtoroid resonators. *Applied Physics Letters*, 85(22):5439–5441, nov 2004.

[80] Kartik Srinivasan, Paul E. Barclay, Oskar Painter, Jianxin Chen, Alfred Y. Cho, and Claire Gmachl. Experimental demonstration of a high quality factor photonic crystal microcavity. *Applied Physics Letters*, 83(10):1915–1917, sep 2003.

[81] G. C. Righini, Y. Dumeige, P. Féron, M. Ferrari, G. Nunzi Conti, D. Ristic, and S. Soria. Whispering Gallery Mode microresonators: Fundamentals and applications. *Rivista del Nuovo Cimento*, 34(7):435–488, 2011.

[82] Samira Hosseini, Fatimah Ibrahim, Ivan Djordjevic, and Leo H Koole. Recent advances in surface functionalization techniques on polymethacrylate materials for optical biosensor applications. *The Analyst*, 139(12):2933–43, 2014.

[83] John Heebner, Rohit Grover, and Tarek Ibrahim. *Optical Microresonators*, volume 138 of *Optical Sciences*. Springer New York, 2008.

[84] Andrey Matsko. *Practical Applications of Microresonators in Optics and Photonics*. CRC Press, Inc., Boca Raton, FL, USA, 1st edition, 2009.

[85] S Arnold, M Khoshsima, I Teraoka, S Holler, and F Vollmer. Shift of whispering-gallery modes in microspheres by protein adsorption. *Optics letters*, 28(4):272–274, 2003.

[86] Julie Lutti, Wolfgang Langbein, and Paola Borri. A monolithic optical sensor based on whispering-gallery modes in polystyrene microspheres. *Applied Physics Letters*, 93(15):3–5, 2008.

[87] S Arnold, S I Shopova, and S Holler. Whispering gallery mode bio-sensor for label-free detection of single molecules: thermo-optic vs. reactive mechanism. *Optics express*, 18(1):281–287, 2010.

[88] A.B. Matsko and V.S. Ilchenko. Optical resonators with whispering-gallery modes-part i: basics. *IEEE Journal of Selected Topics in Quantum Electronics*, 12(1):3–14, jan 2006.

[89] M. L. Gorodetsky and V. S. Ilchenko. Optical microsphere resonators: optimal coupling to high-q whispering-gallery modes. *Journal of the Optical Society of America B*, 16(1):147, jan 1999.

[90] M.L. Gorodetsky and V.S. Ilchenko. High-q optical whispering-gallery microresonators: precession approach for spherical mode analysis and emission patterns with prism couplers. *Optics Communications*, 113(1-3):133–143, dec 1994.

[91] M. L. Gorodetsky, A. A. Savchenkov, and V. S. Ilchenko. Ultimate q of optical microsphere resonators. *Optics Letters*, 21(7):453, apr 1996.

[92] Max Born and Emil Wolf. *Principles of Optics*. Cambridge University Pr., 2002.

[93] R. E. Benner, P. W. Barber, J. F. Owen, and R. K. Chang. Observation of structure resonances in the fluorescence spectra from microspheres. *Physical Review Letters*, 44(7):475–478, feb 1980.

[94] A. Ashkin and J. M. Dziedzic. Observation of optical resonances of dielectric spheres by light scattering. *Applied Optics*, 20(10):1803–1814, may 1981.

[95] L Collot, V Lefèvre-Seguin, M Brune, J. M Raimond, and S Haroche. Very high- q whispering-gallery mode resonances observed on fused silica microspheres. *Europhysics Letters (EPL)*, 23(5):327–334, aug 1993.

[96] S. Arnold. Microspheres, photonic atoms and the physics of nothing. *American Scientist*, 89(5):414–421, 2001.

[97] H. M. Lai, P. T. Leung, and K. Young. Limitations on the photon storage lifetime in electromagnetic resonances of highly transparent microdroplets. 41(9):5199–5204, 1990.

[98] Julius Adams Stratton. *Electro Magnetic Theory*. McGraw-Hill Book Company, Inc., 1941.

[99] B. R. Johnson. Theory of morphology-dependent resonances: shape resonances and width formulas. *Journal of the Optical Society of America A*, 10(2):343, 1993.

[100] Iwao Teraoka, Stephen Arnold, and Frank Vollmer. Perturbation approach to resonance shifts of whispering-gallery modes in a dielectric microsphere as a probe of a surrounding medium. *Journal of the Optical Society of America B*, 20(9):1937, 2003.

[101] S. Schiller. Asymptotic expansion of morphological resonance frequencies in mie scattering. *Applied Optics*, 32(12):2181–2185, apr 1993.

[102] Milton Abramowitz and Irene A. Stegun. *Handbook of Mathematical Functions with Formulas, Graphs, and Mathematical Tables*. Dover, New York, ninth dover printing, tenth gpo printing edition, 1964.

[103] V.B. Braginsky, M.L. Gorodetsky, and V.S. Ilchenko. Quality-factor and nonlinear properties of optical whispering-gallery modes. *Physics Letters A*, 137(7-8):393–397, may 1989.

[104] Xudong Fan, Ian M. White, Siyka I. Shopova, Hongying Zhu, Jonathan D. Suter, and Yuze Sun. Sensitive optical biosensors for unlabeled targets: A review. *Analytica Chimica Acta*, 620(1-2):8–26, 2008.

[105] D. Q. Chowdhury, S. C. Hill, and P. W. Barber. Morphology-dependent resonances in radially inhomogeneous spheres. *Journal of the Optical Society of America A*, 8(11):1702, 1991.

[106] Y Panitchob, G Senthil Murugan, M N Zervas, P Horak, S Berneschi, S Pelli, G Nunzi Conti, and J S Wilkinson. Whispering gallery mode spectra of channel waveguide coupled microspheres. *Optics express*, 16(15):11066–11076, 2008.

[107] a Serpengüzel, S Arnold, and G Griffel. Excitation of resonances of microspheres on an optical fiber. *Optics letters*, 20(7):654–656, 1995.

[108] J C Knight, G Cheung, F Jacques, and T a Birks. Phase-matched excitation of whispering-gallery-mode resonances by a fiber taper. *Optics letters*, 22(15):1129–1131, 1997.

[109] L. Chantada, N. I. Nikolaev, A.L. Ivanov, Paola Borri, and Wolfgang Werner Langbein. Optical resonances in microcylinders: Response to perturbations for biosensing. *Journal of the Optical Society of America B*, 25(8):1312–1321, 2008.

[110] Ganapathy Senthil Murugan, Yuwapat Panitchob, Elizabeth J. Tull, Philip N. Bartlett, Daniel W. Hewak, Michalis N. Zervas, and James S. Wilkinson. Position-dependent coupling between a channel waveguide and a distorted microsphere resonator. *Journal of Applied Physics*, 107(5):053105, mar 2010.

[111] D.B. Murphy. *Fundamentals of Light Microscopy and Electronic Imaging*. Wiley, 2002.

[112] C.I. McPhee, G. Zoriniants, W. Langbein, and P. Borri. Measuring the lamellarity of giant lipid vesicles with differential interference contrast microscopy. *Biophysical Journal*, 105(6):1414 – 1420, 2013.

[113] Wilfried Heller. Remarks on refractive index mixture rules. *The Journal of Physical Chemistry*, 69(4):1123–1129, 1965.

[114] My Polymers. Properties of my133, accessed: 18 august 2013. Technical report, MyPolymer, 2010.

[115] Thomas P. Davis Krzysztof Matyjaszewski. *Handbook of Radical Polymerization*. JOHN WILEY & SONS INC, 2002.

[116] Microchem. Technical report, accessed: 22 september 2016. Technical report, http://www.microchem.com/.

[117] RefractiveIndex.INFO. Refractiveindex database, accessed: 22 september 2018. Technical report, http://refractiveindex.info/, accessed on 29 September, 2016.

[118] Asahi glass. Asahi glass, accessed: 22 september 2016. Technical report, http://www.agc.com/english/index.html, accessed on 29 September, 2016. Supplier of Cytop.

[119] Chemours. Teflon af properties, accessed: 7 june 2017. Technical report, https://www.chemours.com.

[120] 3M. Fc-40 solvent, accessed: 7 june 2017. Technical report, http://multimedia.3m.com/mws/media/64888O/fluorinert-electronic-liquid-fc-40.pdf.

[121] Min K Yang, Roger H French, and Edward W Tokarsky. Optical properties of teflon® af amorphous fluoropolymers. *Journal of Micro/Nanolithography, MEMS, and MOEMS*, 7(3):033010–033010, 2008.

[122] Norland. Norland optical adhesive 133, accessed: 7 june 2017. Technical report, https://www.norlandprod.com/adhesives/NOA133.html.

[123] Mai Trang Do. *Fabrication of submicrometer 3D structures by one-photon absorption direct laser writing and applications*. PhD thesis, 01 2015.

[124] 3M. Novec 7500 solvent accessed 2 june 2018. Technical report, 3M, https://www.3m.com/, 2018.

[125] Agar. Properties of borosilicate coverslips, accessed: 18 august 2018. Technical report, Agar scientific, http://www.agarscientific.com/square-coverglasses-7448.html, 2018.

[126] Inc. Bivar. Technical specification of uvtz-390-15 uv led, accessed: 01 february 2015. Technical report, Bivar, http://www.Bivar.com, 2015.

[127] Hamamatsu. Si pin photodiodes, accessed: 28 may 2014. Technical report, https://www.hamamatsu.com/.

[128] Keithley. Website, accessed: 01 july 2016. Technical report, Keithley Instruments Ltd, http://www.tek.com/keithley, 2016.

[129] LED Engin. Uv led emitter, accessed: 22 april 2016. Technical report, LED ENGIN, http://www.ledengin.com/products/emitters, 2016. LZ1-10UV00 LED, 4V, 700mA, 4.4mm x 4.4mm, 2.8mW, 365nm, 70°.

[130] RS. Supplier of materials for uv exposure unit v 2, toggle switch, power socket, power supply, case, uv led lz1-10uv00. Technical report, RS components, http://uk.rs-online.com/web/, 2016.

[131] a Del Campo and C Greiner. SU-8: a photoresist for high-aspect-ratio and 3D submicron lithography. *Journal of Micromechanics and Microengineering*, 17(6):R81–R95, 2007.

[132] Klaus B Mogensen, Jamil El-Ali, Anders Wolff, and Jörg P Kutter. Integration of polymer waveguides for optical detection in microfabricated chemical analysis systems. *Applied optics*, 42(19):4072–4079, 2003.

[133] SPS-Europ. Supplier of spinner. Technical report.

[134] http://www.mypolymers.com/.

[135] Cargille Labs. Refractive index (matching) liquids, accessed: 22 september 2016. Technical report, http://www.cargille.com/refractivestandards.shtml, accessed on 29 September, 2016. Supplier of Refractive Index (Matching) Liquids.

[136] Veeco. Technical report, accessed: 11 june 2015. Technical report, Veeco, 2015.

[137] Duke. Manufacturer of ps beads, 30 micrometer. Technical report, 2016.

[138] UQG. Bk-7 glass substrate. Technical report, UQG Optics, http://www.uqgoptics.com/, accessed on 16 June, 2016, 2016.

[139] Edmund. Tech notes. Technical report, Edmund Optics Ltd, http://www.edmundoptics.co.uk, accessed on 16 June, 2016, 2016.

[140] Laser 2000. Distributor of sacher laser system. Technical report, Laser 2000, http://www.laser2000.co.uk/index.php, accessed on 16 June, 2016, 2016.

[141] AMS. Distributor of the diode in sacher laser system. Technical report, AMS Technology, http://www.amstechnologies.com/, accessed on 16 June, 2016, 2016.

[142] Alrad. Distributor of e2v line scan camera. Technical report, Alrad Imaging, http://www.alrad.co.uk/index.htm, accessed on 16 June, 2016, 2016.

[143] e2V. Aviiva line scan camera. Technical report, e2v, http://www.e2v.com/, accessed on 16 June, 2016, 2016.

[144] EHD. Distributor of 2d camera. Technical report, EHD, http://www.ehd.de/products/cmoscameras/smx-16x-cameras.pdf,accessed on 16 June, 2017, 2016.

[145] NI. Tech notes. Technical report, National Instruments, http://www.ni.com/en-gb.html, accessed on 16 September, 2016, 2016. Labwindows/CVI, multifunction Data Acquisition (DAQ) board, NI 6259 and Vision Acquisition Software.

[146] Sacher. Manufacturer for laser laser system. Technical report, Sacher Lasertechnik Group, https://www.sacher-laser.com/, accessed on 16 June, 2016, 2016.

[147] Olympus. Immersion oil. Technical report. Supplier of BX-50 olympus microscope.

[148] Nye Lubricants. Index matching fluid. Technical report, Nye Lubricants, http://www.nyelubricants.com/, accessed on 29 September, 2016. Supplier of Thixotropic gel, NyoGel OC-440.

[149] Axicon. Distributor of the neutral density filter. Technical report, Axicon, http://www.alrad.co.uk/index.htm, accessed on 16 June, 2016, 2016.

[150] Thorlabs. Manufacturer of plano convex lens, cylindrical lens, pinhole and components of different mounts. Technical report, Thorlabs, http://www.thorlabs.de/, accessed on 16 June, 2016, 2016. F-Mount Adapter, Pedestal pillar, Posts, Post Holders and Short Bases.

[151] Casix. Distributor of plano convex lens. Technical report, Casix, http://www.casix.com/, accessed on 16 June, 2016, 2016.

[152] Altechna. Manufacturer and distributor of polarization displacer. Technical report, Altechna, http://www.altechna.com/, accessed on 16 June, 2016, 2016.

[153] John N Coupland, Niamh B Shaw, Frank J Monahan, E Dolores O'Riordan, and Michael O'Sullivan. Modeling the effect of glycerol on the moisture sorption behavior of whey protein edible films. *Journal of food engineering*, 43(1):25–30, 2000.

[154] J Rheims, J Köser, and T Wriedt. Refractive-index measurements in the near-IR using an abbe refractometer. *Measurement Science and Technology*, 8(6):601–605, jun 1997.

[155] Mettler Toledo. Mettler Toledo, https://www.mt.com/us/en/home.

[156] Romain Guider, Davide Gandolfi, Tatevik Chalyan, Laura Pasquardini, Alina Samusenko, Cecilia Pederzolli, Georg Pucker, and Lorenzo Pavesi. Sensitivity and limit of detection of biosensors based on ring resonators. *Sensing and Bio-Sensing Research*, 6:99–102, 2015.

[157] Newport. The supplier of the micrometer stage. Technical report, Newport, 2018.

[158] Bangs Labs. Tech notes. Technical report, Bangs Laboratories, Inc., http://www.bangslabs.com/support/technical-support/technotes, accessed on 16 June, 2015.

[159] Yongwon Jung, Jin Young Jeong, and Bong Hyun Chung. Recent advances in immobilization methods of antibodies on solid supports. *The Analyst*, 133(6):697–701, 2008.

[160] Michèle Salem, Yves Mauguen, and Thierry Prangé. Revisiting glutaraldehyde cross-linking: the case of the Arg–Lys intermolecular doublet. *Acta Crystallographica Section F*, 66(3):225–228, Mar 2010.

[161] Thermo Scientific. Crosslinking technology - reactivity chemistries, applications and structure references. Technical report.

[162] Nico J. Mol and Marcel J. E. Fischer. *Amine Coupling Through EDC/NHS: A Practical Approach*, volume 627 of *Methods in Molecular Biology*. Humana Press, 2010.

[163] Polysciences. Polystyrene microspheres, frequently asked questions. accessed: 24 june 2017. Technical report.

[164] Polina Prokopovich, editor. *Biological and Pharmaceutical Applications of Nanomaterial*. 2015.

[165] Dow. Microposit ec solvent, accessed: 7 june 2014. Technical report, https://www.dow.com/.

[166] Casix. Distributor of waveplates. Technical report, Casix, http://www.casix.com/products/glass-optics/instrument-optics/waveplates.shtml,accessed on 16 June, 2017, 2016.

[167] Best. Distributor of pentax line scan lens. Technical report, Best Scientific, http://www.bestscientificweb.com/, accessed on 16 June, 2016, 2016.

[168] Eagleyard. Manufacturer of the diode in sacher laser system. Technical report, Eagleyard, http://www.eagleyard.com/, accessed on 16 June, 2016, 2016.

[169] Crystech. Properties of calcite polarization displacer. Technical report, Crystech, http://www.crystech.com/index.html, accessed on 16 June, 2016, 2016.